Dissertation zur Erlangung des Doktorgrades
der Fakultät für Chemie und Pharmazie
der Ludwig-Maximilians-Universität München

Structural Studies of the Translocases SecYEG-YidC, Bcs1 and PelBC

Cristian Rosales-Hernández

aus

Bogotá, Kolumbien

2025

Erklärung

Diese Dissertation wurde im Sinne von §7 der Promotionsordnung vom 28. November 2011 von Herrn Prof. Dr. Roland Beckmann betreut.

Eidesstattliche Versicherung

Diese Dissertation wurde eigenständig und ohne unerlaubte Hilfe erarbeitet.

München, December 3, 2025

Cristian Rosales-Hernandez

_____

Dissertation eingereicht am:	23.10.2025
1. Gutachter:	Prof. Dr. Roland Beckmann
2. Gutachter:	Prof. Dr. Karl-Peter Hopfner
Mündliche Prüfung am:	28.11.2025

Contents

List of Figures

List of Publications

Substrate-induced assembly and functional mechanism of the bacterial membrane protein insertase SecYEG-YidC.
Busch M[*], Rosales-Hernandez C[*], Kamel M[*], Schaumkessel Y, van der Sluis E, Berninghausen O, Becker T, Beckmann R[**], Kedrov A[**]
bioRxiv 2025.05.26.656142 (2025) doi: 10.1038/s41467-025-60605-8

Mechanistic insights into Bcs1-mediated mitochondrial membrane translocation of the folded Rieske protein.
Rosales-Hernandez C, Thoms M, Berninghausen O, Becker T, Beckmann R[**]
EMBO J 44:3720-3741, (2025), doi: 10.1038/s44318-025-00459-4

Assembly and the gating mechanism of the Pel exopolysaccharide export complex PelBC of *Pseudomonas aeruginosa*.
Benedens M[*], Rosales-Hernandez C[*], Straathof S, Loschwitz J, Berninghausen O, Maglia G, Beckmann R[**], Kedrov A[**]
Nat Comms 16, 5249, (2025), doi: 10.1038/s41467-025-60605-8

---

* Equal Contribution
** Corresponding Author

Contribution Report

This thesis covers research work conducted from April 2021 to November 2025 at the Gene Center of the Ludwig-Maximilians-Universität München, at the laboratory and under the supervision of Prof. Dr. Roland Beckmann. Two of the Publications were a result of collaborative work, performed with Prof. Dr. Alexej Kedrov's Research Group (Synthetic Membrane Systems Lab, Henrich Heine Universität Düsseldorf) and Prof. Dr. Giovanni Maglia (University of Groningen).

Publication 1 (Busch *et al.*, 2025)

As part of this publication, I optimised the cryo-EM sample preparation conditions and worked together with Dr. Otto Berninghausen in cryo-EM data acquisition and data curation. I performed the data analysis, generated the corresponding 3D reconstructions from the data and built the atomic model. I validated and deposited the model and the maps in the PDB database. Together with Dr. Thomas Becker, I analysed and visualised the data. I prepared the cryo-EM data processing figures and participated in the writing of the original and final versions of the manuscript.

Publication 2 (Rosales-Hernandez *et al.*, 2025)

In this publication, I performed the biochemical expression, purification and characterisation of Bcs1 and Bcs1-Rip1 complexes. I generated the cryo-EM samples and optimised the sample preparation conditions. I worked together with Dr. Otto Berninghausen in

cryo-EM data acquisition and data curation. I performed the data analysis, generated the corresponding 3D reconstructions from the data and built atomic models for those reconstructions. I validated and deposited the models and maps in the PDB database. With guidance from Dr. Matthias Thoms, I designed the mutagenesis experiments, generated the respective strains and performed the growth assays. Together with Dr. Thomas Becker, I prepared the initial figures and wrote the original draft of the manuscript. Together with all authors, I wrote the final version of the manuscript.

Publication 3 (Benedens *et al.*, 2025)

As part of this publication, I optimised the cryo-EM sample preparation conditions and worked together with Dr. Otto Berninghausen in cryo-EM data acquisition and data curation. I performed the data analysis, generated the corresponding 3D reconstructions from the data and validated the atomic model generated by Marius Benedens. I deposited the model and the map in the PDB database. I prepared the cryo-EM data processing figures and participated in the writing of the original and final versions of the manuscript.

Summary

The transport of substrates across biological membranes can be broadly classified into translocation of unfolded proteins (both co-translational and post-translational), translocation of folded proteins (exclusively post-translational), and transport of small molecules. In the research work carried out as part of this thesis, structural and functional aspects of a translocase for unfolded proteins in *Escherichia coli*, a translocase of a folded protein in the *Saccharomyces cerevisiae* mitochondrial inner membrane and a transporter of polysaccharides in *Pseudomonas aeruginosa* have been investigated, revealing novel aspects of their mechanism and offering new perspectives into their function in the context of the membranes where they reside.

The SecYEG translocon and the Oxa1 family member YidC from *Escherichia coli*, are central to the insertion and translocation activities in the bacterial membrane. Each of them can handle different substrates independently of the other, but specific substrates, such as the multi-pass membrane protein NuoK, one of the components of the respiratory complex I, require both for efficient insertion. However, a detailed molecular understanding of their cooperation, despite numerous efforts, so far remained elusive. This work presents the first cryo-EM structure of a SecYEG-YidC-NuoK complex, providing a structural basis for the insertion of multi-pass membrane proteins in the bacterial membrane. YidC is found at the back of SecYEG, with NuoK clamped in between, resembling the "back-of-sec" route described for eukaryotes. Furthermore, we have observed that the recruitment of YidC is dependent on the substrate length, as the SecYEG-YidC complex is not observed when the reconstitution is performed with truncated NuoK. Overall, this study has revealed for the first time the organisation of an active SecYEG-YidC bacterial multi-pass translocon,

shedding light into NuoK's insertion pathway and providing a robust method to study the insertion pathway of other membrane protein substrates.

Folded protein transport was investigated using an *in vitro* system comprising Bcs1 and its only but essential substrate Rip1. The single-pass membrane protein Rip1 is first targeted to the mitochondrial matrix, to be later translocated and its N-terminal transmembrane domain inserted into the inner (mitochondrial) membrane. This particular biogenesis route is necessary because Rip1's C-terminal globular domain harbours an iron-sulphur-cluster, which is synthesised and incorporated into Rip1 in the matrix. Bcs1, a heptameric AAA-ATPase embedded in the inner membrane, is the membrane protein responsible for this translocation and insertion activity. Previous studies of the *Saccharomyces cerevisiae* and *Mus musculus* Bcs1 lacking the Rip1 substrate led the to the proposal of an airlock-like mechanism, where Bcs1 alternates between two states, moving the substrate from a matrix-facing to an inner membrane embedded cavity, thus preserving the electrochemical proton gradient. In this work, we present the cryo-EM structures of Bcs1-Rip1 loading and translocation intermediates as well as their functional characterisation, providing experimental support for the airlock mechanism. We identify charge complementarity between interacting surfaces in Bcs1 and Rip1 as a major driver for the docking of the substrate in the matrix vestibule and its subsequent movement towards the inner membrane upon ATP binding. Taken together, these results provide molecular details into the mechanism of Bcs1, regarding how it coordinates substrate movement with ATP binding and hydrolysis, how it preserves the membrane permeability barrier and how the release step might proceed after Rip1 has moved to the inner membrane cavity.

Pseudomonas aeruginosa is an opportunistic human pathogen, particularly risky to immunocompromised patients. The ability of *Pseudomonas aeruginosa* to form biofilms partially explains its successful adaptation to hostile environments. The biofilm matrix is composed by exopolysaccharides such as Pel, which are synthesised and exported by dedicated protein machineries with components present in both the inner and outer membranes. In the outer membrane, a substrate-specific porin mediates the export of the polysaccharide. Interestingly, among the different polysaccharide export machineries, the export of

Pel appears to be mediated not only by the PelB porin, but also by PelC, a lipoprotein attached to the inner leaflet of the outer membrane. Nevertheless, the structural elucidation of PelC or a PelBC complex in *Pseudomonas aeruginosa* remained elusive, leading to open questions regarding the native stoichiometry of the complex and the determinants of its assembly. We present the cryo-EM structure of the PelBC complex reconstituted in lipid nanodiscs and further characterise it through molecular dynamics simulations and biophysical measurements. This approach allowed us to assign a 1:12 stoichiometry for the PelB:PelC complex and to identify the key features in PelC and PelB that stabilise their interaction, as well as elements that could guide the substrate through the porin towards the extracellular space. On the whole, our study has led to a model of substrate translocation across the outer membrane.

List of Abbreviations

AAA-ATPase	ATPase associated with diverse cellular activities
ATPγS	adenosine [γ-thio]triphosphate
BATCH	bacterial adenylate cyclase two-hybrid
Bcs1	ubiquinol-cytochrome c reductase (bc1) synthesis
mBcs1	*Mus musculus* (mouse) Bcs1
yBcs1	*Saccharomyces cerevisiae* (yeast) Bcs1
BD	base subdomain (of Rip1)
BSB	Bcs1-specific β-strands β-a1 and β-a2
BOS	back-of-sec complex
CAML	calcium modulating cyclophilin ligand
EAAT	excitatory amino acid transporter
EMC	ER membrane complex
ER	endoplasmic reticulum
E. coli	*Escherichia coli*
FeBD	Fe_2S_2-binding subdomain (of Rip1)
GalN	galactosamine
GalNAc	N-acetylgalactosamine
GEL	GET and EMC-like complex
GET	guided entry of tail-anchored proteins
GMP	guanosine monophosphate
c-di-GMP	bis-(3'-5')-cyclic dimeric GMP

GRACILE	growth retardation aminoaciduria cholestasis iron overload lactic acidosis
IM	inner membrane
IMS	mitochondrial intermembrane space
ISP	iron-sulphur-cluster containing protein
LD	large domain (of the AAA cassette)
LHCP	light-harvesting chlorophyll-binding protein
LPS	lipopolysaccharide
MD	Bcs1's middle domain
MFS	major facilitator superfamily
MPT	multi-pass translocon
NOMO	nodal modulator protein
OM	outer membrane
OPTI	obligate partner of TMCO1
PAT	protein associated with translocon (complex)
Pel	pellicle polysaccharide
PL1	pore loop 1
Plug-I	internal loop of PelB
Plug-O	outer (external) loop of PelB
Plug-S	short loop of PelB
PMF	proton motive force
PNAG	poly-β-D-N-acetylglucosamine
P. aeruginosa	*Pseudomonas aeruginosa*
PSII	photosystem II
PTC	peptidyl transferase center
RNC	ribosome-nascent chain complex
S. cerevisiae	*Saccharomyces cerevisiae*
SD	small domain (of the AAA cassette)
SND	SRP independent (pathway)

SRP	signal recognition particle
SR	SRP receptor
cpSRP	chloroplast signal recognition particle
TA	tail-anchored membrane protein
TAT	twin-arginine pathway
TM	transmembrane segment
TMCO1	transmembrane and coiled-coil domain protein 1
TMD	transmembrane domain
TMH	transmembrane helix
TMP	transmembrane protein
TPR	tricopeptide repeats
TRC	transmembrane recognition complex
TRC40	transmembrane recognition complex of 40 kDa
tRNA	transfer RNA
P-tRNA	peptidyl-tRNA
UDP	uridine 5'-diphosphate
UPS	unconventional protein secretory systems
WRB	tryptophan-rich basic protein
BhYidC	*Bacillus halodurans* YidC
EcYidC	*Escherichia coli* YidC

Chapter 1

Introduction

Cellular compartmentalization was a key step in the emergence of life. It allowed the segregation of small, organic biomolecules and the establishment of an electrochemical gradient which, ultimately, drove the biosynthesis of bigger assemblies, conferring the cell its ability to perform and control a wide array of functions, including self-replication, and thus to thrive on Earth. Such compartmentalization is thought to have been first achieved on the microporous cavities found inside hydrothermal alkaline vents [Russell and Hall, 1997], where minerals, organized in an inorganic layer, acted as a semipermeable barrier that separated the compartment where biochemical reactions took place from the outside world. Despite its limitations, this primitive cell form led to the appearance of organic molecules with a special chemistry such as polypeptides, nucleotides and lipids. The lipids, constituted by a polar head and an apolar core, spontaneously form special structural arrangements, minimizing the exposure of its hydrophobic moieties to water molecules. Evolution made use of such molecules in building a more flexible and versatile semipermeable membrane, the lipid bilayer, that released the primitive cell from its restricted location and allowed life not only to diversify but to adapt to a remarkable variety of conditions across the planet.

Alongside the evolution of the cell membrane, proteins associated to it evolved to carry out the many different tasks required by the cell. Accordingly, membrane proteins can interact with the membrane in different ways, for example through covalent links to hydrophobic molecules (i.e. membrane anchors) or through noncovalent interactions

mediated by the residues in their polypeptide chains. Most of the membrane proteins, accounting for 30% of the mammalian proteome [von Heijne, 2007] span the membrane, which has a length of approximately 5 nm, by embedding segments of their polypeptide chain in an α-helix or β-sheet conformation into the hydrophobic core, while exposing other segments to both sides of the lipid bilayer. These are generally known as transmembrane proteins (**Figure 1.1**).

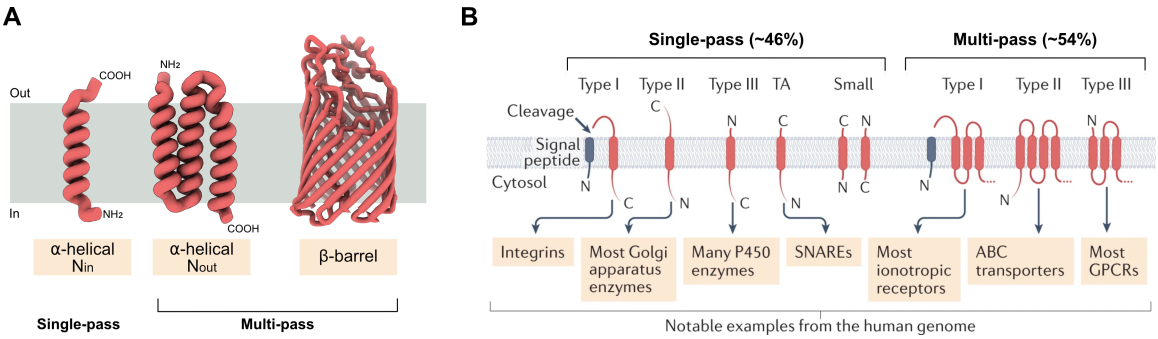

Figure 1.1: Integral transmembrane proteins. (**A**) The polypeptide chains of transmembrane proteins (TMPs) can adopt α-helical or β-sheet conformations, spanning the membrane one (single-pass) or multiple (multi-pass) times, and have their N-terminus oriented towards the inner (N_{in}) or the outer (N_{out}) side of the membrane. (**B**) Distribution and salient examples of human α-helical TMPs and classification according to their topology in Type I: containing a signal peptide inserted in N_{in} which after cleavage leads to an N_{out} topology, Type II: N_{in}, Type III: N_{out}, Type IV: tail-anchored (TA) membrane proteins, which contain a single TMD close to their C-terminus and are inserted in an N_{in} topology. Figure adapted from [Hegde and Keenan, 2022].

The α-helical and β-sheet conformations minimize the exposure of the polar peptide bond to the hydrophobic core of the membrane, while maximizing the formation of hydrogen bonds. While α-helical chains usually contain around 20-30 amino acids, 10 amino acids or fewer are enough to form a β strand that traverses the lipid bilayer. However, while hydrogen bond donors are stabilized with nearby acceptor residues inside a single α-helical segment, the hydrogen bond donors of one β strand find their acceptors in another β strand. This imposes a restriction on the overall structure of the membrane protein, as α-helical proteins can have as little as one segment inserted in the membrane, while β-sheets are restricted to cylindrical arrangements of β strands where all hydrogen bonds

are satisfied simultaneously. Depending on how many times the polypeptide chain crosses the membrane, transmembrane proteins are further classified as single-pass or multi-pass transmembrane proteins. Single-pass proteins have been observed only in an α-helical conformation, while multi-pass proteins can adopt structures made of either α-helical bundles or β-barrels. Moreover, the orientation of the N-terminal domain of an α-helical membrane protein is used to define its topology (i.e., its position relative to the compartment where the protein is synthesised), which can be N_{in} (N_{cyt}), when the N-terminus is oriented towards the compartment, or N_{out} (N_{exo}), when it is oriented towards the exterior. The topology is determined by the identity of the protein and, in turn, by its biogenesis pathway. Being invariant, it allows the classification of transmembrane proteins in four types (**Figure 1.1B**).

The core of the helical bundle in α-helical multi-pass transmembrane proteins is not necessarily hydrophobic and can contain polar and charged amino acids. This confers functional diversity, as they can interact with hydrophilic molecules coming from both sides of the membrane (i.e. receptors) and, in some cases, form hydrophilic paths that lower the energetic barrier of crossing the hydrophobic core of the bilayer (i.e. transporters). In a similar way, the amino acids exposed to the inside of β-barrel multi-pass proteins exhibit high compositional variability, depending on the protein function. However, a β-barrel structure is less flexible than an α-helical bundle because, in contrast to the fixed positions of the β strands, the interactions between different α-helical segments are weaker, allowing them to move and change position relative to one another. This impacts the variety of functions a β-barrel can carry out and explains to some extent why α-helical multi-pass proteins are more abundant in nature.

Considering its paramount importance to the cell's homeostasis and viability, the question of how proteins are synthesised, inserted and folded into an active form in the lipid bilayer or translocated across it, has always been an intriguing one. Since the initial identification of signal sequences and postulation of their role in targeting [Milstein et al., 1972, Blobel and Dobberstein, 1975] to the most recent visualization of a multi-pass translocon [Smalinskaitė et al., 2022], an enormous body of knowledge has been

built around the mechanisms of biogenesis, insertion and translocation. Yet, many details of these processes remain unknown. In the first part of this introduction (Section 1.1), an overview of the different factors involved in these mechanisms will be presented. In the second part, the translocation of fully folded proteins (Section 1.2) and small molecules (Section 1.3) across the membrane will be discussed.

1.1 Membrane protein biogenesis and protein translocation

A wide variety of factors are involved in the biogenesis of membrane proteins, tailored to the needs of each specific membrane and cellular context. All bacterial, archaeal and endoplasmic reticulum (ER) membranes (which themselves are believed to have evolved from the archaeal membrane [Baum and Baum, 2014]) possess members of the Oxa1 (called Oxa1 in mitochondria, Alb3 in chloroplasts and YidC in bacteria) or the SecY (called SecY in prokaryotes and endosymbionts, Sec61 in *S. cerevisiae* and Sec61α in other organisms) families. They are proteins central to the mechanisms of targeting, insertion and translocation of α-helical proteins into and through the membrane, as is the case for secreted proteins that possess a cleavable first α-helical transmembrane domain [Voorhees and Hegde, 2016]. Oxa1 and SecY families will be discussed in more detail in the following sections. Different, specialized machineries handle protein import and insertion in mitochondria [Busch et al., 2023] and chloroplasts [Nellaepalli et al., 2023], as well as the insertion of β-barrel membrane proteins, which are present exclusively in the outer membranes of bacteria and endosymbiotic organelles [Tomasek and Kahne, 2021]. The reader is referred to the respective references for details on those machineries.

1.1.1 Oxa1 protein family

An essential step in membrane protein biogenesis is the partition of hydrophobic segments, the transmembrane domains (TMDs), into the lipid core of the membrane and the translocation of hydrophilic segments across it. For some polypeptides with short hydrophilic segments located at the N- or C- termini or connecting two TMDs, the energy cost of translocation is paid off by the energy minimization achieved by inserting the TMDs into the lipid bilayer [White and Wimley, 1999], and thus a spontaneous insertion is possible. However, the longer the hydrophilic segment or the more TMDs a protein has, the lower the likelihood is of an unassisted insertion, and competing interactions might lead to aggregation.

It is presumed that the evolution of a protein that acted both as a ribosome receptor and an insertase enabled the concomitant emergence of membrane proteins with multiple TMDs by providing a translation location close to the membrane surface and stabilizing TMD pairs by protecting them from the other nascent TMDs. Such central activities are carried out by proteins belonging to the Oxa1 family and, remarkably, at least one of their members is present in today's archaeal, bacterial and eukaryotic membranes (ER and endosymbiont-derived organelles), highlighting their importance for membrane protein biogenesis. Among the members of the family, the most notable ones are YidC, Alb3 and Oxa1, located in the bacterial, the thylakoidal and the inner mitochondrial membrane, respectively [Hennon et al., 2015]. Furthermore, bioinformatic studies allowed the inclusion of Get1, EMC3 and TMCO1, remote homologs of YidC found in ER membrane (**Figure 1.2A**)[Anghel et al., 2017]. Interestingly, substrates of YidC, Alb3 and Oxa1 are mainly associated with energy transduction functions, e.g. respiration or light-harvesting, highlighting their potential role in the early stages of evolution. The conservation of their catalytic function is such, that Oxa1 and YidC can replace each other both as ribosome binding platform and as insertase [van Bloois et al., 2005, Preuss et al., 2005], while Alb3 can replace YidC's insertion activity [Benz et al., 2009, Jiang et al., 2002].

Oxa1 family members share a three-TMD helical fold (**Figure 1.2B,C**). These TMDs

are arranged in a conical conformation, leading to the formation of a groove accessible from both sides of the membrane. This groove is lined by hydrophilic and positively charged residues, constituting a docking site for the hydrophilic segments handled by the Oxa1 family members. In addition, the length of the TMDs favours a local membrane thinning, destabilizing the lipid core at the protein insertion site (**Figure 1.2D**). These two features are suggested as the main functional characteristics with which Oxa1 members facilitate the insertion of certain membrane proteins with multiple TMDs and hydrophilic segments of up to ca. 50 amino acids [Hegde and Keenan, 2022, Hennon et al., 2015]. In addition, a hairpin-like cytoplasmic region and a C-terminal extension, which vary in length and amino acid composition for the different members of the family, mediate substrate recruitment and interaction with different binding partners, further supporting their insertion and translocation activity [McDowell et al., 2021].

Oxa1

The oxidase assembly factor, Oxa1, is located in the inner mitochondrial membrane. It is responsible for the insertion of all membrane proteins encoded by the mitochondrial genome and some nuclear-encoded substrates [Hennon et al., 2015]. Its positively charged C-terminal tail engages with the mitochondrial ribosome, thus catalysing co-translational insertion of the organelle encoded subunits of oxidative phosphorylation complexes [Hell et al., 2001]. Additionally, it assists in the post-translational insertion of the nuclear-encoded targets that follow the conservative import pathway (Section 1.1.3), such as the ATP dependent permease Mdl1, as well as those following alternative pathways, such as the ATP/ADP carrier protein Aac2 [Hildenbeutel et al., 2012]. Besides Oxa1, a closely related paralog, Oxa2, is also present in mitochondria. Having a shorter C-terminal tail, Oxa2 loses the ribosomal interaction, and its main known activity is the post-translational insertion of the strongly charged, mitochondrially encoded, Cox2 C-terminal domain [Funes et al., 2004]. However, this activity can be taken over by Oxa1 in absence of Oxa2, pointing to a more central, upstream role of the former in membrane

protein insertion.

Alb3

Alb3 was first discovered in the chloroplasts of *Arabidopsis thaliana* [Sundberg et al., 1997]. It is involved in the insertion of the light-harvesting chlorophyll-binding protein (LHCP), a core component of the photosynthetic system II (PSII). To that end, Alb3 interacts with the transit complex formed by the chloroplast signal-recognition particle (cpSRP) machinery and a post-translationally processed LHCP peptide. This interaction is mediated by the C-terminal tail, which is intrinsically disordered but folds upon interaction with the cpSRP [Falk et al., 2010]. Similarly to the mitochondrial case, a second paralog, Alb4, has also been found in the thylakoid membrane. Alb4 knock-down mutants display an altered chloroplast ultrastructure but don't seem to be essential for its biogenesis [Gerdes et al., 2006]. Alb4 has been shown to influence the steady state levels of the CF_1CF_0-ATP synthase and interact with some of its subunits, probably resembling the roles of Oxa1 and YidC in the membrane insertion of subunits of the ATPase synthase homologs. Interestingly, while Alb4 can rescue the lethal phenotype observed in *E. coli* YidC depletion strains, it doesn't compensate for the absence of Alb3, supporting its non-redundant function in chloroplast homeostasis [Benz et al., 2009].

YidC

YidC is found in the membrane of Gram-positive and Gram-negative bacteria and it is responsible for the insertion of a wide variety of substrates. Its insertion activity can be accomplished both independently and in combination with the SecYEG translocon (Section 1.1.3). In the Sec-independent pathway, it associates with the translating ribosome, mediating the co-translational insertion of substrates such as F_0c (an F_1F_0-ATP syntase subunit), MscL (a mechanosensitive channel), TssL (a component of the type VI secretion system), and the phage proteins M13 and Pf3 [Hennon et al., 2015].

The crystal structures of *Bacillus halodurans* (BhYidC) [Kumazaki et al., 2014a] and

E. coli (EcYidC) [Kumazaki et al., 2014b] have provided important insights into YidC's structure and function. The core TMHs of YidC are bundled together, forming a hydrophilic groove exposed to both the cytoplasmic side and the interior of the membrane. The helices are interconnected via two cytoplasmic and two extracellular regions. One of the cytoplasmic regions is composed by two moderately hydrophobic helices, forming a hairpin-like structure that exhibits flexibility relative to the core. On the extracellular side, one of the regions consists of an amphipathic helix that lies parallel to the membrane plane and is embedded in the membrane. Functional analysis of the residues in the hydrophilic groove has shown that a conserved arginine residue (R72 in BhYidC), which confers a strong positively charged potential, is necessary to sustain insertion activity, as mutations that abolish the positive charge exhibit reduced insertion and a lethal phenotype. Similarly, mutations in the hairpin-like region lead to decreased YidC-mediated membrane insertion, suggesting a role in the initial interaction with the substrate and subsequent handling, as has been recently confirmed [Laskowski et al., 2021].

An additional element of YidC is present in Gram-negative bacteria, protruding from the N-terminal core of TMHs, as visualised in the EcYidC crystal structure (**Figure 1.2A**) [Kumazaki et al., 2014b]. This periplasmic domain, referred to as P1, includes a cleft that resembles the sugar binding pocket of galactose mutarotase enzymes, but lacks the sugar binding motif. The orientation of P1 positions it away from the membrane, making the interaction with substrate proteins unlikely. Instead, the cleft is thought to be a docking site for periplasmic macromolecules. This activity, however, is not essential for the function of YidC, which can be inferred from its lack of conservation outside Gram-negatives.

All these structural features support a Sec-independent model for the insertion of single-pass transmembrane proteins, where a negatively charged N or C terminal tail is first recognised by the hairpin-like domain and subsequently directed towards the conserved positively charged residue in the hydrophilic groove. Next, favoured by the electrochemical gradient and the local membrane thinning, the energy barrier for the translocation of the charged tail is lowered and, consequently, the tail is released to the extracellular side of the membrane.

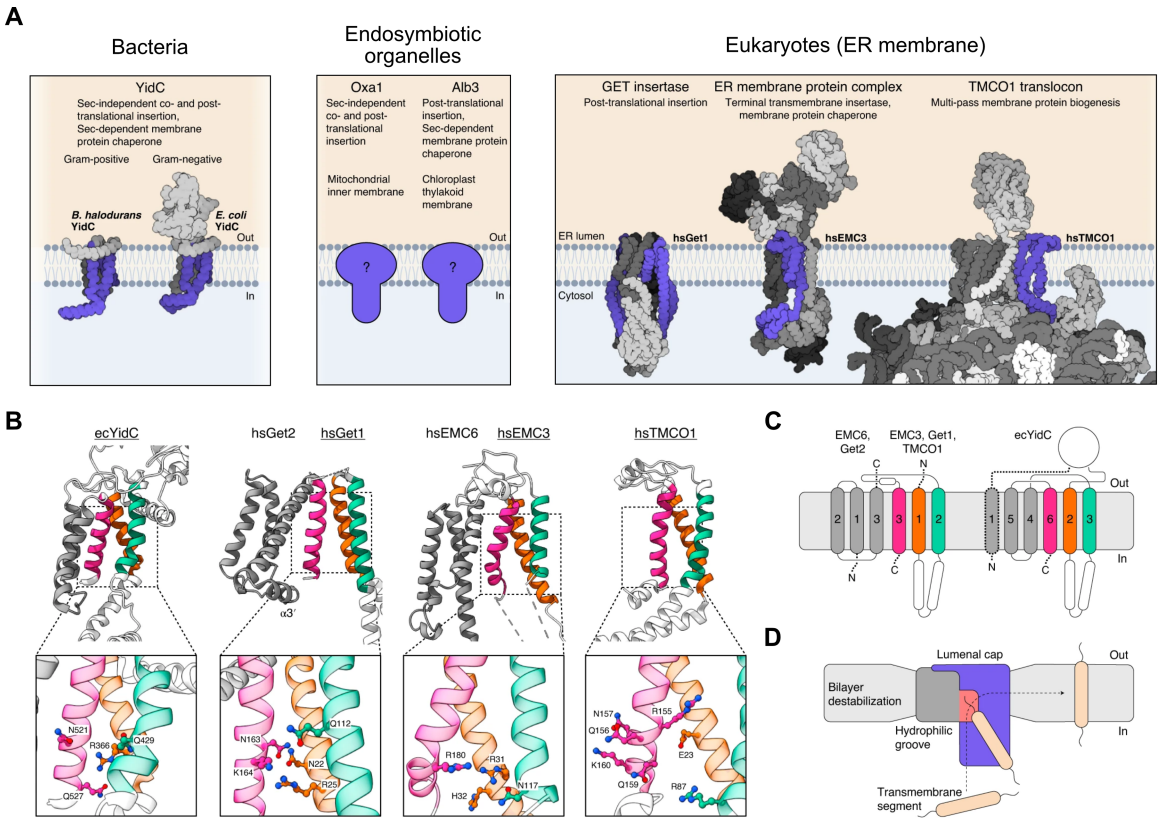

Figure 1.2: The Oxa1 family. (**A**) Prominent members of the Oxa1 family in bacteria, endosymbiotic organelles and the ER membrane. (**B**) The three-TMD fold (coloured) and the hydrophilic groove are structurally conserved in Oxa1 members, usually accompanied by three additional TMDs in the same protein (YidC) or in a protein partner. (**C**) Organisation of TMDs in the different Oxa1 members, displaying the three-TMD fold (coloured) and the accompanying TMDs (grey), the shared hairpin-like loop and the unique cytoplasmic domain in *E. coli*. (**D**) Model of facilitated TMD insertion by the Oxa1 members. Membrane thinning and the hydrophilic groove reduce the energetic barrier for translocation of hydrophilic residues across the bilayer. Figure adapted from [McDowell et al., 2021].

Oxa1 members in the ER

Bioinformatics and biochemical analyses led to the identification of multiple archaeal and eukaryotic membrane proteins related to Oxa1/Alb3/YidC, including the "YidC-like protein 1" (Ylp1) and members of the "guided-entry of tail-anchored proteins" (GET) pathway, the "ER membrane complex" (EMC) family, and the "transmembrane and coiled-coil domains 1" (TMCO1) family (**Figure 1.2A**) [Anghel et al., 2017].

The GET pathway is involved in the targeting and insertion of tail-anchored (TA) pro-

teins in the ER membrane (**Figure 1.1B**). Its membrane spanning components, known as Get1/Get2 in yeast (WRB/CAML in mammals), form a 2:2 heterotetramer that interacts with the central targeting factor Get3 (TRC40) to coordinate TA protein post-translational insertion [Schuldiner et al., 2008].The insertase activity of Get1/Get2 relies on a membrane thinning mechanism and the hydrophilic groove formed by Get1, whose TMDs adopt the conformation typical of the Oxa1 family [McDowell et al., 2023].

In the multi-subunit EMC, the Oxa1 family member EMC3 constitutes a pseudo-symmetric, membrane spanning core along with EMC6, EMC1 and EMC5. Crosslinking experiments have shown that EMC3 interacts with the substrates of the complex, which are low-hydrophobicity TA proteins and the first TMD of multi-pass membrane proteins that exhibit an N_{out} (N_{exo}) topology. Additionally, it has been observed that a hydrophilic vestibule and, particularly, the conserved residues R31 and R180, are required for the insertion activity of the complex, resembling the strategy employed by YidC [Pleiner et al., 2020].

TMCO1 is an ER membrane protein whose function was not initially connected to membrane protein biogenesis but had been linked to different human disorders such as glaucoma and intellectual disability. After being identified as a relative of the Oxa1 family, TMCO1's predicted ribosome association was confirmed [Anghel et al., 2017]. In addition, TMCO1 has been characterised as part of a "multi-pass translocon" constituted by the Sec translocon (Section 1.1.2) and the abundant ER proteins CCDC47, Nicalin, TMEM147 and NOMO [McGilvray et al., 2020]. More recently, the protein C200rf24 was identified to be an obligate partner of TMCO1 (OPTI), in a homologous way as Get2 is to Get1 or EMC6 is to EMC3 (**Figure 1.2**). These proteins have been grouped in the BOS (back-of-sec; Nicalin, TMEM147 and NOMO) and GEL (GET and EMC-like; TMCO1 and C200rf24) heterocomplexes which, together with PAT (CCDC47 and Asterix [Chitwood and Hegde, 2020]), assemble at the back of the Sec translocon to assist the co-translational insertion and folding of multi-pass membrane proteins [Sundaram et al., 2022] (Section 1.1.3). The concrete role TMCO1 plays in substrate recognition and insertion is yet to be characterized.

1.1.2 The Sec translocon

The members of the Oxa1 family generally transport membrane proteins that possess hydrophilic segments of up to ca. 50 amino acids [Hennon et al., 2015]. The evolution of a transporter that created a hydrophilic conduit across the lipid bilayer likely allowed membrane proteins to have longer hydrophilic segments, thus increasing their complexity and variety of functions, as well as enabling protein secretion. This transporter is known as SecY (Sec61α in higher eukaryotes), a pseudo-symmetric, membrane-spanning channel that provides an aqueous tunnel for the transport of long hydrophilic segments and can laterally release TMDs into the membrane.

SecY/Sec61α associates with SecG and SecE (Sec61β and Sec61γ), forming the Sec translocon, a heterotrimeric complex found in the membranes of bacteria, archaea and eukaryotes (ER and some endo-symbiont derived organelles). SecY/Sec61α and SecE/Sec61γ are essential for cell viability and are highly conserved, while SecG/Sec61β is non-essential and not universally conserved [Park and Rapoport, 2012]. The translocon, like other protein channels, couples the transport of its substrates to sources that can provide a driving force for translocation, depending on the mechanism of insertion (Section 1.1.3). The free energy minimisation resulting from the partition of a hydrophobic TMD into the lipid bilayer is thought to be the major driving force for co-translational insertion and translocation [Cymer et al., 2015]. In post-translational mechanisms, an additional energy source is supplied by ATP hydrolysis, carried out by protein partners such as BiP in the ER or SecA in bacteria [Van den Berg et al., 2004].

The channel formed by SecY/Sec61α is composed of 10 TMDs, which can be grouped in a TM1-TM5 and a TM6-TM10 half (**Figure 1.3A**). These two halves are related by a two-fold rotational pseudo-symmetric axis and share conserved structural features with Oxa1, indicating that SecY/Sec61α potentially evolved from an antiparallel, Oxa1-like, homo-dimeric ancestor [Lewis and Hegde, 2021]. The halves define the geometry of the channel, adopting an hourglass-like conformation around a central pore with cavities of 20–30 Å in diameter, one opening towards the cytoplasmic side, the other one facing the

extracellular side. The fusion of the halves through a loop between TM5 and TM6 at the back acts as a hinge, allowing the interface between TM2 and TM7 to open in a clam-like manner, constituting what is defined as the lateral gate. SecE/Sec61γ wraps around SecY/Sec61α, keeping the halves together and closing the back side, while SecG/Sec61β has only limited contacts with the channel [Van den Berg et al., 2004].

In addition to the lateral gate, two elements in SecY/Sec61α determine its mechanism of translocation: the plug and the pore ring (**Figure 1.3A**). The plug is a short helix that occupies the extracellular cavity of the channel, blocking the substrate path in the resting (idle) state. The pore ring is a cluster of six hydrophobic residues (I75, V79, I170, I174, I260, L406 in *M. jannaschii*), located at the narrowest point of the channel that, during the idle state, keeps the permeability barrier of the membrane by hindering the passage of small molecules and separates the cytoplasmic and extracellular sides [Van den Berg et al., 2004]. In the translocating state, the folded first N-terminal TMD segment of a substrate induces the opening of the lateral gate at the cytoplasmic side [Kater et al., 2019] and snorkels into the channel, inserting as a loop (**Figure 1.3B**) [Li et al., 2016]. The downstream amino acids at the C-terminal of this segment are threaded through the pore ring, displacing the plug helix. At this stage, two of the pore ring hydrophobic residues, I75 and I170, are excluded from the ring and are instead replaced by the substrate chain, which in turn acts as a seal, keeping the permeability barrier (**Figure 1.3C**). If the downstream amino acids form a second TMD segment, it starts folding in the extracellular cavity after crossing the pore ring. In later stages, the two TMDs slide out of the channel into the lipid bilayer through the lateral gate [Ou et al., 2025].

1.1.3 Mechanisms of α-helical membrane protein biogenesis

The biogenesis of secretory and α-helical membrane proteins can be divided in a targeting phase and an insertion/translocation phase. In the targeting phase, the newly synthesised polypeptide is directed to the membrane either post-translationally, that is, after translation has finished and the full chain has exited the ribosome, or co-translationally, when the

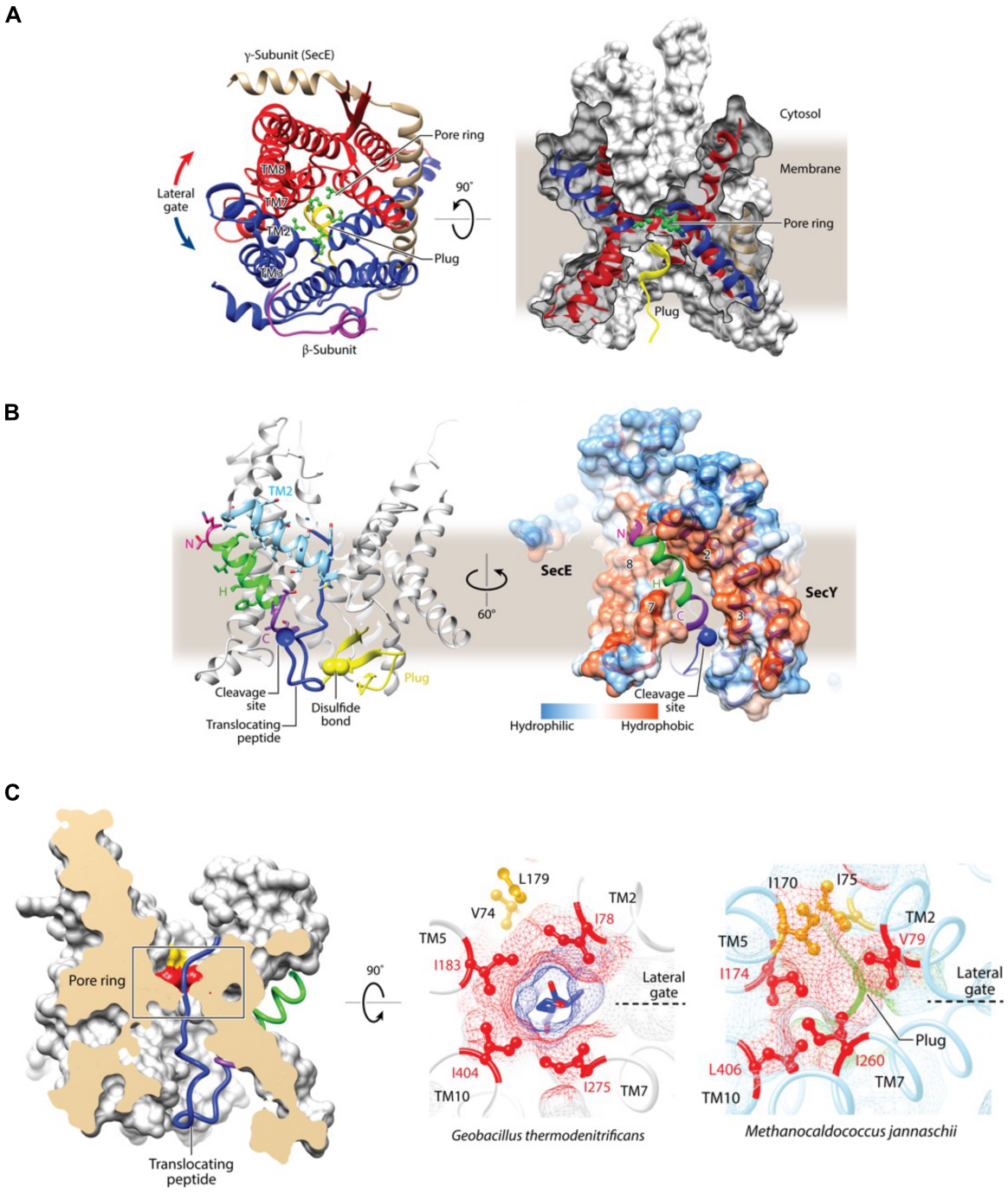

Figure 1.3: The Sec translocon. (**A**) Structure of the Sec61$\alpha\beta\gamma$ translocon in the resting (idle) state. Left panel: the N-terminal half (TM1-TM5, blue), the C-terminal half (TM6-TM10, red), the lateral gate, pore ring and plug are displayed. Right panel: a cut-view into the protein channel allows for a better visualisation of its pseudo-symmetric nature and the relative positions of the pore ring and the plug. (**B**) Left panel: SecY channel in the translocating (open) state, engaged with a signal peptide (green), docked at the interface between TM2 (light blue) and TM7 (omitted for clarity) with a displaced plug helix (yellow). Right panel: an electrostatic surface representation displays the relative hydrophobicity around the docked signal peptide. (**C**) Comparison of SecY's pore ring residues in a substrate engaged (left and central panels) vs a resting state (right panel). The substrate position keeps the permeability barrier during threading through the channel. Figure adapted from [Rapoport et al., 2017].

N-terminal segment of the nascent chain, in complex with the ribosome, is targeted to the membrane and inserted, allowing translation to occur concomitantly with the insertion of subsequent TMDs or the translocation of hydrophilic domains [Rapoport et al., 2017].

Co-translational targeting

In the co-translational mode, the ribosome-nascent chain complex (RNC) is first scanned by the signal recognition particle (SRP), a highly conserved RNA-protein complex that can interact with the ribosome and the exposed N-terminal segment of the nascent chain (**Figure 1.4**) [Walter and Blobel, 1981a, Walter and Blobel, 1981b, Keenan et al., 1998]. For secretory proteins, this N-terminal segment encodes a cleavable sorting signal composed of 7 to 12 hydrophobic amino acids, whereas for membrane proteins it can feature a TMD of around 20 hydrophobic amino acids [Park and Rapoport, 2012]. The RNC-SRP complex is then relocated to the membrane, where binding of SRP to its membrane-bound receptor (SR), followed by GTP hydrolysis, leads to the transfer of the RNC to the Sec translocon and to the release of the SRP to the cytosol, allowing its recycling in a new cycle of scanning and targeting [Halic and Beckmann, 2005]. Most multi-pass membrane proteins use this mechanism, as it prevents the premature folding of TMDs and their exposure to the aqueous environment, which could potentially lead to aggregation and misfolding.

For some proteins, the N-terminal segment is not hydrophobic enough, or the first TMD is located far downstream, which prevents their efficient binding to SRP. These substrates might be translocated by alternative mechanisms such as the SRP-independent pathway (SND) [Aviram et al., 2016]. The three protein components of SND were originally described in *S. cerevisiae* and named SND1, SND2 and SND3. While SND1 is a ribosome associated cytosolic protein [Fleischer et al., 2006], SND2 and SND3 are predicted to be membrane spanning, potentially acting as membrane receptors in the pathway. However, a recent study has shown that the human homologue of SND2, TMEM208, accelerates substrate release in the SRP pathway [Wang and Hegde, 2024], and that SND3 displays structural features like those of insertases in the Oxa1 family [Yang et al., 2025],

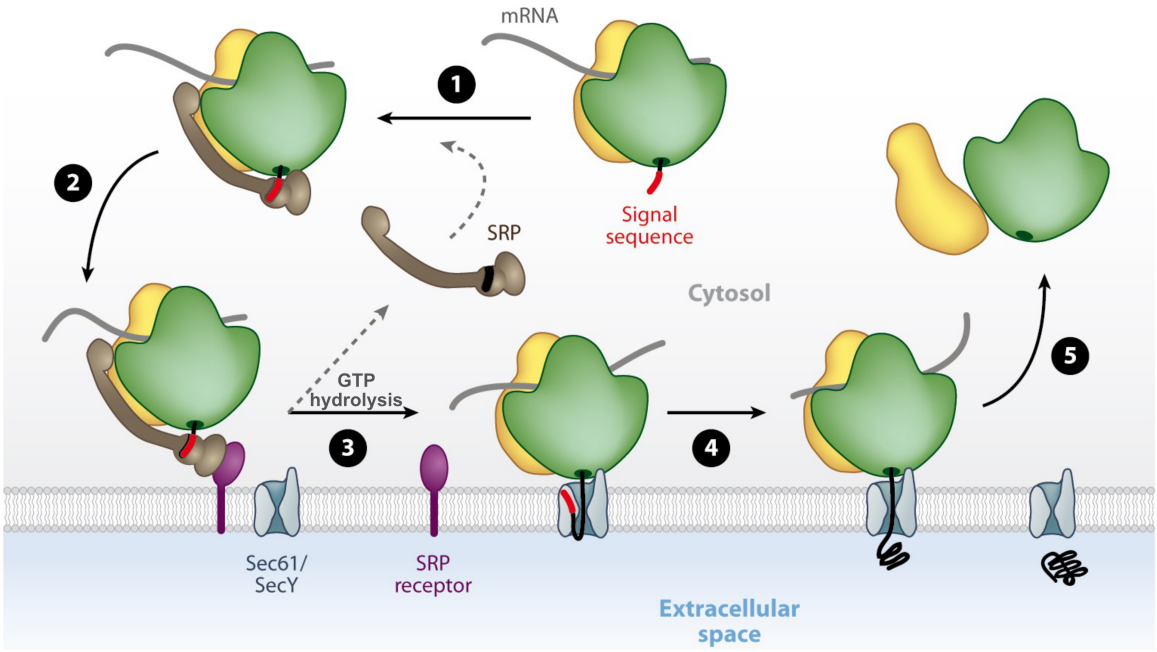

Figure 1.4: Co-translational targeting and translocation. (1) After the signal sequence has exited the ribosome, it is recognised by the SRP, which accommodates it in a hydrophobic binding pocket and targets it to the membrane-bound SRP receptor (2). Upon GTP hydrolysis, the SRP is disengaged and returns to the cytosolic pool, whereas the RNC remains docked at the Sec translocon (3). Translation proceeds to completion threading the nascent protein through the SecY/Sec61α protein channel (4) and leading to the recycling of the ribosomal subunits (5). Figure adapted from [Park and Rapoport, 2012].

pointing to a partial dependence of SND on SRP and a wider range of activities not limited to targeting.

Post-translational targeting

In post-translational targeting, chaperones and cytosolic factors, such as calmodulins in mammals [Shao and Hegde, 2011] or Hsp40 and Hsp70 proteins in yeast [Ngosuwan et al., 2003], shield the nascent chain, keeping it in a translocation competent unfolded state, and deliver it to the membrane once it is released from the ribosome [Rapoport et al., 2017, Aviram and Schuldiner, 2017]. In *S. cerevisiae*, the Hsp70 protein Ssa1 hands over the substrate to an ER-membrane resident heptameric complex constituted by the proteins Sec62, Sec63, Sec72, Sec72 and the Sec translocon, also known as

the SEC complex [Tripathi et al., 2017]. In *E. coli*, SecB acts as a cytosolic chaperone and delivers the substrate to SecA [Hartl et al., 1990], an ATPase belonging to the RecA family which also associates with the Sec translocon [Zimmer et al., 2008]. A special case of post-translational targeting is carried out by the Get3/TRC40 chaperone, responsible for handing over TA proteins to the Get1/Get2 (WRB/CAML) heterodimer. In TA proteins, a single TMD is located close to the C-terminus, precluding the SRP pathway from handling their targeting. Interestingly, Get3/TRC40 binds the hydrophobic helix by providing a hydrophobic pocket, resembling the SRP and calmodulin binding modes [Mateja et al., 2015].

Insertion/translocation

The Sec translocon is a core component in the biogenesis of many single-pass and multi-pass membrane proteins. In the co-translational pathway, the ribosome binds to SecY/Sec61α through the loop 6/7 (between TM6 and TM7) and the loop 8/9 (TM8 and TM9), altering its overall conformation and causing a slight opening of the lateral gate [Kater et al., 2019, Shaw et al., 1988, Tsukazaki et al., 2008]. This interaction renders the channel in a "primed" or ready for substrate engagement state [Voorhees et al., 2014, Gogala et al., 2014]. A primed state is also observed in the SecA post-translational pathway, as the SecA-SecY interaction is mediated by the loop 8/9, inducing similar structural rearrangements in the channel upon SecA binding [Zimmer et al., 2008]. The subsequent engagement of a protein substrate with SecY/Sec61α leads to a conformational change where the lateral gate is fully open and the hydrophobic signal sequence or the TMD intercalates between TM2 and TM7, changing the conformation of the plug and making the aqueous channel accessible [Li et al., 2016]. The binding of the hydrophobic segment to the lateral gate and accompanying plug displacement initiates translocation by allowing a downstream hydrophilic segment to be threaded across the membrane. As the channel itself does not impose a limit to the number of amino acids that can be threaded, this hydrophilic segment can constitute the soluble domain of a secretory protein as well as a soluble domain or loop

connecting two TMDs. In the case of a secretory protein, once the C-terminus has been translocated, SecY/Sec61α closes and a signal peptidase releases the soluble domain to the extracellular space or ER lumen. In contrast, when the downstream element to the translocated hydrophilic segment is a TMD, it enters SecY/Sec61α and is released to the membrane through the lateral gate [Do et al., 1996, Yost et al., 1983]. In this case, cleavage of the signal peptide will give rise to a membrane protein with an orientation defined as type I (N_{exo}): the N-terminus is exposed to the extracellular space or ER lumen. Alternatively, when the hydrophobic segment docked at the lateral gate is a TMD and no additional TMDs are present downstream, the resulting orientation is defined as type II (N_{cyt}): the C-terminus is exposed to the extracellular or luminal side of the membrane (**Figure 1.5A**).

The hydrophilic segments translocated through Sec are generally long (more than 50 amino acids). If the hydrophilic segments are short (ca. 50 amino acids or less), the insertion can proceed independently of the Sec translocon, assisted by Oxa1 family members. This activity is mainly co-translational, except for proteins where a single hydrophobic segment or TMD is only around 70 amino acids away from the C-terminus, such as TA proteins (**Figure 1.1B** and **Figure 1.5B**). The insertion of TA proteins starts after the GET complex component Get3/TRC40 hands over the hydrophobic TMD to its membrane receptor constituted by the Get1/Get2 (WRB/CAML) heterodimer. Both Get1/WBR and Get2/CAML have cytosolic domains capable of interacting with the TA-bound Get3/TRC40 dimer but, while Get2-Get3 (CAML-TRC40) interaction does not promote the release of the TMD, the Get1/WRB hairpin-like domain can dislodge the TMD and orient the hydrophilic segment towards the hydrophilic groove, enabling its translocation, while the TMD is released laterally to the membrane [McDowell et al., 2020].

The TMDs of some TA proteins exhibit low to moderate hydrophobicity and thus are only inefficiently targeted by Get3/TRC40 [Mateja et al., 2015, Rao et al., 2016]. Those cases are preferentially handled by the EMC complex, which has been shown to capture TA proteins, most likely by transient binding to its cytosolic domain, and direct them to the membrane [Guna et al., 2018]. The main insertase activity is then carried

out by the Oxa1 family member EMC3, where the hydrophilic groove probably binds and assists the translocation of the TA C-terminus, while inserting the TMD into the membrane [Anghel et al., 2017, O'Donnell et al., 2020]. The EMC complex has also been associated with the insertion of a third type of membrane protein topology, namely the type III (N_{exo}) which, despite having an inverted topology compared to TA proteins, also possesses short N-terminal hydrophilic domains (**Figure 1.5C**) [Chitwood et al., 2018]. Multi-pass membrane proteins that exhibit a combination of short and long hydrophilic

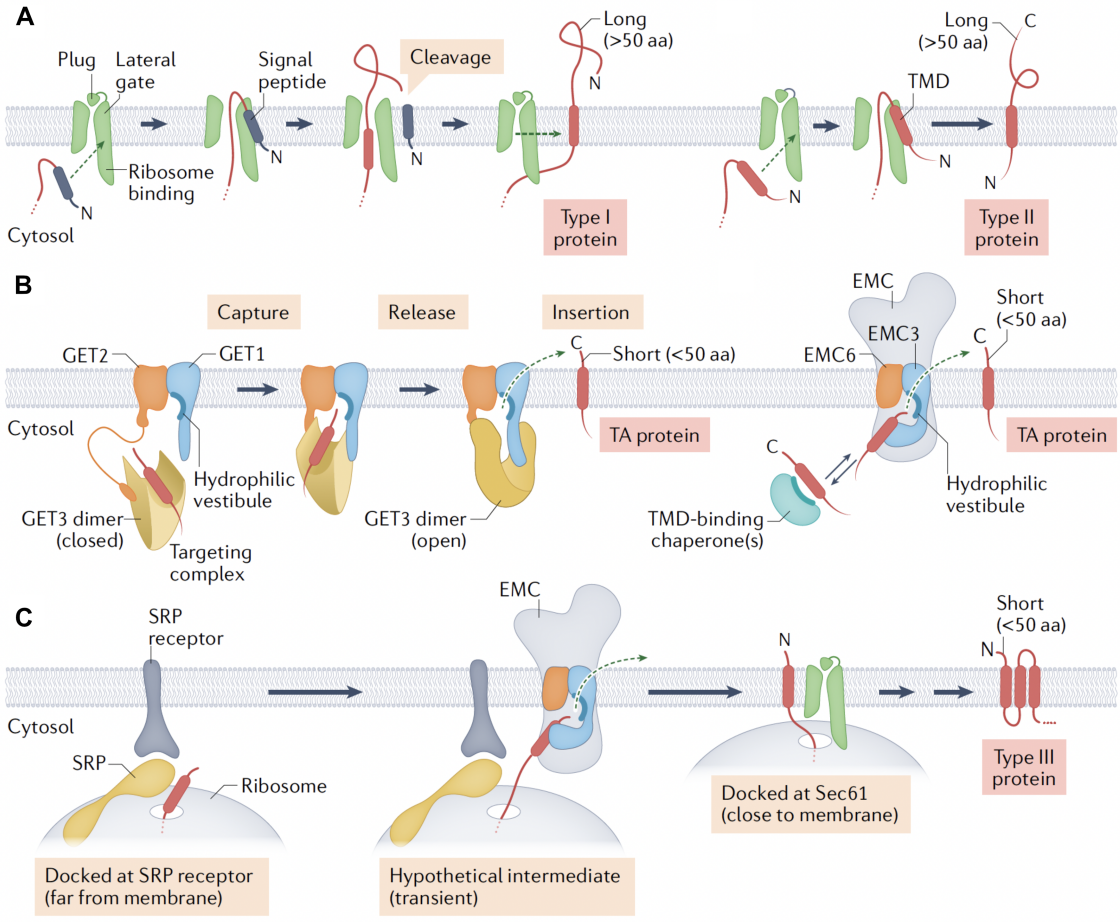

Figure 1.5: Mechanism of insertion of the first TMDs of multi-pass membrane proteins. Depending on key substrate features the insertion route is handled by Sec or Oxa1 family members. (**A**) Type I and Type II proteins are inserted via the lateral gate of SecY/Sec61α. (**B**) TA proteins are inserted via the GET or EMC machineries. (**C**) Type III proteins are inserted by Oxa1 family members. Figure adapted from [Hegde and Keenan, 2022].

segments interconnecting their TMDs use both the Sec translocon and Oxa1 family members, with the ribosome acting as a hub that recruits and directs the nascent chain to the corresponding factors (**Figure 1.6**). In some cases, the coexistence of both the Sec translocon and the Oxa1 family member(s) is not possible due to steric hindrance constrains. Such is the case of type III (N_{exo}) multi-pass membrane protein insertion, where the SRP would need to first deliver the N-terminal TMD to EMC before Sec can engage the ribosome (**Figure 1.5C**) [Chitwood and Hegde, 2019]. For type II (N_{cyt}) multi-pass substrates, the targeting of the TMD to Sec is presumably followed by the recruitment of the BOS, GEL and PAT complexes, which not only act as insertases, but provide an environment that facilitates the proper folding of the TMDs. This is especially important because some TMDs in multi-pass membrane proteins are usually slightly hydrophilic [Hessa et al., 2007], as they require hydrophilic side chains to form channels, binding and catalytic sites. If those residues are directly exposed to the lipid bilayer, they can be recognised by quality control mechanisms that degrade them [Hegde and Keenan, 2022]. Consequently, they need to be protected during insertion and folding by intramembrane chaperones such as Asterix in the PAT complex, which has been reported to directly engage semi hydrophilic TMDs in the ER membrane [Chitwood and Hegde, 2020]. The complex formed by BOS, GEL, PAT and Sec has been recently visualised by cryo-EM (**Figure 1.6A**), providing a structural basis for a unified model of membrane protein biogenesis (**Figure 1.6B**) [Smalinskaitė et al., 2022, McGilvray et al., 2020]. The protein components of these complexes are widely conserved in metazoans, which is coherent with the increased complexity of their membrane proteome. The question of whether such assemblies are also used by prokaryotes, which lack PAT, BOS and GEL components [Li et al., 2016, Guna et al., 2018] remains open.

1.1.4 Research question and aim of Publication 1

In bacteria, some multi-pass membrane proteins, such as NuoK, require both SecYEG and YidC for their correct insertion. It is a long-standing question how SecYEG and

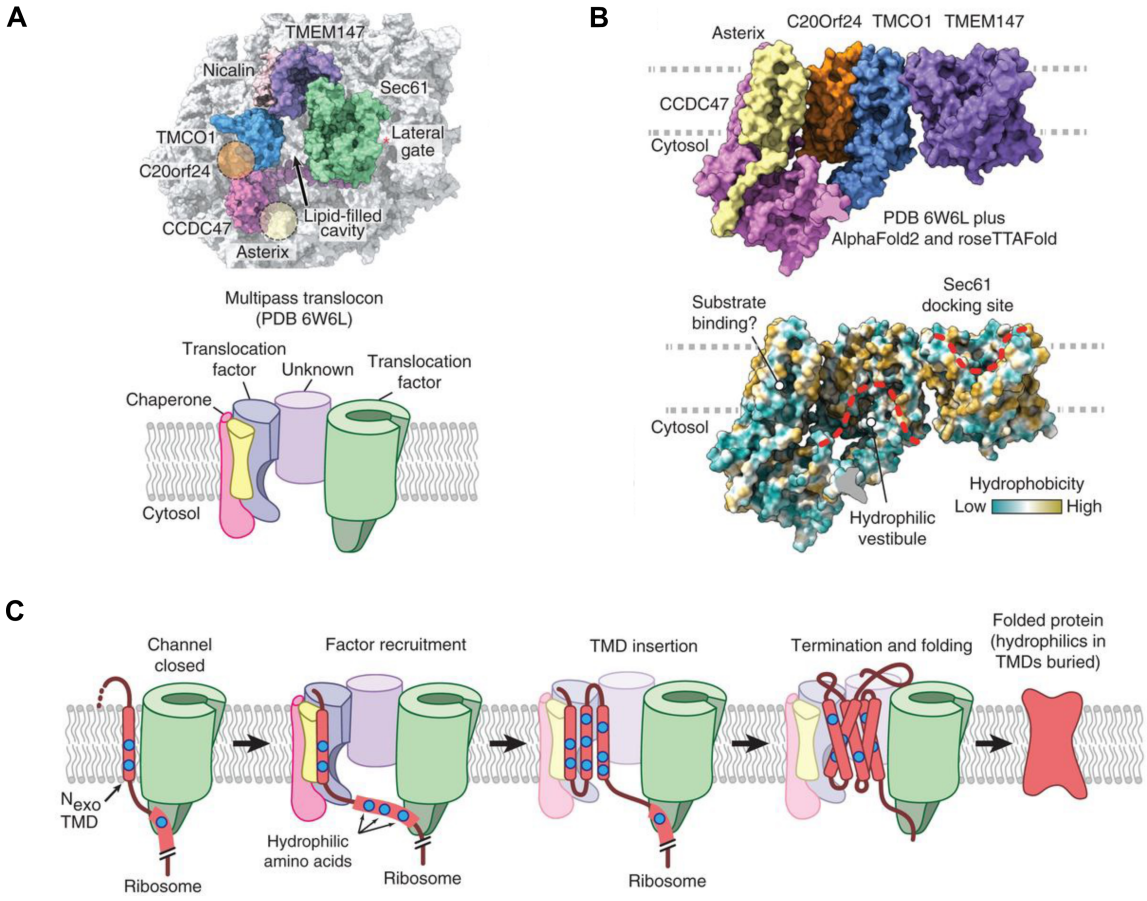

Figure 1.6: Multi-pass membrane protein insertion by the BOS-GEL-PAT-Sec complex. (**A**, top) Relative organisation of each complex around Sec61, viewed from the ER. The putative localisation of the proteins C20Orf24 and Asterix is displayed by dashed circles, and the lipid-filled cavity formed by the assembly is indicated. (**A**, bottom) Scheme of the assembly and the role of each complex. (**B**, top) Atomic model based on PDB 6W6L and predicted models for C20Orf24 and Asterix displaying the surface facing the lipid-filled cavity. (**B**, bottom) Lipid-filled cavity facing surface coloured according to the hydrophobicity of its residues. The docking site of Sec61 in TMEM147, the hydrophilic vestibule in TMCO1 and a potential substrate binding domain in Asterix are indicated. (**C**) Model for the insertion of a multi-pass membrane protein at the back of Sec61, after the first TMD has been inserted in an N_{out} (N_{exo}) topology (**Figure 1.5C**). The hydrophilic residues in the downstream TMDs are handled by Asterix, as the proper folding of the membrane protein is chaperoned in the lipid-filled cavity. Short connecting loops between TMDs can be translocated through the hydrophilic vestibule in TMCO1. Figure adapted from [Smalinskaitė and Hegde, 2023].

YidC cooperate during insertion and folding of these substrates. One possibility is that, in analogy to the eukaryotic MPT, YidC plays a similar role as BOS/PAT/GEL. However, available structural data is limited to RNC-SecY or RNC-YidC, as the structure of a SecYEG-YidC complex has so far remained elusive. The aim of Publication 1 was to combine structural and biochemical approaches to study the interaction between SecYEG and YidC from *E. coli* in order to understand how the synthesis of the multi-pass membrane substrate NuoK induces their assembly and to identify key features of bacterial multi-pass membrane insertion by the SecYEG-YidC complex.

1.2 Translocation of folded proteins across membranes

In contrast to the translocation of unfolded proteins, the mechanisms of folded protein translocation are more diverse. For example, the unconventional protein secretory systems (UPS) have different mechanisms of transport such as direct translocation through pore formation (type I), direct translocation through ABC transporters (type II), secretion through endocytic compartments (type III) or Golgi bypass of integral membrane proteins (type IV) [Dimou and Nickel, 2018]. UPS have also been observed in bacteria [Ebner and Götz, 2019]. A unifying characteristic of the proteins that follow these pathways is the lack of a targeting or leading sequence. Another instance of folded protein translocation occurs at the peroxisomal membrane, where proteins with a C-terminal (S/A/C)-(K/R/H)-L [Brocard and Hartig, 2006] or N-terminal R-(L/V/I/Q)-XX-(L/V/I/H)-(L/S/G/A)-X-(H/Q)-(L/A) [Petriv et al., 2004] peroxisomal targeting sequence (PTS) are recognised by their respective PEX5 (PTS1) and PEX7 (PTS2) adaptors, which target them to the nuclear pore-like receptor PEX13 in the membrane to be subsequently imported into the peroxisomal matrix [Léon et al., 2006, Pei and Dalbey, 2022, Skowyra et al., 2024, Wu and Zhuang, 2025].

In archaea, bacteria, chloroplasts and mitochondria of some species, the twin-arginine pathway (TAT) is the main route for translocation of folded substrates. These substrates

play key roles in respiratory and photosynthetic energy metabolism, iron and phosphate acquisition, cell division, cell motility, quorum sensing, organophosphate metabolism, resistance to heavy metals and symbiotic nitrogen fixation [Palmer and Berks, 2012]. The mitochondria of several species have lost the machinery required for this pathway many times during evolution [Petrů et al., 2018] and, instead, an alternative pathway dependent on the AAA-ATPase Bcs1 evolved to replace it [Wagener et al., 2011]. These pathways will be discussed in more detail in the following sections.

1.2.1 The TAT Pathway

The substrates of the TAT pathway possess an N-terminal targeting signal composed of a highly conserved twin-arginine motif defined as SRRXFLK, where the consecutive arginines have a very low variability and the other residues occur with a frequency higher than 50% [Berks, 1996]. This signal sequence has an overall architecture similar to the Sec targeting signal, exhibiting a tripartite structure with an N-terminal basic region, a middle hydrophobic region and a polar C-terminal region with a signal peptidase recognition site (**Figure 1.7A**). The crucial difference is, however, that the basicity of Sec targeted signals can be borne by arginine as well as lysine residues, whereas replacement of arginine for lysine in the twin-arginine motif impacts the efficiency of the TAT pathway [Stanley et al., 2000]. Other important differences are a less hydrophobic character of the middle region [Cristóbal et al., 1999] and a basic amino acid in the C-terminal region of TAT signals, the latter preventing an association with the Sec translocon [Bogsch et al., 1997]. Additional substrates that do not have the TAT targeting sequence can be translocated if they bind a small-subunit partner carrying the signal [Rodrigue et al., 1999]. Two families of proteins, termed TatA and TatC, constitute the machinery involved in substrate recognition and translocation. While some minimal TAT pathways contain only one type of TatA and TatC, most of them contain an additional member of the TatA family, called TatB (**Figure 1.7B**) [Berks et al., 2014]. TatC proteins comprise six TMDs arranged to form a cavity capped on the periplasmic (thylakoidal lumen in chloroplasts, intermembrane

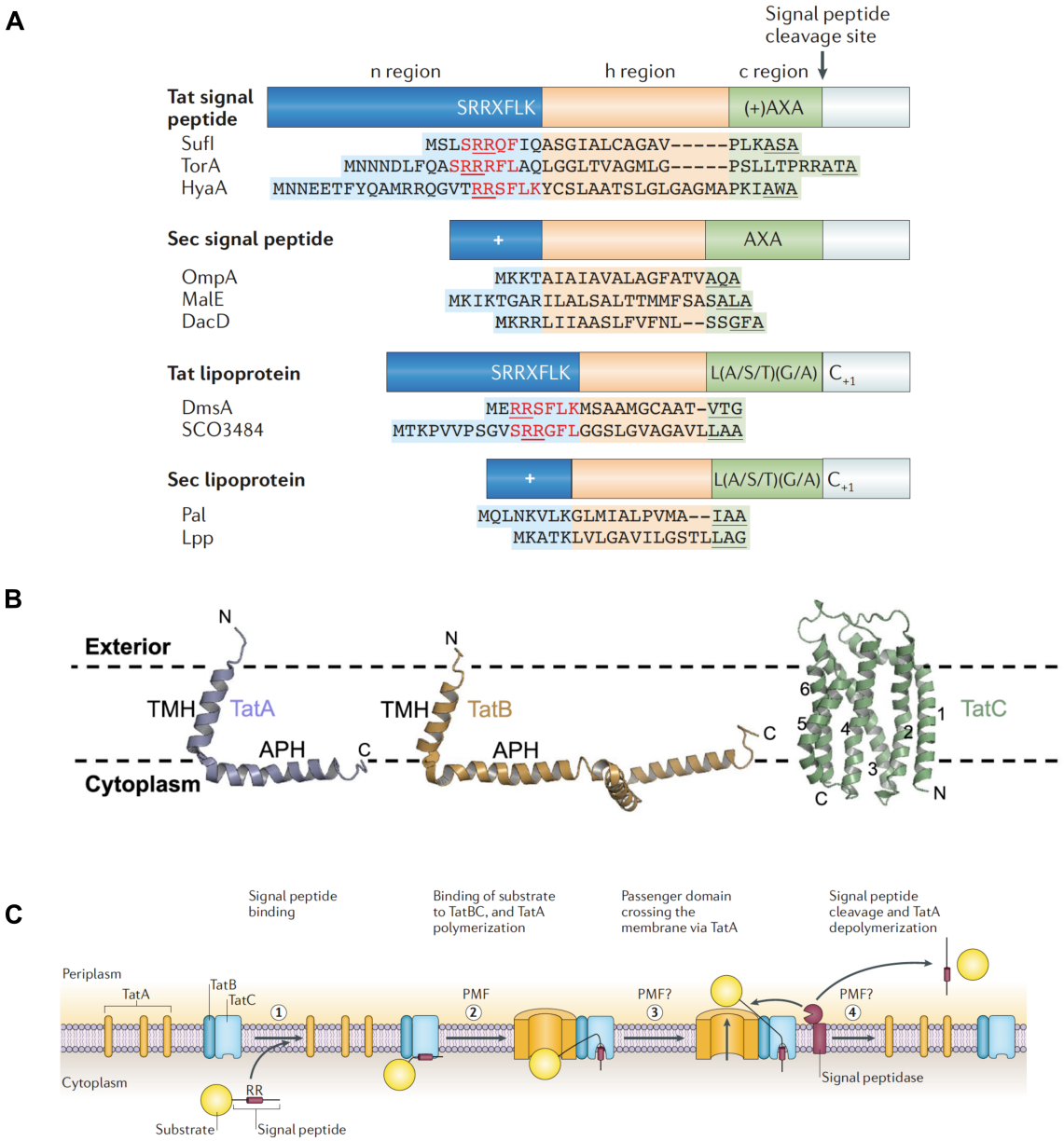

Figure 1.7: The TAT pathway. (**A**) Comparison of the Tat and Sec signal peptide structure, highlighting key differences such as the twin-arginine motif (SRRXFLK) and the presence of a positively charged residue in the c region ((+)AXA) of Tat signals. (**B**) The three main constituents of the TAT pathway, TatA, TatB and TatC. (**C**) Model of TatABC mediated translocation across the membrane. The binding of the signal peptide to a TatBC receptor complex triggers the oligomerisation of TatA subunits which, in turn, form a pore to facilitate the movement of the folded substrate. Cleavage of the signal sequence and posterior release are followed by TatA de-oligomerisation and return of TatBC to the resting state. Panel (**A**) and (**C**) adapted from [Palmer and Berks, 2012]. Panel (**B**) adapted from [Palmer and Stansfeld, 2020].

space in mitochondria) leaflet of the membrane by a surface helix and two parallel surface loops. Two of the TMDs, 5 and 6, are too short to span the lipid bilayer, enabling a possible route from the inside of the cavity towards the periplasm by means of membrane thinning [Rollauer et al., 2012, Berks, 2015]. TatA members contain a short hydrophobic N-terminal TMD, oriented almost perpendicularly to a downstream amphipathic helix facing the cytosolic (stroma in chloroplasts, matrix in mitochondria) leaflet of the membrane. A cytosolic facing, unstructured C-terminal tail is located further downstream, whose deletion does not abolish TAT translocation activity [Berks, 2015].

In the resting state (i.e. without substrate engaged), crosslinking data support a model where a complex, formed by TatA, TatB and TatC in a 1:1:1 stoichiometry, is present in the membrane as trimeric or tetrameric assemblies [Palmer and Stansfeld, 2020]. One face of the N-terminal helix of TatB is predicted to interact with TMD 5 and 6 of TatC while the opposite face interacts with TMD 1, facilitating the oligomerisation of the complex [Alcock et al., 2016]. Recently, analysis of the Tat translocation machinery in chloroplasts has suggested that the substrate receptor complex is formed by a trimeric core of TatC subunits, to which an equimolar amount of TatB is loosely bound yielding a $TatB_3C_3$ assembly [Reimers et al., 2025]. Even though only the TatBC complex is stable enough to be isolated, TatA is associated adjacent to the TatB binding site *in vivo* [Alcock et al., 2016, Habersetzer et al., 2017].

Under the current model (**Figure 1.7C**), the transport activity is initiated by binding of the signal sequence to a conserved cytosolic patch in TatC [Rollauer et al., 2012], followed by internalisation and a conformational change where TatB is displaced by TatA, likely triggered by the extensive contacts established between the middle hydrophobic region of the signal and TatB. This structural rearrangement leads to the proton motive force (PMF) dependent recruitment of additional TatA subunits [Alcock et al., 2013], which oligomerise and lead to the formation of either a pore of variable size or a region of transient bilayer disruption that facilitates the movement of the folded substrate across the membrane [Berks, 2015, Patel et al., 2014]. After translocation, the signal sequence is cleaved, TatA dissociates, and the system returns to the resting state [Palmer and Stansfeld, 2020].

Despite major advances, structural elucidation of the TatABC complex has remained challenging and, in consequence, a deep molecular understanding of its mechanism is still lacking.

1.2.2 The Bcs1 Pathway

Some of the most relevant TAT substrates are the iron-sulphur cluster proteins (ISPs) such as qcrA (belonging to the Menaquinol-cytochrome reductase complex in bacteria), petC (present in the Cytochrome b6-f complex in chloroplasts), and Rip1 (a subunit of the Cytochrome bc-1 (bc1) complex in mitochondria). In the mitochondrial case, however, not all species rely on the TAT pathway, as its genes are only found in some protists [Petrů et al., 2018] and plant mitochondria [Carrie et al., 2016]. Most of the opsithokont (i.e. Fungi, Metazoa and related species) genomes, with only *Monosiga brevicollis* [Burger et al., 2003] and *Oscarellidae* [Wang and Lavrov, 2007] as exceptions, lack genes encoding the TAT pathway. Instead, Bcs1, an inner mitochondrial membrane (IM) bound AAA-ATPase, has been identified as the dedicated protein involved in fully folded Rip1 translocation and insertion [Wagener et al., 2011, Nobrega et al., 1992, Cruciat et al., 1999], when the TAT machinery is absent. Notably, no other substrates of Bcs1 are known to date.

Rip1 ISP

Rip1, also known as Rieske protein [Rieske et al., 1964], is one of the catalytically active subunits of bc1, together with cytochrome b and cytochrome c1. It is formed by three main domains: an N-terminal domain containing a mitochondrial matrix targeting sequence and an α-helical membrane spanning segment; a globular C-terminal domain exposed to the intermembrane space (IMS), harbouring a Fe_2S_2 cluster; and a short, flexible domain that connects the former two. In the bc1 complex, which exists as an obligate homodimer in the IM, the N-terminus of Rip1 interacts with the cytochrome b subunit of one monomer,

while the C-terminus interacts with the cytochrome c1 subunit of the second monomer [Hunte et al., 2000].

The nuclear encoded Rip1 polypeptide, containing 215 amino acids in *S. cerevisiae*, is synthesised in the cytosol and targeted to the mitochondrial matrix. After import through the TOM-TIM23 machinery [Hartl et al., 1986, van Loon et al., 1987], the first 22 amino acids, comprising the matrix targeting signal, are cleaved by the matrix processing peptidase, leading to a Rip1 intermediate (i-Rip1). In a following step, that occurs after assembly of i-Rip1 into bc1 [Nett and Trumpower, 1999], the mitochondrial intermediate peptidase further cleaves eight residues of the N-terminus, resulting in a mature Rip1 (m-Rip1) of 185 amino acids. This two-step post-translational processing of Rip1 contrasts with the single-step cleavage that occurs in mammals where, in addition, the cleaved pre-sequence is kept in the bc1 complex [Brandt et al., 1993].

The import of Rip1 into the matrix, before targeting to its final location in the IM/IMS, is required for the assembly of the Fe_2S_2 cluster by the iron-sulphur cluster assembly machinery (ISC) (**Figure 1.8**) [Kispal et al., 1999, Lill and Freibert, 2020]. The cluster sits in the Fe_2S_2-binding subdomain (FeSD), coordinated by the residues C159, H161, C178, and H181, along with a disulfide bond formed between C164 and C180. This subdomain is structurally supported by a bundle of β strands denominated the base subdomain (BD). Together, these subdomains are key structural elements whose proper folding determines the electron transfer activity of Rip1 [Hunte et al., 2000]. It is not clear whether the folding of Rip1's C-terminus happens before or concomitantly with the Fe_2S_2 assembly process, but a folded conformation is required for translocation and insertion into the IM [Wagener et al., 2011]. The matrix chaperone Mzm1 (LYRM7/MZM1L in humans) stabilizes this transport-competent folded state and, even though it is not required for translocation [Cui et al., 2012, Sánchez et al., 2013], its mutation or deletion impairs bc1 complex assembly and thus respiration [Atkinson et al., 2011]. For its final targeting, the IM bound Bcs1 recognises the Rip1 substrate, translocates the C-terminal domain to the IMS and laterally releases the N-terminal domain into the IM [Wagener et al., 2011]. The assembly of Rip1 is one of the latest steps in the biogenesis of bc1, after a dimerised intermediate of

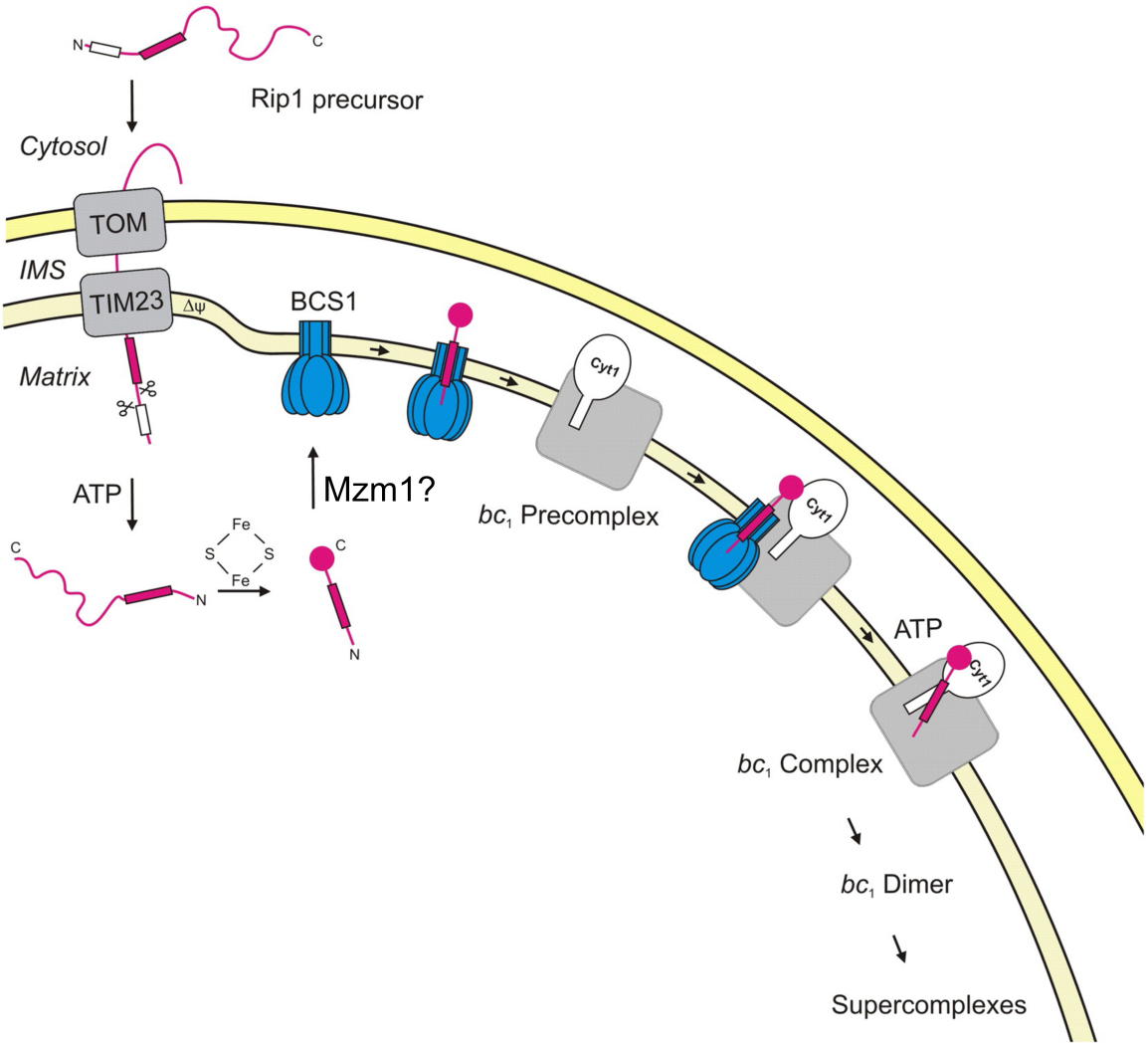

Figure 1.8: Rip1 biogenesis pathway. The Rip1 precursor (p-Rip1) is translocated across TOM and TIM23 into the mitochondrial matrix, where it is post-translationally processed to remove its targeting sequence (22 amino acids), leading to an intermediate form (i-Rip1). The iron-sulphur cluster is assembled concomitantly with the removal of additional eight residues from the N-terminus, resulting in the mature form (m-Rip1), which is stabilised by the matrix chaperone Mzm1. It is not clear whether Mzm1 hands over m-Rip1 directly to Bcs1. After translocation by Bcs1, Rip1 is laterally released, and the bc1 complex biogenesis can move forward. Figure adapted from [Wagener et al., 2011].

around 500 kDa (Intermediate III) containing cytochrome b, cytochrome c1, Cor1, Cor2, Qcr6, Qcr7 and Qcr8 has been assembled [Ndi et al., 2018]. It was initially proposed that Rip1 insertion into bc1 could be a pre-requisite for its dimerization [Cruciat et al., 2000]. However, it has been shown that the dimerization is an early event in the biogenesis of bc1, independent of Rip1 incorporation [Conte et al., 2015, Stephan and Ott, 2020]. At this step, Qcr9 insertion into the intermediate III is required for the assembly of Rip1 [Phillips et al., 1993]. Once Rip1 is incorporated, the last subunit, Qcr10, can associate with bc1 and the functional complex is complete.

The Bcs1 AAA-ATPase

The *BCS1* (ubiquinol-cytochrome c reductase (bc1) synthesis) gene was first discovered by screening respiratory deficient mutants in *S. cerevisiae*, which exhibited a substantial decrease in the levels of Rip1 assembled into the bc1 complex. The product of the gene, Bcs1, was found to be essential for the expression of a catalytically active bc1, being particularly involved in the handling of Rip1, as over-expression of the substrate could not rescue the observed phenotype [Nobrega et al., 1992]. Similarly, mutations in the human ortholog, *BCS1L*, have been found to be the cause of different human diseases related to bc1 complex deficiency due to failed Rip1 assembly [De Meirleir et al., 2003] such as the GRACILE [Ramos-Arroyo et al., 2009] and the Björnstad [Hinson et al., 2007] syndromes. Bcs1 is imported via the TOM-TIM23 machinery and anchored to the IM via an N-terminal TMH, downstream of which the IM targeting signal is located [Folsch et al., 1996]. Its matrix facing C-terminus contains a conserved AAA-ATPase domain (ATPases associated with diverse cellular activities [Erdmann et al., 1991, Tomoyasu et al., 1993]) that diverges from several clades in the superfamily [Frickey and Lupas, 2004]. The AAA domain resembles the D1 domain of AAA-ATPases such as p97/Cdc48, but it lacks a second domain (D2) and a pore loop region [Wagener and Neupert, 2012], core features of the family involved in substrate handling (binding, unfolding, translocation) (**Figure 1.9**) [Wagener and Neupert, 2012, Martin et al., 2008]. The absence of these features and the

fact that translocation of a fully folded Rip1 substrate poses a different challenge, compared to the threading of unfolded peptide chains, raised the question of whether Bcs1 would follow the well-known "hand-over-hand" mechanism [Puchades et al., 2020], as many AAA-ATPases do, or an alternative mechanism would be in place [Wagener and Neupert, 2012].

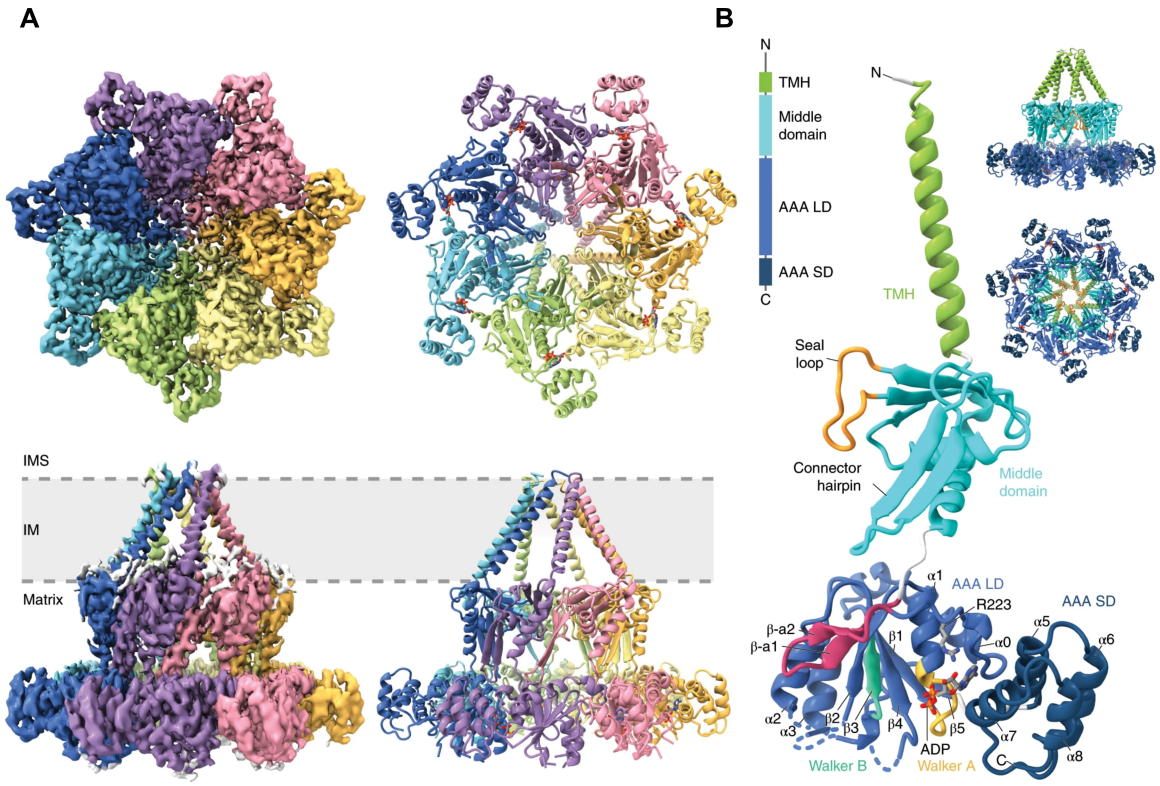

Figure 1.9: Structure of Bcs1. (**A**) Matrix (top) and side views (bottom) of a cryo-EM 3D reconstruction (left) and corresponding atomic model (right) of Bcs1 in the ADP bound state. (**B**) Structural details of one Bcs1 protomer, TMH: transmembrane helix, MD: middle domain, AAA: AAA-ATPase (LD): large or (SD): small domain. Figure adapted from [Kater et al., 2020].

In recent years, structural studies on *M. musculus* (mBcs1) [Tang et al., 2020] and *S. cerevisiae* (yBcs1) [Kater et al., 2020] shed light on Bcs1's tertiary and quaternary structure. Unexpectedly, Bcs1 exclusively forms homoheptameric oligomers, in contrast to most of the AAA-ATPases characterised so far, which form homohexameric rings [Iyer et al., 2004, Vale, 2000, Zhang et al., 2021]. This oligomeric assembly not only grants it a wide matrix

facing vestibule with a pore of around 40 Å, big enough to accommodate a folded Rip1 (around 30 Å), but allows for a basket-like arrangement of the TMHs, therewith an IM embedded vestibule is created. A middle, Bcs1 specific domain close to the matrix-IM interface separates both vestibules, acting as a seal and potentially restricting the free movement of molecules between them [Kater et al., 2020, Tang et al., 2020].

Bcs1 undergoes major conformational changes upon nucleotide binding. In yBcs1, three main states (one ADP bound state and two Apo states) outline a transition from ADP-bound state to Apo state, characterised by changes in the matrix vestibule and the middle domain. yBcs1's (456 amino acids) N-terminal TMH comprises amino acids 53-83, followed by the seal-forming middle domain (MD, amino acids 84-202), a large (LD, amino acids 203-387) and a small (SD, amino acids 388-449) AAA domains. The MD contains a loop, termed the seal loop, protruding towards the central axis of the heptamer, and a β-hairpin, termed the connector hairpin (CH), that interacts with the LD. In the ADP state, yBcs1 exhibits a matrix pore diameter of 40 Å, a tightly closed MD seal and CH loops pointing towards the matrix. During the transition from the ADP state through the two Apo states (Apo1 and Apo2), its AAA domain (SD and LD) rotates inwards, closing the matrix pore from 40 Å to around 30 Å (Apo1), followed by an outward movement of the CH and a slight opening of the MD seal (Apo2) [Kater et al., 2020]. Notably, even though mBcs1 appears to have structurally similar ADP and Apo states, the trend of inwards movement of the AAA domain, together with the outwards movement of the CH and opening of the seal continues upon ATP binding. mBcs1 bound to ATPγS, a non-hydrolysable ATP analogue, displays a constricted matrix vestibule and a wide-open MD seal, suggesting that ATP binding might trigger a major conformational change where the matrix and IM vestibules are connected, what could allow the substrate to be translocated from one to the other [Tang et al., 2020].

These observations lead to the proposal of an "airlock-like" mechanism for the translocation of Rip1 across the IM, divided in three main steps (**Figure 1.10**) [Kater et al., 2020]. First, a transport competent Rip1 docks in the matrix vestibule of Bcs1. In the second step, ATP binding causes a major constriction of the matrix vestibule and opening of the

MD seal, allowing the movement of Rip1 towards the IM vestibule. Finally, the third step would involve the lateral release of Rip1 N-terminus to the IM and release of the C-terminus to the IMS. A salient feature of this mechanism is the requirement for a concerted ATP hydrolysis, opposed to the sequential hydrolysis observed in the hand-over-hand mechanism [Puchades et al., 2020]. Evidence for such concerted hydrolysis cycle was obtained by means of high-speed atomic force spectroscopy (HS-AFM), where a transition between protomers was observed to be at least three orders of magnitude faster than the mean half-life of ADP or ATP bound states [Pan et al., 2023]. The concerted mechanism and controlled gating of the MD seal are also consistent with the requirement of maintaining the proton gradient across the IM.

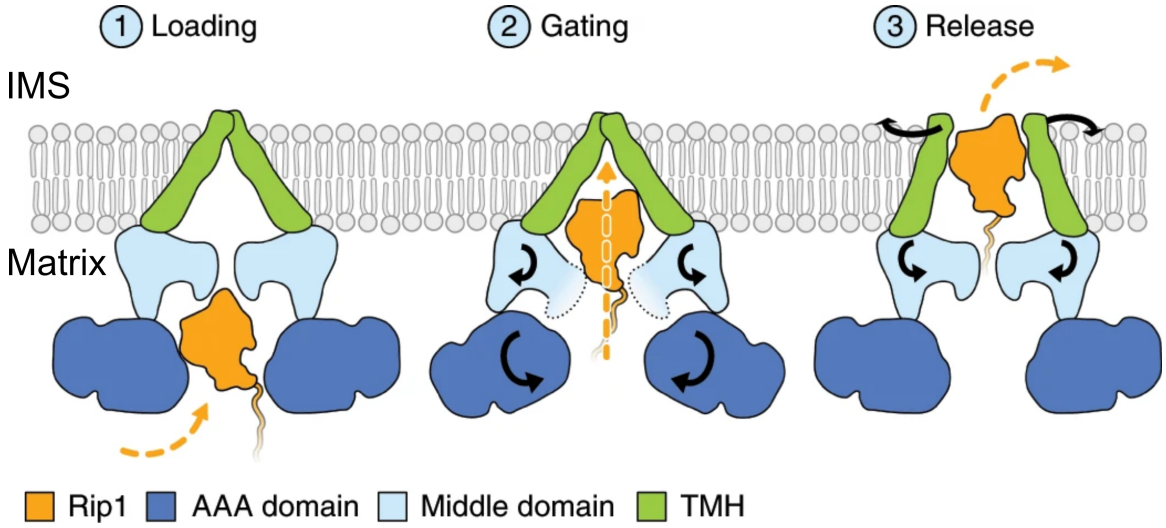

Figure 1.10: Model of the airlock-like mechanism of Bcs1-mediated Rip1 translocation. Bcs1 is proposed to translocate Rip1 in three main steps: first, a loading step where Rip1 docks at the matrix vestibule, followed by a second step where the middle domain opens to allow the movement of the substrate towards the IMS vestibule and a third step, where the TMH domain opens to allow the lateral release of Rip1 into the IM. Figure adapted from [Kater et al., 2020].

1.2.3 Research question and aim of Publication 2

The airlock-like mechanism offers a plausible explanation of how Bcs1 translocates its fully folded substrate across the IM without disrupting the electrochemical proton gra-

dient. However, the question remains how and when Bcs1 binds Rip1 and what are the molecular details of that interaction. The aim of Publication 2 was to capture stable Bcs1-Rip1 translocation intermediates and determine their 3D structure by cryo-EM to confirm the proposed airlock mechanism. Furthermore, another goal was to characterise different binding modes of Bcs1 to Rip1, identifying the necessary elements for translocation, and provide a clearer picture of how Bcs1 coordinates Rip1 movement across the IM during the ATP hydrolysis cycle.

1.3 Transport of small molecules across membranes

The permeability barrier of the lipid bilayer not only restricts the free movement of polypeptides and folded proteins (Section 1.2) but also affects the rate of diffusion of small molecules and ions. While small hydrophobic or non-polar molecules, such as CO_2 and O_2, readily diffuse down their concentration gradient, lipid bilayers are virtually impermeable to polar molecules such as H_2O and urea, as well as to ions like Na^+, K^+ and Mg^{2+}. However, these and many other charged chemical species, also called solutes, are central to different cellular processes and, therefore, the cell has evolved mechanisms to control the rate at which they are imported and exported across the membrane.

The mechanisms of transport are divided in passive transport and active transport, each carried out by specialized, multi-pass membrane proteins. Passive transporters facilitate the movement of solutes in the direction of their concentration gradient. They can perform this activity by alternating between inwardly and outwardly open conformations that expose their binding sites to opposing sides of the membrane (e.g. members of the major facilitator superfamily (MFS) such as GLUT transporters [Chen and Phelix, 2019, Deng et al., 2015]), or by providing an aqueous conduit spanning the lipid bilayer. In contrast, active transporters use a source of energy as the driving force for the transport of solutes against their concentration gradient. The sources can be the energy stored in the electrochemical gradient of a different solute (e.g. the sodium dependent, excitatory

amino acid transporters EAATs [Kato et al., 2022]), the energy released by ATP hydrolysis (ABC transporters [Thomas and Tampé, 2020], P-type ATPases [Palmgren, 2023] and F-/V- ATPases [Kühlbrandt, 2019, Chen et al., 2022]), and the energy coming from photons (bacteriorhodopsin [Haupts et al., 1999]) or released by redox reactions (cytochrome c oxidase [Wikström and Sharma, 2018]). Many similarities exist between transporters mediating passive and active transport. Most active transporters also alternate between inwardly and outwardly open conformations during transport and, by experimentally adjusting the solute concentrations at both sides of the membrane, they have been shown to reverse their direction of transport [Garrahan and Glynn, 1966, Mintz et al., 1990]. However, in the case of transport coupled to the gradient of an ion, the conformational changes are only triggered in presence of the solute, which prevents dissipation of the gradient uncoupled to transport.

Passive transporters forming an aqueous passage across the membrane are called channels. Because their interaction with the solute is more transient, their rate of transport is faster than other types of transporters. Specialised channels transport ions such as Na^+, K^+, Cl^- or Ca^{2+}, among others, with high selectivity [Catacuzzeno et al., 2025] through gates regulated by different external stimuli such as ligands (ligand-gated) or in response to the membrane potential (voltage-gated). Other channels are more permissive, allowing the passage of small ions and polar molecules through the outer membranes (OMs) of bacteria, mitochondria and chloroplasts [Bölter and Soll, 2001, Vergalli et al., 2020]. They are collectively referred to as porins and are in many cases multi-pass β-barrel membrane proteins. Salient examples are OmpF in *E. coli* [Cowan et al., 1992], VDAC in mitochondria [De Pinto, 2021] and OEP21 in chloroplasts [Günsel et al., 2023].

An important class of porins includes those involved in the secretion of synthase-dependent polysaccharide chains in gram-negative bacteria (**Figure 1.11**). These polysaccharides are required in the formation of biofilms, essential for the establishment of sessile bacterial communities, which confer them resistance to different chemical and physical stressors in the environment as well as to antimicrobial agents [Liu et al., 2024]. A common component in biofilms of *Enterobacteriaceae* is phosphoethanolamine-cellulose, which

is transported to the extracellular space by BcsC, an OM β-barrel porin contacting the IM through a long, N-terminal domain with tetratricopeptide repeats (TPR), involved in substrate handling during export [Acheson et al., 2019]. Other examples in gram negatives include the OM β-barrel porins for transport of alginate and poly-β-D-N-acetylglucosamine (PNAG), AlgE and PgaA, respectively [Whitney and Howell, 2013]. *P. aeruginosa*, an opportunistic, gram-negative pathogen secretes, together with alginate and Psl, the pellicle polysaccharide (Pel) for biofilm formation, critical for its virulence and persistence [Franklin et al., 2011]. Translocation of Pel across the OM is proposed to occur through PelB, a β-barrel porin structurally similar to BcsC and PgaA [Marmont et al., 2017a]. Details of the Pel biosynthesis and export machinery will be discussed in the following section.

1.3.1 Pel transport in *Pseudomonas aeruginosa*

Pel polysaccharide biosynthesis and export are performed by the proteins encoded in the PelABCDEFG operon, PelA-G (**Figure 1.11D**) [Franklin et al., 2011], all essential for the pellicle formation [Friedman and Kolter, 2004, Vasseur et al., 2005]. Its assembly process starts in the cytosol, with the polymerisation of galactosamine (GalN) into a linear N-acetyl-α-1,4-GalNAc homopolymer [Le Mauff et al., 2022]. This reaction is catalysed by the cytosolic glycosyl-transferase PelF [Ghafoor et al., 2013], which binds uridine 5'-diphosphate (UDP) [Jennings et al., 2015, Marmont et al., 2020] and, therefore, potentially uses UDP-GalNAc as substrate. The biosynthesis of Pel is allosterically regulated by binding of bis-(3'-5')-cyclic dimeric GMP (c-di-GMP) to the cytosolic domain of PelD, an IM protein with four TMDs in its N-terminus [Lee et al., 2007, Whitney et al., 2012]. Also in the IM, the proteins PelE, containing two TMDs and a TPR domain, and PelG, containing twelve TMDs, are potentially involved in multimerization with PelD and electrochemical gradient coupled transport of the nascent polymer across the IM, respectively [Franklin et al., 2011]. Based on bacterial adenylate cyclase two-hybrid (BATCH) assays, different interactions between each of these components have been observed, indi-

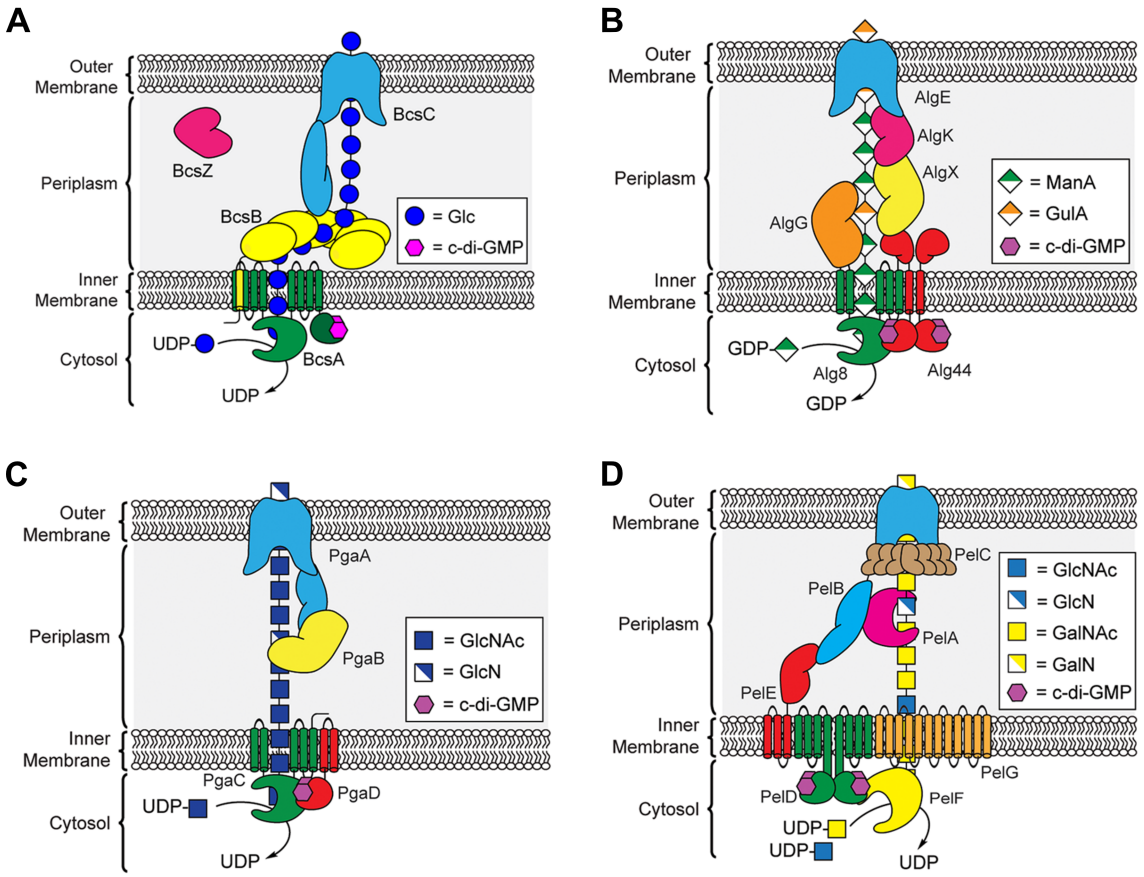

Figure 1.11: Biofilm exopolysaccharide biosynthesis machineries. The main components of each machinery are displayed for (**A**) cellulose, (**B**) alginate, (**C**) PNAG and (**D**) Pel. Among their shared features is the use of a specialized porin (BcsC, AlgE, PgaA or PelB), through which the assembled polysaccharide is exported, and a c-di-GMP binding component in the IM, which enables allosteric control of the polysaccharide biosynthesis. Figure adapted from [Poulin and Kuperman, 2021].

cating that an IM localized complex integrated by PelDEFG acts as the Pel polysaccharide synthase [Whitfield et al., 2020]. In this complex, PelD, most likely as a homodimer [Whitney et al., 2012], allosterically regulates the assembly of the polymer carried out by PelF, which is subsequently translocated through PelG. The BATCH assays have also suggested that contrary to what was previously postulated [Franklin et al., 2011], the TPR domain of PelE localises to the cytosol and not to the periplasm. In this way, PelE would act as a hub both at the IM, through its two TMDs, and the cytoplasm, through its TPR domain, coordinating the organisation and crosstalk between the other subunits. The

structural elucidation of PelDEFG in presence of c-di-GMP and substrate could shed light into the organisation of the different domains in the active state of the complex.

After its translocation into the periplasm, PelA modifies Pel via its deacetylase and glycoside hydrolase domains [Van Loon et al., 2025]. The selective removal of acetyl groups from GalNAc by the former transforms the homopolymer into a chain of dimeric repeats containing both galactosamine and N-acetylgalatosamine, conferring it a positively charged surface [Colvin et al., 2013]. The hydrolase domain generates a cell-free form of the polymer, relevant for *P. aeruginosa* virulence [Razvi et al., 2023]. PelA has been observed to interact with the N-terminal TPR domain of PelB, the OM porin proposed to ultimately export the modified Pel to the extracellular space [Marmont et al., 2017b], bridging the path from the IM machinery to the PelB pore and modulating the deacetylation/hydrolysis activity of PelA [Van Loon et al., 2025]. A characteristic trait of the Pel export machinery, compared to other polysaccharide export systems, is the involvement of a lipoprotein bound to the inner leaflet of the OM, PelC [Franklin et al., 2011]. The crystal structure of a PelC homolog from *Paraburkholderia phytofirmans* allowed the visualisation of its ring-shaped dodecameric assembly [Marmont et al., 2017a]. The observation that the periplasm-facing side of the ring is negatively charged suggested that, during deacetylated Pel transport, PelC directs the nascent polymer towards the OM. Additionally, the previous assignment of the C-terminal helix as a TM domain could be re-evaluated [Franklin et al., 2011, Vasseur et al., 2007], leading to the conclusion that, instead, PelB, whose C-terminal domain is predicted to form a β-barrel porin [Keiski et al., 2010], could form the channel through which Pel is secreted.

1.3.2 Research question and aim of Publication 3

Bioinformatic analyses have shown that numerous gram-positive and gram-negative bacterial species have a Pel biosynthesis locus, underscoring the conservation and potential relevance of the Pel biosynthesis pathway in biofilm formation [Whitfield and Howell, 2021].

However, PelB, PelC or a PelBC complex from *P. aeruginosa* have so far eluded structural characterisation, raising the question of what the determinants for the assembly of the PelBC complex are, how the transport of Pel is coordinated and whether the dodecameric assembly is also observed in association with PelB or alternative stoichiometries are possible. The aim of Publication 3 was to combine structural characterisation, molecular dynamics simulations and biophysical studies in order to identify the critical elements for PelBC assembly, and propose a model of Pel translocation across the OM.

Chapter 2

Publications

2.1 Publication 1 | Substrate-induced assembly and functional mechanism of the bacterial membrane protein insertase SecYEG-YidC

Substrate-induced assembly and functional mechanism of the bacterial membrane protein insertase SecYEG-YidC

Max Busch[1,*], Cristian Rosales Hernandez [2, *], Michael Kamel [1, #, *], Yulia Schaumkessel [1, ¥], Eli van der Sluis [2, §], Otto Berninghausen [2], Thomas Becker [2], Roland Beckmann [2, ✉], Alexej Kedrov [1, 3, ✉]

[1] Synthetic Membrane Systems, Institute of Biochemistry, Heinrich Heine University Düsseldorf, Germany

[2] Gene Center Munich, Ludwig Maximilian University Munich, Germany

[3] Interfaculty Center for Membrane Research, Heinrich Heine University Düsseldorf, Germany

Current affiliations:

[#] Dept. Biology, Osnabrück University, Germany

[¥] Institute of Biochemistry and Molecular Biology I, Heinrich Heine University Düsseldorf, Germany

[§] Kavli Institute of Nanosciences, Technical University of Delft, the Netherlands

[*] These authors contributed equally to this work

[✉] Corresponding authors

Abstract

The universally conserved Sec translocon and the YidC/Oxa1-type insertases mediate biogenesis of α-helical membrane proteins, but the molecular basis of their cooperation has remained disputed over decades. A recent discovery of a multi-subunit insertase in eukaryotes has raised the question about the architecture of the putative bacterial ortholog SecYEG-YidC and its functional mechanism. Here, we combine cryogenic electron microscopy with cell-free protein synthesis in nanodiscs to visualize biogenesis of the polytopic membrane protein NuoK, the subunit K of NADH-quinone oxidoreductase, that requires both SecYEG and YidC for insertion. We demonstrate that YidC is recruited to the back of the translocon at the late stage of the substrate insertion, in resemblance to the eukaryotic system, and in vivo experiments indicate that the complex assembly is vital for the cells. The nascent chain does not utilize the lateral gate of SecYEG, but enters the lipid membrane at the SecYE-YidC interface, with YidC being the primary insertase. SecYEG-YidC complex promotes folding of the nascent helices at the interface prior their insertion, so the examined cellular pathway follows the fundamental thermodynamic principles of membrane protein folding. Our data provide the first detailed insight on the elusive insertase machinery in the physiologically relevant environment, highlight the importance of the nascent chain for its assembly, and prove the evolutionary conservation of the gate-independent insertion route.

Introduction

Integral membrane proteins (IMPs) constitute up to 30 % of a genome content for each organism and determine the functionality of the cellular membranes[1]. Biogenesis of α-helical IMPs at the cytoplasmic membrane of bacteria and the endoplasmic reticulum (ER) in eukaryotes typically occurs in a co-translational manner: The nascent transmembrane helices (TMHs) emerging from the ribosome are identified by the signal recognition particle (SRP) and delivered in the form of ribosome-nascent chain complexes (RNCs) to the universally conserved Sec translocon that facilitates their insertion in the lipid bilayer [2,3]. The translocon of *Escherichia coli* (*E. coli*) is a heterotrimeric complex composed of SecY, SecE and SecG proteins forming a central pore. N- and C-terminal halves of the central subunit SecY may open laterally in a clam-shell manner, thus opening a lipid-exposed gap between the opposing TMHs 2b and 7. This gap, commonly referred as the “lateral gate”, has been seen as the exclusive site for the nascent TMHs to partition into the lipid phase, both for bacterial SecYEG and the homologous Sec61αβγ in eukaryotes. This model was supported by extensive biochemical studies [4,5] and more recently by structural insights, commonly focusing on signal peptides of secretory proteins and single-span IMPs exposing their N-terminal end into the cytoplasm [6-8]. However, polytopic IMPs have their TMHs in alternating topology, suggesting higher complexity within the biogenesis pathways [9,10].

Folding of numerous bacterial IMPs relies on a cooperative action between SecYEG and the essential and ubiquitous membrane protein insertase YidC [11]. YidC may distort the cytoplasmic lipid leaflet and facilitate folding and membrane insertion of the nascent IMPs [12,13]. Extensive intermolecular cross-linking studies suggested that YidC is located in front of the lateral gate of SecYEG where it could access the nascent TMHs emerging from the lateral gate [5,14], and the model was further supported by low-resolution cryo-EM analysis [15]. Remarkably, the AlphaFold model predicts a position of YidC of *E. coli* and other Gram-negative bacteria at the back of SecYEG, and diverse architectures are predicted for the homologs from Gram-positive bacteria, such as

Bacillus subtilis (Suppl. Figure 1). In all the cases, the model confidence is low, suggesting that other factors, such as the bound ribosome and/or the nascent chain may be required for the complex assembly.

Recent biochemical and high-resolution cryo-EM studies of the eukaryotic insertase machinery revealed that the YidC homolog TMCO1 was located at the back of the Sec61 complex, being a component of the large multi-subunit complex BOS-GEL-PAT [16,17]. Furthermore, insertion of a nascent polytopic IMP occurred not via the lateral gate, but between Sec61 and the BOS complex, thus challenging the long-standing paradigm in the field. The accumulated controversy between the insights from the eukaryotic homologs and the conventional model of the SecYEG-YidC complex has raised the question about the mechanism of IMP folding in bacteria and the architecture and dynamics of the insertion machinery. To tackle this issue, here we employed nanodisc-reconstituted SecYEG-YidC and cell-free protein synthesis (CFPS) to analyze the biogenesis of the polytopic IMP NuoK, the subunit K of the NADH-quinone oxidoreductase that requires both insertases for proper membrane integration and folding in *E. coli* [18]. By means of cryo-EM, we describe the detailed architecture of the RNC-bound SecYEG-YidC complex, where YidC is recruited to the back of SecYEG in the substrate-dependent manner thus indeed resembling the architecture of the eukaryotic insertase machinery. The nascent chain emerging from the SecY-bound ribosome is routed away from the lateral gate to the crossed SecY TMH 10 and SecE TMH 3 and then handed over to YidC to be inserted into the lipid bilayer via the dedicated groove. Overall, the data elucidate the functional architecture of the bacterial cotranslational IMP insertion machinery and reveal the evolutionary conservation of the “back-of-Sec" insertion route, thereby offering a new perspective on membrane protein biogenesis in bacteria.

Results

SecYEG and YidC-dependent insertion in nanodiscs

We set out to elucidate the architecture of the SecYEG-YidC complex by means of cryo-electron microscopy (cryo-EM) using lipid-based nanodiscs as a well-defined system for studying IMP insertion [6,19,20] (Figure 1A). To co-reconstitute both SecYEG and YidC in the relevant topology and to avoid their stochastic distribution among the nanodiscs, YidC and SecE were genetically fused via a cleavable linker (Suppl. Figure 2A), while the non-essential catioinic C-terminal end of YidC was removed to exclude spontaneous electrostatic interactions with the ribosome observed *in vitro* [19,21]. The fusion protein was expressed and isolated together with SecY and SecG subunits (Figure 1B). The complex was reconstituted into a sufficiently large nanodisc formed by MSP2N2 scaffold protein (expected diameter up to 17 nm) and treated with the HRV-3C protease to release YidC from SecE [22] (Figure 1C and Suppl. Figure 2B-D). As a result, each nanodisc contained one copy of both SecYEG and YidC, presumably in the correct orientation, while the dimensions of the surrounding lipid bilayer would allow for lateral diffusion of the proteins, assembly of the functional complex and insertion of the nascent TMHs. Supporting this notion, the molecular weight distribution of the nanodisc-embedded SecYEG-YidC complexes centered at 290 kDa (Figure 1D), and the difference from the calculated total protein weight of ~225 kDa likely reflected the presence of the co-reconstituted lipids.

We focused on biogenesis of *E. coli* NuoK (Suppl. Figure 3A), as both *in vivo* and *in vitro* experiments confirmed its dependence on SecYEG and YidC [18,23]. To ensure sequential incorporation of nascent NuoK TMHs into the membrane and reduce the risk of erroneous insertase:substrate complexes, we supplied the SecYEG-YidC nanodiscs to the CFPS reaction based on *E. coli* S30 extract. With that, the translating ribosomes were targeted to SecYEG-YidC, presumably by the endogenous SRP and the SRP receptor FtsY, to initiate nascent IMP insertion. To form a defined co-translational insertion intermediate, the gene construct coded for the first three TMHs of NuoK (NuoK^{86}) followed by a 31 aa long linker, incl. HA-tag and a C-terminal ribosome stalling sequence SecM* [24,25] (Suppl. Figure 3B and C). With this construct, after CFPS, the SecM* peptide and the linker/tag would occupy the exit tunnel of the stalled ribosome, while all three NuoK TMHs would be exposed and accessible for the insertase complex (Figure 1A).

Visualiation of the active RNC:insertase complex

The purified NuoK^{86}-RNC:SecYEG-YidC complexes were stabilized by rapid glutaraldehyde crosslinking before vitrification and cryo-EM analysis. After 3D classification followed by focused classification and refinement of the tunnel exit region, we obtained a structure of this complex with an average resolution of 2.4 Å (Suppl. Figure 4). The reconstruction showed a ribosome programmed with tRNAs in the A- and P-sites, a continuous nascent chain density ranging from the CCA-end of P-site tRNA to the tunnel exit and a clear density below the exit tunnel accounting for SecYEG and YidC embedded into a nanodisc of approx. 15 nm in diameter (Figure 1E and F). Focused refinement of the nanodisc density resulted in a local resolution of 3 to 5 Å for SecYEG and 4 to 7 Å for most parts of YidC (Suppl. Figure 4B and C) and allowed unambiguous docking of the modelled SecYEG-YidC complex with only minor adjustments (Suppl. Figure 5). The structure shows the RNC-bound SecYEG in the center of the nanodisc, while YidC is positioned at the back side of SecYEG near SecE TMH 3, with the large P1 domain of YidC exposed to the “periplasmic” side of the nanodisc. An additional density accounting for TMH 2 and TMH 3 of NuoK appears between SecYEG and YidC,

building extensive interactions with both proteins within the membrane and at the interface (Figure 1E). At lower contour levels, an additional transmembrane density appeared near NuoK TMH 2, which likely represents NuoK TMH 1 (Suppl. Figure 5F), though YidC TMH 1 could not be excluded.

As YidC was initially fused with SecE TMH 1 near the lateral gate, it must have relocated substantially within the lipid-filled nanodisc after the linker cleavage. To test whether the localization of YidC was not artificially induced by the chemical crosslinking, we carried out cryo-EM analysis of the non-crosslinked NuoK^{86}-RNC:SecYEG-YidC sample (Suppl. Figure 6). Though somewhat weaker and less well resolved, YidC density was clearly present in the same position at the back of SecYEG, implying that the crosslinked sample reflects the endogenous architecture of the substrate-bound SecYEG-YidC machinery.

Architecture of the SecYEG-YidC insertase

The clear density for all TMHs of SecY, SecE and SecG present in the local refined map offered the by now best-resolved view on the translocon structure in the physiologically relevant lipid environment (Figure 2A; Suppl. Figure 5). As observed previously for SecYEG-only assemblies, SecY is anchored via its cytoplasmic loops 6/7 and 8/9 to the tunnel exit of the large ribosomal subunit 50S (Figure 2B and C). Interestingly, SecY loop 6/7 is somewhat remodeled compared to the previously reported RNC-FtsQ:SecYEG assembly [6]. To avoid a clash with the NuoK nascent chain, the loop shifts away from the exit tunnel towards H6/7 and uL23 (Suppl. Figure 7A). Here, Tyr-258 is tightly accommodated in a pocket formed by bases A91, U92 and G93 of H7, while Arg-256 stacks on A63 of H6, and Arg-255 interacts with the loop of uL23 (His-70/Gly-71/Gln-72) (Figure 2B). In fact, this distortion in loop 6/7 leads to a global re-positioning of SecYEG with respect to the ribosome, with the 50S tilting by ~10° towards the N-terminal half of SecYEG (Suppl. Figure 7B). Contacts between the loop 8/9 with 50S are established via Lys-348 with the flipped-out base C490 of 23S rRNA helix H24 and a stacking interaction between SecY Arg-357 with A1392 (H53) that may be stabilized by a salt bridge with Glu-18 of the proximate ribosomal protein uL23 (Figure 2C). Further interactions are via the backbone of SecY Lys-347 with U1318 (H50) and Arg-340, Lys-364 with the flipped-out base A1535 of H59. The C-terminal cytoplasmic extension of SecY TMH 10 is bowed at Met-425/Ser-426 toward the SecY loop 8/9, so another contact is formed with the flipped-out base C490 of rRNA H24 (likely via Ala-436) (Figure 2D). As this SecY:ribosome contact was absent in earlier SecYEG:ribosome structures [6,7,9], we speculated that its formation is associated with the specific nascent chain routed for insertion. Notably, the lateral gate formed by TMHs 2b and 7 is in a tightly closed conformation indicating that it is not employed by the NuoK nascent chain, and the central pore is sealed by the "plug" domain, TMH 2a of SecY (Suppl. Figure 7B and C).

The conformation of YidC within the RNC-bound complex clearly deviates from the structure of isolated YidC obtained via X-ray crystallography [26] (Suppl. Figure 5E). The paddle domain, i.e. the hairpin built of helices CH1 and CH2 at the cytoplasmic interface, shifts by 1 nm to the periphery of the complex. There, it appears in close vicinity to the ribosomal protein uL24, but does not form a direct contact (Figure 2A). With that, it allows the passage of the nascent chain (Figure 2E), as described below. Furthermore, YidC TMH 6 is located at the periphery of the nanodisc, and its C-terminal extension is not required for the ribosome:SecYEG-YidC assembly, though this polypeptide is essential for binding to an RNC in absence of SecYEG *in vitro* [19], and it is also important for the homologous ribosome:Oxa1 interactions in mitochondria [27]. The large density at the periplasmic side matched the structure of the YidC P1 domain known from crystallography studies [26,28]. With respect to SecYEG, YidC is oriented with its TMH 3 facing TMH 3 of SecE, and the tip of the paddle domain faces the N-terminal end of SecY, in agreement with the efficient crosslinks observed in *E. coli* membranes between the residue 399 of YidC and SecY [14]. At the periplasmic side, the essential amphipathic helix EH1 and SecY TMH 5 (Figure 2E) form the only pronounced direct contact between these two proteins. In agreement with the AlphaFold2 model and our map in this region, this contact is mediated by SecY Arg-211 and YidC Asp-329 forming a salt bridge (discussed below). Apart from the salt bridge, SecYEG and YidC are held together mainly by the NuoK^{86} nascent chain, i.e. TMH 3 at the cytoplasmic interface and TMH 2 within the membrane region, suggesting that YidC is likely recruited to the RNC-bound SecYEG in a substrate-dependent manner.

Routing and insertion of the nascent NuoK

The nascent chain could be unambiguously traced from the CCA-end of P-site tRNA to the tunnel exit site within the ribosome (Figures 1F and 3A). All side chains of the SecM* stalling element ($_{111}$WWWPRIRGPP$_{120}$) were resolved with Pro-120 attached to the CCA-end of the A-site tRNA, while the preceding modified motif $_{117}$RGP$_{119}$ ($_{163}$RAG$_{165}$ in SecM) was coupled to the CCA-end of the P-site tRNA (Figure 3A). The conformation of the stalling peptide, tRNAs and critical bases in the peptidyl-transferase center were highly similar to the structure of SecM-stalled *E. coli* ribosome [29], indicating the same trapping mechanism as described for the RAG/P motif and its modified versions. Further, residues Arg-115 and Arg-117 interacted with PSU2504 and A2062, and the aromatic rings of the tryptophan motif ($_{112}$WWW$_{114}$) with bases A2059 and U2586 in the 23S rRNA (Figure 3B). Less resolved density accounting for the linker and the HA-tag continues from the constriction by uL4 and uL22 towards the tunnel exit (Figure 1F).

At the mouth of the tunnel exit, the NuoK nascent chain acquires a helical fold accounting for three C-terminal turns of its TMH 3 docked between the SecY loops 6/7, 8/9 and C-terminal TMH 10 extension and the tip of uL24 (Figure 3C). This newly formed arrangement of SecY creates a hydrophobic pocket in the otherwise hydrophilic environment of the tunnel exit and the solvent, that allows early folding and accommodation of a short hydrophobic TMH (Figure 3D). Strikingly, the emerging nascent chain is not routed into the central channel or the lateral gate of SecY. Once approaching the cytoplasmic funnel of SecY, NuoK TMH 3 density is kinked by approx. 120° towards the back side of the SecYEG, and so it acquires an interfacial topology laying over TMH 3 of SecE and TMH 10 of SecY (Figure 3E). These crossed TMHs form a sawhorse-like crevice at the membrane interface oriented toward YidC. In its turn, the paddle domain of YidC covers the nascent NuoK helix from the cytoplasmic side and completes a triangular window for the hydrophobic substrate. This observation is also consistent with previously proposed interactions of the evolutionary conserved paddle with substrates [13]. Like the SRP M-domain or Get3/TRC40, the YidC paddle contains a “methionine bristle” for client binding and indeed, our structure now shows how the membrane-facing Met-408 and Met-409 in CH2 interact with NuoK TMH 3 prior its insertion (Figure 3E). Notably, replacing these methionine residues with lysines, but not alanine, rendered a cold-sensitive phenotype in *E. coli* upon depletion of the wild-type YidC (Figure 3F, Suppl. Figure 8). We speculate that the effect originates from defects in IMP biogenesis, and that the apolar environment provided by the paddle domain is an important factor for the nascent IMP folding at the lipid membrane interface prior the insertion, in agreement with the physical considerations [30].

The close association of YidC with SecYEG ensures immediate hand-over of the nascent chain to the YidC insertase, and the position of NuoK TMH 2 in our structure elucidates the insertion route (Figure 4A). The membrane-inserted NuoK TMH 2 is separated from TMH 3 by the kink, likely the short flexible loop, in a close contact with YidC TMH 3 at the level of Cys-423 of the insertase. NuoK TMH 2 occupies the wide groove between YidC TMHs 3 and 5, i.e. the functional insertase site described in previous studies[20,31]. As the groove narrows towards the periplasm, the N-terminal end of NuoK TMH 2 is expelled from the helical bundle of YidC, being fully exposed to the lipid environment. Notably, the visualized NuoK does not reach YidC TMH 2 and does not interact with Arg-366 located deep in the YidC groove (Figure 4A). This residue was shown to be important for YidC functionality, as it destabilizes the lipid membrane and potentially interacts with charged/polar insertion substrates [12,32]. Although not observed in our structure, we cannot exclude that this interaction is formed at other stages of NuoK insertion, or it may be specific for particular nascent IMPs.

Determinants for the SecYEG-YidC assembly

Since the structure of SecYEG-YidC is organized around the NuoK insertion intermediate, we next asked how specific elements of the nascent chain may affect the complexes’ assembly. As YidC involvement in NuoK biogenesis was previously linked to Glu-36 and Glu-72 residues within TMH 2 and TMH 3 of the nascent IMP, respectively [18], we substituted both glutamates with lysines and performed cryo-EM analysis of the NuoK^{86mut}-RNC:SecYEG-YidC complexes (Figure 4B; Suppl. Figure 9). Despite the charge inversion and without the glutaraldehyde stabilization, the YidC density was observed in the same position at the back of SecYEG as upon wild-type NuoK insertion. However, when the length of the nascent chain was reduced to 48 amino acids, so only TMH 1 and TMH 2 of NuoK were exposed from the ribosome (NuoK^{48}-RNC), only the RNC-bound SecYEG was resolved within the nanodisc. The signal for YidC was lost, so the insertase remained mobile within the surrounding membrane, and the nanodisc manifested the characteristic tilt by ~10° (Figure 4C; Suppl. Fig. 10). Thus, we concluded that the SecYEG-YidC complex is dynamically assembled to mediate insertion of a nascent IMPs emerging via the “back of Sec” route, and the YidC recruitment may not depend on specific charge within the substrate, but may rely on other determinants, such as the length and the folding status of the emerging chain.

Interestingly, the sequence-based prediction of the SecYEG-YidC assembly by AlphaFold showed a very similar arrangement of YidC versus SecYEG as observed in our insertion intermediate in nanodiscs, despite the absence of the ribosome and the nascent chain. Here, the salt bridge between SecY Arg-211 (TMH 5) and YidC Asp-329 (end of EH1) may be a key interaction between the two proteins (Figure 4D and Suppl. Fig. 11A). This salt bridge is found among multiple distant Gram-negative species, but it is absent in Gram-positives, such as *B. subtilis*, which correlated with differences in the AlphaFold predictions (Suppl. Figure 1). This further suggested that the charged interaction is not essential but may serve to stabilize the dynamic complex. Thus, we speculated that disrupting this interaction may be detrimental for IMP biogenesis and affect the cell viability. Accordingly, we tested the importance of the salt bridge by replacing YidC Asp-329 with either alanine or arginine. Both YidC variants could be recombinantly expressed and purified, suggesting that the mutated proteins were correctly folded (Suppl. Figure 11B and C). When testing the functional complementation of these YidC variants in *E.coli* FTL10 strain, we observed that the plasmid-encoded YidC^{D329A} fully supported the cell growth under depletion of the wild-type YidC (Figure 4E; Suppl. Figure 11D). Strikingly, introducing a positive

charge was detrimental for the cellular viability, similar to the known effect of a minor deletion within the proximate EH1 [20]. Thus, we concluded that the salt bridge indeed plays a stabilizing role upon the assembly of the dynamic SecYEG-YidC complex, while the electrostatic repulsion rendered via the YidC^{D329R} mutation prohibits YidC docking, causing defects in IMP folding, either at the insertion or intramembrane assembly stage.

Comparison of bacterial and eukaryotic insertases

Guiding of the NuoK nascent chain to the back side of SecYEG for YidC-mediated insertion manifests an obvious resemblance to the route of multi-spanning IMP biogenesis in the ER of eukaryotes [17]. Here, the ribosome-bound Sec61 translocon serves as a core for the substrate-dependent assembly of a super-complex including BOS (back-of-Sec61) and GEL (GET- and EMC-like) complexes. We thus compared the arrangement of the *E. coli* SecYEG-YidC insertase with the human Sec61-BOS-GEL-PAT machinery trapped with a nascent chain of rhodopsin[17] (Figure 5). The bacterial insertase forms a compact assembly, where YidC is tightly packed against SecYEG and the inserted part of NuoK, providing a simple solution for transferring the nascent chain from the ribosome to the insertion-competent groove of YidC. In contrast, the loosely packed eukaryotic super-complex extends far from the Sec61 core and the resolved nascent chain, and it forms a lipid-filled “peninsula”. Remarkably, the YidC homolog TMCO1 (a constituent of the GEL complex) is found more than 3 nm away from Sec61 with its paddle domain oriented towards the rest of GEL. The interaction with the core translocon is mediated via the BOS subunit TMEM147 that largely overlaps with the position of YidC in the bacterial machinery. Interestingly, also the route of the nascent chain differs between two structures: While the membrane-inserted opsin TMH 3 and the RNC-bound linker were found in the orthogonal geometry to the membrane without interactions with the BOS-GEL subunits (Figure 5B), we report here that the TMHs of NuoK required distinct YidC domains for insertion and folding at the interface. The involvement of YidC at different stages of NuoK biogenesis correlates with its dual role as insertase and as chaperone for nascent IMPs.

The structure of the eukaryotic machinery suggests that blockade of the lateral gate by the CCDC47 protein of the PAT complex is a possible determinant to guide a nascent chain to the alternative exit [17]. Here, the extended helices of CCDC47 at the cytoplasmic interface reach the N-terminal half of Sec61α, the SecY homolog, and restrict its mobility required for opening the gate (Figure 5B), so the nascent IMP is forced to follow the Sec61-GEL-BOS insertion route. Within the bacterial insertase, the C-terminal end of SecY at the RNC:SecYEG interface may play a similar role, though using a different mechanism. In presence of the NuoK TMH 3 emerging from the tunnel mouth, this SecY extension forms a contact with the rRNA base C490 and hinders the access to the lateral gate. Thus, it may favor the alternative route for the growing nascent chain to the back of SecYEG. Strikingly, shortening of the SecY C-terminus and deletion of Lys-433 and Lys-434 involved in RNA binding appeared lethal for the cells[33], highlighting the importance of this poorly studied element of SecYEG.

Discussion

Variations in TMH topologies and lengths, appearance of partially unfolded regions and charged residues within the membrane core, point to the complexity in IMP biogenesis across the kingdoms of life. Membrane insertion of hydrophobic TMHs via the lateral gate of the SecYEG/Sec61$\alpha\beta\gamma$ translocon has been described as a general route towards IMP folding and assembly. The universal paradigm has been lately challenged by the discovery of the eukaryotic insertase machinery, the novel multi-subunit complex BOS-GEL-PAT, that facilitates IMP insertion at the back of the ribosome-bound Sec61 away from the lateral gate. The discovery of a novel insertion route in eukaryotes has immediately raised a question about the evolutionary conservation of the mechanism. Here, we describe how the bacterial machinery composed of SecYEG and YidC insertases mediates the biogenesis of the multi-spanning IMP NuoK. Cryo-EM of the lipid-embedded complex has revealed the substrate-dependent recruitment of YidC to the ribosome-bound SecYEG and visualized the route taken by the nascent chain from the ribosome to the lipid membrane. Differently to the lactose permease folding intermediates assessed in a recent study [10], the NuoK nascent chain does not pass the lateral gate, but it folds within the hydrophobic pocket formed by SecY loops and leaves via the sawhorse-shaped crevice at the back, where it is encountered and inserted by YidC. Here, the conserved and partially hydrophobic paddle domain of YidC assists in handover of the pre-folded nascent chain from SecYEG to YidC. The SecYEG-YidC assembly is induced by the nascent chain of sufficient length, and it is stabilized by the salt bridge between SecY and YidC at the periplasmic interface. Although somewhat different in details and complexity level, the overall architecture of the active SecYEG-YidC complex manifests a conceptual similarity to the eukaryotic Sec61-BOS-GEL-PAT insertase machinery. Thus, our results not only validate the existence of the alternative insertion pathway in bacteria and reveal the path of the nascent chain but also strongly suggest an evolutionary link between the distant systems.

Multiple studies have described interactions of nascent IMPs with the lateral gate of SecYEG and suggested that YidC is located in proximity to access the emerging nascent TMHs [5,14,10]. Our findings do not exclude such architecture, though no relevant classes were observed in the acquired cryo-EM data

sets in this study. It remains to be explained what factors determine the route of nascent IMPs, i.e. the triage between the lateral gate and the "back-of-Sec" insertion, and also what features of the nascent chain serve as signals for YidC recruitment. For NuoK biogenesis, the necessity of YidC was previously linked to the anionic residues within the substrate, e.g. via interactions with YidC Arg-366 [18]. However, we show that YidC is docked at the back of SecYEG also when the charges within the NuoK TMHs are inverted, while no contact with Arg-366 is observed. Notably, the involvement of YidC at the late stage of NuoK biogenesis correlates with the recent findings that both YidC and the evolutionary related EMC complex facilitate insertion of the C-terminal TMHs of polytopic IMPs [34,35]. This final insertion event would occur post-translationally when the translation termination happens soon after the synthesis of the last TMH. NuoK would be an example of such IMP: In absence of the stalling introduced here for the purpose of the structural analysis, the nascent polypeptide chain would be released from the peptidyl transferase center, and the membrane insertion of NuoK TMH 3 complex would occur post-translationally. As both YidC and EMC ensure folding of post-translationally delivered clients [16,36,37], the C-terminal TMHs of polytopic IMPs may utilize the same recognition and insertion routes, while the SecYEG-YidC assembly would facilitate the efficient substrate delivery.

The topology acquired by NuoK in the nanodisc is another puzzling outcome of our study. The model based on the resolved TMHs suggests that the N-terminus of the insertion intermediate is oriented into the cytoplasm, thus being inverted in comparison to NuoK within the assembled complex I (Suppl. Figure 3A). One explanation may be that the non-native topology originated from the experimental *in vitro* set-up, as the employed nanodiscs lack the physiological trans-membrane electrostatic potential, an important factor for the IMP orientation. However, if the electrostatic potential was a decisive factor, we would expect to find NuoK in two different topologies in cryo-EM reconstructions, possibly utilizing different insertion routes, while only one class was experimentally observed. Thus, an alternative scenario seems plausible: Several IMPs, such as four-TMH EmrE, were shown to undergo the complete topology inversion in the last step of their folding, and a single charged residue here can be decisive for the final orientation [38,39,40]. As NuoK does not contain long loops between the TMHs but contains a stretch of three arginine residues within its C-terminal end, it is tempting to speculate that the protein acquires its correct topology in the cellular membrane once the complete polypeptide chain is released from the ribosome. The flip-flop of the inserted TMHs may be promoted by the proximate YidC, as the insertase would distort the lipid bilayer and so destabilize the NuoK intermediate that eventually results in the new topology.

Our study delivers a new, direct view on the organization of the bacterial SecYEG-YidC insertase machinery, and the revealed architecture is calling for detailed investigation on its dynamics, as well as re-evaluation of the earlier data. One current limitation of the employed nanodisc-based system is the pre-defined stoichiometry of SecYEG and YidC within the complex, while YidC is substantially more abundant in the bacterial membrane [41]. Thus, even larger insertase complexes may be envisioned for the cellular membrane, where multiple YidC copies could manage biogenesis of polytopic IMPs, resembling the Sec-BOS-GEL machinery of the eukaryotes (Figure 5). Experiments on the native bacterial membranes, such as those by cryogenic electron tomography [42], as well as reconstituted systems will be of the utmost importance to explore such modes of interaction and deliver detailed and possibly direct insights on the key process of membrane protein biogenesis.

Acknowledgements

The authors would like to thank Hanna Kratzat, Susanne Rieder and Charlotte Ungewickel for the support with the cryo-EM collection and initial data analysis, Joana Musial for assistance with cloning and biochemical characterization of the SecYEG-YidC construct, Laura Czech and Gert Bange for the support upon the development of CFPS procedure, and Arnold J.M. Driessen and Florian Altegoer for discussions. The work was funded by German Research Foundation (DFG, grants Ke1879/3 and Collaborative Research Center 1208, project A10 to A.K.), European Research Council (Advanced Grant "CryoTranslation" to R.B.)

Contributions

MB: biochemical sample preparation and analysis, *in vivo* experiments; CRH: cryo-EM data processing, model building and visualization; MK: biochemical sample preparation and analysis; YS: CFPS development; EvdS: design and characterization of the SecYEG-YidC insertase; OB: cryo-EM data collection and curation; TB: cryo-EM data analysis and visualization; RB and AK: project conceptualization and supervision, funding acquisition. The initial manuscript was prepared by MB, CRH and AK, and edited/commented by all the co-authors.

Additional information

Supplementary information is available for this paper.

Correspondence and requests should be addressed to Roland Beckmann (Beckmann@genzentrum.lmu.de) and Alexej Kedrov (Kedrov@hhu.de).

Figures

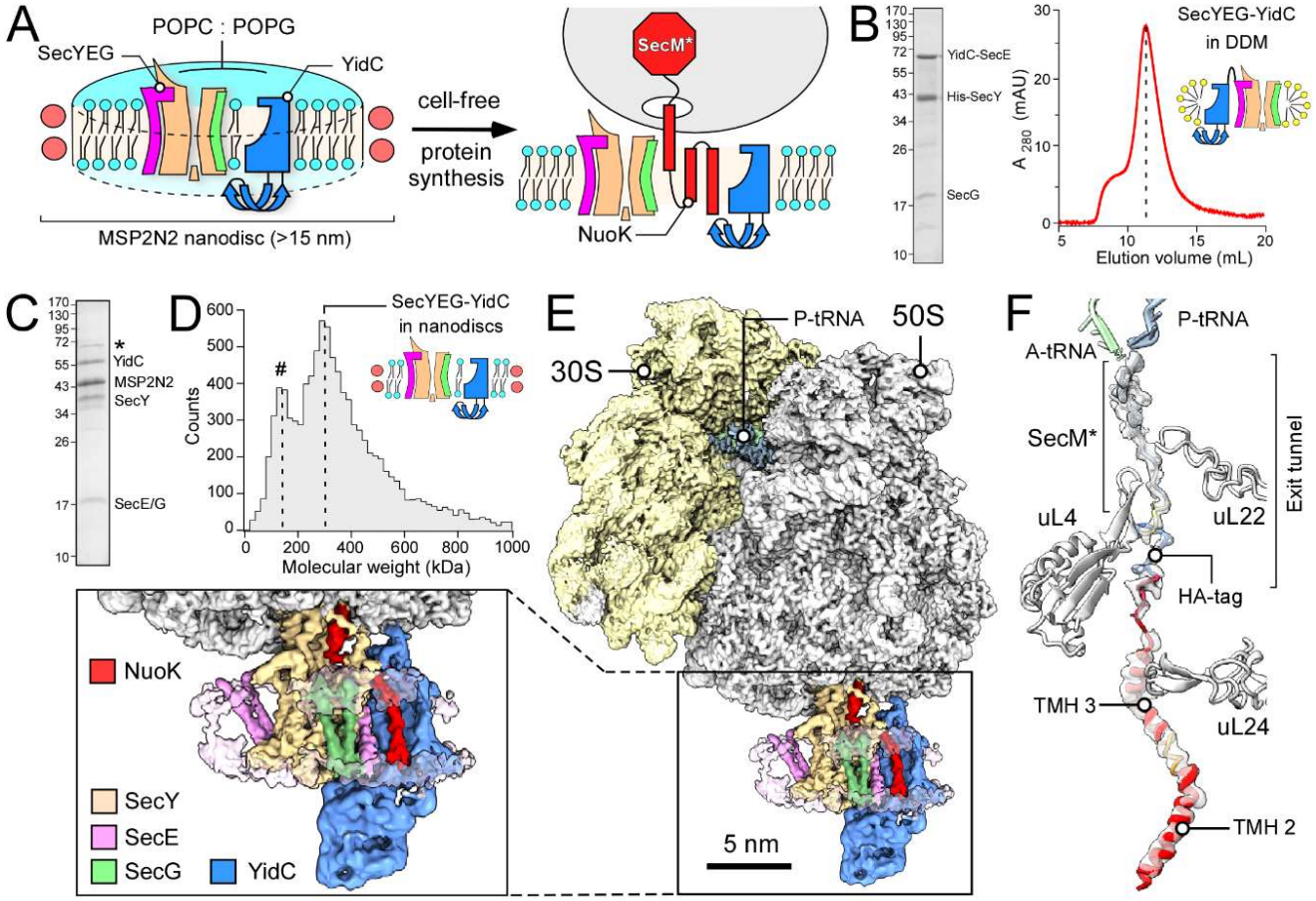

Figure 1. Substrate-induced assembly of the RNC:SecYEG-YidC complex.

(A) Scheme of the assay to study NuoK biogenesis. SecYEG and YidC are co-reconstituted into MSP2N2-based nanodisc in presence of POPC.POPG lipids and introduced into CFPS reaction. Synthesis of the substrate NuoK is interrupted by SecM* stalling sequence, so the stable insertion intermediate is formed for structural analysis.

(B) SDS-PAGE of the affinity-purified SecYEG-YidC fusion insertase complex, with the subunits indicated. Right: Size exclusion chromatography profile of the isolated insertase complex.

(C) SDS-PAGE of the nanodisc-reconstituted SecYEG-YidC complex after the protease treatment. The minor band at 70 kDa (*) corresponds to the residual YidC-SecE fusion protein.

(D) Mass photometry recording of isolated SecYEG-YidC nanodiscs manifests the main peak at 290 kDa. The minor peak at 130 kDa (#) corresponds to the nanodiscs loaded only with lipids.

(E) Cryo-EM reconstruction of NuoK^{86}-RNC:SecYEG-YidC assembly. Shown is a composite map consisting of isolated densities of the ribosome subunits 30S and 50S, P-site peptidyl-tRNA ("P-tRNA") and focused refined SecYEG-YidC, with subunits and the substrate NuoK indicated.

(F) Isolated density of the nascent chain NuoK (in transparent) with fitted model; tRNAs and the ribosomal proteins lining the exit tunnel are indicated.

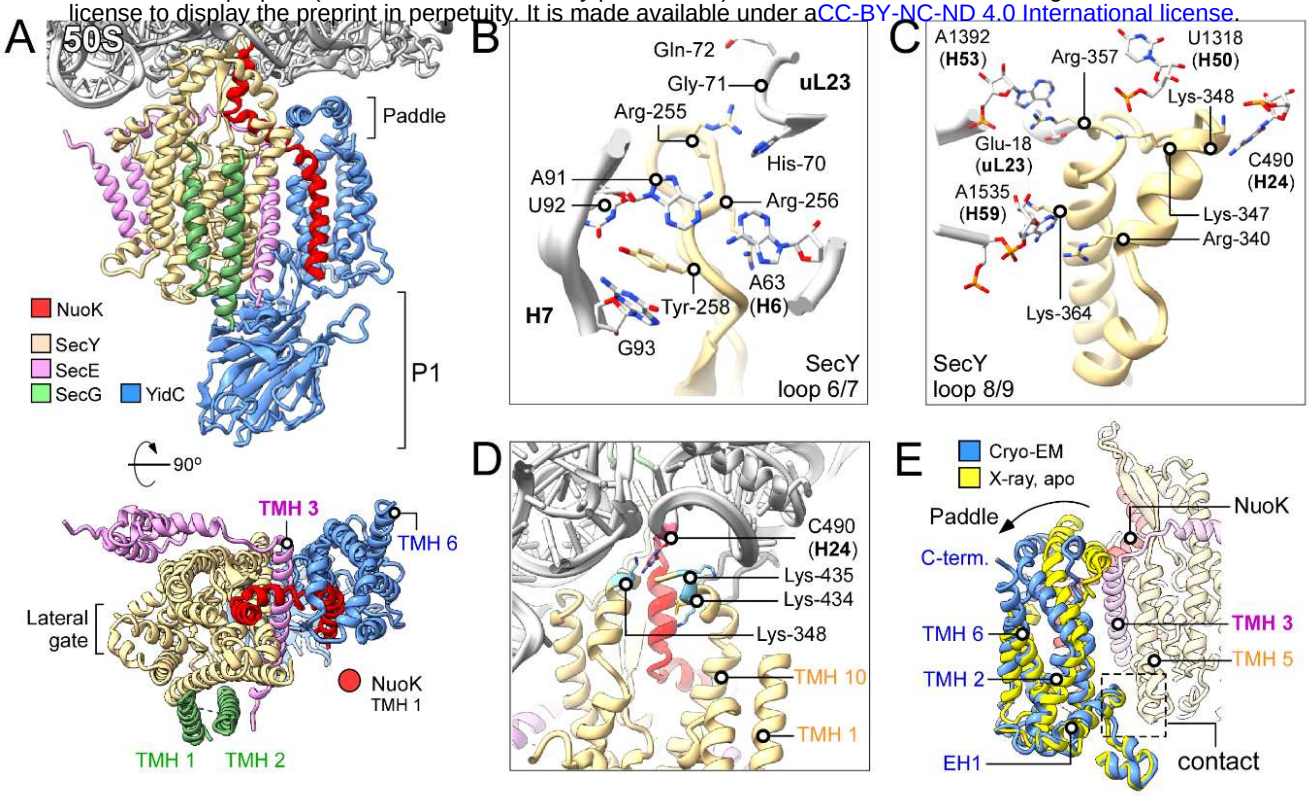

Figure 2. Architecture of SecYEG-YidC insertase and its interactions with the RNC.

(**A**) Molecular model of the SecYEG-YidC insertase complex bound to NuoK^{86}-RNC. The putative position of the membrane-inserted NuoK TMH 1 is indicated as a red circle in the cytoplasmic view (bottom).

(**B, C**) The network of ribosome:SecYEG interactions mediated by SecY cytoplasmic loops 6/7 and 8/9.

(**D**) The C-terminal extansion of SecY contacts the flipped-out base C490 of 23S rRNA. This interaction is likely stabilized by Lys-435 close to the H24 rRNA backbone and Lys-348 stacking on the C490 from the opposite site.

(**E**) Overlay of X-ray and cryo-EM structures of YidC highlight the conformational change within the insertase. The movement of the YidC paddle domain upon entry of the NuoK nascent chain is indicated with an arrow. The closest SecY-YidC contact at the periplasmic side is indicated with the dashed box.

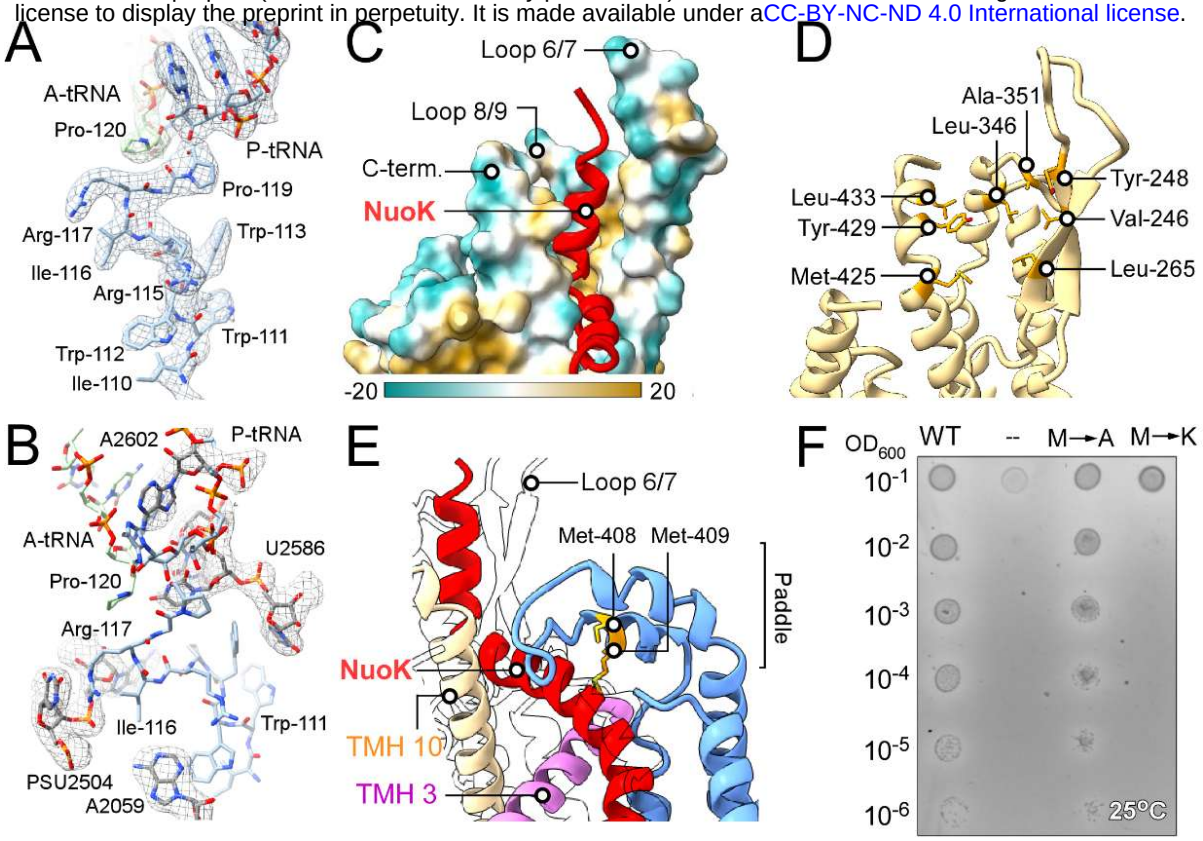

Figure 3. **SecYEG and YidC jointly mediate delivery of the nascent chain to the membrane**.

(**A**) Isolated cryo-EM density (transparent mesh) of the SecM* stalling sequence in the ribosomal exit tunnel with the fitted model. The residues of SecM* peptide are indicated.

(**B**) Model for the SecM*:ribosome interactions. Hallmark bases of the PTC and involved in SecM* binding are shown as in SecM-stalled ribosome (PDB 8QOA), fitted into the respective density in (transparent mesh).

(**C**) Surface representation of the molecular model for SecY cytoplasmic loops 6/7, 8/9 and the C-terminal tail colored according to the molecular lipophilicity potential (scale bar shown). The emerging NuoK nascent chain (red ribbon) acquires α-helical fold within the hydrophobic pocket.

(**D**) The indicated apolar residues form the hydrophobic pocket for the nascent chain folding.

(**E**) Zoom view on the molecular model for the SecYEG-YidC complex highlighting the route of the folded NuoK TMH 3 (red ribbon) from SecYE to YidC. The methionine residues within the YidC paddle domain are indicated.

(**F**) Complementation test using wild-type YidC ("WT"), mutants YidC$^{M408A, M409A}$ ("M→A") and YidC$^{M408K, M409K}$ ("M→K") and empty vector ("--") in presence of glucose at 25°C.

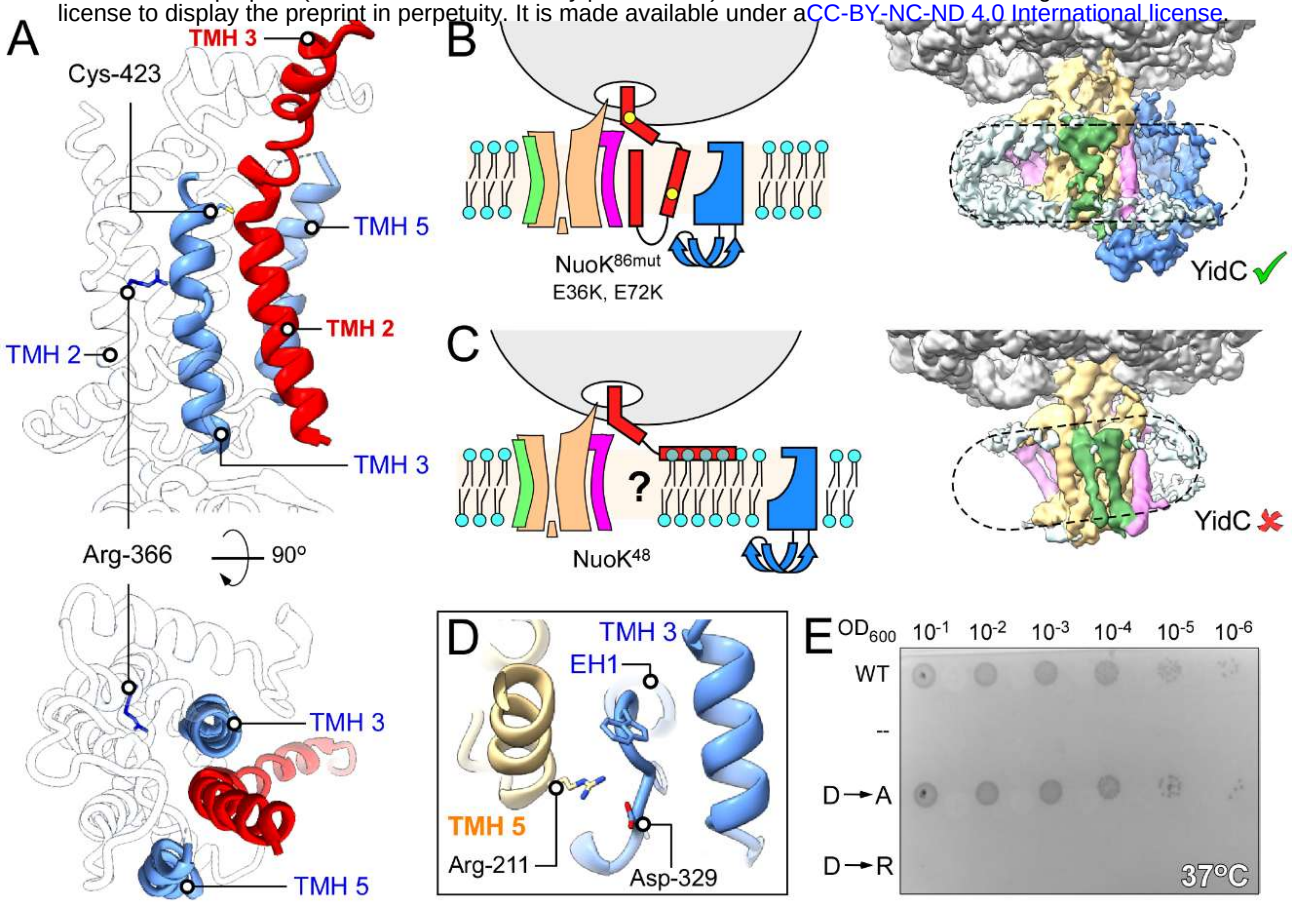

Figure 4. YidC-mediated insertion of the nascent membrane protein.

(**A**) View on the molecular model of YidC focusing on the insertion groove between TMHs 3 and 5 with the accommodated NuoK TMH2. Arg-366 within YidC TMH 2 is not involved in interactions with the nascent chain. The rest of YidC is shown in transparent.

(**B**) Insertion model of the NuoK^{86} intermediate bearing E36K, E72K mutations (yellow circles) and the corresponding cryo-EM map (right). The outline of the nanodisc is shown with the dashed line.

(**C**) The insertion model of the NuoK^{48} intermediate and the corresponding cryo-EM map (right). The outline of the nanodisc is shown with the dashed line. The color code in (**B**) and (**C**) is as in Figure 1E.

(**D**) View on the molecular model of the SecY-YidC complex focusing on the closest contact site at the periplasmic interface. A putative salt bridge is formed between SecY Arg-211 and YidC Asp-329.

(**E**) Complementation test using wild-type YidC (“WT”), mutants YidC^{D329A} (“D→A”) and YidC^{D329R} (“D→R”) and empty vector (“--”) in presence of glucose at 37°C.

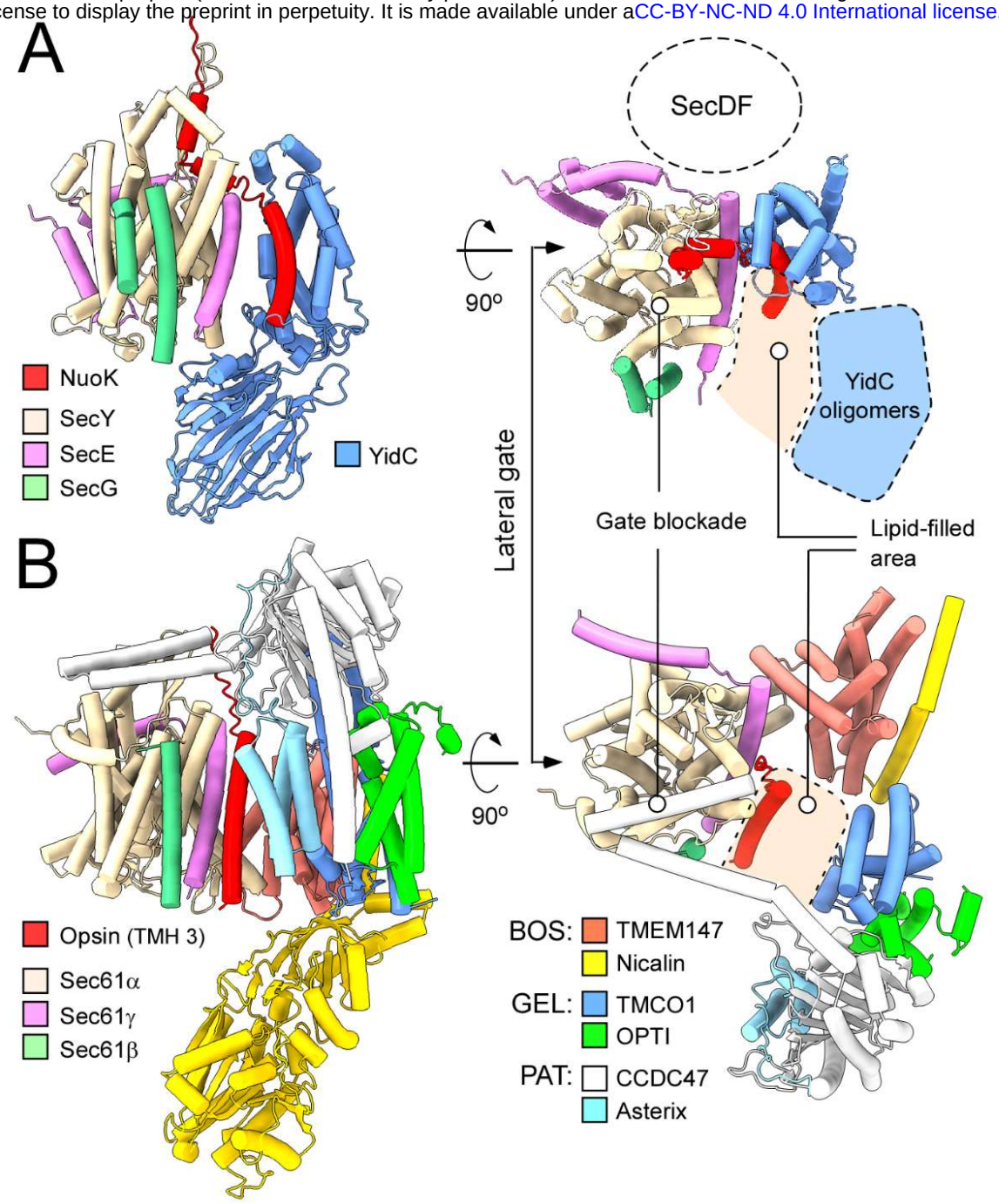

Figure 5. Comparison of the bacterial and eukaryotic IMP insertases.

(A) Side and cytoplasmic views on *E. coli* SecYEG-YidC assembly and the route of the NuoK nascent chain. The putative position of the accessory SecDF complex is indicated, based on a high-confidence AlphaFold3 prediction. A hypothetical position of YidC oligomers is shown in blue.

(B) Side and cytoplasmic views on the eukaryotic insertase with the subcomplexes and individual subunits indicated. The partially resolved route of the opsin nascent chain is indicated. Similar structural and functional features of the bacterial and eukaryotic machineries are shown.

Methods

Molecular cloning

The primers were synthesized by Eurofins Genomics and Merck/Sigma-Aldrich. Sequencing was conducted by Eurofins Genomics and Microsynth AG. The used restriction enzymes and cloning kits, incl. the Phusion High-Fidelity DNA polymerase and the Gibson assembly kits were purchased by New England Biolabs.

The genes encoding for SecYEG-YidC complex were cloned in a pBAD-TOPO (Thermo Fisher Scientific) derived vector (plasmid ID pEM472). The gene encoded for *E. coli* YidC (1-535) was fused to the N-terminus of SecE with a sequence coding for HRV-3C protease cleavage site inserted in between; the construct also contained a N-terminally decahistidine-tagged SecY and unmodified SecG. The construct was created using conventional restriction-ligation cloning techniques. For the IMP substrate, the DNA encoding 86 amino acids of *E. coli* NuoK and the C-terminal extension containing the HA-tag for immunodetection, a linker and the SecM* stalling sequence (FSTPVWIWWWPRIRGPP) (Ref. [29]) was synthesized by GenScript Biotech (Netherlands), and the construct was cloned cloned into pRSET vector (Thermo Fisher Scientific) via SalI/HindIII restriction sites. The gene encoding NuoK^{48} nascent chain was prepared by removing the fragment corresponding to NuoK residues 49-86 via PCR, followed by blunt-end ligation.To study the effects of point mutations within YidC in complementation assays, the YidC mutants were cloned into pTrc99A-based plasmid pKAD107 [19]. For the expression of the YidC mutants, the corresponding genes were cloned into pBAD-based plasmid [20].

Expression of the membrane insertases

E.coli C41(DE3)Δ*ompF*-Δ*acrAB* strain [43] transformed with the pEM472 plasmid was grown in LB medium supplemented with 100 µg/mL ampicillin at 37°C while shaking at 180 rpm. Upon reaching OD_{600} 0.6, expression of the fused SecYEG-YidC complex was induced by adding 0.5 % arabinose (w/v) and carried out for 2.5 h. Cells were harvested and lysed using a microfluidizer (M-110P, Microfluidics Corp.), and the debris was removed by centrifugation at 18000 g for 10 min (SS34 rotor, Sorvall/Thermo Scientific). Membranes were isolated by ultracentrifugation at 42000 rpm for 1 h (45Ti rotor, Beckman Coulter). Membranes were then suspended in the solubilization buffer (50 mM Hepes-KOH pH 7.4, 150 mM KOAc, 5 % glycerol, 200 µM tris(2-carboxyethyl)phosphine (TCEP), 1 % n-dodecyl β-maltoside (DDM; Glycon Biochemicals GmbH) for 1 h at 4°C. The solubilized material was centrifuged at 21,380 x *g* for 10 min at a tabletop centrifuge (Hermle Z 216 MK, Hermle Labortechnik GmbH) and the supernatant was incubated with Ni^{2+}-NTA agarose resin (Macherey-Nagel GmbH & Co. KG) for 1 h at 4°C. The resin was washed with 50 mM Hepes-KOH pH 7.4, 500 mM KOAc, 5 % glycerol (v/v), 200 µM TCEP, 0.05 % DDM, 10 mM imidazole and the target protein was eluted with 50 mM Hepes-KOH pH 7.4, 150 mM KOAc, 5 % glycerol, 200 µM TCEP, 0.05 % DDM, 300 mM imidazole. The elution fractions were concentrated and subjected to size exclusion chromatography (SEC) in 50 mM Hepes-KOH pH 7.4, 150 mM KOAc, 5 % glycerol, 0.05% DDM using Superdex 200 Increase GL 10/300 column with ÄKTA Pure set-up (Cytiva). The protein concentration was determined spectrophotometrically (NeoDot, NeoBiotech) using calculated extinction coefficient of 134,000 M^{-1} cm^{-1}. Expression of YidC mutants, $YidC^{D329A}$ and $YidC^{D329R}$, was achieved using pBAD-based plasmid and the proteins were solubilized and purified in DDM according to the previously published protocol [20].

Assembly of SecYEG-YidC nanodiscs

To prepare the nanodiscs, liposomes were first formed using 1-palmitoyl-2-oleoyl-glycero-3-phosphocholine (POPC; 70 mol %) and 1-palmitoyl-2-oleoyl-sn-glycero-3-phospho-(1-rac-glycerol) (POPG; 30 mol %) (Avanti Polar Lipids, Inc). The lipids were mixed from chloroform stocks to achieve the desired ratio, the solvent was evaporated and the liposomes were prepared, as described [6]. The detergent-purified SecYEG-YidC complexes were reconstituted in MSP2N2-based nanodiscs in a protein:MSP:lipid molar ratio of 1:4:400 following the published protocol [6]. After forming the nanodiscs, the linker connecting YidC and SecE was cleaved by HRV-3C protease for 1 h at 4°C and SEC was performed in in 50 mM HEPES-KOH pH 7.4, 150 mM KOAc, 5 % glycerol using Superose 6 Increase GL 10/300 column with ÄKTA Pure set-up. SEC fractions containing SecYEG-YidC nanodiscs were concentrated to ~10 µM using Amicon Ultra-4, Ultracel 30 K centrifugal filters (Merck/Millipore). Mass photometry measurements were performed using Two^{MP} instrument (Refeyn Ltd.) calibrated in the range from 66 to 1,048 kDa with NativeMark Unstained Protein Standard (Invitrogen/Thermo Fisher Scientific).

Cell-free protein synthesis

E. coli S30 extract for CFPS was prepared based on previously published protocols [44]. Briefly, *E.coli* BL21(DE3) cells were transformed with TargoTron pAR1219 plasmid (Sigma-Aldrich) encoding for T7 RNA polymerase. 2 L of 2x YPTG media was inoculated with 100 mL overnight cultures, the cells were grown to OD_{600} 0.5, and the T7 RNA polymerase expression was induced with 1 mM IPTG. The cells were further grown to reach OD_{600} 1.0 and then they were harvested at 7500 rpm for 15 min (FiberLite F8-6x1000y rotor, Piramoon Technologies Inc.). The cell pellet was washed three times with 10 mM Tris-acetate pH 8, 60 mM KOAc, 14 mM $Mg(OAc)_2$, and 1 mM PMSF, and the pellet was resuspended in the same buffer at the ratio of 1 mL per 1 g pellet. Subsequently, cells were lysed by sonication (10 times, 15 s on, 30 s off, 50 % power, 5 pulsed cycles) (Sonopuls GM2200, Bandelin). The lysate was cleared via two-steps

centrifugation, 12,000 x *g* for 15 min and 30,000 x *g* for 30 min (S120 AT6 rotor, Sorvall /Thermo Fisher). The supernatant was aliquoted and stored at -75°C.

The CFPS reaction was composed of 40 % S30 extract, the master mix (10 mM ammonium acetate, 130 mM KOAc, 33 mM sodium pyruvate, 1.5 mM spermidine, 1 mM putrescine, 4 mM sodium oxalate, 1.2 mM ATP, 0.85 mM of GTP, CTP and UTP, 34 µg/ml folinic acid, 170.6 µg/mL of *E.coli* tRNA MRE 600 (Roche Diagnostics GmbH), 0.33 mM NAD^+, 0.26 mM coenzyme A and 2 mM of each amino acid), and $Mg(OAc)_2$. The optimum $Mg(OAc)_2$ concentration was identified for each new batch of the S30 extract upon screened within the range of 0 to 12 mM and using synthesis of the yellow fluorescent protein as a read-out. For NuoK synthesis, at least 7 ng/µL plasmid DNA encoding the nascent chain was added to the reaction, as well as at least 100 nM of the nanodisc-reconstituted SecYEG-YidC. CFPS reactions were performed at 37°C for 1 h while shaking at 450 rpm. The synthesis/stalling was evaluated via Western-blotting using monoclonal antibodies against the HA-tag (sc-7392, Santa Cruz Biotechnology).

Isolation of ribosomes from CFPS reactions

To isolate the ribosomes, 10-40 % linear sucrose gradients were formed in SW40 tubes (Beckman Coulter) using the Gradient Station (BioComp Instruments). CFPS reactions (100 µL) were loaded on top of the gradients and the samples were centrifuged for 16 h at 16,500 rpm (SW40 Ti rotor; Beckman Coulter). The gradients were fractionated using the Gradient Station while monitoring the absorbance at 280 nm (A_{280}). The peaks with the ribosomal fractions occurring in the sucrose concentration range of 20-25 % were pooled together and incubated with Ni^{2+}-NTA agarose resin (Macherey-Nagel GmbH & Co. KG) for 1 h at 4°C. The resin was washed with 50 mM Hepes-KOH pH 7.4, 500 mM KOAc, 25mM $Mg(OAc)_2$, 10 mM imidazole. The complexes were eluted with 50 mM Hepes-KOH pH 7.4, 150 mM KOAc, 25 mM $Mg(OAc)_2$, 300 mM imidazole and concentrated using an Amicon Ultra-4 Ultracel 30 K centrifugal filters (Merck/Millipore) while exchanging the buffer to 50 mM Hepes-KOH pH 7.4, 150 mM KOAc, 25 mM $Mg(OAc)_2$. The presence of the nascent chain with ribosomes was confirmed by a western blot against the HA-tag. The concentration of ribosomes was then estimated by measuring the absorbance at 260 nm (A_{260}).

In order to improve the resolution of the cryo-EM data on $NuoK^{86}$-RNC:SecYEG-YidC, glutaraldehyde was added to the purified samples. The sample was diluted 5-fold to prevent inter-particle crosslinking, and it was then incubated with 0.1 % glutaraldehyde (v/v) for 15 min on ice and quenched by 100 mM Tris-HCl pH 7.5. Afterwards the sample was concentrated using a Amicon Ultra-4, Ultracel 30 K centrifugal filters, flash-frozen and stored at -75°C before grid preparation.

Cryo-EM sample preparation and data collection

Isolated NuoK-RNC:SecYEG-YidC samples were supplemented with (1H, 1H, 2H, 2H-perfluoro-octyl)-β-D-maltopyranoside (FOM, Anatrace) to a final concentration of 0.03% to favor random orientation of the particles and plunge frozen. For each grid, 3.5 µL of the sample was applied onto glow-discharged Quantifoil Cu 300 mesh R3/3 grids with an additional 2 nm layer of carbon. After a waiting time of 45 s, the grids were blotted for 3 s and plunge frozen in liquid ethane at 4°C and 100% humidity using a Vitrobot Mark IV (Thermo Fisher Scientific). Data collection for RNC-NuoK:SecYEG-YidC samples was performed at 300 keV using a Titan Krios microscope equipped with a Falcon 4i direct electron detector and a SelectrisX imaging filter (all Thermo Fisher Scientific) at a pixel size of 0.727 Â. Dose-fractioned movies were collected in a defocus range from -0.5 to 3.0 µm and with a total dose of 40 e^- per $Å^2$, fractionated in 40 frames to obtain a total dose of 1 e^- per $Å^2$ per frame. Gain correction, movie alignment and summation of movie frames was performed using MotionCor2 [45]. Further processing, including CTF estimation, was carried out in cryoSPARC v4.4 [46].

Data processing

For the crosslinked $NuoK^{86}$-RNC:SecYEG-YidC complex, 27,660 micrographs were selected. Blob Picker was used to pick 1,420,623 particles which were sorted by 2D classification, yielding a subset of 636,995 particles. An ab-initio job with 2 classes was run to further clean the particle set. A consensus refinement of 582,663 particles resulted in a map of 70S with clear extra density below the tunnel exit. A soft mask covering this region (accounting for nanodisc, SecY/YidC and eventually the NuoK nascent chain) was used to sort the particles into 6 classes, using a 3D Classification job. Two of the classes, representing a total of 221,144 particles, displayed a strong SecYEG and YidC density. The class with best resolved nascent chain density containing 113,368 particles (19.5 %) was selected and refined to a final resolution of 2.44 Å. Local refinement was performed on the tunnel exit region yielding a map with a final resolution of 3.76 Å. This map was used to build the atomic model for the NuoK:SecYEG-YidC assembly (PDB: 9RBF; EMDB:XXX; EMDB:XXX (local refinement); EMDB:XXXX (composite map)). Data processing for this dataset is summarized in Suppl. Figure 4.

For the non-crosslinked $NuoK^{86}$-RNC:SecYEG-YidC assembly, 10,234 micrographs were selected and manually curated. A total of 693,102 particles was picked with Blob Picker and sorted by 2D classification to generate templates for the Template Picker job. From 2,300,222 template-picked particles, 406,978 were selected after 2D classification. An ab-initio job (three classes) allowed further cleaning of the data set. A consensus refinement with a set of 217,418 particles resulted in a map of 70S ribosome with clear extra density below the tunnel exit. Focused sorting into five classes in the tunnel exit region yielded a class of

33,912 particles showing density for the extramembrane P1 domain of YidC. These particles were used to train a TOPAZ picking model, which resulted in 360,610 particles. The particles were further curated and focused sorted into a final class of 70,670 particles. This class was refined to a final resolution of 2.73 Å (EMD-53587). A local refinement in the SecYEG-YidC region yielded a map with a final resolution of 3.19 Å (EMD-53589). Data processing for this dataset is summarized in Suppl. Figure 6.

For the NuoK^{86mut}-RNC:SecYEG-YidC complex assembled upon NuoK$^{E36K,\ E72K}$ synthesis Blob picker was used to pick an initial set of 586,721 particles from 9,099 micrographs. The particles were curated and after 2D classification, a subset of 287,399 particles was used to generate an ab-initio reconstruction (two classes) of 70S ribosomes with extra density for the insertase complex. The same set was further used to generate templates for template picking, which resulted in 2,057,403 particles, from which a final set of 56,980 particles was obtained after extensive 2D and 3D classification. The particles were fed into a TOPAZ training job, obtaining 433,249 particles after picking and extraction. These particles were used to generate a consensus refinement and focused sorted into eight classes. The class with the best resolved insertase region, comprising 48,952 particles, was further refined to generate a reconstruction with final resolution of 2.87 Å (EMD-53584). A local refinement with a mask in the translocon region generated a map of 3.20 Å (EMD-53585). Data processing for this dataset is summarized in Suppl. Figure 9.

For the NuoK^{48}-RNC:SecYEG-YidC complex assembled upon synthesis of the early NuoK intermediate, an initial set of 741,311 particles was picked using a Blob picker job based on 21,440 micrographs. The particles were cleaned by 2D classification jobs to yield a final 511,016 particle set. An ab-initio reconstruction (two classes) job was used to generate an initial map of the ribosome-bound SecYEG in the nanodisc. Successive, focused 3D-classifications from a consensus refinement were used to obtain a final class of 66,486 particles. These particles were refined to a final resolution of 2.62 Å (EMD-53560). A local refinement with a mask in the translocon region resulted in a reconstruction of 2.90 Å (EMD-53568). Data processing for this dataset is summarized in Suppl. Figure 10.

For visualization of all cryo-EM maps, consensus maps were generated consisting of isolated density for the 70S ribosome from the global refinements and isolated density for the nanodisc-embedded insertase from the local refinements.

Model building and refinement

A molecular model was built for the crosslinked NuoK^{86}-RNC:SecYEG-YidC complex. For the 70S ribosome a previously released model based of high-resolution cryo-EM maps of a 70S ribosome and a SecM-stalled RNC were used as templates (PDB IDs 7K00, 8QOA) 29,47. The model for the tRNA-Gly (in SecM) was changed to tRNA-Pro and the mRNA model was adusted from GCU-GGC-CCU (Ala-Gly-Pro in SecM) to GGU-CCU-CCG (Gly-Pro-Pro in SecM*). A model for the SecYEG-YidC assembly was generated based on the rigid body fitting the AlphaFold3 prediction of this complex (see also Suppl. Figure 4) that was fitted into the locally refined cryo-EM density with only minor adjustments (see also Suppl. Figure 5). For the nascent chain, the modified SecM* sequence could be modelled de novo based on well-resolved density for this region (Figue 3A). Less-resolved density was present to fit the backbone and a few bulky side chains for major parts of glycine-serine linker and the HA-tag (Figure 1F). The NuoK TMH 2 and 3 were identified based on the rod-like shape of extra density present at the mouth of the exit tunnel and between SecY and YidC (Figure 1F). While at the given resolution we cannot be sure about the exact register, we positioned residues 73-82 of NuoK THM 3 into the corresponding density supporting the predeicted α-helical conformation. 70S ribosome and SecYEG-YidC atomic models were processed independently in multiple rounds of manual real-space refinement in Coot v0.9.8.95 [49]. The models were later merged and further refined in Phenix v1.20.1-4487 [50]. The Molprobity tool was used for model validation. Visualization was done in UCSF ChimeraX v1.9 [51].

Complementation assay

The complementation assay was prepared as described before [19]. Briefly, a single colony of FTL10 cells [52] transformed with either YidC-encoding plasmid or empty pTrc99A vector was grown in LB medium with 0.2% arabinose, 25 µg/mL kanamycin and 100 µg/mL ampicillin for 16 h at 37°C at 180 rpm. The overnight cultures were diluted to an OD_{600} of 0.05 and grown until the early logarithmic phase before diluting them all to an OD_{600} of 0.1 and doing a subsequent serial dilution. 5 µL of each diluted culture were transfered on the plates (LB agar supplemented with 25 µg/mL kanamycin, 100 µg/mL ampicillin and either 0.2% arabinose or 0.2% glucose). The plates were incubated for 16 h at 37°C or 24 h at 25°C.

Data availability

The cryo-EM structural data have been deposited in the Electron Microscopy Data Base (EMDB) and the Protein Data Bank (PDB) repositories under the accession numbers EMD-53892, EMD-53893, EMD-53894 and PDB-9RBF (NuoK^{86}-RNC:SecYEG-YidC (crosslinked); EMD-53587 and EMD-53589 (NuoK^{86}-RNC:SecYEG-YidC); EMD-53584 and EMD-53585 (NuoK^{86mut}-RNC:SecYEG-YidC); EMD-53560 and EMD-53568 (NuoK^{48}-RNC:SecYEG-YidC).

References

1 von Heijne, G. The membrane protein universe: what's out there and why bother? *J Intern Med* **261**, 543-557 (2007). https://doi.org/10.1111/j.1365-2796.2007.01792.x

2 Itskanov, S. & Park, E. Mechanism of Protein Translocation by the Sec61 Translocon Complex. *Cold Spring Harb Perspect Biol* **15** (2023). https://doi.org/10.1101/cshperspect.a041250

3 Cymer, F., von Heijne, G. & White, S. H. Mechanisms of integral membrane protein insertion and folding. *J Mol Biol* **427**, 999-1022 (2015). https://doi.org/10.1016/j.jmb.2014.09.014

4 du Plessis, D. J., Berrelkamp, G., Nouwen, N. & Driessen, A. J. The lateral gate of SecYEG opens during protein translocation. *J Biol Chem* **284**, 15805-15814 (2009). https://doi.org/10.1074/jbc.M901855200

5 Sachelaru, I. *et al.* YidC occupies the lateral gate of the SecYEG translocon and is sequentially displaced by a nascent membrane protein. *J Biol Chem* **288**, 16295-16307 (2013). https://doi.org/10.1074/jbc.M112.446583

6 Kater, L. *et al.* Partially inserted nascent chain unzips the lateral gate of the Sec translocon. *EMBO Rep* **20**, e48191 (2019). https://doi.org/10.15252/embr.201948191

7 Jomaa, A., Boehringer, D., Leibundgut, M. & Ban, N. Structures of the E. coli translating ribosome with SRP and its receptor and with the translocon. *Nat Commun* **7**, 10471 (2016). https://doi.org/10.1038/ncomms10471

8 Voorhees, R. M. & Hegde, R. S. Structure of the Sec61 channel opened by a signal sequence. *Science* **351**, 88-91 (2016). https://doi.org/10.1126/science.aad4992

9 Bischoff, L., Wickles, S., Berninghausen, O., van der Sluis, E. O. & Beckmann, R. Visualization of a polytopic membrane protein during SecY-mediated membrane insertion. *Nat Commun* **5**, 4103 (2014). https://doi.org/10.1038/ncomms5103

10 Ou, X. *et al.* SecY translocon chaperones protein folding during membrane protein insertion. *Cell* **188**, 1912-1924 e1913 (2025). https://doi.org/10.1016/j.cell.2025.01.037

11 Steinberg, R., Knupffer, L., Origi, A., Asti, R. & Koch, H. G. Co-translational protein targeting in bacteria. *FEMS Microbiol Lett* **365** (2018). https://doi.org/10.1093/femsle/fny095

12 Chen, Y. *et al.* YidC Insertase of Escherichia coli: Water Accessibility and Membrane Shaping. *Structure* **25**, 1403-1414 e1403 (2017). https://doi.org/10.1016/j.str.2017.07.008

13 McDowell, M. A., Heimes, M. & Sinning, I. Structural and molecular mechanisms for membrane protein biogenesis by the Oxa1 superfamily. *Nat Struct Mol Biol* **28**, 234-239 (2021). https://doi.org/10.1038/s41594-021-00567-9

14 Petriman, N. A. *et al.* The interaction network of the YidC insertase with the SecYEG translocon, SRP and the SRP receptor FtsY. *Sci Rep* **8**, 578 (2018). https://doi.org/10.1038/s41598-017-19019-w

15 Botte, M. *et al.* A central cavity within the holo-translocon suggests a mechanism for membrane protein insertion. *Sci Rep* **6**, 38399 (2016). https://doi.org/10.1038/srep38399

16 Page, K. R. *et al.* Role of a holo-insertase complex in the biogenesis of biophysically diverse ER membrane proteins. *Mol Cell* **84**, 3302-3319 e3311 (2024). https://doi.org/10.1016/j.molcel.2024.08.005

17 Smalinskaite, L., Kim, M. K., Lewis, A. J. O., Keenan, R. J. & Hegde, R. S. Mechanism of an intramembrane chaperone for multipass membrane proteins. *Nature* **611**, 161-166 (2022). https://doi.org/10.1038/s41586-022-05336-2

18 Price, C. E. & Driessen, A. J. M. Conserved negative charges in the transmembrane segments of subunit K of the NADH:ubiquinone oxidoreductase determine its dependence on YidC for membrane insertion. *J Biol Chem* **285**, 3575-3581 (2010). https://doi.org/10.1074/jbc.M109.051128

19 Kedrov, A. *et al.* Elucidating the native architecture of the YidC: ribosome complex. *J Mol Biol* **425**, 4112-4124 (2013). https://doi.org/10.1016/j.jmb.2013.07.042

20 Kedrov, A. *et al.* Structural Dynamics of the YidC:Ribosome Complex during Membrane Protein Biogenesis. *Cell Rep* **17**, 2943-2954 (2016). https://doi.org/10.1016/j.celrep.2016.11.059

21 Kohler, R. *et al.* YidC and Oxa1 form dimeric insertion pores on the translating ribosome. *Mol Cell* **34**, 344-353 (2009). https://doi.org/10.1016/j.molcel.2009.04.019

22 Ritchie, T. K. *et al.* Chapter 11 - Reconstitution of membrane proteins in phospholipid bilayer nanodiscs. *Methods Enzymol* **464**, 211-231 (2009). https://doi.org/10.1016/S0076-6879(09)64011-8

23 Price, C. E. & Driessen, A. J. YidC is involved in the biogenesis of anaerobic respiratory complexes in the inner membrane of Escherichia coli. *J Biol Chem* **283**, 26921-26927 (2008). https://doi.org/10.1074/jbc.M804490200

24 Cymer, F., Hedman, R., Ismail, N. & von Heijne, G. Exploration of the arrest peptide sequence space reveals arrest-enhanced variants. *J Biol Chem* **290**, 10208-10215 (2015). https://doi.org/10.1074/jbc.M115.641555

25 Kempf, N. *et al.* A Novel Method to Evaluate Ribosomal Performance in Cell-Free Protein Synthesis Systems. *Sci Rep* **7**, 46753 (2017). https://doi.org/10.1038/srep46753

26 Kumazaki, K. *et al.* Crystal structure of Escherichia coli YidC, a membrane protein chaperone and insertase. *Scientific Reports* **4** (2014). https://doi.org/10.1038/srep07299

27 Haque, M. E., Spremulli, L. L. & Fecko, C. J. Identification of protein-protein and protein-ribosome interacting regions of the C-terminal tail of human mitochondrial inner membrane protein Oxa1L. *J Biol Chem* **285**, 34991-34998 (2010). https://doi.org/10.1074/jbc.M110.163808

28 Ravaud, S., Stjepanovic, G., Wild, K. & Sinning, I. The crystal structure of the periplasmic domain of the Escherichia coli membrane protein insertase YidC contains a substrate binding cleft. *J Biol Chem* **283**, 9350-9358 (2008). https://doi.org/10.1074/jbc.M710493200

29 Gersteuer, F. *et al.* The SecM arrest peptide traps a pre-peptide bond formation state of the ribosome. *Nat Commun* **15**, 2431 (2024). https://doi.org/10.1038/s41467-024-46762-2

30 White, S. H. & Wimley, W. C. Membrane protein folding and stability: physical principles. *Annu Rev Biophys Biomol Struct* **28**, 319-365 (1999). https://doi.org/10.1146/annurev.biophys.28.1.319

31 Yuan, J., Phillips, G. J. & Dalbey, R. E. Isolation of cold-sensitive yidC mutants provides insights into the substrate profile of the YidC insertase and the importance of transmembrane 3 in YidC function. *J Bacteriol* **189**, 8961-8972 (2007). https://doi.org/10.1128/JB.01365-07

32 Kumazaki, K. *et al.* Structural basis of Sec-independent membrane protein insertion by YidC. *Nature* **509**, 516-520 (2014). https://doi.org/10.1038/nature13167

33 Chiba, K., Mori, H. & Ito, K. Roles of the C-terminal end of SecY in protein translocation and viability of Escherichia coli. *J Bacteriol* **184**, 2243-2250 (2002). https://doi.org/10.1128/JB.184.8.2243-2250.2002

34 Wu, H., Smalinskaite, L. & Hegde, R. S. EMC rectifies the topology of multipass membrane proteins. *Nat Struct Mol Biol* **31**, 32-41 (2024). https://doi.org/10.1038/s41594-023-01120-6

35 Kalinin, I. A. *et al.* Features of membrane protein sequence direct post-translational insertion. *Nat Commun* **15**, 10198 (2024). https://doi.org/10.1038/s41467-024-54575-6

36 Anghel, S. A., McGilvray, P. T., Hegde, R. S. & Keenan, R. J. Identification of Oxa1 Homologs Operating in the Eukaryotic Endoplasmic Reticulum. *Cell Rep* **21**, 3708-3716 (2017). https://doi.org/10.1016/j.celrep.2017.12.006

37 Hennon, S. W., Soman, R., Zhu, L. & Dalbey, R. E. YidC/Alb3/Oxa1 Family of Insertases. *J Biol Chem* **290**, 14866-14874 (2015). https://doi.org/10.1074/jbc.R115.638171

38 Seurig, M., Ek, M., von Heijne, G. & Fluman, N. Dynamic membrane topology in an unassembled membrane protein. *Nat Chem Biol* **15**, 945-948 (2019). https://doi.org/10.1038/s41589-019-0356-9

39 Seppala, S., Slusky, J. S., Lloris-Garcera, P., Rapp, M. & von Heijne, G. Control of membrane protein topology by a single C-terminal residue. *Science* **328**, 1698-1700 (2010). https://doi.org/10.1126/science.1188950

40 Woodall, N. B., Hadley, S., Yin, Y. & Bowie, J. U. Complete topology inversion can be part of normal membrane protein biogenesis. *Protein Sci* **26**, 824-833 (2017). https://doi.org/10.1002/pro.3131

41 Urbanus, M. L. *et al.* Targeting, insertion, and localization of Escherichia coli YidC. *J Biol Chem* **277**, 12718-12723 (2002). https://doi.org/10.1074/jbc.M200311200

42 Gemmer, M. *et al.* Visualization of translation and protein biogenesis at the ER membrane. *Nature* **614**, 160-167 (2023). https://doi.org/10.1038/s41586-022-05638-5

43 Kanonenberg, K. *et al.* Shaping the lipid composition of bacterial membranes for membrane protein production. *Microb Cell Fact* **18**, 131 (2019). https://doi.org/10.1186/s12934-019-1182-1

44 Zubay, G. In vitro synthesis of protein in microbial systems. *Annu Rev Genet* **7**, 267-287 (1973). https://doi.org/10.1146/annurev.ge.07.120173.001411

45 Zheng, S. Q. *et al.* MotionCor2: anisotropic correction of beam-induced motion for improved cryo-electron microscopy. *Nat Methods* **14**, 331-332 (2017). https://doi.org/10.1038/nmeth.4193

46 Punjani, A., Rubinstein, J. L., Fleet, D. J. & Brubaker, M. A. cryoSPARC: algorithms for rapid unsupervised cryo-EM structure determination. *Nat Methods* **14**, 290-296 (2017). https://doi.org/10.1038/nmeth.4169

47 Watson, Z. L. *et al.* Structure of the bacterial ribosome at 2 A resolution. *Elife* **9** (2020). https://doi.org/10.7554/eLife.60482

48 Abramson, J. *et al.* Accurate structure prediction of biomolecular interactions with AlphaFold 3. *Nature* **630**, 493-500 (2024). https://doi.org/10.1038/s41586-024-07487w

49 Emsley, P. & Cowtan, K. Coot: model-building tools for molecular graphics. *Acta Crystallogr D Biol Crystallogr* **60**, 2126-2132 (2004). https://doi.org/10.1107/S0907444904019158

50 Adams, P. D. *et al.* PHENIX: a comprehensive Python-based system for macromolecular structure solution. *Acta Crystallogr D Biol Crystallogr* **66**, 213-221 (2010). https://doi.org/10.1107/S0907444909052925

51 Goddard, T. D. *et al.* UCSF ChimeraX: Meeting modern challenges in visualization and analysis. *Protein Sci* **27**, 14-25 (2018). https://doi.org/10.1002/pro.3235

52 Hatzixanthis, K., Palmer, T. & Sargent, F. A subset of bacterial inner membrane proteins integrated by the twin-arginine translocase. *Mol Microbiol* **49**, 1377-1390 (2003). https://doi.org/10.1046/j.1365-2958.2003.03642.x

2.2 Publication 2 | Mechanistic insights into Bcs1-mediated mitochondrial membrane translocation of the folded Rieske protein

Article

SOURCE DATA | TRANSPARENT PROCESS | OPEN ACCESS | CHECK FOR UPDATES

THE EMBO JOURNAL

Mechanistic insights into Bcs1-mediated mitochondrial membrane translocation of the folded Rieske protein

Cristian Rosales-Hernandez, Matthias Thoms, Otto Berninghausen, Thomas Becker & Roland Beckmann ✉

Abstract

A functional mitochondrial respiratory chain requires coordinated and tightly regulated assembly of mitochondrial- and nuclear-encoded subunits. For bc1 complex (complex III) assembly, the iron–sulfur protein Rip1 must first be imported into the mitochondrial matrix to fold and acquire its 2Fe–2S cluster, then translocated and inserted into the inner mitochondrial membrane (IM). This translocation of folded Rip1 is accomplished by Bcs1, an unusual heptameric AAA ATPase that couples ATP hydrolysis to translocation. However, the molecular and mechanistic details of Bcs1-mediated Rip1 translocation have remained elusive. Here, we provide structural and biochemical evidence on how Bcs1 alternates between conformational states to translocate Rip1 across the IM. Using cryo-electron microscopy (cryo-EM), we identified substrate-bound pre-translocation and pre-release states, revealing how electrostatic interactions promote Rip1 binding to Bcs1. An ATP-induced conformational switch of the Bcs1 heptamer facilitates Rip1 translocation between two distinct aqueous vestibules—one exposed to the matrix, the other to the intermembrane space—in an airlock-like mechanism. This would minimize disruption of the IM permeability barrier, which could otherwise lead to proton leakage and compromised mitochondrial energy conversion.

Keywords Bcs1; Cryo-EM; Folded Protein Translocation; Mitochondria; Rieske
Subject Categories Membranes & Trafficking; Organelles; Structural Biology
https://doi.org/10.1038/s44318-025-00459-4
Received 13 December 2024; Revised 25 April 2025; Accepted 25 April 2025
Published online: 23 May 2025

Introduction

In eukaryotes, 50–75% of proteins are transported to organelles or secreted outside the cell. To enter the endoplasmic reticulum (ER), mitochondria and chloroplasts, proteins need to translocate across or insert into lipid membranes. Here, transport is mediated by so-called translocators or translocons, which serve as protein-conducting channels. Typically, these translocons, such as the Sec complex in the ER or the Tim-Tom import machinery of mitochondria, recognize fully unfolded or only marginally folded (α-helical secondary structure) proteins as translocation competent substrates (for review see (Rapoport et al, 2017; Wiedemann and Pfanner, 2017)). Thereby, these translocons can accommodate a plethora of very different substrates. In contrast, the translocation of fully folded proteins is rather rare and is usually observed only as soon as folding and maturation to the native state is not possible in the final target compartment. For example, for many proteins that require insertion of complex cofactors such as iron-sulphur (Fe–S), iron-nickel (Fe–Ni) or molybdopterin clusters via enzymatic assembly factors, the maturation is completed before translocation (Berks, 1996; Santini et al, 1998; Sargent et al, 1998). In bacteria, chloroplasts and some *archaea*, such proteins are usually translocated by the twin-arginine translocase pathway (Tat pathway) (Frain et al, 2019; Palmer and Stansfeld, 2020). The main translocator unit is the small membrane protein TatA that has been suggested to oligomerize for cargo transport, but the exact mechanism still remains enigmatic. Mitochondria, however, lost the Tat system during evolution while still dealing with translocation of the highly conserved Fe–S cluster-containing Rieske protein (Rip1 in yeast). Rieske is part of the ubiquinol-cytochrome-c reductase, also known as bc1 respiratory chain complex or complex III in bacteria, mitochondria and chloroplasts (RIESKE et al, 1964) that is responsible for oxidation of the membrane pool of ubiquinol and reduction of cytochrome c in the mitochondrial intermembrane space (IMS) (Crofts, 2004; Xia et al, 2013). Rieske is a small integral membrane protein, with an N-terminal transmembrane helix (TMH) and a globular C-terminal domain bearing the 2Fe–2S cluster, which is exposed to the IMS (Harnisch et al, 1985). In mitochondria, Rieske has a dedicated translocator named Bcs1 (bc1 synthesis 1) (Aldridge et al, 2008; Bachmann et al, 2006; De Buck et al, 2007) which is a member of the AAA-ATPase family. While members of this class usually are enzymes that couple ATP hydrolysis with distinct unfolding or disaggregation activities, Bcs1 belongs to an outlying clade (Frickey and Lupas, 2004) and functions as a translocator for folded proteins.

Mitochondrial assembly of yeast Rip1 and its insertion into the bc1 complex is a multistep process (Wagener and Neupert, 2012). The Rip1 precursor carries a mitochondrial matrix targeting signal and is

Department of Biochemistry, Gene Center, University of Munich, Feodor-Lynen-Str. 25, 81377 Munich, Germany. ✉E-mail: beckmann@genzentrum.lmu.de

initially imported into the matrix of mitochondria via the general import pore by TOM and TIM23 complexes (Hartl et al, 1986; van Loon et al, 1987). Subsequently, the 30 amino acid long mitochondrial targeting pre-sequence is removed in the matrix in two processing steps (Graham and Trumpower, 1991) and the C-terminal domain folds and acquires its 2Fe–2S cluster (FeS domain) (Kispal et al, 1999; Wagener et al, 2011). During late stages of assembly, Rip1 can associate with the small protein Mzm1 (Cui et al, 2012), which was shown to prevent aggregation and proteolytic decay of Rip1 in the matrix. Finally, the completely folded Rieske C-terminal domain translocates from the matrix to the IMS while the N-terminal TMH inserts into the inner mitochondrial membrane (IM) (Wagener et al, 2011), leading to bc1 complex maturation. Initially, it was suggested that incorporation of Rieske protein into the bc1 complex by Bcs1 could be a prerequisite for the dimerization of bc1 and super complex formation (Cruciat et al, 2000). More recently, it has been shown that dimerization and further super complex formation can be observed in the absence of Rip1 (Conte et al, 2015; Stephan and Ott, 2020).

First structural insights into the architecture of the Bcs1 complex were gained from cryo-EM and X-ray crystallography studies of yeast (*Saccharomyces cerevisiae*) and mouse (*Mus musculus*) Bcs1 (yBcs1 and mBCS1, respectively) (Kater et al, 2020; Tang et al, 2020). Here, contrary to most AAA-ATPases that form hexameric rings with rather narrow central pores, Bcs1 was shown to form heptameric rings with a significantly wider pore and two large vestibules. This characteristic heptameric architecture is a result of specific features of the Bcs1 protomers. One protomer consists of three domains, a transmembrane helix (TMH) at the N-terminus, a Bcs1-specific β-sheet-containing middle domain and a C-terminal AAA cassette (Kater et al, 2020; Tang et al, 2020). Upon assembly, the seven TMHs form the transmembrane domain (TMD), a basket-like structure in the IM establishing a large and partly aqueous space in the hydrophobic lipid bilayer (also called IM vestibule). Towards the matrix side, the middle domains are assembled into a proteinaceous ring that forms a seal-like structure (seal pore), whereas the seven AAA cassettes form a second cavity opening to the matrix side (matrix vestibule).

Structural analyses have shown that the arrangement of the individual domains with respect to each other can undergo changes leading to global rearrangements of the Bcs1 quaternary structure, giving rise to the idea of an airlock-like translocation mechanism for Rieske. The pre-translocation state, as represented by structures of the ADP-bound state of yBcs1 (Kater et al, 2020) as well as ADP- and Apo states of mBCS1 (Tang et al, 2020) showed a large matrix vestibule formed by AAA and middle domains that would be wide enough to accommodate the folded FeS domain of Rip1. These structures also show the seal between the matrix and the IM vestibules to be closed. The two yeast Apo states both show a compaction of the matrix vestibule but differ in the conformation of the middle domain that leads to an opening of the seal pore. When bound to ATPγS as observed with mBCS1 (6UKS and EMD-20811) the size of the matrix vestibule is further reduced while the seal pore is opened, indicating that ATP binding may trigger transient opening to gate Rieske from the matrix to the IM vestibule. Notably, in both yBcs1-Apo2 and mBCS1-ATPγS structures, the basket-TMHs are largely disordered, indicating that the basket may open both vertically to release the FeS domain and laterally to release the Rieske TM for integration into the adjacent bc1 complex.

This proposed mechanism was further corroborated by a high-speed atomic force microscopy (HS-AFM) and line scanning (HS-AFM-LS) study (Pan et al, 2023) using purified mBCS1 in different nucleotide states (ATPγS, ADP, apo), confirming the nucleotide-dependent conformational changes and manifesting the concerted nature of such changes in Bcs1. Yet, for a long time, how substrate recognition, translocation and membrane insertion are coupled to the Bcs1's ATPase cycle remained enigmatic due to a lack of substrate-bound Bcs1 structures. Only recently, a low-resolution cryo-EM structure of mBCS1 bound to bovine Rieske FeS domain (Iron-Sulphur Protein extrinsic domain; ISP-ED) gave first insights into the substrate recognition step (Zhan et al, 2024). Here, a bulky extra density was indeed found inside the matrix vestibule, asymmetrically bound to one or two protomers of the Bcs1 heptamer that adopted the ADP-bound conformation of mBCS1. Yet, limited resolution did not allow to determine the orientation of the ISP-ED of Rieske or to unambiguously assign the nucleotide state in Bcs1.

Thus, several key questions regarding the Bcs1-mediated Rieske translocation mechanism remain open. First, it is unclear in which conformational state of Bcs1 substrate recognition takes place. Second, the molecular basis of substrate recognition and accommodation remains to be established. This is especially important with respect to positioning of the Rieske TM that needs to be inserted into the IM in an N_{Matrix}-C_{IMS} topology. Third, so far, no structural information on the actual gating step from the matrix vestibule into the IM vestibule is available which would be required to allow the transition of the Rieske protein from the matrix into the IM vestibule.

Here, we present cryo-EM structures of in vitro reconstituted yeast Bcs1-Rip1 complexes under various conditions. We observed in a 3.4 Å resolution structure that Rip1 binds to Bcs1 in the Apo state. We could position the Rip1-FeS domain as well as parts of the TM segment inside the Bcs1 matrix vestibule based on resolved secondary structure. This further allowed us to map residues in Bcs1 and Rip1 crucial for substrate accommodation, mutation of which leads to respiratory growth defects. We further show structures of Bcs1 in two distinct ATPγS states, which display a largely constricted matrix vestibule. We could visualize Rip1 in one of the two states, relocated through the wide-open seal pore into the IM vestibule. We conclude that ATP binding to substrate-loaded Bcs1 leads to compaction of the matrix vestibule and, at the same time, to gating of the substrate into the IM vestibule, accompanied with a conformational change of the middle domains that results in opening of the TMD helices.

Results

Structure of Bcs1-Rip1-FeS in the substrate loading state

To obtain stable Bcs1-bound Rip1 translocation intermediates, we chose an in vitro reconstitution approach using purified components. Therefore, we first developed a protocol for rapid affinity purification of Bcs1 solubilized in digitonin from *S. cerevisiae* (Appendix Fig. S1A,D). For Rip1, we chose two constructs (Appendix Fig. S1B,C), one containing only the C-terminal FeS domain but lacking the N-terminal TM segment (Rip1-FeS; aa 83–215) and one that still contains parts of the TM (Rip1-TM; aa

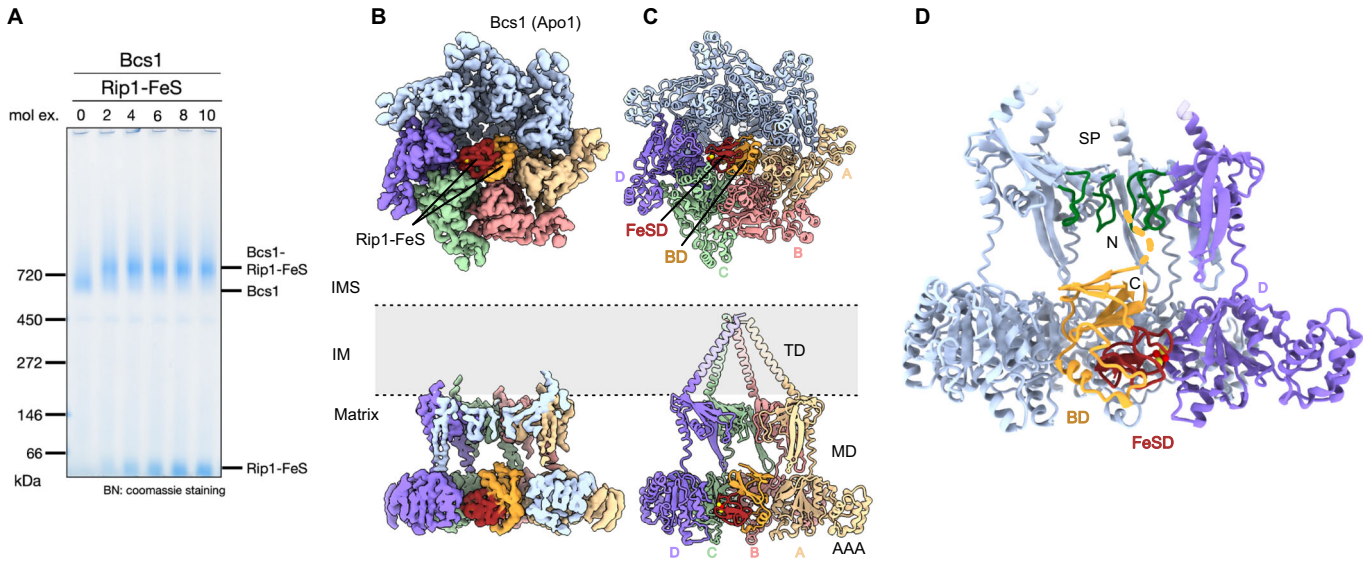

Figure 1. Structure of a Bcs1-Rip1 substrate loading complex.

(A) Blue native (BN) gel showing the in vitro reconstitution of the Bcs1-Rip1 complex. Purified Rip1-FeS was added to purified Bcs1 in the absence of any nucleotide in increasing molar excess as indicated. **(B, C)** Cryo-EM structure **(B)** and molecular model **(C)** of the Bcs1-Rip1-TM complex. Upper panels are bottom views from the matrix side, lower panels cut side views to highlight the Rip1 position. The transmembrane basket helices were flexible in our maps, and the model shown represents their position in the Apo1 conformation (Kater et al, 2020). They are shown transparent to indicate that they are not present in our map. Protomers interacting with Rip1 are color-coded and labeled from **(A–D)**. **(D)** Orientation of Rip1-FeS in the Bcs1 matrix vestibule. The N- and C-terminus of Rip1 are facing the seal pore (SP) and the dashed line indicates the putative position of N-terminal residues (including the TM helix). IMS intermembrane space, IM inner membrane, TD transmembrane domain, MD middle domain, AAA AAA-ATPase domain, BD base domain, FeSD 2Fe–2S cluster binding subdomain. The 2Fe–2S cluster is shown in a sphere representation, where yellow spheres represent the sulfur atoms and red spheres represent the iron atoms. Source data are available online for this figure.

31–55 and 66–215) and that was shown to be successfully integrated into the bc1 complex (Ramabadran et al, 1997). Both proteins were expressed in *E. coli* and affinity purified using a twin Strep tag (Appendix Fig. S1E,F). Bcs1 heptamer and Rip1 were further purified by size-exclusion chromatography and Bcs1 was checked for quality and oligomerization state by negative stain TEM (Appendix Fig. S1D). Binding of Rip1 to Bcs1 was monitored by a size shift of the apparent molecular weight in Blue native gel electrophoresis (BNGE) as described before (Wagener et al, 2011) (Fig. 1A; Appendix Fig. S1E,F). This shift (from about 700 to 800 kDa) occurred as Rip1-FeS or Rip1-TM were added in at least twofold molar excess over Bcs1 in the absence of any nucleotide.

Accordingly, cryo-EM samples were prepared from in vitro reconstituted Bcs1-(Rip1-FeS) and Bcs1-(Rip1-TM) complexes and subjected to Single Particle Analysis. 3D reconstruction of both samples yielded classes with clear Rip1 density within the Bcs1 matrix vestibule (Appendix Figs. S2 and S3). Those classes (of 106,497 particles for Bcs1-(Rip1-FeS); of 57,257 particles for Bcs1-(Rip1-TM)) were refined to a final resolution of 3.5 Å and 3.4 Å, respectively with local resolution ranging from 3.0 to 6.5 Å (Appendix Fig. S4). This allowed us to unambiguously identify the Rip1-FeS domain (30 Å in diameter) and determine its orientation within the Bcs1 matrix vestibule, resulting in a near-complete molecular model for a stable Bcs1-Rip1 pre-translocation intermediate (Fig. 1C).

Both Bcs1-(Rip1-FeS) and Bcs1-(Rip1-TM) complexes displayed a very similar overall architecture, with Bcs1 adopting the same conformation as observed in Apo1 state of yBcs1 (Kater et al, 2020) (Figs. 1B and EV1). This state adopts a closed seal pore, but the matrix vestibule was already somewhat more compacted when compared to the ADP state. In addition, no ADP density was found in the ATP-binding pocket of any of the seven protomers (Fig. EV2A,B). Notably, the substrate loading state clearly differs from mBCS1, where Apo and ADP states adopt the same conformation (Tang et al, 2020; Zhan et al, 2024). Since the Bcs1-(Rip1-TM) reconstruction showed a slightly better resolution and overall map quality, it was used for molecular model building and the detailed structure will be discussed based on this map (Appendix Table S1).

Rip1-FeS introduces asymmetry in the matrix vestibule by exclusively contacting the AAA domains of four Bcs1 protomers, henceforth called protomers A–D (Fig. 1C). It binds to Bcs1 with the 2Fe–2S cluster binding subdomain (FeSD) tightly packing against protomers C and D while the large (base) domain (BD) is exposed to protomers A and B (Fig. 1C). Based on resolved secondary structure including several side chains in the Rip1-FeS density (Appendix Fig. S4A, left panel and Fig. EV3), we could position the FeS domain with its N- and C-termini facing towards the seal pore locking up the IM vestibule. In this orientation, the N-terminal TM helix would also face towards the IM vestibule (Fig. 1D).

In Bcs1, we identified two highly conserved charged motifs, the EWR motif (E212-R214) and the DDR motif (D300-R302), that contain residues exposed to the FeS domain of Rip1 (Fig. 2A, left panel; Appendix Fig. S5). The EWR motif was located in the Bcs1-specific β-strands β-a1 and β-a2 (BSB) that extend the canonical six β sheets in the AAA domain, whereas the DDR motif was located at the tip of helix α2, following one of the loops (pore loop 1 (PL1)) corresponding

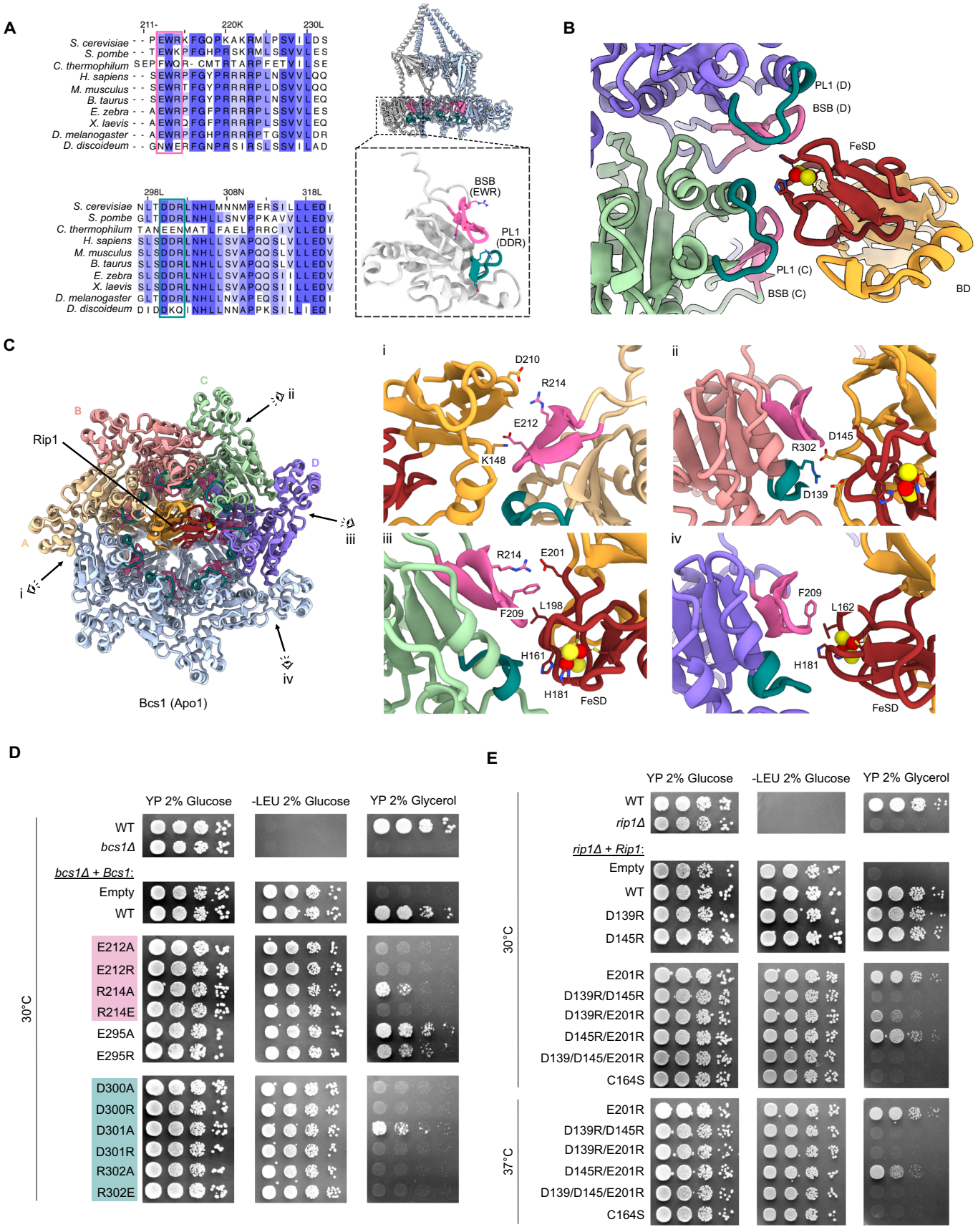

Figure 2. Conserved motifs mediate the interaction between Bcs1 and Rip1-FeS.

(A) Multiple sequence alignment displaying two conserved motifs (EWR motif and DDR motif) and their location in the Bcs1 protomer. **(B)** Close-up view highlighting the interaction between Bcs1 protomers C and D with the Rip1-FeSD. **(C)** Left panel: Bottom view on the Bcs1-Rip1-TM complex. View directions for close-up views (i-iv; right panels) are indicated. Right panel: Zoom on the interactions of protomers A (i), B (ii), C (iii), and D (iv) with Rip1-FeS. Side chains of interacting residues, including the conserved EWR motif (E212 and R214) and the DDR motif (R302), are indicated. The 2Fe–2S cluster is shown in a sphere representation, where yellow spheres represent the sulfur atoms and red spheres represent the iron atoms. **(D)** Mutational analysis of Bcs1 residues in EWR and DDR motifs based on a growth assay (tenfold serial dilutions) of yeast cells on a fermentable (glucose) or non-fermentable (glycerol) carbon source. Right panel shows the growth control on rich media (YP), middle panel is a control for the presence of the Bcs1-expressing plasmid, left panel shows growth on YP with glycerol. Growth was monitored at 30 °C unless indicated. **(E)** Growth assays for Rip1 were carried out in a similar way on a *rip1Δ* background and from a Rip1-expressing plasmid (see "Methods" for details). **(D, E)** Are an excerpt of the comprehensive combined display shown in Appendix Fig. S6, reduced here to emphasize the residues discussed in the text and shown in **(A–C)**. Source data are available online for this figure.

to the substrate-binding pore loops in canonical AAA-ATPases (Fig. 2A, right panel). First, we observed that the BSB and PL1 from protomers C and D are forming contacts to the Rip1-FeSD (Fig. 2B). Second, the EWR and DDR motifs—together with F209—formed a module that contributes to substrate contacts in all four interacting protomers (Fig. 2C). Thereby, a characteristic positive charge distribution pattern is established in the matrix vestibule that is complementary to several negatively charged residues, e.g., D139, D145, E201 and D210 in the Rieske substrate. However, in each protomer, these residues can exhibit a different binding mode complementary to the surface properties of the Rip1-FeS.

We next tested whether the above-described charged residues in Bcs1 and Rip1 are indeed involved in transient complex formation and are thus important for Bcs1-mediated translocation. We expressed Bcs1 and Rip1 mutants under the control of Bcs1 endogenous promotor in a *bcs1Δ* and a *rip1Δ* yeast strain while checking for respiratory growth defects in a non-fermentable carbon source. Indeed, we found that Bcs1 charge inversion mutations in the EWR and the DDR motives were not viable in YP medium containing glycerol. For E212, D300 and R302, also mutations to alanine were lethal in respiratory conditions, whereas R214A and D301A show only a mild effect. In contrast, mutants of an unrelated residue in the vicinity of the DDR motif show no lethal effect (E295, located in PL1) (Fig. 2D; Appendix Fig. S6A). For Rip1, we find that single charge inversion mutations (D139R, D145R, E201R and D210R) did not show any growth defect while double mutations indeed show lethal phenotypes on a non-fermentable carbon source (Fig. 2E; Appendix Fig. S6B). To support our hypothesis that a charge complementarity between Rip1 and Bcs1 is required for Rip1 translocation, we performed a multiple sequence alignment of Rip1 homologs in species that use both Bcs1 (in mitochondria) and the Tat pathway (petC in chloroplasts or qcrA in prokaryotes). The alignment shows that D139, D145, E201 are conserved only in cases where Bcs1 is required for translocation (Fig. EV4A,B). In contrast, only D139 is conserved in chloroplasts, and none of the three residues are conserved in prokaryotes. Moreover, we note that these residues are exposed to the surface when Rip1 is integrated into complex III, indicating that they are not required for complex III activity (Fig. EV4C–E).

Bcs1 undergoes conformational changes upon nucleotide binding

Our observation of the pre-translocation state in the absence of any bound nucleotide (Fig. EV2A,B) suggests that subsequent binding of ATP or ATP hydrolysis may trigger substrate translocation. This question was addressed using BNGE-based binding assays as shown above. When incubated in presence of nucleotides, Bcs1 exhibits characteristic migration shifts, which can be correlated with conformational changes that lead to different electrophoretic mobilities in the gel. After incubation with ADP or ATP (for 10 min), we observed a similar size shift (from about 700 to 750 KDa) in BNGE as upon addition of Rip1-FeS (Figs. 1A and 3A). Here, we assume that, in the case of ATP, the resulting band represents also the ADP state, since Bcs1 hydrolyzes ATP in vitro at an average rate of 27 nmol ATP / nmol yBcs1 (heptamer) / min (Appendix Fig. S1G). The observed size shift thus reflects the conformational change of Bcs1 from the Apo state to the ADP state. Interestingly, ATPγS incubation caused a smaller but still clearly discernable size shift when compared to ATP or Rip1-FeS, indicative of another distinct conformation of Bcs1.

To test this hypothesis, we determined the structure of Bcs1 bound to ATPγS by cryo-EM. Here, we were able to distinguish two conformations of Bcs1 after 3D classification that differed from previously observed yBcs1 classes. These two subsets (here termed ATPγS1 and ATPγS2) were refined to an overall resolution of 2.6 and 2.7 Å, respectively (local resolution ranging from 2.2 to 5 Å for both ATPγS states (Appendix Figs. S7–S9). Both reconstructions showed Bcs1 in an entirely different, more compacted conformation when compared to the other observed nucleotide states (Fig. 3B) from yeast (Bcs1-Apo1 and Bcs1-ADP), but its overall architecture was similar to mBCS1-ATPγS (Tang et al, 2020). ATPγS density was observed in each of the seven protomers as well (Fig. EV2C,D). Notably, our reconstructions showed a substantially narrowed matrix vestibule of ~20 Å in diameter as opposed to ~40 Å and ~30 Å in the ADP or apo states, respectively. This dimension is incompatible with substrate binding at the matrix side and coincided with a wide-open seal ring of 30 Å diameter (only 15 Å in the ADP and Apo1 states) large enough to accommodate Rip1 during translocation (Fig. 3B). Moreover, the basket TM helices are in a defined position and clearly resolved in ATPγS1, occupying a similar position as observed in yeast ADP or Apo1 states, tightly held together by a hydrophobic seal in IMS leaflet of the IM. In ATPγS2, however, the TM domain becomes more flexible, especially in the hydrophobic seal region (Fig. 3B; Appendix Fig. S8A).

For both of our ATPγS states, the arrangement of the AAA-ATPase domains relative to each other was significantly different from yBcs1-Apo1 and yBcs1-ADP (Fig. 3C). The observed inward rotation for the transition between ADP- and Apo state is even more pronounced for both ATPγS states (of approx. 25° from

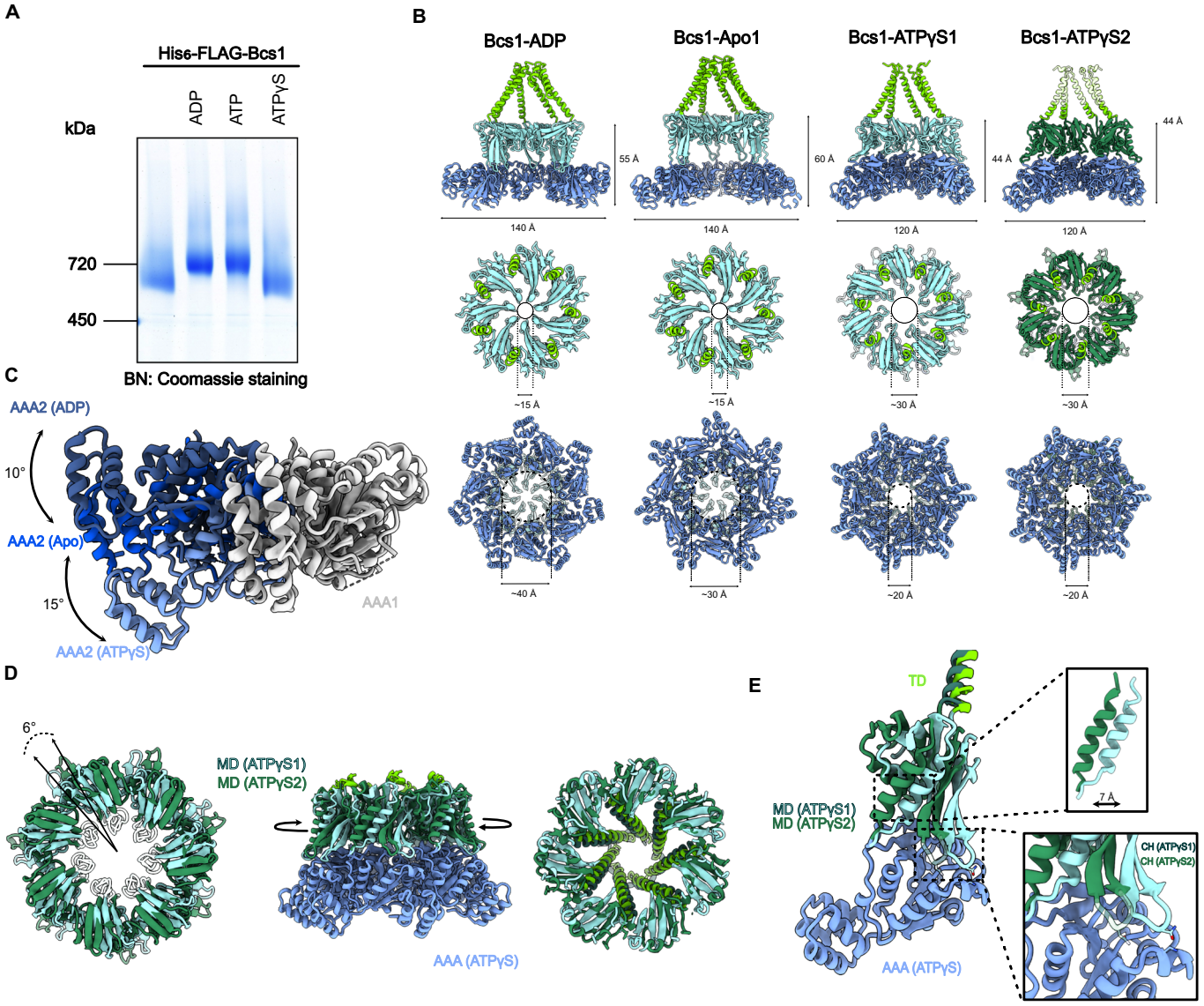

Figure 3. Conformational dynamics of Bcs1.

(**A**) Blue native (BN) gel showing the Bcs1 oligomer after incubation with ADP, ATP and ATPγS. (**B**) Comparison of molecular models for Bcs1-ADP, Bcs1-Apo1 (Kater et al, 2020) as well as two states of Bcs1 bound to ATPγS (ATPγS1 and ATPγS2). Upper panels show cut side views, middle panels show top views from the IMS side at the middle domains and lower panels bottom views from the matrix side at the AAA domains. Note the compaction of Bcs1, the opening of the seal pore and the narrowing of the matrix vestibule in the ATPγS states. (**C**) Conformational rearrangements of the AAA domain from the ADP via Apo1 to ATPγS states: when aligned to the AAA domain of one protomer (AAA1) the neighboring AAA domain undergoes in inward rotation (10° from ADP to Apo1; 15° from Apo1 to ATPγS) relative to AAA1. (**D**) Overlay of the two ATPγS states: The ring formed by the middle domains rotates versus the AAA ring by 6° as shown in a top view (left panel) and a side view (right panel). The seal loops are shown transparent, indicating that they are largely delocalized. (**E**) Comparison of the two ATPγS states in one isolated protomer. The middle domain shifts with respect to the AAA domain by 7 Å. In ATPγS1 the CH of the neighboring protomer forms a contact with the large AAA domain involving E124, N125 (CH) and K250, S253 (AAA). In ATPγS2 the CH dissociates, and the loop becomes more flexible as indicated by transparency. Source data are available online for this figure.

ADP- to -ATPγS- and 15 degrees from Apo1- to ATPγS state). For the middle domains, we observe a similar tilt motion away from the membrane plane as observed for the transition from ADP (or Apo1) to the Apo2 state (Appendix Fig. S10). We also observed the outward movement of the connector hairpin (CH) that can adopt two positions (see below). Thus, as also observed in the Apo2 state, both ATPγS states show a wide opening of the seal pore (res 161–168) with seal loop residues being largely delocalized in these structures.

The two ATPγS states can be distinguished from each other mainly by the orientation of the middle versus the AAA domains (Fig. 3D). While the conformation of the AAA domains is essentially the same, we observed a rotation of the middle domains of 6° degrees against the AAA domains, leading to a shift of the

middle domains by 7 Å away from the AAA domain in each protomer (Fig. 3E). Notably, the same shift and rotation also apply to the TD helices that rotate with the middle domains as rigid bodies (Fig. 3D, right panel). This rotation may also lead to destabilization of the TD, which would explain why its helices are less defined in the ATPγS2 state.

Of note, in ATPγS1, the CH forms a contact with the large AAA domain of the neighboring protomer (D124/N125 of the CH with K250 and S253 of AAA), but this contact breaks after the transition to ATPγS2, concomitantly leading to a higher flexibility of the CH loop (Fig. 3E; Appendix Fig. S9A). A direct contact between the CH and AAA domain was also observed for the ADP state, here involving N287 and R313 of the AAA (Kater et al, 2020). This suggests that the conformation of the CH may be an important signal for the status of translocation and that the CH may transmit changes in the MDs, e.g., due to the presence of substrate or unpacking of seal loops, to the AAA domains. In our structures, however, in the ATPγS-bound nucleotide binding site we do not detect any significant differences when comparing the AAA domains in both states.

Taken together, yBcs1 in the ATPγS state shows a severely contracted matrix vestibule — as observed for mBCS1 — which is too small to bind the substrate in the loading state. However, this closing of the matrix vestibule together with the widening of the seal pore suggests that the two observed ATPγS conformations may also occur at intermediate stages of substrate gating, as also proposed before for mBCS1 (Pan et al, 2023; Tang et al, 2020; Zhan et al, 2024).

ATPγS locks the Bcs1-Rip1 complex in a substrate gating intermediate

To establish conditions for the stabilization of the Bcs1-Rip1 translocation intermediate, we performed binding assays as described above using Rip1-FeS and Rip1-TM with ATP and non-hydrolysable ATPγS and varied the order of component addition for complex assembly (Fig. 4A). When adding Rip1-FeS followed by ATP, the BNGE bands became rather smeary indicating multiple conformations, probably due to a mixture of states occurring at various stages of translocation (Fig. 4A, lane 5). We observed a similar smeary appearance of the bands when first adding ATP for 10 min and then Rip1-FeS (Fig. 4A, lane 7). When adding ATPγS followed by Rip1-FeS (Fig. 4A, lane 8), no further size shift was observed when compared to adding only ATPγS (Fig. 4A, lane 4), indicating no or only weak binding of Rip1-FeS to Bcs1 in the ATPγS state, which is in line with our observation that the matrix vestibule is constricted in this state and cannot accommodate the substrate. However, we saw a clear difference when Rip1-FeS was added first, followed by ATPγS (Fig. 4A, lane 6). Here, the bands became again rather smeary with no clear shift anymore towards higher apparent molecular weight. We conclude that after Rip1-FeS binds to Bcs1 the addition of ATPγS induces a conformation of Rip1-FeS-bound Bcs1 that is different from the one observed for Bcs1-Rip1-FeS in Apo state and different from the Bcs1-ATPγS. We hypothesized that Rip1 binding to Bcs1 is required prior to ATP, e.g., in the Apo state as shown above or in the ADP state. Addition of a non-hydrolysable ATP analog before incubation with substrate most likely locks Bcs1 in a constricted conformation entirely preventing access of Rip1 to the Bcs1 matrix vestibule.

We thus structurally analyzed the pre-formed Bcs1-Rip1 complex incubated with ATPγS by cryo-EM. Single particle analysis showed Bcs1 again in the two ATPγS states and, in addition, we obtained one class (70,366 particles) that displayed extra density for Rip1-FeS in the IM vestibule (Fig. 4B), refined to an overall resolution of 3.1 Å (local resolution ranging from 2.7–7.5 Å) (Fig. 4B; Appendix Figs. S8 and S9). Interestingly, we exclusively observed Rip1 bound to Bcs1 in the ATPγS2 conformation, with all seven ATP-binding pockets exhibiting ATPγS density (Fig. EV2E), the only difference to the unbound ATPγS2 state being that the TD basket helices were now completely delocalized. We find an extra density of ~30 Å in diameter for Rip1 in the aqueous cavity between the middle domain and the TD basket and it appears to be, at least partly, clogging the seal pore from the IM side, indicating that the substrate itself could play a role for maintenance of the permeability barrier during and immediately after translocation. Notably, however, in contrast to the loading state, the density for Rip1-FeS in the IM vestibule did not display any obvious orientation preference, as confirmed by a rather low local resolution. Moreover, we observed that the central loops of the middle domain appear more delocalized compared with the unbound ATPγS2 state. We thus were not able to position the Rip1-FeS domain in a distinct orientation, and no specific contacts with Bcs1 could be identified.

We conclude that binding of ATPγS to a pre-formed Bcs1-Rip1 complex triggered a conformational change in Bcs1, i.e., matrix vestibule constriction and opening of the seal pore, that results in translocation of the substrate from the matrix vestibule into the IM vestibule. This translocation step apparently coincides with the rotation of the middle domains against the AAA domains, leading to a partial opening on the TM basket. Translocation into the IM vestibule then resulted in the delocalization of the TD domain, a prerequisite for the eventual release of the folded substrate into the IMS (Rip1-FeS) and the IM (Rip1-TM domain). Failure to hydrolyze ATPγS, however, leads to a —at least partial—locking of the substrate inside the IM vestibule as observed in our structure, thus leading us to speculate that ATP hydrolysis may be coupled with substrate release.

In addition to the matrix vestibule constriction, an additional driving force for the movement of Rip1-FeS toward the IM vestibule may be the electrostatic interaction between the partially negatively charged surface of the substrate and the positively charged residues that line the inner walls of the IM vestibule in Bcs1 (Fig. 4C). Indeed, one plausible model fitting our Rip1 density would position the N-terminus of Rip1 towards the matrix side exposing the negative charges towards the TD basket (Figs. 4C and EV5). Furthermore, several positively charged residues are conserved across different species (Appendix Fig. S5), amongst them R69 and R81. We thus investigated R69 and R81 mutants for respiratory growth defects in a non-fermentable carbon source as described above (Fig. 4D). We observed that R69A and R69E mutations lead to a lethal phenotype. Moreover, R81 mutations show a detectable growth defect. Of note, mutation of R81 in *H. sapiens* (R45C) is one of the mutations associated with the GRACILE syndrome (Al Qurashi et al, 2022), which highlights the role of selective pressure on maintaining a positively charged surface in this region of Bcs1.

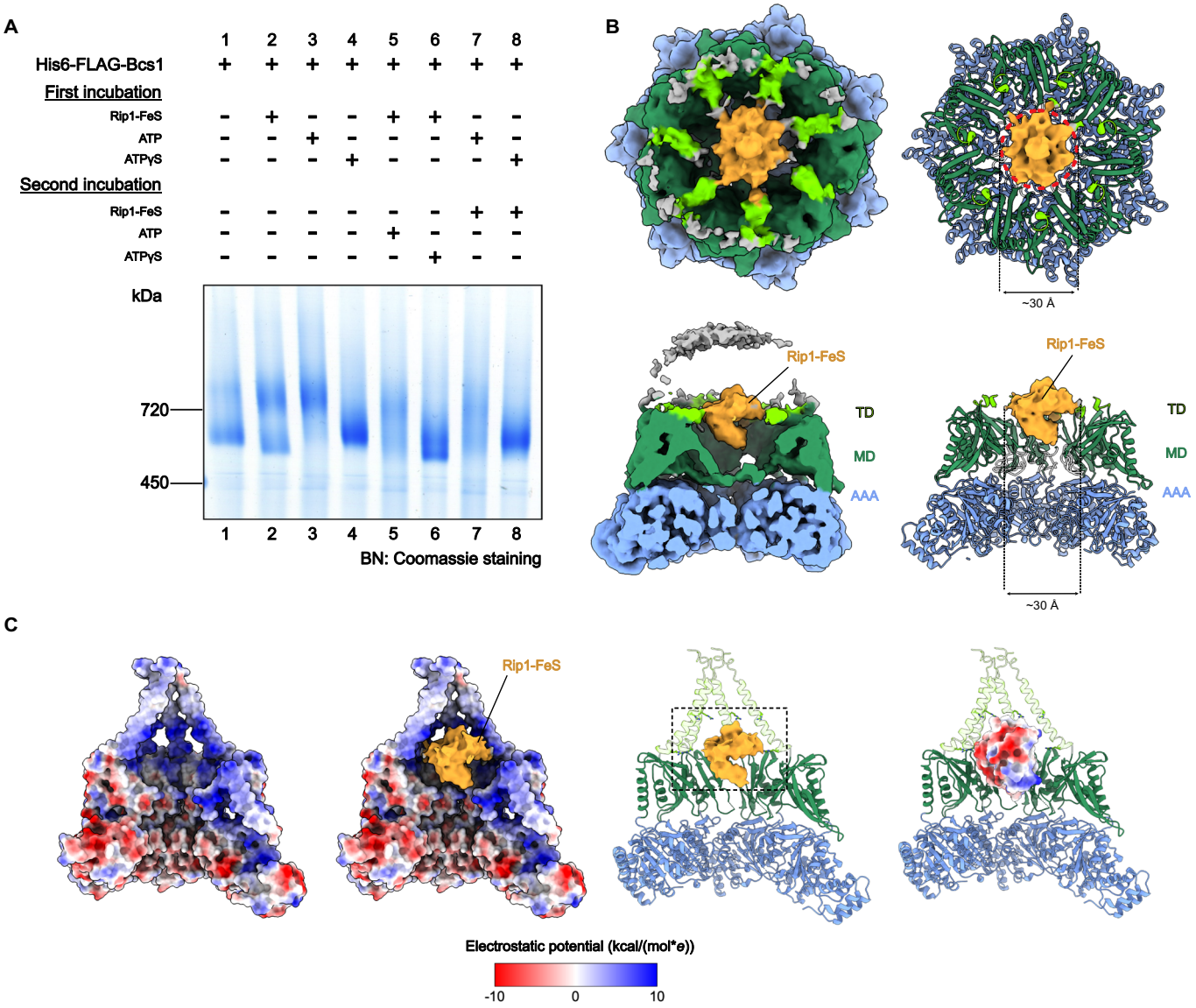

Figure 4. Structure of a Bcs1-Rip1 substrate gating intermediate in ATPγS2 state.

(**A**) Blue native (BN) gel showing the in vitro reconstitution of the Bcs1-Rip1 complex in the presence of ATP and ATPγS. Purified Rip1-FeS was added to purified Bcs1 prior to (lanes 5, 6) or after (lanes 7, 8) the addition of the nucleotide. (**B**) Cryo-EM structure (left panels) and molecular model (right panels) of a Bcs1-ATPγS-Rip1-FeS gating complex. Upper panels show top views from IMS side, lower panels cut side views. The seal loops are shown transparent as in Fig. 3D. Approximate size of the Rip1-FeS density is indicated. (**C**) Cut side view of the electrostatic potential map of Bcs1-ATPγS2 (leftmost panel), Rip1-FeS density superimposed into the electrostatic potential map of Bcs1-ATPγS2 (left panel), Rip1-FeS density superimposed in the atomic model of Bcs1-ATPγS2 (right panel) and Rip1-FeS model docked in the atomic model of Bcs1-ATPγS2 (rightmost panel), displaying the overall charge distribution on the IM vestibule, substrate surface and substrate density. The relative position of the substrate in the central panel was approximated according to the extra density detected in the IM vestibule as shown in (**B**). A display of TD flexibility is omitted in the electrostatic map for better visualization of the overall location of the positively charged patch, but it is indicated in the atomic model, where it is shown as transparent. (**D**) Close-up view of enclosed area in C (right panel) displaying the position of conserved positively charged residues surrounding the substrate density. TD flexibility is indicated by the transparency of the helices. (**E**) Mutational analysis of the positively charged residues in Bcs1 TD based on a growth assay as described in Fig. 2. This panel is an excerpt of the comprehensive combined display shown in Appendix Fig. S6, reduced here to emphasize the residues discussed in the text and shown in (**D**). Source data are available online for this figure.

Discussion

The translocation of a fully folded protein across the inner mitochondrial membrane requires a source of energy for directional movement across the hydrophobic barrier of the lipid bilayer and, at the same time, must at large preserve the membrane permeability barrier to maintain the proton gradient across the IM. We found how Bcs1-mediated Rieske translocation meets these requirements by employing an airlock-like mechanism that can be divided into three principal steps, loading of Bcs1 with the Rieske, gating of Rieske through the Bcs1 pore and release of both, the folded FeS domain into the IMS and the TM helix into the lipid bilayer of the IM (Fig. 5). In this work, we were able to visualize Rieske translocation intermediates, providing structural insights into the loading and gating steps of Rieske translocation.

Interestingly, we observe stable complex formation between Bcs1 and Rip1 only in the apo state (Apo1), i.e., with no nucleotide bound. Our structure of this complex clearly showed a substrate loading state with the Rip1-FeS stably accommodated within the Bcs1 matrix vestibule. A similar position was observed previously in the cryo-EM structure of the bovine Rieske FeS domain bound to the mammalian mBCS1 (Zhan et al, 2024). Unfortunately, however, the resolution of this structure did not allow for unambiguous positioning of the FeS domain, identification of molecular interactions or identification of the nucleotide state of mBCS1.

Our structure provides molecular details for the interaction between Rip1-FeS and Bcs1 and allows for the unambiguous positioning of the Rip1-FeS binding four Bcs1 protomers. In this conformation the C-terminus as well as the N-terminal region that would be following the TM domain, that were not visualized, are facing towards the seal pore of Bcs1. The Rip1-FeS interacts mainly via positively charged residues in Bcs1 and negatively charged patches on the Rip1 which form complementary surfaces. Here, we identified the DDR and EWR motifs in Bcs1 that interact with the substrate surface and showed that mutation of charged residues within those motifs was lethal in respiratory conditions, underlining their functional importance. In the observed position, the Rip1-FeS is transiently restricted in its orientation within Bcs1. This distinct mode of interaction may enable Bcs1 to probe the folding state of the substrate, explaining why mutants disturbing the characteristic antiparallel β-structure of the FeSD are deficient for translocation (Wagener et al, 2011). This is also in line with our observation, that reduction of the disulfide bond between C164 and C180, important for the overall fold of Rip1, results in a substrate unable to bind Bcs1 (Fig. EV3B). The indirect probing of the presence of the 2Fe–2S cluster by Bcs1 may explain why it is not an absolute prerequisite for the translocation and IM insertion of Rip1 but required for its efficiency (Graham and Trumpower, 1991). Thus, the binding preference of Bcs1 to properly folded and 2Fe–2S cluster containing Rip1 over only partially folded Rip1 lacking the 2Fe–2S cluster appears to be established by the large interaction region in the matrix vestibule which is complementary to the fully folded Rip1.

Binding of folded Rip1 to the open matrix vestibule of Bcs1 is sterically only possible in the apo and ADP-bound states. Since we never observed Rip1 bound to Bcs1 in the ADP-bound state biochemically or by cryo-EM, we speculate that Rip1 either binds to the apo state directly or triggers the release of ADP when engaging Bcs1. This would be in agreement with the clearly different conformations of Bcs1 observed in the apo or ADP-bound state. This is different from the observations in the mammalian system where the mBCS1 loading complex (Zhan et al, 2024) adopted the ADP conformation. However, since mBCS1 ADP and Apo states were indistinguishable at the reported resolution of 7.2 Å it is unclear whether in the mammalian system the Rieske initially binds to the ADP state followed by ADP release, or whether ADP release is coupled to substrate release as suggested for mBCS1 (Zhan et al, 2024).

But how does ATP binding or ATP hydrolysis eventually trigger Rip1 translocation after its recruitment to the matrix vestibule? Here, we were able to determine the structures of Bcs1 in the presence of ATPγS with and without bound Rip1. We observed that upon nucleotide (ATP) binding, Bcs1 undergoes a substantial conformational change, displaying a dramatic narrowing of the matrix vestibule and concomitant opening of the seal pore. In the absence of Rip1, we found an equilibrium of two distinct ATPγS states, ATPγS1 and ATPγS2, which differ by a rotation of the Bcs1 MD accompanied with a (partial) delocalization of the TM basket forming the matrix vestibule. Interestingly, we could trap Rip1 in the ATPγS2 state after incubation of Bcs1 with Rip1 followed by the addition of ATPγS. In this structure, we find Rip1 translocated through the open seal pore into the IM vestibule, likely still clogging the pore from the IM side. Rip1 may be trapped in this position because, as described in a previous study (Wagener et al, 2011), release requires ATP hydrolysis and resetting of its conformation to the ADP state. Moreover, it was shown that TM deletion mutants, as used in this study, were retained in the Bcs1 complex in in vitro chase experiments in the presence of another slow-hydrolysable ATP analog, AMP-PNP. Notably, the Rip1-FeS

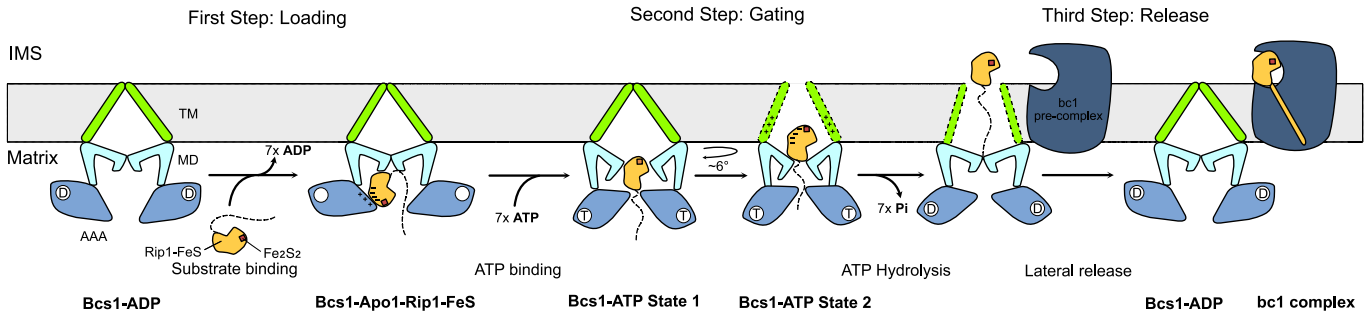

Figure 5. Airlock mechanism of Bcs1-mediated Rip1 translocation across the IM.

Schematic representation of the different states that Bcs1 goes through during Rip1 translocation. Dashed lines represent structural flexibility of transmembrane segments in Rip1 and Bcs1. Positive and negative charges are indicated in the Bcs1-Apo-Rip1-FeS and Bcs1-ATP State 2 as plus and minus signs.

is now located in the aqueous funnel of the IM vestibule clad by a number of positively charged residues that may again attract the negatively charged Rip1-FeS. Yet, in this state we do not observe any distinct interactions between Bcs1 and Rip1, indicating that the Rip1-Bcs1 interaction is not well defined but rather allows for multiple orientations of Rip1. Comparing the two structures of Rip1-bound Bcs1 in the substrate loading and gating states clearly suggests that ATP binding triggers a conformational change in Bcs1 that leads to unidirectional translocation of the Rip1-FeS from the matrix vestibule to the IM vestibule. Our structures thus confirm and refine the proposed airlock-like mechanism by which a concerted constriction of the matrix vestibule would push the Rip1-FeS towards the seal pore, which opens the gate into the IM vestibule. Charge complementarity between the positively charged surface of the IM vestibule of Bcs1 and the negatively charged surface of Rip1 may serve as an additional driving force and may also prevent the dissociation of the substrate back into the mitochondrial matrix upon ATP binding.

Based on these findings, we propose a refined model for Bcs1-mediated Rip1 translocation across the IM (Fig. 5). Our structure of the substrate loading state clearly shows that Bcs1 is in the nucleotide-free state when bound to the Rip1-FeS. In the next step ATP can now bind to the substrate loading complex, which leads to a conformational change in the entire Bcs1 heptamer. The dramatic constriction of the matrix vestibule drives translocation in the direction of the seal pore that opens to allow charge-driven passage of Rip1 to the IM vestibule. ATP binding results in at least two intermediates, here described as ATPγS1 and ATPγS2. We propose that the first intermediate, that we never observe with a bound Rip1, may occur only at an early stage of the translocation. In this very transient state, Rip1 may still be bound at or within the seal pore and the Bcs1 TM basket is closed. Rotation of the middle domain partially opens the TM basket allowing Rip1 to be accommodated in the IM vestibule, leading to a pre-release state. Moreover, our structures give a hint on how the permeability barrier during this translocation process may be maintained. Although contacts between translocated Rip1 and Bcs1 are loose and the resolution is thus rather poor, it appears plausible that the substrate itself is part of the permeability barrier by contributing to the closure of the seal pore. Another possibility is that the compacted AAA domains at the matrix side, as observed in the ATPγS states, also contribute to form a barrier. At least at low contour levels, we observe in our density maps that the central pore to the matrix is closed, presumably by flexible loops. The final step to complete the translocation process is the release of the Rip1-FeS to the IMS and the integration of the Rip1-TM into the IM bilayer, eventually allowing integration into the bc1 complex.

This step has been shown to be ATP hydrolysis dependent (Wagener et al, 2011), and can be assumed to reset the conformation to the observed ADP state. We speculate that this conformational transition from the ATP to the ADP state may occur with the Bcs1 TMD basket still open towards the IMS, as observed in the ATPγS2 state. This would allow for release of the Rip1-FeS domain into the IMS and for the Rip1-TM to laterally integrate into the IM. It should be noted that for the final release of the Rip1-TM it would be sufficient for the basket helices of the TD of Bcs1 to laterally open and allow for partitioning of the Rip1-TM into the bilayer of the IM. Unfortunately, the visualization of the basket helices appears to be difficult and not only reflecting conformational differences but rather qualitative and quantitative aspects in the different datasets (Appendix Table S2).

Therefore, while our structures provide mechanistic details for the loading and gating step, several fundamental questions remain open with respect to the insertion and release of Rieske's TM by Bcs1. The native topology of all Rieske proteins is TM N_{Matrix} – C_{IMS}, i.e., the N-terminus faces the matrix side while the C-terminal FeS is in the IMS. Notably, in our loading state, the Rip1-TM would be positioned facing towards the seal pore, but we cannot visualize it in our structure indicating that it is not (yet) ordered. Nevertheless, inversion of the globular FeS orientation relative to the pre-translocation state (Fig. 1D) would be required to adopt the native topology. This inversion may occur during the transition of the FeS through the seal pore. Notably, in other species like *M. musculus* and *H. sapiens*, the N-terminal region is even extended by a folded globular domain, representing another subunit of the bc1 complex, which remains in the matrix side of the membrane after insertion of Rip1. Consequently, in contrast to the situation in yeast, release of this N-terminus requires a complete lateral opening of the mBCS1 protomers, a step that was suggested to occur during ADP/ATP exchange for mBCS1 (Zhan et al, 2024). But even in the simpler situation in yeast, where the Rip1-TM just must laterally slip through the basket helices of Bcs1, it remains largely elusive at which exact stage of the ATPase cycle, and under which conditions the Rieske TM is released into the IM. It was shown before that

Bcs1 can interact with the bc1 complex (Zara et al, 2009) and although one study demonstrates that translocation and release of Rip1 are apparently independent of bc1 (Wagener et al, 2011), it is tempting to speculate that under physiological conditions Rieske TM release is coupled to the nearby presence of an assembly intermediate of the bc1 complex. Interestingly, it has recently been shown that folded Rieske interacts with an inner membrane-bound factor after Bcs1 translocation and insertion, during bc1 assembly (Zerbes et al, 2025). Eventually, ATP hydrolysis or release of ADP and exchange to ATP may be triggered or influenced by bc1 or another factor, yet so far experimental evidence for this hypothesis is lacking. In this context, we noted that in vitro Bcs1 permanently hydrolyzes ATP in the absence of substrate, which is highly unlikely to occur in vivo, further speaking for a contribution of the native membrane environment to Bcs1's ATPase cycle regulation. Thus, based on our structural work, we suggest that after Rip1-bound Bcs1 arrived in the pre-release state, ATP hydrolysis occurs in a conditional manner and leads to a transition state with the substrate still loosely bound to Bcs1. A direct handover and proper insertion into the bc1 pre-complex are then accompanied by Bcs1 dissociation and transition to the ADP state. Further experiments will be required to answer this question.

Methods

Reagents and tools table

Reagent/resource	Reference or source	Identifier or catalog number
Experimental models		
S. cerevisiae W303	Thomas and Rothstein, 1989	
S. cerevisiae W303 *bcs1Δ*::natNT2	This study	
S. cerevisiae W303 *rip1Δ*:: natNT2	This study	
E. coli DH5α	NEB	C2987
E. coli BL21	Novagen	70235-M
Recombinant DNA		
pETDuet-TwinStrep-3C-Rip1$^{\Delta 30, \Delta 55\text{-}65}$	This study	
pETDuet-TwinStrep-3C-Rip1$^{\Delta 81}$	This study	
YEplac112-GAL-His$_6$-FLAG-Bcs1	This study	
YCplac111-P.Rip1-Rip1$^{\Delta 30}$	This study	
YCplac111-P.Bcs1-FLAG-Bcs1	This study	
Chemicals, enzymes, and other reagents		
Kaiser SC Single Drop-Out -LEU	Formedium	DSCK1004
Phusion High Fidelity DNA Polymerase	NEB	M0531S
Digitonin	Calbiochem	300410
GDN (glyco-diosgenin)	Anatrace	GDN101
His cOmplete Resin	Roche	5893682001
Strep-Tactin XT 4Flow	Iba	2-5010-025
Superose 6 Increase 10/300 GL	Cytiva	29091596
Superdex 200 Increase 10/300 GL	Cytiva	28990944
NativePAGE gels	Thermo Fisher	BN1003BOX
ATPγS	Jena Bioscience	NU-406-5
Software		
Cryosparc v4.4	Punjani et al, 2017	
Alphafold Database	http://alphafold.ebi.ac.uk	
ISOLDE	Croll, 2018	
Coot	Emsley and Cowtan, 2004	
ChimeraX v1.8	Goddard et al, 2018	
Phenix	Adams et al, 2010	
ImageJ (Fiji)	Schindelin et al, 2012	
GraphPAD Prism v10	Dotmatics	
Affinity Designer 2	Affinity	
Other		
Titan Krios + Falcon 4i + SelectrisX Energy Filter	Thermo Fisher	
Vitrobot Mark IV	Thermo Fisher	
ÄKTA Pure	Cytiva	
Tecan Infinite M1000	Tecan	

Plasmids, strains, and growth conditions

The coding region of the yBcs1 gene (YDR375C, residues 1-456) was cloned into a YEplac112 vector, downstream to a GAL bidirectional promotor and a N-terminal 6xHis-FLAG-3C tag. The plasmid was transformed into a *Saccharomyces cerevisiae* W303 (Thomas and Rothstein, 1989) *bcs1Δ* strain using the lithium acetate method. For the overexpression of yBcs1, a single colony isolated from a YPG plate (1% yeast extract, 2% peptone, 2% glucose, 2% Bacto-agar) was grown at 30 °C on synthetic complete media lacking leucine, containing 2% glucose (SDC-LEU-Glucose) to a final OD_{600} of 1.0. The cells were then shifted to YPGal (1% yeast extract, 2% peptone, 2% galactose) and further grown until an OD_{600} of ~4.0 was reached. Cells were harvested and flash frozen for storage at −80 °C.

The yRip1 gene without the mitochondrial targeting sequence (YEL024W, residues 30–215) was cloned into a pET-Duet plasmid after truncation of the mitochondrial targeting sequence and the full transmembrane helix coding region (residues 30–81) or only a hydrophobic segment (residues 55–64), downstream to a N-terminal TwinStrep-3C tag. For protein expression, the plasmids were transformed to an *Escherichia coli* BL21 strain. Single colonies isolated from LB-Amp plates (lysogeny-broth, 100 µg/mL ampicillin) were grown at 37 °C in LB-Amp liquid media to an OD_{600} of 0.5–0.7, induced with IPTG to a final concentration of 0.5 mM, and supplemented with $Fe_2(SO_4)_3$ and L-Cysteine to a final concentration of 0.5 mM. The cells were further grown for 18 h at 16 °C. Cells were harvested and flash frozen for storage at −80 °C.

For the growth assays shown in Figs. 2D and 4E and Appendix Fig. S6A, the upstream UTR region (250 bp) of the yBcs1 gene was cloned to a YCplac111 vector (YCplac111-P.Bcs1). N-terminal

FLAG-tagged yBcs1 (1-456) was cloned downstream, and selected mutations were introduced by site-directed mutagenesis based on standard PCR techniques using Phusion polymerase (NEB). The mutations were confirmed by sequencing. The constructs were transformed as described above to the *bcs1Δ* strain. A single colony was grown in SDC-LEU-Glucose to an OD_{600} of 1.5–2.0 and then diluted to 1.0 with fresh media. Serial 10-fold dilutions were spotted on YP plates containing either 2% glucose or 2% glycerol and on SDC-LEU-Glucose plates. The plates were incubated for 2–3 days at 30 °C, or at 37 °C where indicated.

For the growth assays shown in Fig. 2E and Appendix Fig. S6B, the upstream UTR region (322 bp) and the mitochondrial targeting sequence (1–30) of the yRip1 gene were cloned to a YCplac111 vector (YCplac111-P.Rip1). yRip1 (31–215) was cloned downstream and selected mutations were introduced by site-directed mutagenesis based on standard PCR techniques using Phusion polymerase (NEB). The mutations were confirmed by sequencing. The constructs were transformed as described above to a *rip1Δ* strain. A single colony was grown in SDC-LEU-Glucose to an OD_{600} of 1.5–2.0 and then diluted to 1.0 with fresh media. Serial 10-fold dilutions were spotted on YP plates containing either 2% glucose or 2% glycerol and on SDC-LEU-Glucose plates. The plates were incubated for 2–3 days at 30 °C, or at 37 °C where indicated. Contrast enhancement of the digital images was carried out with ImageJ (Fiji) (Schindelin et al, 2012) only for visualization purposes (see Source Data for Original Images).

Protein expression and purification

For purification of Bcs1, pelleted yeast cells were thawed and resuspended in lysis buffer (2 mL/g pellet; 0.65 M Sorbitol, 100 mM Tris pH 8.0, 5 mM EDTA pH 8.0, 5 mM aminocaproic acid, 0.2% BSA, 1 mM PMFS). Cells were lysed after two passages in a Cell Disruptor (Constant Systems Ltd.) at 2500 bar. Supernatants were clarified by centrifugation, 30 min at 3000 g. The membrane fraction was separated by ultracentrifugation, 1 h at 120,000 × *g*. Crude membranes were washed once in SW buffer (0.65 M Sorbitol, 100 mM Tris pH 7.5, 5 mM aminocaproic acid, 1 mM PMFS) and centrifuged for further 30 min at 120,000 × *g*. The pelleted membranes were then resuspended in SH buffer (0,65 M Sorbitol, 10 mM HEPES pH 7.5), aliquoted to an approximate total protein concentration of 10 mg/mL, and flash frozen for storage at −80 °C. For solubilization, membranes were resuspended in solubilization buffer (30 mM HEPES pH 7.5, 150 mM potassium acetate, 3% digitonin) to a final protein concentration of 5 mg/mL. After 1 h incubation at 4 °C, the insoluble fraction was separated by ultracentrifugation for 30 min at 120,000 × *g*. The supernatants were incubated with pre-equilibrated (AP buffer: 30 mM HEPES pH 7.5, 150 mM KCl, 5% glycerol, 5 mM Imidazole, 0.1% digitonin) His cOmplete resin (Roche) for 2.5 h, 4 °C. They were subsequently washed with AP buffer supplemented with 50 mM imidazole and eluted with AP buffer supplemented with 250 mM imidazole. Selected fractions were pooled and concentrated in a 100 kDa cut-off Amicon (Merck). The concentrated sample was injected to a Superose 6 Increase 10/300 GL (Cytiva) column and run with SEC-GDN buffer (30 mM HEPES pH 7.5, 150 mM KCl, 5% glycerol, 0.024% glyco-diosgenin (GDN)). Final fractions were concentrated as described before and flash frozen or used immediately for downstream experiments.

For the purification of Rip1 constructs, frozen pellets were thawed and resuspended in lysis buffer (10 mL/g pellet; 100 mM Tris pH 8.0, 150 mM NaCl, 10% glycerol, 1 mM PMFS, 1x cOmplete protease inhibitor cocktail (Roche)). Cells were lysed after two passages in a Cell Disruptor (Constant Systems Ltd.) at 1250 bar. Supernatants were clarified by centrifugation, 15 min at 3000 × *g* followed by 25 min at 36,000 × *g*. The supernatant was passed twice through a bed of pre-equilibrated (Strep-AP buffer: 25 mM HEPES pH 7.5, 150 mM NaCl, 10% glycerol) Strep-Tactin® XT 4Flow® (iba) resin. The resin was washed with Strep-AP, and the protein was eluted on the same buffer supplemented with 50 mM Biotin. The fractions were incubated with 3C-protease for 90 min and then concentrated in a 3 kDa cut-off Amicon for injection to a Superdex 200 Increase 10/300 GL (Cytiva) column, run with SEC buffer (30 mM HEPES pH 7.5, 150 mM KCl, 5% glycerol). Selected fractions were concentrated as before and flash frozen or used immediately.

ATPase activity assay

Bcs1 ATPase activity was measured using the NADH (nicotinamide adenine dinucleotide)-coupled assay. Bcs1 (heptamer) in a final concentration of 65 nM (heptamer) was incubated in absence or in presence of 163 nM, 325 nM or 650 nM Rip1-TM substrate for 10 min at 25 °C in assay buffer (25 mM HEPES pH 7.5, 50 mM KCl, 2 mM $MgCl_2$, 0.024% GDN, 0.1 mg/mL BSA). After incubation, reactions were mixed with phosphoenolpyruvate 0.5 mM, NADH 0.1 mM, lactate dehydrogenase-pyruvate kinase (Merck) 25 U/mL and ATP 1 mM, to a final volume of 50 µL. Reactions were incubated at 30 °C, and fluorescence decay was monitored at 454 nm for 60 min in a Tecan Infinite M1000 plate reader. ATP concentration was calculated by interpolation in an ADP standard curve in the range 10–100 µM.

BN-PAGE

Samples for BN-PAGE were prepared as follows. Bcs1 and Rip1 concentration was quantified using a Pierce™ BCA Protein Assay kit (Thermo Fisher Scientific). In total, 30 pmol of Bcs1 (heptamer) were diluted in BN-buffer (15 mM HEPES pH 7.5, 30 mM KCl, 5% glycerol, 0.1% digitonin) and incubated with varying quantities of Rip1 substrate (from 0 up to tenfold excess) in presence or absence of nucleotides and $MgCl_2$ (1 mM ADP, ATP or ATPγS, 2 mM $MgCl_2$). The final reaction volume was 30 µL. Depending on the experiment, the sample was incubated with substrate 10 min at 25 °C followed by the addition of the respective nucleotide and further incubated 10 min at 25 °C, or vice versa. The samples were mixed with NativePAGE™ Sample buffer (4X) and loaded to a NativePAGE™ gel (Thermo Fisher Scientific). Contrast enhancement of the digital images was carried out with ImageJ (Fiji) (Schindelin et al, 2012) only for visualization purposes (see Source Data for Original Images).

Cryo-EM sample preparation and data collection

For the Bcs1-Apo-Rip1-FeS or Rip1-TM sample, 30 pmol of Bcs1 (heptamer) were incubated with a 10-fold excess of substrate for 20 min at 25 °C in BN-buffer. For the Bcs1-ATPγS sample, Bcs1 was incubated in BN-buffer supplemented with 2 mM ATPγS and

2.5 mM $MgCl_2$, for 20 min at 25 °C. For the Bcs1-ATPγS-Rip1-FeS sample, Bcs1 was first incubated with substrate in BN-buffer supplemented with 2.5 mM $MgCl_2$ for 10 min at 25 °C, followed by ATPγS addition to a final concentration of 2 mM and incubated for an additional 10 min. After incubation, all samples were kept on ice until plunge-freezing. A drop of 3.5 µL was applied onto glow-discharged Quantifoil Au 300 mesh R2/2 grids with an additional 3 nm layer of carbon. After incubation for 45 s, the grids were blotted for 3 s and plunge-frozen in liquid ethane, using a Vitrobot Mark IV (Thermo Fisher Scientific). Data collection was performed at 300 keV using a Titan Krios microscope equipped with a Falcon 4i direct electron detector and a SelectrisX Energy Filter (all Thermo Fisher Scientific) at a physical pixel size of 0.727 Å. Dose-fractioned movies were collected in a defocus range from −0.5 to 3.0 µm with a total dose of 60 e- per $Å^2$ and fractionated in 60 frames to obtain a total dose of 1 e- per $Å^2$ per frame.

Data processing

Gain correction, movie alignment, and summation of movie frames were performed using MotionCor2 (Zheng et al, 2017). Further processing was carried out in CryoSPARC v4.4 (Punjani et al, 2017). CTF parameters for the micrographs were estimated using CTFFIND4 (Rohou and Grigorieff, 2015) (Bcs1-Apo-Rip1-FeS) or the Patch CTF Estimation job (Bcs1-Apo-Rip1-TM, Bcs1-ATPγS1/2, Bcs1-ATPγS2-Rip1-FeS).

Bcs1-Apo-Rip1-FeS

Particle picking on 6044 micrographs was carried out by running a Blob Picker job, resulting in 800,580 particles. The particle set was extracted using a box size of 360 pixels, binned four times. 2D classification allowed the selection of a subset of 68,540 particles, which was used to train TOPAZ (Bepler et al, 2019). After TOPAZ particle picking, a set of 667,578 particles was selected and further cleaned by one round of 2D classification. In all, 546,208 particles belonging to good classes were used to generate an ab initio model, using the Ab-Initio Reconstruction job with three classes. After an initial round of heterogeneous refinement, the map with best features was employed to generate a consensus refinement of the entire particle set. Particles were then further classified in a second round of heterogeneous refinement, where a class with 320,760 particles displayed the best substrate density and was thereby selected for downstream refinement. Particles were re-extracted, two times binned, and sorted by unmasked 3D classification with 4 classes. In total, 309,698 particles from the best class were used in a focused 3D-classification job with three classes, where a circular mask covered the substrate density. A final subset of 106,497 particles was re-extracted and refined by a non-uniform refinement job, without imposing symmetry (C1), to a final resolution of 3.56 Å.

Bcs1-Apo-Rip1-TM

A total of 1,415,540 particles were picked by a blob picker job on 13,310 micrographs. After extraction with a box size of 360 pixels, binned four times, the set was cleaned by successive 2D classification rounds, resulting in a subset of 119,984 particles, subsequently used for TOPAZ training. From TOPAZ picks, a total of 460,919 particles were cleaned with an additional 2D classification run and refined by a heterogeneous refinement job with 4 classes, using the Bcs1-Apo-Rip1-FeS map as reference. A class of 149,392 particles displaying the best resolved features was run in a second round of heterogeneous refinement. After the refinement, a set of 109,143 particles was re-extracted without binning, and a focused 3D classification with a mask in the substrate density was performed. A final subset of 57,257 particles was refined by a non-uniform refinement job (C1 symmetry) to a final resolution of 3.46 Å.

Bcs1-ATPγS1/2

An initial set of 877,660 particles picked with Blob Picker from 8825 micrographs was used to generate templates for template picking. A set of 367,217 particles was obtained, extracted with a box size of 360 pixels, binned two times, and cleaned by successive rounds of 2D classification. 165,566 particles were selected, and a consensus map was obtained by homogeneous refinement. Multiple rounds of heterogeneous refinement with 4 classes were run to improve the quality of the map. A set of 234,802 particles belonging to a class with well-resolved features was obtained and refined by non-uniform refinement (C1 symmetry). 3D classification with two classes resulted in a class of 142,262 (61%, state S1) and a class of 92,540 (39%, state S2) differing by a rotation of 6° on the middle domain of Bcs1 and a worse resolved transmembrane region (state S2). The classes were re-extracted without binning and further refined by non-uniform refinement, enforcing C1 or C7 symmetry, to a final resolution of 2.92 Å (state S1–C1), 2.58 Å (state S1–C7), 3.09 Å (state S2–C1), and 2.74 Å (state S2–C7).

Bcs1-ATPγS2-Rip1-FeS

From a subset of 2024 micrographs, 874,465 particles were picked using blob picker followed by template picker, extracted with a box size of 360 pixels, binned two times, and processed by successive rounds of 2D classification. 165,865 particles belonging to good classes were used to generate an ab initio model, using the Ab-Initio Reconstruction job. The particles were also used as templates for particle picking and 1,415,352 total particles were obtained from the full data set (18,385 micrographs). The map obtained was refined by non-uniform refinement (C1) and a heterogeneous refinement with three classes was performed to sort for overall structural heterogeneity. A class with the best structural features, containing 567,113 was re-extracted, two times binned and refined by non-uniform refinement. The refined map was used as input for a focused 3D-classification job, with a mask on the inner membrane vestibule. One class of 80,299 particles with strong density was selected. To confirm that the density was not an artifact from the processing methodology, the particles were input to an ab initio reconstruction job with two classes. This resulted in a junk class and a well-resolved class of 70,453 particles. These particles were re-extracted without binning and refined by non-uniform refinement (C1) to a final average resolution of 3.07 Å.

Model building

A model of Bcs1 from the AlphaFold database (http://alphafold.ebi.ac.uk) was used to build the Bcs1-Apo-Rip1-FeS and Bcs1-Apo-Rip1-TM models. To model the substrate chain, the residues 82-215 of Rip1 from a model of the yeast cytochrome bc1 complex (PDB accession number 1KB9) were used. For the ATPγS models, an initial model was obtained using Modelangelo (Jamali

et al, 2024) on the Bcs1-ATPγS1 (C7) map. Real-space refinement was performed manually in COOT (Emsley and Cowtan, 2004). Multiple rounds of density fitting, and refinement were subsequently performed using ISOLDE (Croll, 2018) and real-space refinement in Phenix (Adams et al, 2010) . MolProbity (Chen et al, 2010) was used for model validation in Phenix. Docking and visualization of maps and models was done in ChimeraX (Goddard et al, 2018).

Data availability

Cryo-EM density maps and atomic models have been deposited in the Electron Microscopy Data Bank (EMDB https://www.ebi.ac.uk/emdb/) and Protein Data Bank (PDB https://www.rcsb.org/) data bases under the accession codes EMD-51561 (Bcs1-Apo-Rip1-FeS), EMD-51537 and PDB:9GS2 (Bcs1-Apo-Rip1-TM), EMD-51552 and PDB:9GSN (Bcs1-ATPγS1 C7), EMD-53185 (Bcs1-ATPγS1 C1), EMD-51605 and PDB:9GU9 (Bcs1-ATPγS2 C7), EMD-53189 (Bcs1-ATPγS2 C1), and EMD-51562 (Bcs1-ATPγS2-Rip1-FeS).

The source data of this paper are collected in the following database record: biostudies:S-SCDT-10_1038-S44318-025-00459-4.

Expanded view data, supplementary information, appendices are available for this paper at https://doi.org/10.1038/s44318-025-00459-4.

Peer review information

A peer review file is available at https://doi.org/10.1038/s44318-025-00459-4

References

Adams PD, Afonine PV, Bunkóczi G, Chen VB, Davis IW, Echols N, Headd JJ, Hung LW, Kapral GJ, Grosse-Kunstleve RW et al (2010) PHENIX: a comprehensive Python-based system for macromolecular structure solution. Acta Crystallogr D Biol Crystallogr 66:213–221

Al Qurashi M, Mustafa A, Aga SS, Ahmad A, El-Farra A, Shawli A, Al Hindi M, Hasosah M (2022) Clinical and diagnostic characteristics of complex III mitopathy due to novel BCS1L gene mutation in a Saudi patient. BMC Med Genomics 15:63

Aldridge C, Spence E, Kirkilionis MA, Frigerio L, Robinson C (2008) Tat-dependent targeting of Rieske iron-sulphur proteins to both the plasma and thylakoid membranes in the cyanobacterium Synechocystis PCC6803. Mol Microbiol 70:140–150

Bachmann J, Bauer B, Zwicker K, Ludwig B, Anderka O (2006) The Rieske protein from Paracoccus denitrificans is inserted into the cytoplasmic membrane by the twin-arginine translocase. FEBS J 273:4817–4830

Bepler T, Morin A, Rapp M, Brasch J, Shapiro L, Noble AJ, Berger B (2019) Positive-unlabeled convolutional neural networks for particle picking in cryo-electron micrographs. Nat Methods 16:1153–1160

Berks BC (1996) A common export pathway for proteins binding complex redox cofactors? Mol Microbiol 22:393–404

Chen VB, Arendall WB, Headd JJ, Keedy DA, Immormino RM, Kapral GJ, Murray LW, Richardson JS, Richardson DC (2010) MolProbity: all-atom structure validation for macromolecular crystallography. Acta Crystallogr D Biol Crystallogr 66:12–21

Conte A, Papa B, Ferramosca A, Zara V (2015) The dimerization of the yeast cytochrome bc1 complex is an early event and is independent of Rip1. Biochim Biophys Acta 1853:987–995

Crofts AR (2004) The cytochrome bc1 complex: function in the context of structure. Annu Rev Physiol 66:689–733

Croll, TI (2018) ISOLDE: a physically realistic environment for model building into low-resolution electron-density maps. Acta Crystallogr D Struct Biol, 74:519–530

Cruciat CM, Brunner S, Baumann F, Neupert W, Stuart RA (2000) The cytochrome bc1 and cytochrome c oxidase complexes associate to form a single supracomplex in yeast mitochondria. J Biol Chem 275:18093–18098

Cui TZ, Smith PM, Fox JL, Khalimonchuk O, Winge DR (2012) Late-stage maturation of the Rieske Fe/S protein: Mzm1 stabilizes Rip1 but does not facilitate its translocation by the AAA ATPase Bcs1. Mol Cell Biol 32:4400–4409

De Buck E, Vranckx L, Meyen E, Maes L, Vandersmissen L, Anné J, Lammertyn E (2007) The twin-arginine translocation pathway is necessary for correct membrane insertion of the Rieske Fe/S protein in Legionella pneumophila. FEBS Lett 581:259–264

Emsley P, Cowtan K (2004) Coot: model-building tools for molecular graphics. Acta Crystallogr D Biol Crystallogr 60:2126–2132

Frain KM, Robinson C, van Dijl JM (2019) Transport of folded proteins by the Tat system. Protein J 38:377–388

Frickey T, Lupas AN (2004) Phylogenetic analysis of AAA proteins. J Struct Biol 146:2–10

Goddard TD, Huang CC, Meng EC, Pettersen EF, Couch GS, Morris JH, Ferrin TE (2018) UCSF ChimeraX: meeting modern challenges in visualization and analysis. Protein Sci 27:14–25

Graham LA, Trumpower BL (1991) Mutational analysis of the mitochondrial Rieske iron-sulfur protein of Saccharomyces cerevisiae. III. Import, protease processing, and assembly into the cytochrome bc1 complex of iron-sulfur protein lacking the iron-sulfur cluster. J Biol Chem 266:22485–22492

Harnisch U, Weiss H, Sebald W (1985) The primary structure of the iron-sulfur subunit of ubiquinol-cytochrome c reductase from Neurospora, determined by cDNA and gene sequencing. Eur J Biochem 149:95–99

Hartl FU, Schmidt B, Wachter E, Weiss H, Neupert W (1986) Transport into mitochondria and intramitochondrial sorting of the Fe/S protein of ubiquinol-cytochrome c reductase. Cell 47:939–951

Jamali K, Käll L, Zhang R, Brown A, Kimanius D, Scheres SHW (2024) Automated model building and protein identification in cryo-EM maps. Nature 628:450–457

Kater L, Wagener N, Berninghausen O, Becker T, Neupert W, Beckmann R (2020) Structure of the Bcs1 AAA-ATPase suggests an airlock-like translocation mechanism for folded proteins. Nat Struct Mol Biol 27:142–149

Kispal G, Csere P, Prohl C, Lill R (1999) The mitochondrial proteins Atm1p and Nfs1p are essential for biogenesis of cytosolic Fe/S proteins. EMBO J 18:3981–3989

Madeira F, Madhusoodanan N, Lee J, Eusebi A, Niewielska A, Tivey ARN, Lopez R, Butcher S (2024) The EMBL-EBI Job Dispatcher sequence analysis tools framework in 2024. Nucleic Acids Res 52:W521–W525

Palmer T, Stansfeld PJ (2020) Targeting of proteins to the twin-arginine translocation pathway. Mol Microbiol 113:861–871

Pan Y, Zhan J, Jiang Y, Xia D, Scheuring S (2023) A concerted ATPase cycle of the protein transporter AAA-ATPase Bcs1. Nat Commun 14:6369

Punjani A, Rubinstein JL, Fleet DJ, Brubaker MA (2017) cryoSPARC: algorithms for rapid unsupervised cryo-EM structure determination. Nat Methods 14:290–296

Ramabadran RS, Japa S, Beattie DS (1997) Assembly of deletion mutants of the Rieske iron-sulfur protein into the cytochrome bc1 complex of yeast mitochondria. J Bioenerg Biomembr 29:45–54

Rapoport TA, Li L, Park E (2017) Structural and mechanistic insights into protein translocation. Annu Rev Cell Dev Biol 33:369–390

Rieske JS, Zaugg WS, Hansen RE (1964) Studies on the electron transfer system. LIX. Distribution of iron and of the component giving an electron paramagnetic resonance signal at G = 1.90 in subfractions of complex 3. J Biol Chem 239:3023–3030

Rohou A, Grigorieff N (2015) CTFFIND4: Fast and accurate defocus estimation from electron micrographs. J Struct Biol 192:216–221

Santini CL, Ize B, Chanal A, Müller M, Giordano G, Wu LF (1998) A novel sec-independent periplasmic protein translocation pathway in *Escherichia coli*. EMBO J 17:101–112

Sargent F, Bogsch EG, Stanley NR, Wexler M, Robinson C, Berks BC, Palmer T (1998) Overlapping functions of components of a bacterial Sec-independent protein export pathway. EMBO J 17:3640–3650

Schindelin J, Arganda-Carreras I, Frise E, Kaynig V, Longair M, Pietzsch T, Preibisch S, Rueden C, Saalfeld S, Schmid B et al (2012) Fiji: an open-source platform for biological-image analysis. Nat Methods 9:676–682

Stephan K, Ott M (2020) Timing of dimerization of the bc(1) complex during mitochondrial respiratory chain assembly. Biochim Biophys Acta Bioenerg 1861:148177

Tang WK, Borgnia MJ, Hsu AL, Esser L, Fox T, de Val N, Xia D (2020) Structures of AAA protein translocase Bcs1 suggest translocation mechanism of a folded protein. Nat Struct Mol Biol 27:202–209

Thomas BJ, Rothstein R (1989) Elevated recombination rates in transcriptionally active DNA. Cell 56:619–630

van Loon AP, Brändli AW, Pesold-Hurt B, Blank D, Schatz G (1987) Transport of proteins to the mitochondrial intermembrane space: the 'matrix-targeting' and the 'sorting' domains in the cytochrome c1 presequence. EMBO J 6:2433–2439

Wagener N, Ackermann M, Funes S, Neupert W (2011) A pathway of protein translocation in mitochondria mediated by the AAA-ATPase Bcs1. Mol Cell 44:191–202

Wagener N, Neupert W (2012) Bcs1, a AAA protein of the mitochondria with a role in the biogenesis of the respiratory chain. J Struct Biol 179: 121–125

Waterhouse AM, Procter JB, Martin DM, Clamp M, Barton GJ (2009) Jalview Version 2—a multiple sequence alignment editor and analysis workbench. Bioinformatics 25:1189–1191

Wiedemann N, Pfanner N (2017) Mitochondrial machineries for protein import and assembly. Annu Rev Biochem 86:685–714

Xia D, Esser L, Tang WK, Zhou F, Zhou Y, Yu L, Yu CA (2013) Structural analysis of cytochrome bc1 complexes: implications to the mechanism of function. Biochim Biophys Acta 1827:1278–1294

Zara V, Conte L, Trumpower BL (2009) Evidence that the assembly of the yeast cytochrome bc1 complex involves the formation of a large core structure in the inner mitochondrial membrane. FEBS J 276:1900–1914

Zerbes RM, Colina-Tenorio L, Bohnert M, von der Malsburg K, Peikert CD, Mehnert CS, Perschil I, Klar RFU, de Boer R, Kram A et al (2025) Coordination of cytochrome bc1 complex assembly at MICOS. EMBO Rep 26:353–384

Zhan J, Zeher A, Huang R, Tang WK, Jenkins LM, Xia D (2024) Conformations of Bcs1L undergoing ATP hydrolysis suggest a concerted translocation mechanism for folded iron-sulfur protein substrate. Nat Commun 15:4655

Zheng SQ, Palovcak E, Armache JP, Verba KA, Cheng Y, Agard DA (2017) MotionCor2: anisotropic correction of beam-induced motion for improved cryo-electron microscopy. Nat Methods 14:331–332

Acknowledgements

We thank Susanne Rieder and Charlotte Ungewickell for assistance with cryo-EM sample handling and data collection, Mariia Likhodeeva and Prof. Dr. Karl-Peter Hopfner (LMU, Gene Center Munich) for support with ATPase activity measurements, Dr. Dejana Mokranjac (LMU, BioCenter) and the members of the MitoClub for critical comments and suggestions, Dr. Birgitta Beatrix and Dr. Nives Ivić for their support with heterologous protein expression. This work was supported by funding from the German Research Foundation (Deutsche Forschungsgemeinschaft DFG; grant Nr. 510674444 to RB) and the European Research Council (ERC, Advanced Grant Nr. ADG 885711 to RB).

Author contributions

Cristian Rosales-Hernandez: Conceptualization; Data curation; Formal analysis; Validation; Investigation; Visualization; Methodology; Writing—original draft; Writing—review and editing. **Matthias Thoms**: Methodology; Writing—review and editing. **Otto Berninghausen**: Data curation. **Thomas Becker**: Validation; Visualization; Methodology; Writing—original draft; Writing—review and editing. **Roland Beckmann**: Conceptualization; Supervision; Funding acquisition; Methodology; Writing—original draft; Project administration; Writing—review and editing.

Source data underlying figure panels in this paper may have individual authorship assigned. Where available, figure panel/source data authorship is listed in the following database record: biostudies:S-SCDT-10_1038-S44318-025-00459-4.

Funding

Open Access funding enabled and organized by Projekt DEAL.

Disclosure and competing interests statement

The authors declare no competing interests.

Expanded View Figures

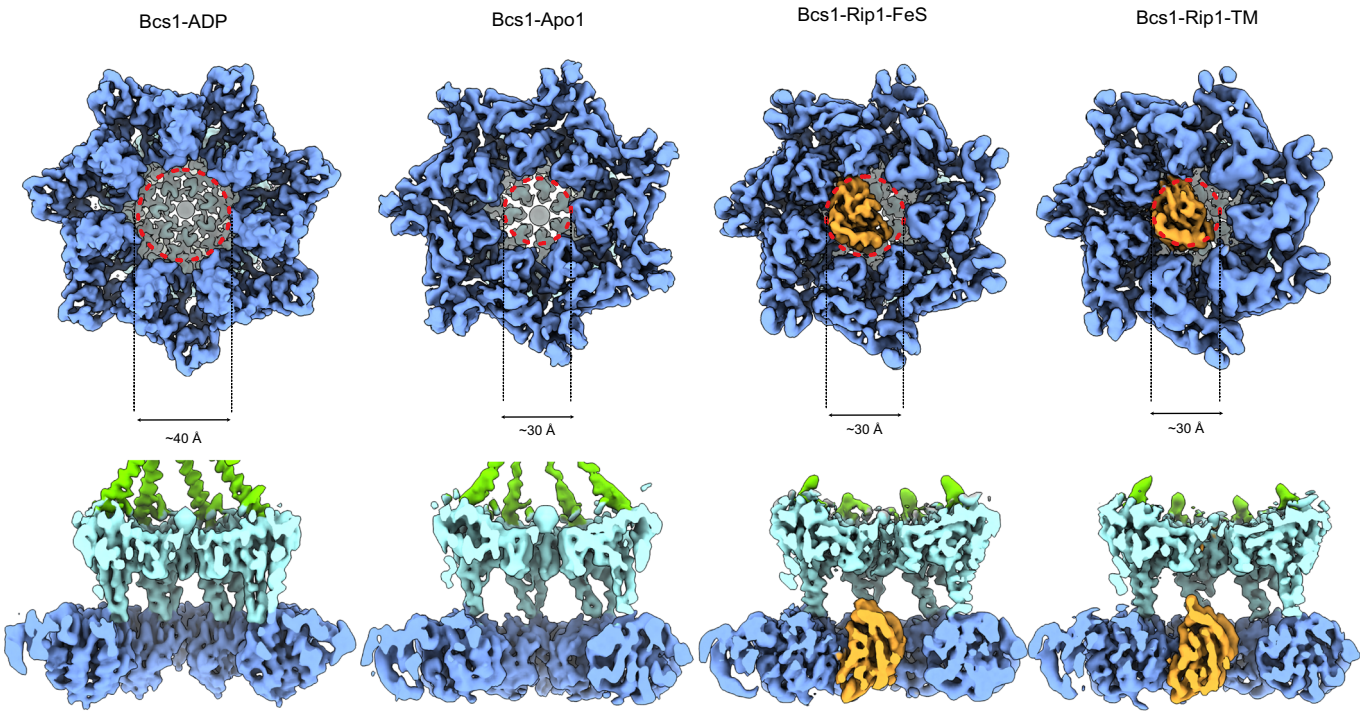

Figure EV1. Comparison of yeast Bcs1 structures in ADP and Apo1 states.

Cryo-EM structures shown at bottom (upper row) and side views (lower row) of Bcs1 in ADP state, Apo1 state (Kater et al, 2020) and bound to Rip1-FeS and Rip1-TM. Note that the Rip1-bound conformation of Bcs1 is Apo1. Red circles represent the diameter of the matrix vestibule.

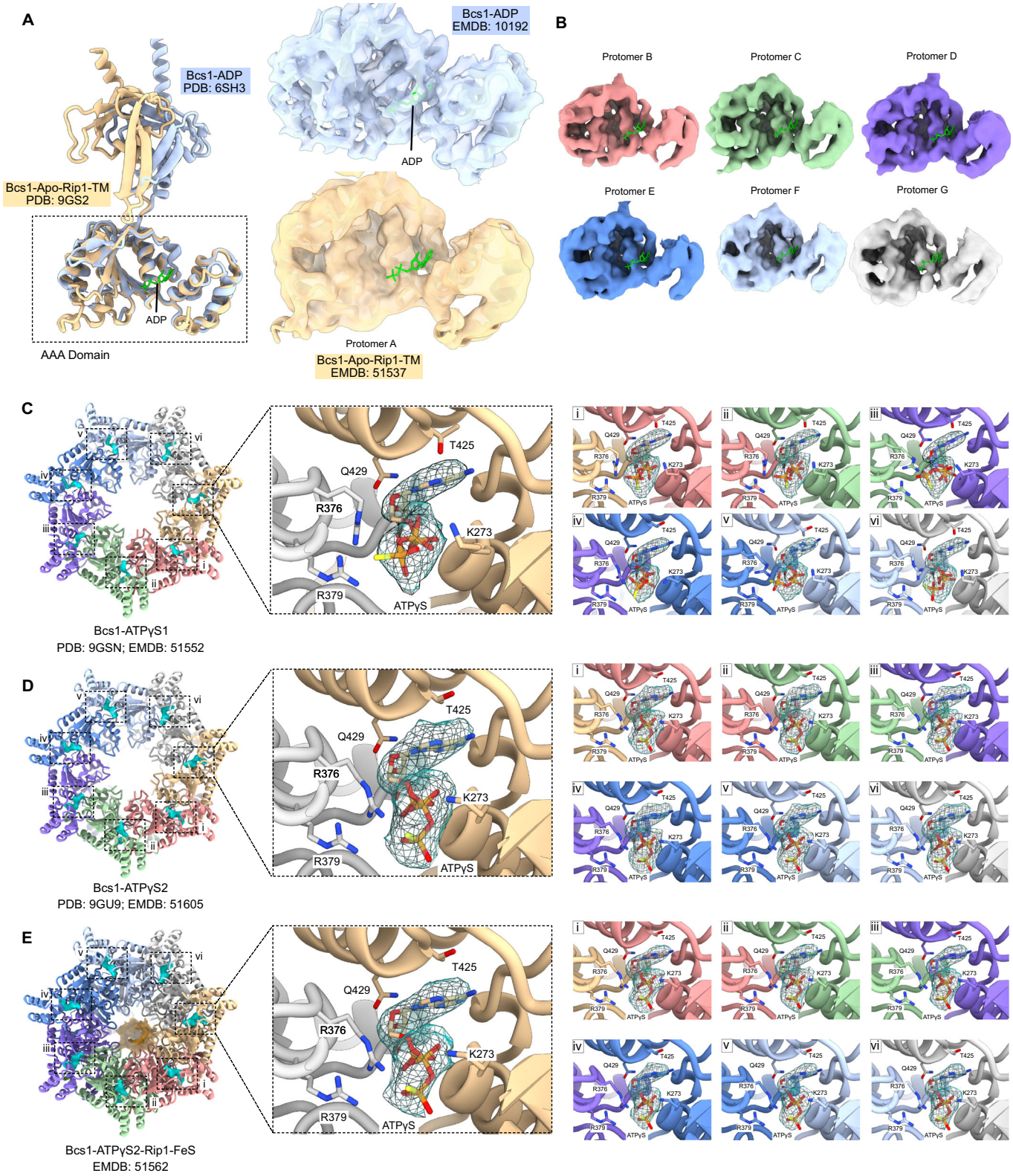

Figure EV2. ATP-binding pocket occupancy in the different Bcs1 states.

(**A**) Left panel: Alignment of the atomic models of Bcs1-ADP (PDB:6SH3, chain A) and Bcs1-Apo1-Rip1-TM (PDB:9GS2, chain A), displaying the relative position of ADP in the binding pocket. Right panel: Close-up view on the AAA domain of protomer A of Bcs1 and map superposition, highlighting the density of ADP found in the Bcs1-ADP state (top) and absent in Bcs1-Apo1-Rip1-TM (bottom). (**B**) ADP nucleotide model superimposed on the AAA domain density of the protomers B-G of Bcs1-Apo1-Rip1-TM. (**C**) Left panel: Bottom view of Bcs1- ATPγS1 and isolated ATPγS density. Highlighted in squares are a close-up view of the density in the protomer A and, in boxes i-vi, ATPγS densities for protomers B-G. Right panel: Close-up views of the enclosed regions i-vi. (**D**) same as in C for Bcs1- ATPγS2. (**E**) Same as in (**C**) for Bcs1- ATPγS2-Rip1-FeS.

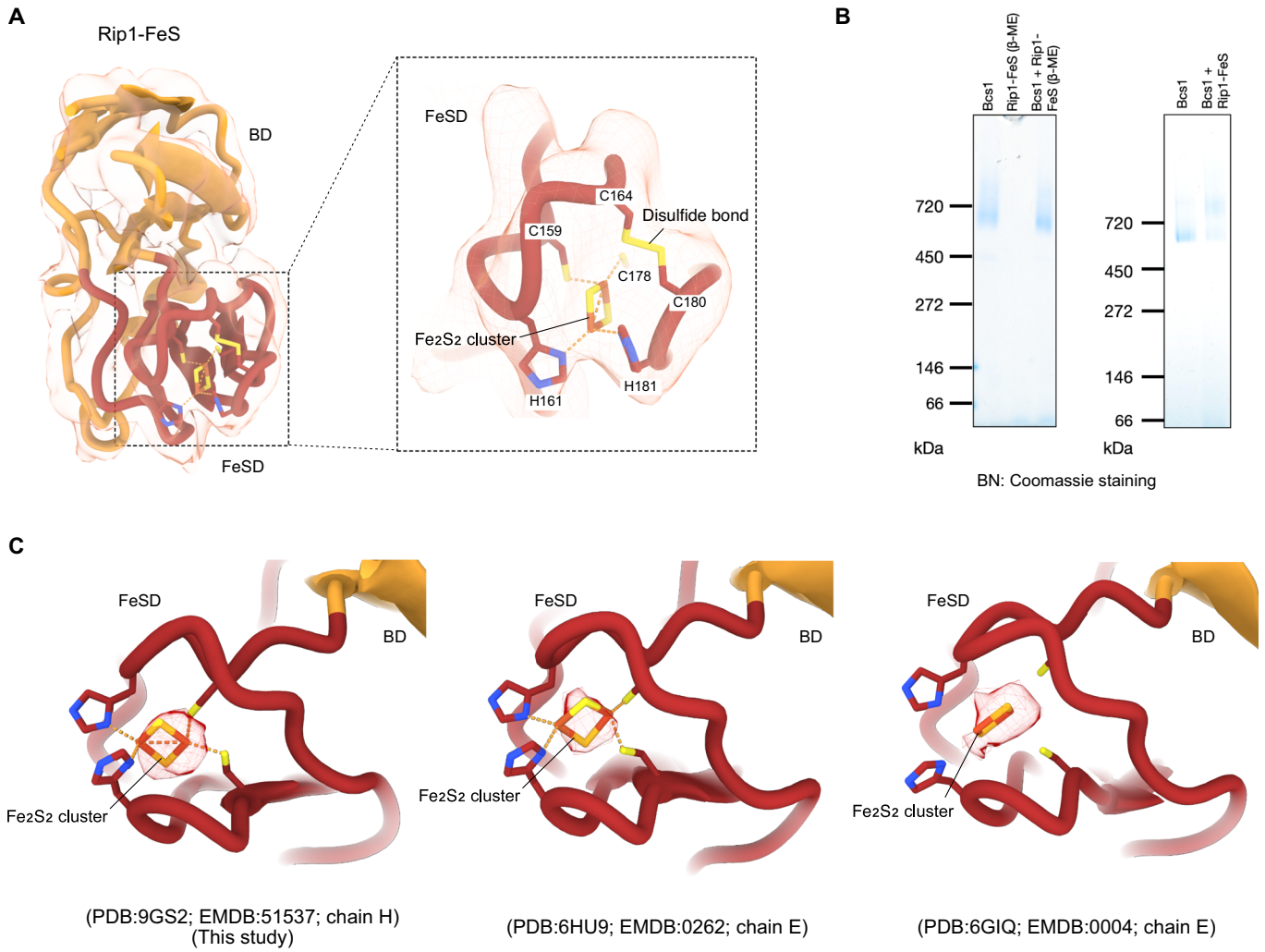

Figure EV3. Structural details of Rip1-FeS bound to Bcs1 in the Apo1 state.

(**A**) Left panel: Rip1-FeS atomic model fitted into density, highlighting the FeSD domain. Right panel: Close-up view on the FeSD displaying the residues involved in coordination of the 2Fe-2S and the disulfide bond between C164 and C180. The 2Fe-2S cluster is shown in a stick representation, where yellow sticks represent the sulphur atoms and red sticks represent the iron atoms. (**B**) Blue Native (BN) gel showing the effect of β-mercaptoethanol (β-ME) on the binding of purified Rip1-FeS to Bcs1 (left) compared to Rip1-FeS purified in the absence of β-ME. (**C**) Comparison of the Rip1-associated 2Fe-2S cluster densities from Bcs1-Apo1-Rip1-TM and active CIII complex Cryo-EM maps. Source data are available online for this figure.

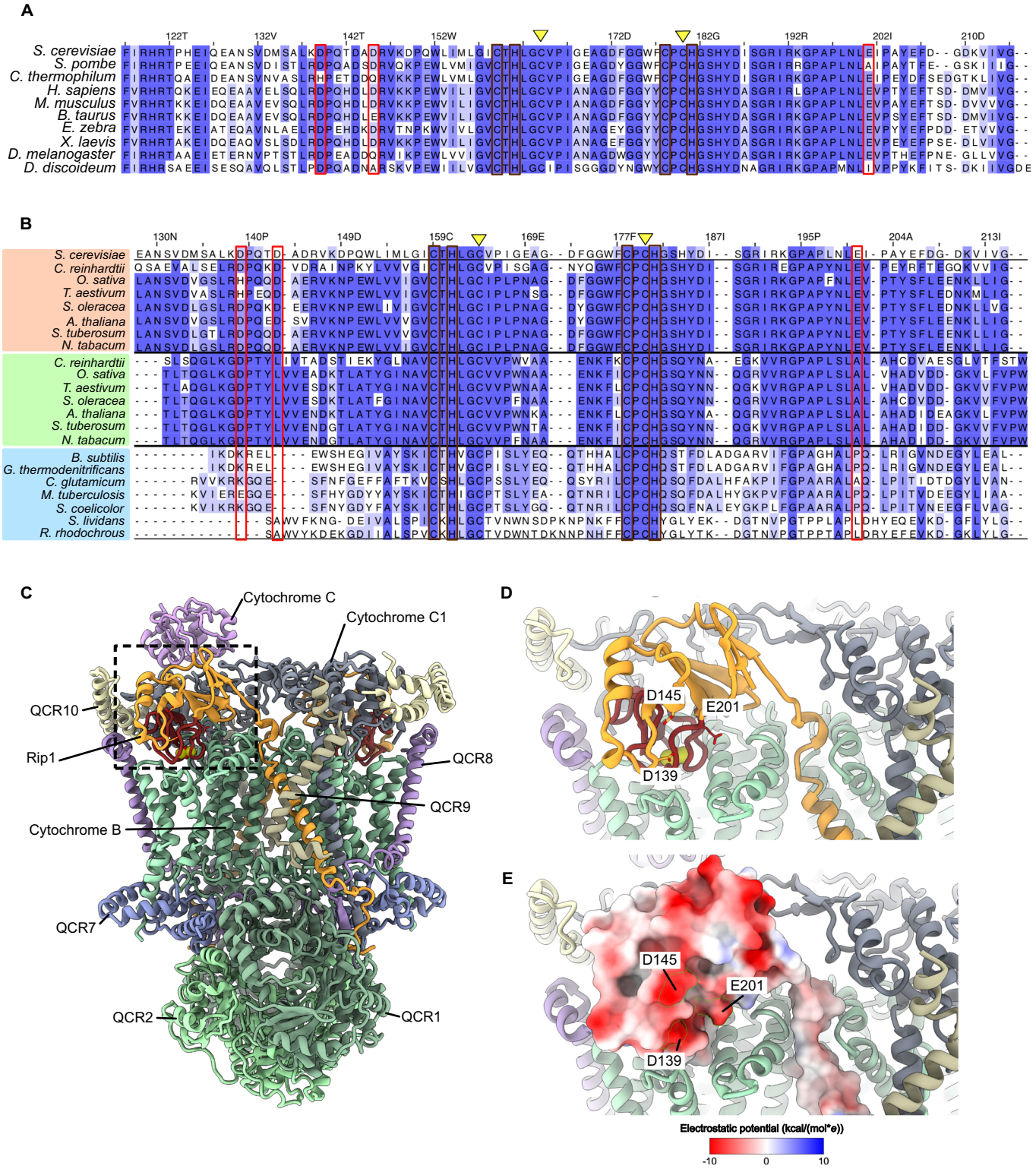

Figure EV4. Conserved residues on the Bcs1-interaction surface of Rip1.

(**A**) Multiple sequence alignment of the globular domain of Rip1 from selected species generated by Clustal Omega (Madeira et al, 2024) and displayed using Jalview (Waterhouse et al, 2009). Enclosed in red boxes are some of the negatively charged residues (D139, D145, E201) that interact with Bcs1 during translocation, in brown boxes are the residues responsible for the coordination of the 2Fe–2S cluster (C159, H161, C178, H181) and yellow arrows point to the residues that form a structurally relevant disulfide bond (C164, C180). The amino acids are colored according to their percentage of identity. (**B**) Multiple sequence alignment as in (**A**) but comparing the mitochondrial (pink box) Rip1 homolog of photosynthetic species with its chloroplast homolog petC in the same species (green box) and its prokaryotic homolog qcrA from prokaryote species (light blue box). (**C**) Structure of the fully assembled dimeric bc1 complex (PDB: 1KYO), highlighting the position of the globular domain of one of the two Rip1 subunits. (**D**) Close-up view on the enclosed region from (**C**), displaying Rip1 negatively charged amino acids. (**E**) Same view as in (**D**) but displaying the negatively charged electrostatic surface. The 2Fe–2S cluster is shown in a sphere representation, where yellow spheres represent the sulfur atoms and red spheres represent the iron atoms.

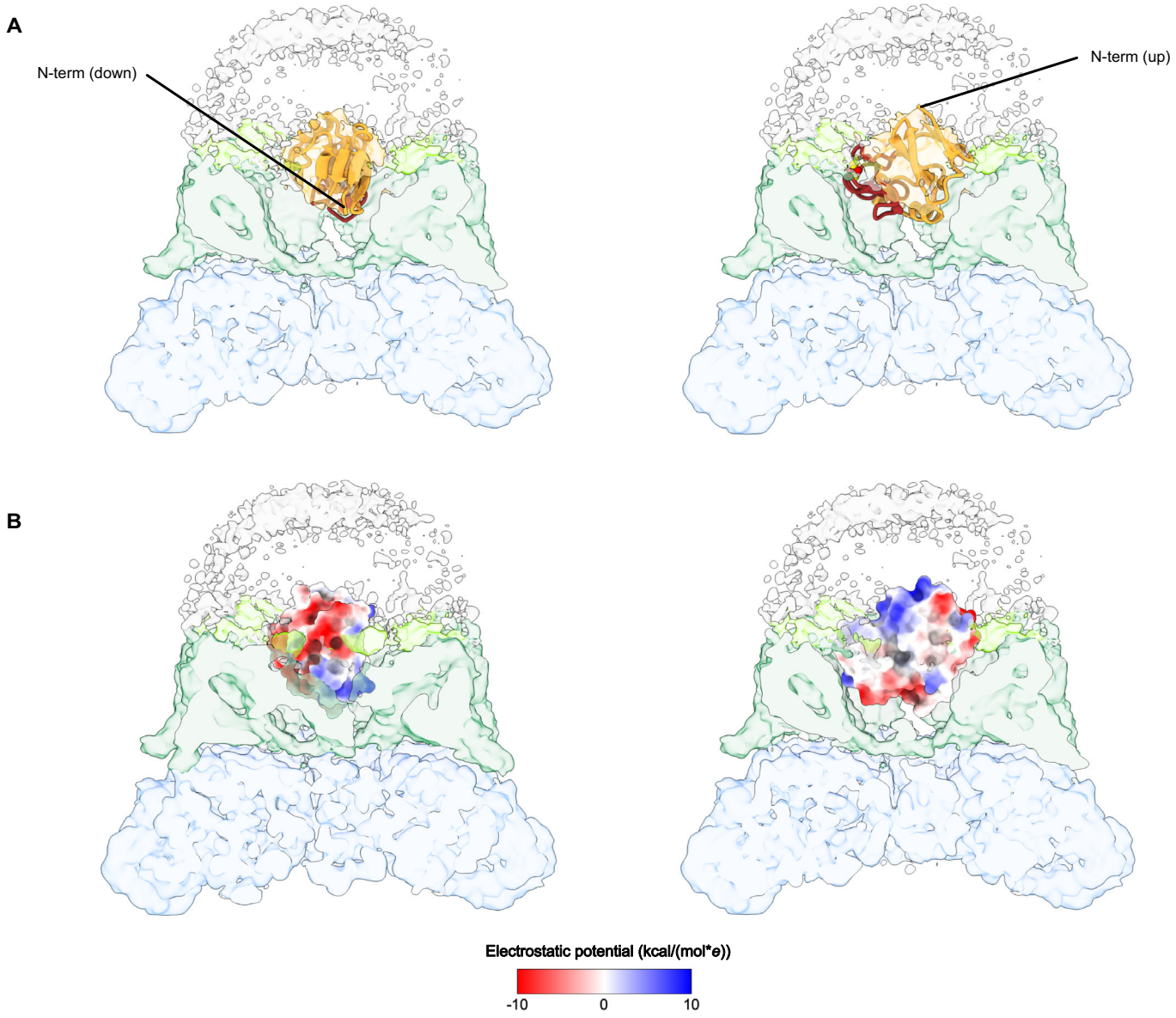

Figure EV5. Plausible orientations of Rip1-FeS in the translocation state.

(**A**) Cut side view of the atomic model of Rip1-FeS docked into the Bcs1-ATPγS2-Rip1-FeS map in an orientation that locates the N-terminal residues towards the mitochondrial matrix (left) or towards the IMS (right). The 2Fe–2S cluster is shown in a sphere representation, where yellow spheres represent the sulfur atoms and red spheres represent the iron atoms. (**B**) Electrostatic surface representation of the models displayed in (**A**).

2.3 Publication 3 | Assembly and the gating mechanism of the Pel exopolysaccharide export complex PelBC of Pseudomonas aeruginosa

nature communications

Article

https://doi.org/10.1038/s41467-025-60605-8

Assembly and the gating mechanism of the Pel exopolysaccharide export complex PelBC of Pseudomonas aeruginosa

Received: 25 November 2024

Accepted: 28 May 2025

Published online: 05 June 2025

Check for updates

Marius Benedens[1,5], Cristian Rosales-Hernandez[2,5], Sabine A. P. Straathof[3], Jennifer Loschwitz[1], Otto Berninghausen[2], Giovanni Maglia[3], Roland Beckmann[2] ✉ & Alexej Kedrov[1,4] ✉

The pathogen *Pseudomonas aeruginosa* enhances its virulence and antibiotic resistance upon formation of durable biofilms. The exopolysaccharides Pel, Psl and alginate essentially contribute to the biofilm matrix, but their secretion mechanisms are barely understood. Here, we reveal the architecture of the outer membrane complex PelBC for Pel export, where the essential periplasmic ring of twelve lipoproteins PelC is mounted on top of the nanodisc-embedded β-barrel PelB. The PelC assembly is stabilized by electrostatic contacts with the periplasmic rim of PelB and via the membrane-anchored acyl chains. The negatively charged interior of the PelB β-barrel forms a route for the cationic Pel exopolysaccharide. The β-barrel is sealed at the extracellular side, but molecular dynamic simulations suggest that the short loop Plug-S is sufficiently flexible to open a tunnel for the exopolysaccharide transport. This gating model is corroborated by single-channel conductivity measurements, where a deletion of Plug-S renders a constitutively open β-barrel. Our structural and functional analysis offers a comprehensive view on this pathogenicity-relevant complex and suggests the route taken by the exopolysaccharide at the final secretion step.

The Gram-negative bacterium *Pseudomonas aeruginosa* is an opportunistic human pathogen that accounts for nearly 20% of all nosocomial infections, being a major risk factor for immunocompromised patients and those with cystic fibrosis[1]. *P. aeruginosa* infections build up a burden for the healthcare systems worldwide due to the prolonged hospitalization period and the associated costs. The primary challenges to combat this versatile bacterium are its rapidly developing antibiotic resistance and formation of extensive durable biofilms, both in tissues upon host invasion and on diverse abiotic surfaces. Stability of the biofilms is mediated by the complex composition of the matrix, where the exopolysaccharides—alginate, Psl and Pel—serve to embed cells, ensure the mechanical strength of the matrix and provide attachment sites for secreted virulence factors[2]. Despite the highest biomedical relevance of the exopolysaccharides of *P. aeruginosa*, the understanding of the molecular mechanisms behind their secretion is poor.

Pel is the major constituent of *P. aeruginosa* pellicles, i.e., films formed at the water-air interface, and it plays a key role at early stages of the biofilm formation at solid surfaces. Pel has been recently identified in other β-, δ-, and γ-proteobacteria, but also several extremophiles and Gram-positive bacteria[3]. *P. aeruginosa* Pel is composed of α−1-4-linked N-acetyl-D-galactosamine residues, which are partially deacetylated in the periplasm, so the Pel exopolysaccharide acquires positive charge along the secretion pathway[4]. This charge is utilized

[1]Synthetic Membrane Systems, Institute of Biochemistry, Heinrich Heine University Düsseldorf, Düsseldorf, Germany. [2]Gene Center Munich, Ludwig Maximilian University of Munich, Munich, Germany. [3]Chemical Biology, Groningen Biomolecular Sciences & Biotechnology Institute, University of Groningen, Groningen, The Netherlands. [4]Interfaculty Center for Membrane Research, Heinrich Heine University Düsseldorf, Düsseldorf, Germany. [5]These authors contributed equally: Marius Benedens, Cristian Rosales-Hernandez. ✉e-mail: beckmann@genzentrum.lmu.de; kedrov@hhu.de

then to crosslink the extracellular DNA thus contributing to the matrix assembly[5]. Other roles of Pel involve stabilization of the adhesin CdrA and complementation for defects in the outer membrane, as deletion of the major structural protein OprF stimulates Pel accumulation at the cell surface (reviewed in ref. 2).

Secretion of Pel in the Gram-negative *P. aeruginosa* assumes the polysaccharide translocation across the inner and outer membranes (Fig. 1), and the genes essential for the process are encoded in a single *pelABCDEFG* operon. The polysaccharide elongation mediated by the glycosyltransferase PelF in the cytoplasm is coupled to the synthase-dependent translocation through the inner membrane complex of PelD, PelE, and PelG subunits, in a still unknown fashion (Fig. 1A)[6]. Upon crossing the periplasm, Pel is partially deacetylated by PelA and then translocated through the outer membrane via PelB[7]. PelB is composed of a C-terminal β-barrel preceded by the helical scaffold, built of multiple tetratricopeptide repeats (TPR). The length of the modelled scaffold exceeds 20 nm, thus being sufficiently long to span the periplasm (Supplementary Fig. 1A). Notably, the N-terminal end of PelB contains 22 apolar and aromatic residues, which may form a transmembrane helix within the inner membrane without a cleavage site for the signal peptidase (Supplementary Fig. 1B). Thus, PelB of *P. aeruginosa*, as well as its multiple homologs in other species, may physically bridge two membranes, with the TPR scaffold forming a passage for the polysaccharide across the periplasm.

The β-barrel of PelB is assumed to form a complex with PelC lipoproteins, a hallmark of the Pel system in Gram-negative bacteria. PelC is essential for the polysaccharide transport, and several mutations within PelC were identified which inhibited the biofilm formation, either via direct interactions with the polysaccharide or due to their involvement in the PelBC complex assembly[8]. The exact role of PelC in the exopolysaccharide translocation is not clear. A partial crystal structure of PelC from *Paraburkholderia phytofirmans* solved in the absence of the membrane and the lipid anchors revealed the protomers arranged into a dodecameric ring with a 3.2 nm-wide pore in the center[8], and the negative charge on the periplasm-facing side of PelC was suggested to assist in translocation of the cationic polysaccharide. The width of the PelC pore matches closely the diameter of the modelled PelB structure (Supplementary Fig. 2), and AlphaFold-based modelling of the complex in 1:12 stoichiometry provides a high-confidence assembly, where the TPR domain of PelB is placed within the central pore of the PelC ring[9]. However, models of a similar confidence could also be rendered at different stoichiometries, either

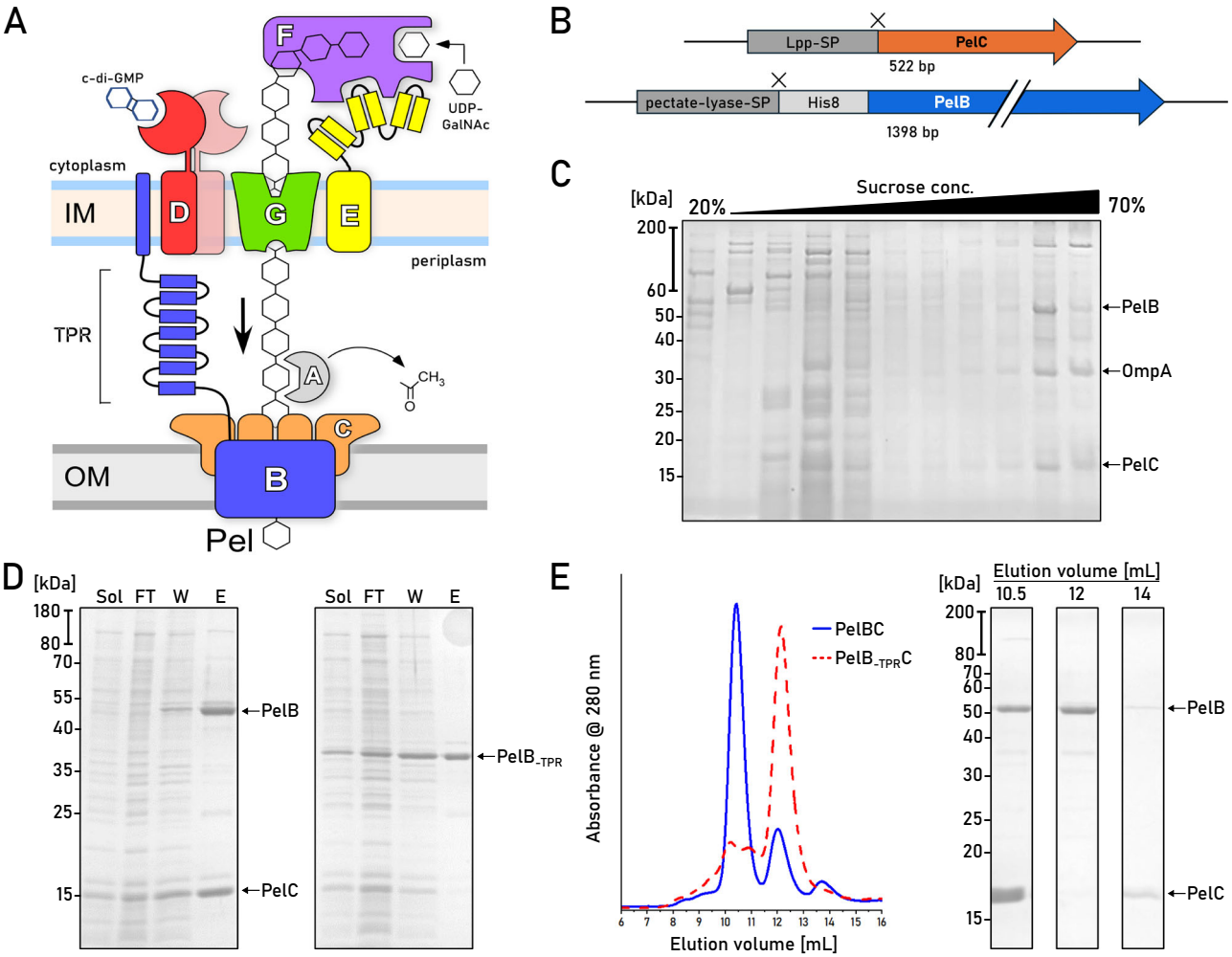

Fig. 1 | Isolation of the natively assembled PelBC complex of *P. aeruginosa*. **A** Putative organization of the synthesis/secretion machinery for the Pel exopolysaccharide in *P. aeruginosa*. **B** Gene constructs of PelB and PelC in the pETDuet-1 vector. Cleavage sites after the signal peptides (SP) of both proteins are indicated as "X". **C** SDS-PAGE of the membrane isolates after the sucrose gradient shows PelB and PelC co-occurring in late fractions characteristic for the outer membrane vesicles. A reference band for the outer membrane protein A (OmpA) is indicated. **D** SDS-PAGE of immobilized metal affinity chromatography on PelBC with His-tagged PelB variants, wild-type (left) and the truncated PelB lacking the periplasmic helical scaffold (right, $PelB_{-TPR}$). Loaded fractions: "Sol." - detergent-solubilized material; "FT" - flow-through; "W" - wash, "E" - elution. **E** Left: Size-exclusion chromatograms of the PelBC samples from (**D**). Right: SDS-PAGE of the major SEC fractions collected for the wild-type PelBC. Each biochemical experiment was at least repeated twice independently. Source data are provided as a Source Data file.

having less PelC subunits (ratio 1:11) or more (ratios 1:13 and above) (Supplementary Fig. 2). Since the assemblies of lipoproteins in solution and at the membrane interface may differ[10], visualizing the actual architecture of the PelBC complex remains an open task. The experimentally determined structure would also explain the functionally-defective PelC mutants, and potentially address protein:lipid interactions for the lipoproteins and the transmembrane β-barrel. Critically, the modelled PelB barrel does not manifest a substantially wide conduit at the extracellular side for the polysaccharide translocation, being sealed by several loops. Though the model may reflect the idle state of the channel, the experimental structure determination is required to understand the functional dynamics of the complex.

Here, we employed cryogenic electron microscopy (cryo-EM) to visualize the structure of the PelBC complex of *P. aeruginosa* in the lipid-based nanodiscs, reaching a final resolution of 2.5 Å. Next to the overall architecture of the asymmetric complex of 250 kDa, we report extensive protein:lipid interactions formed by both the lipoproteins and the β-barrel and discover that the periplasm-exposed helical domains of PelB and the highly conserved tryptophan of PelC are essential for the assembly of the complex. The acquired structure suggests the route of the exopolysaccharide across the channel, and it is further used to design single-channel conductivity experiments and computational simulations, which jointly provide first evidence for PelB conformational dynamics in the lipid membrane.

Results

Isolation and nanodisc reconstitution of the intact PelBC complex

To establish heterologous expression of the PelBC complex, both genes were cloned into pETDuet-1 vector under individual T7 promotors. To facilitate the efficient export of the synthesized proteins into the periplasm via the Sec machinery, the signal sequence of PelC was substituted with the signal sequence of Lpp, the highly abundant Braun's lipoprotein of *Escherichia coli*. PelB was expressed as the C-terminal fragment (residues 762–1193) containing three periplasmic TPR repeats and the transmembrane β-barrel, which were preceded with the conventional signal sequence of pectate lyase B of *Erwinia carotovora* and the octa-histidine tag (Fig. 1B). Based on the AlphaFold models (Supplementary Fig. 2), we assumed that the truncated periplasmic region of PelB would be sufficient to interact with the PelC subunits. Once expressed in *E. coli* C41(DE3) Δ*ompF* Δ*acrAB* strain[11], the protein localization to the outer membrane was validated by the ultracentrifugation in the sucrose density gradient: Both proteins appeared within the high-density fraction together with OmpA, an intrinsic marker for the outer membrane vesicles (Fig. 1C)[11].

Both PelB and PelC were extracted from the membranes with the mild non-ionic detergent DDM. IMAC based on the N-terminal histidine-tag of PelB resulted in co-purification of substantial amounts of PelC (Fig. 1D), suggesting that the proteins resided as a complex. The PelB-PelC isolates manifested three distinct peaks in size exclusion chromatography (SEC, Fig. 1E): The major peak contained both PelB and the excess of PelC and it was observed at 10.5 mL elution volume suggesting the molecular weight of ~300 kDa, while the downstream peaks at 12 mL and 14 mL contained PelB and PelC, respectively. The appearance of the tag-less free PelC subunits in the latter peak indicated partial disassembly of the detergent-solubilized complex after the IMAC stage. To prevent that, SEC-purified PelBC complexes were immediately reconstituted into nanodiscs in presence of POPC:POPG lipids (molar ratio 70:30). The chosen scaffold protein MSP1D1 builds nanodiscs of ~8 nm inner diameter[12] that should be sufficient to accommodate the β-barrel of PelB and the acyl chain anchors of PelC lipoproteins, assuming the ring-shaped assembly. SEC of PelBC-nanodiscs resulted in a major peak at ~10.5 mL where PelB, PelC, and MSP1D1 were found, followed by minor amounts of PelB-only nanodiscs (Fig. 2A). The lipid environment of nanodiscs greatly stabilized the complex, as no dissociation of PelC was observed in SEC, so the lipoprotein remained anchored within the lipid layer.

Cryo-EM resolves the architecture of the PelBC complex in the lipid bilayer

The nanodisc-stabilized PelBC complexes were subjected to cryogenic electron microscopy (cryo-EM). From around 30,000 movies, 4.8 million particles were picked for downstream processing. In reference-free 2D class averages, a balanced distribution of side and top views of the PelBC complex was observed (Fig. 2B and Supplementary Fig. 3), and the nanodisc density could be well-recognized in side views, with the outer diameter of 9 nm in agreement with the previous reports[13]. Notably, no classes displaying stoichiometry different from 1:12 PelB:PelC were obtained. The homogeneity of the particle distribution allowed for a 3D reconstruction of the PelBC complex at 2.5 Å resolution with no symmetry imposed (Supplementary Figs. 3 and 4). Extensive sorting was carried out to look for different conformations of the complex, but no major structural differences between the classes were detected. A focused classification on PelB resulted in a class with the best resolved β-barrel with short α-helical loops and the N-terminal helical extension, which subsequently led to the final map used for model building (Fig. 2C, D). In agreement with the prediction, the complex is composed of a single PelB barrel built of 16 antiparallel β-strands embedded in the lipid bilayer and a dodecameric ring of PelC lipoproteins mounted at the periplasmic side (Fig. 2E). The β-barrel is centrally positioned within the nanodisc, without contacts to the edges which could otherwise distort the conformation. Notably, the architecture of PelB is similar to bacterial transporters for cellulose (BcsC)[14] and PNAG (PgaA)[15], which share the overall fold of the 16-stranded β-barrel, with partially structured loops occluding the extracellular exit of the channel (Supplementary Fig. 6). At the periplasmic side of PelB, two TPR domains resolved from the residues Gly-803 and the intermediate helix ("stalk") are located within the PelC ring, being docked at multiple lipoprotein subunits, as described below. The preceding PelB residues ranging from Asn-762 to Ile-802 remained unresolved, likely due to their higher flexibility.

The interior of the PelB β-barrel is predominantly negatively charged, where the charge is distributed asymmetrically, being largely concentrated on strands 11 to 14 (Fig. 3A). The anionic cluster faces the groove within the TPR domains, so the cationic Pel polysaccharide may employ this route for entering the channel driven by the electrostatic interactions. The anionic wall is continued with the negatively charged and partially structured loops forming the bottom of the barrel at the extracellular side with no tunnel sufficiently wide for the EPS passage (Fig. 3B, C). As a major element here, a short α-helix between the strands 7 and 8 (further referred as Plug-I) is bent inwards the central cavity of PelB where it lays perpendicular to the barrel axis (Fig. 3C). Plug-I forms several contacts within the barrel, first of all via Arg-999 to Tyr-922 in β-strand 2 and Glu-935 in β-strand 3, and so it may serve to stabilize the barrel. Plug-I is opposed by a glycine-rich loop between the C-terminal β-strands 15 and 16 (Plug-S), and together these two loops occlude the exit tunnel of PelB (Fig. 3B). The loop between the β-strands 11 and 12 (Plug-O) is exposed to the solvent at the extracellular side forming a "dome" over the barrel. Though only a small part of this 31 residues-long loop builds an α-helix, the polypeptide chain is well-resolved in cryo-EM, so Plug-O is rigid under the experimental conditions. Comparison of the resolved *P. aeruginosa* PelB structure with the models of PelB homologs from other *Pseudomonas* species shows high conservation of the extracellular loops, apart the Plug-O (Supplementary Figs. 7 and 8). Here, broad variations in the length and the putative structures are observed, suggesting that the loop architecture evolves in response to the certain habitat of the bacteria and/or its specie-specific LPS layer.

Similar to the barrel interiors (Fig. 3), the extracellular side of *P. aeruginosa* PelB is highly anionic with the net charge of −11 (Asp+Glu:

https://doi.org/10.1038/s41467-025-60605-8

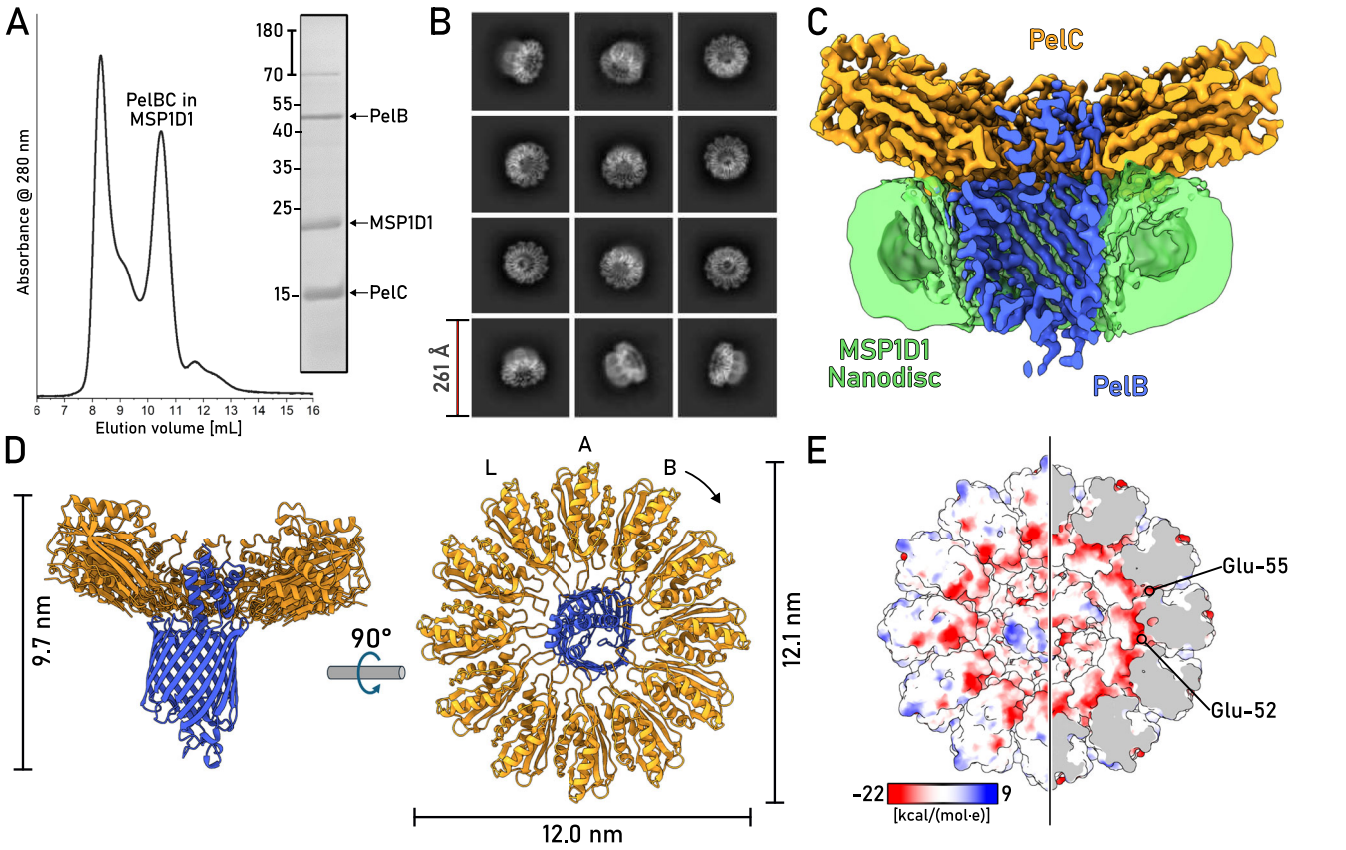

Fig. 2 | Structure of the PelBC complex embedded into the lipid membrane. **A** SEC of PelBC reconstituted into the MSP1D1-based nanodisc and SDS-PAGE of the fraction at 10.5 mL elution volume used for cryo-EM analysis. **B** Characteristic 2D classes found upon cryo-EM data processing show various projections of the assembled PelBC complexes in the nanodiscs. **C** Final 3D reconstruction (cross-section) of the PelBC complex in the nanodisc. PelB is colored in blue, PelC in golden, nanodisc/lipids in green. **D** The structural model of the PelBC complex, PelB in blue, PelC in golden. PelC subunits labeled from "A" to "L", so the subunit A approaches the N-terminal end of the PelB β-barrel. The Plug-S loop occupying the exit tunnel of PelB is seen in the periplasmic view (right). **E** The electrostatic potential at the periplasmic surface of the PelC ring (left) and under the capping loop (right). Each biochemical experiment was at least repeated twice independently. Source data are provided as a Source Data file.

−18, Arg+Lys: 7), which appears as a common feature among PelB homologs in *Pseudomonas* species (Supplementary Fig. 8). Such charge distribution is also seen for several *P. aeruginosa* porins, incl. PA4067 (OprG; PDB ID 2 × 27), PA3280 (OprO; 4RJX), and PA3279 (OprP, 2O4V), and the negative charge may serve to repel the phosphate groups of the surrounding LPS cores. In context of the polysaccharide secretion, it may also be involved in functional opening/closing of the barrel, and/or providing the electrostatic driving force for translocation of the cationic Pel. For the outer membrane transporters of partially cationic polysaccharides, such as bacterial phosphoethanolamine cellulose and PNAG, the electrostatic interactions at the exit of the secretion machinery were proposed to facilitate the directed transport[15].

As a unique feature of the Pel translocation system, twelve PelC subunits assemble in a ring at the periplasmic side of the PelB barrel (Figs. 2 and 4), and so they repeat the architecture of the crystallized PelC of *P. phytofirmans*[8]. Beneficially, the cryo-EM map visualizes the complete periplasm-facing loop-helix turn (residues 70–98) that was not resolved in the crystal structure, due to its flexibility apparent from the current reconstruction (Fig. 4A and Supplementary Fig. 4). The loop-helix segment caps the PelC subunit beneath and shields the excessive negative charge rendered by the glutamates in positions 52 and 55 (Fig. 2E), but also provides negative charge via Asp-79 and Asp-84 lining the central pore (Fig. 4A). At the membrane interface, the extended loop of PelC (further referred as D-loop, for the conserved Asp-119 within) is exposed into the central pore. The electronegative potential rendered by Asp-119 was previously related to PelC:exopolysaccharide interactions[8], as altering the charge here abolished the biofilm formation. However, within the assembled complex those aspartates are buried at the PelB-PelC interface and build multiple contacts with the surface-exposed arginine residues of PelB, such as 905, 944, 1018, 1114, 1122, and 1190 (Fig. 4B, C), thus playing rather a structural role. Noteworthy, with glycine residues in positions 117 and 120, the D-loop is sufficiently flexible, so individual PelC subunits adapt their conformations to the proximate structural features of PelB, i.e., the helical domain and the periplasmic loops (Fig. 4B).

Two PelC subunits, C and D, build electrostatic interactions with the stalk helix of PelB (Fig. 4D), and the preceding TPRs are stabilized in defined positions by interactions with PelC subunits B/C/-D and I/J/-K, so these two repeats are well-resolved within the central pore. To test the role of the helical region in the PelBC assembly and stability, we co-expressed PelC with the truncated PelB variant containing only the β-barrel domain. Though both proteins could be extracted from the membrane, no PelC was co-purified with PelB in absence of the stalk helix and the TPR domains (Fig. 1D, E), suggesting that the conserved domain is crucial for the protein:protein interaction, and it may serve as a nucleation site for the PelC ring assembly.

The PelBC complex is stabilized via multiple protein:lipid interactions

The 3D reconstruction of the nanodisc-embedded complex reveals several rod-shaped densities proximate to PelBC (Fig. 5A, B). Within the

https://doi.org/10.1038/s41467-025-60605-8

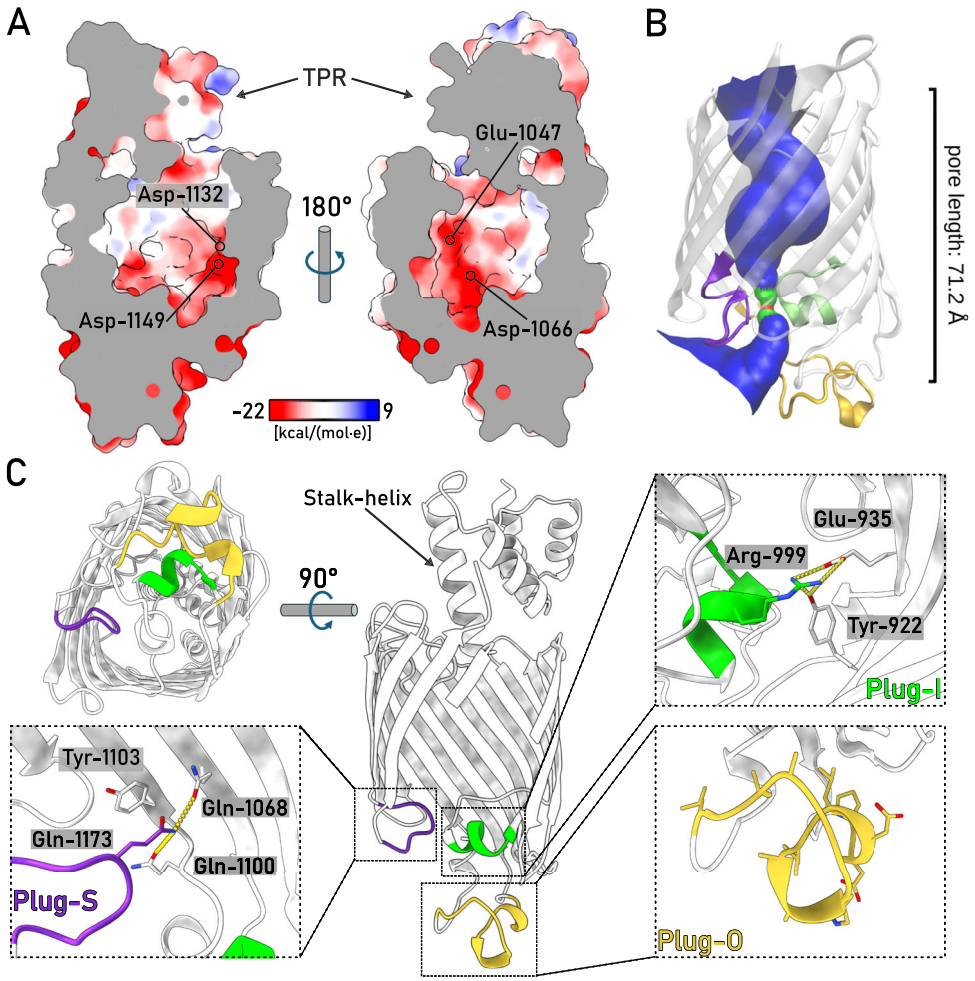

Fig. 3 | The architecture of the PelB β-barrel. A The charge distribution inside the PelB β-barrel is asymmetric, with anionic residues localized at the β-strands 11–14 and the bottom of the barrel. Representative residues are indicated. **B** The tunnel across the β-barrel is rendered by HOLE algorithm, shown in blue. The bottleneck impermeable for water molecules is indicated in red, and the areas accessible for a single water molecule are in green. The extracellular loops are colored accordingly to the (**C**). **C** Detailed view on the extracellular loops Plug-I (green), Plug-S (violet), and Plug-O (yellow) of PelB and the interactions which stabilize their positions in the resolved structure. The universally conserved residue Tyr-1103 near the Plug-S loop is indicated.

periplasmic leaflet, most of those densities emerge from the N-termini of PelC subunits, so they are unambiguously assigned to the covalently bound acyl chain anchors. For several PelC subunits, all three acyl chains conjugated to the N-terminal cysteine are resolved, reaching up to 16 carbon atoms (Fig. 5C). The anchor chains of individual PelC subunits are sandwiched between two Trp-149 residues, one from the same PelC, and one from a preceding subunit, a configuration that potentially facilitates docking of the lipoproteins at the membrane interface. Compared to the membrane-less crystal structure[8], Trp-149 residues undergo rotation towards the lipid bilayer (Fig. 4A), so their indole rings immerse into the hydrophobic core of the membrane. Previous in vivo analysis showed that *P. aeruginosa* biofilm formation at the water-air interface was severely inhibited once Trp-149 was replaced by alanine[8]. To test whether this functional defect arose from the complex assembly, we expressed $PelC_{W149A}$ mutant either alone or in combination with PelB. PelC was targeted to the outer membrane in both cases, however we found a detrimental effect of the mutation on stability of the PelBC complex, as only PelB barrel without the lipoproteins could be isolated (Supplementary Fig. 9). Thus, we concluded that Trp-149 stabilizes the lipid anchors within the assembled PelBC complex, possibly by suppressing their dynamics, and it may facilitate the oligomerization of the subunits into the ring.

The lipid anchors of PelC subunits reside at 3–4 Å distance from the PelB barrel, and so do not interact with the protein. However, multiple densities were found at the surface of PelB, which occupy the grooves formed by the membrane-facing aromatic and apolar residues (Fig. 5A, B). Those were assigned to acyl chains of the phospholipids, which were either co-purified with the PelBC complex, or were provided upon the nanodisc reconstitution. A fully resolved lipid molecule was located between the PelC subunits H and I, forming extensive interactions with the lipoproteins and the barrel (Fig. 5D). Based on the size and the interactions with the proximate polar residues which coordinate the head group, the density was assigned to a zwitterionic lipid, either PE or PC (Supplementary Figs. 10 and 11). The best-fitting PE could be co-isolated from the bacterial membrane, while PC is a constituent of the synthetic nanodisc, which could replace an endogenous PE molecule upon the reconstitution. Remarkably, a continuous density was resolved in a groove crossing the strands 1–2 and 13–16 that stapled N- and C-terminal ends of the β-barrel. The density spanning from the periplasmic to the extracellular sides of PelB likely arises from averaging of two acyl chains that belong to lipids in the opposing leaflets. In the native bacterial membrane, the groove would be partially filled by a lipid A molecule in the extracellular leaflet. In support of this hypothesis, a cationic cluster of Lys-888, Lys-897, and Arg-921 is found at the extracellular side of the groove, offering a docking site for the phosphate head groups (Fig. 5B). On the other side of the barrel, a similar cluster of Arg-1071 (β-strand 11) and Arg-1102 (β-strand 12) is formed near a hydrophobic groove, which appears to be

https://doi.org/10.1038/s41467-025-60605-8

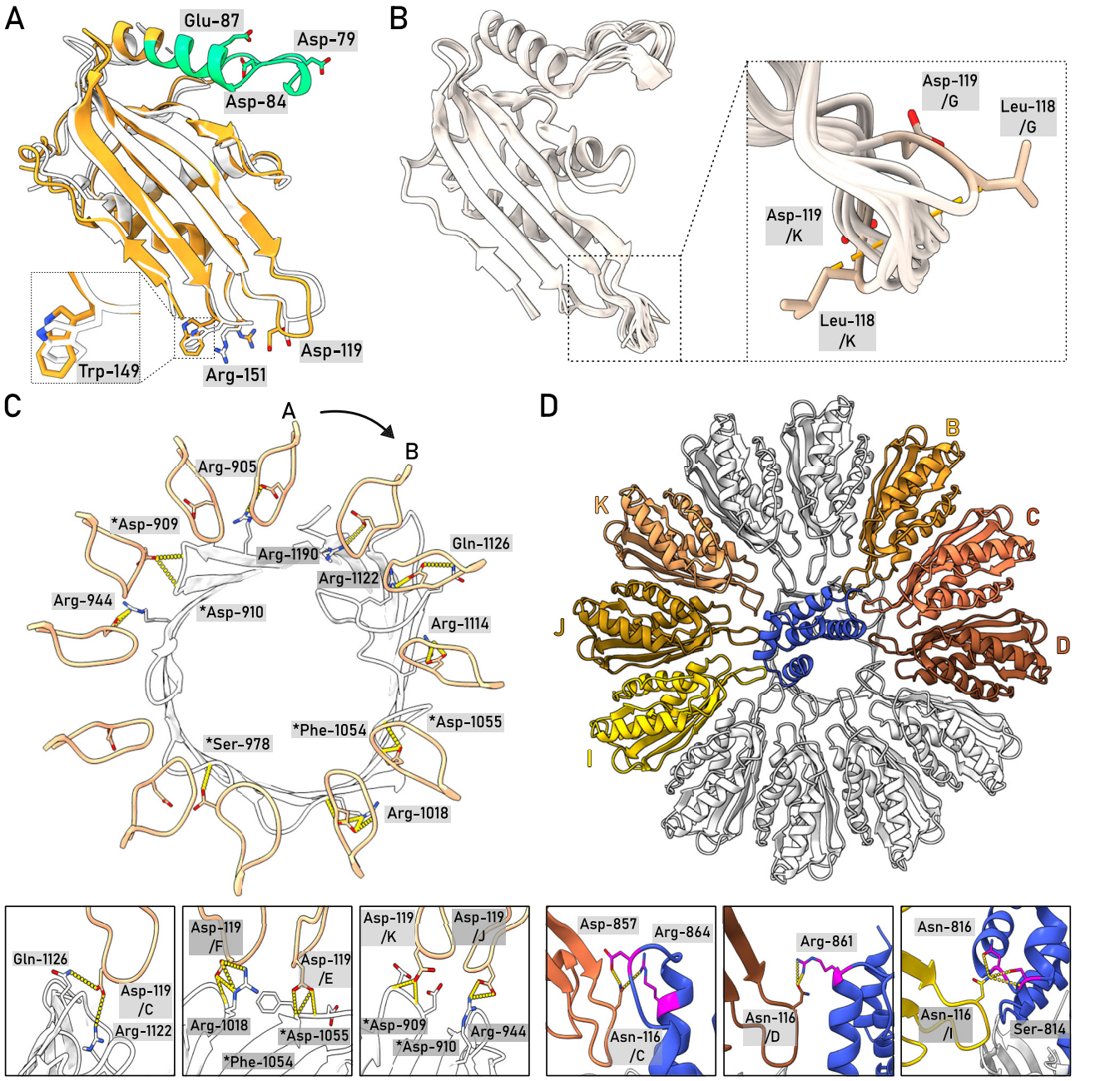

Fig. 4 | The architecture of the PelC ring and PelC:PelB interactions. A Cryo-EM structure of *P. aeruginosa* PelC, subunit E (orange), aligned with the partial crystal structure of PelC from *P. phytofirmans* (white). The capping loop absent in the crystal structure is shown in green. **B** Alignment of 12 PelC subunits resolved in the cryo-EM structure. Due to the subunit-specific interactions with PelB, the pore-exposed D-loops manifest different conformations (zoomed), where the deviations measured for Leu-118 Cβ reach up to 8.5 A for subunits K and G. **C** The residue Asp-119 within the D-loop of multiple PelC subunits is involved in interactions with the periplasmic loops of PelB (residues indicated). PelB residues which interact via the backbone amide group are indicated with asterisk. **D** Several PelC subunits (colored) build electrostatic interactions with the helical scaffold of PelB (shown in blue). Subunits (**C** and **D**) interact with the stalk helix, and subunits B and I-K with the TPR domain.

well-conserved feature among *Pseudomonas* species (Supplementary Fig. 8), suggesting that the PelB structure is evolutionary tuned to facilitate interactions with lipid A molecules.

The dynamic extracellular loops of PelB open a tunnel for Pel export

The cryo-EM analysis revealed a single conformation of PelB, where the groove within the periplasmic TPR's is aligned with the pore at the extracellular side of PelB between the strands 12–16 and the opposing Plug-I, thus forming a route for the polysaccharide. Notably, Tyr-1103 in the proximity of the pore is conserved among PelB homologs, being occasionally substituted by phenylalanine, and the residue is also found in the BcsC structure[14], so it may be involved in the EPS translocation, e.g., via CH-pi interactions with the pyranoside rings. However, the exit pore within the resolved PelB structure is occluded by the glycine-rich loop Plug-S (Fig. 3) with a bottleneck width of 4 Å (Fig. 3B). Such a narrow tunnel cannot be employed for the polysaccharide translocation requiring a width of ~8 Å (Ref. 16), so a conformational change, such as dislocation of Plug-S, must occur to open the conduit. As the Plug-O loop is not structurally conserved even among close PelB homologs in *Pseudomonas* species and it extends away from the barrel, it is unlikely that the loop plays a

https://doi.org/10.1038/s41467-025-60605-8

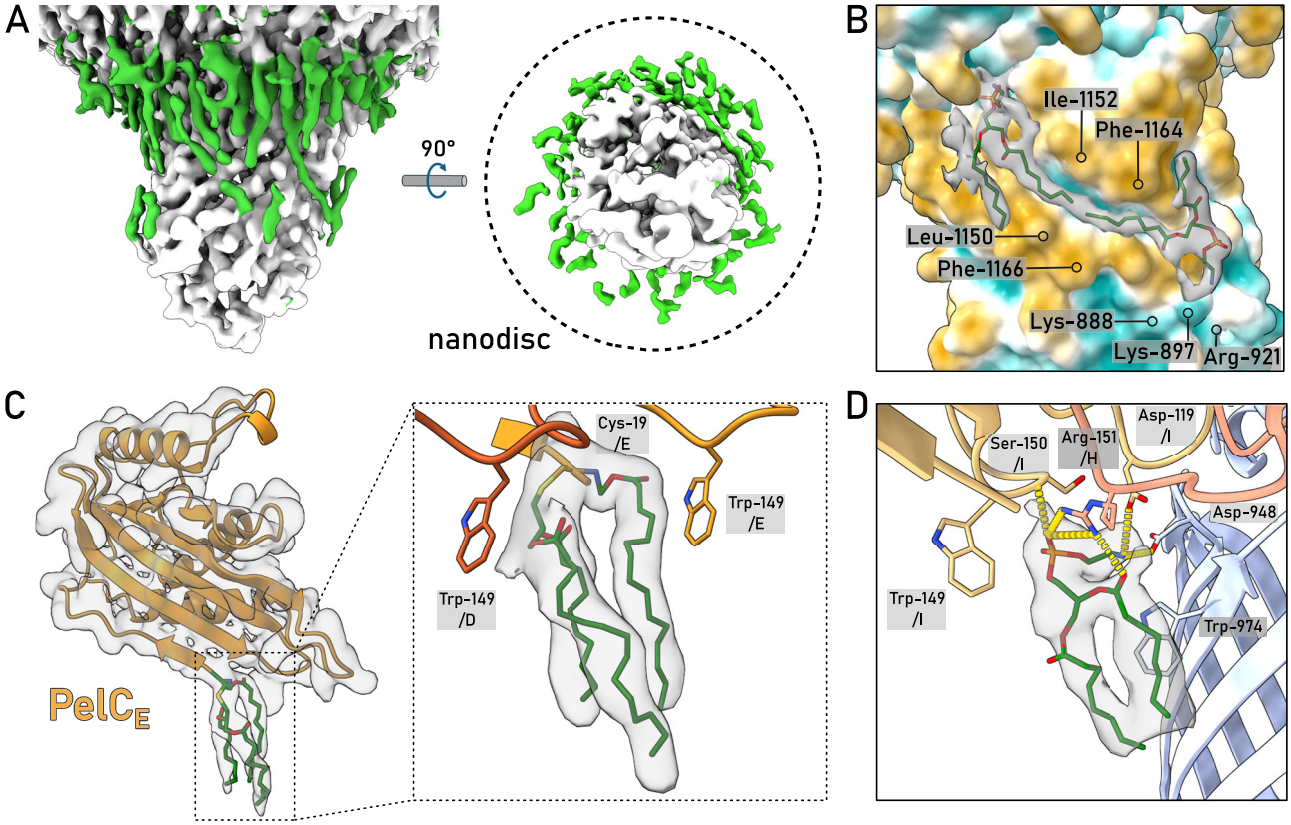

Fig. 5 | The proximate lipid environment of the PelBC complex. A Non-proteinaceous densities (green) within the nanodisc assigned to the stably docked lipid acyl chains and the lipoprotein anchors. The approximate nanodisc borders are indicated as a dashed line in the view from the extracellular side (right). The density of the PelC ring is removed for clarity. **B** The acyl chains docked within the hydrophobic groove of the β-barrel formed by Leu-1150, Ile-1152 and mainly Phe-1164 and Phe-1166. At the extracellular side, Lys-888, Lys-897, and Arg-921 form a cationic cluster as docking site for phosphate head groups. **C** The N-terminal acyl chains of the lipoprotein PelC (as example, the subunit E is shown) are stabilized by Trp-149 residues from two subunits, (**D** and **E**). **D** Modelled structure and the interaction network of a phosphatidylethanolamine molecule proximate to PelC subunits H and I.

Table 1 | Summary of simulations on PelB under different conditions

System and conditions	Size [atoms]	Runs	Cumulated time [μs]
EC-LPS, 150 mM KCl, 37 °C	184,012	3 × 500 ns	1.5
PA-LPS, 150 mM KCl, 37 °C	145,971	3 × 500 ns	1.5
EC-LPS, 150 mM NaCl, 25 °C	184,012	3 × 500 ns	1.5
PA-LPS, 150 mM NaCl, 25 °C	145,971	3 × 500 ns	1.5
POPC:POPG, 150 mM NaCl, 25 °C	105,713	3 × 500 ns	1.5
POPC:POPG, 150 mM NaCl + 100 mM $CaCl_2$, 25 °C	105,707	3 × 500 ns	1.5
POPC:POPG, 150 mM NaCl, 25 °C, pH 3.5, 25 °C	106,029	2 × 500 ns	1.0
Plug-O mutant, POPC/POPG, 150 mM NaCl, 25 °C	102,598	3 × 500 ns	1.5
Plug-S mutant, POPC/POPG, 150 mM NaCl, 25 °C	104,249	3 × 500 ns	1.5
Total			13.0

PA P. aeruginosa, EC E. coli, LPS Lipopolysaccharide, PA-LPS: LPS with one O-antigen unit (outer leaflet) and DOPE:DPPG:DPPE (inner leaflet) at molar ratio 46:31:23[41]. EC-LPS: 100% LPS with five O-antigen units (outer leaflet) and POPE:POPG:PVCL (inner leaflet) at molar ratio 75:20:5.

key role in the protein gating, though its involvement cannot be excluded a priori.

We speculated that the PelB conformation, first of all positions of its extracellular loops, may be affected by multiple physiological factors, such as presence of divalent cations, LPS, and/or variations in the temperature. To test whether those factors induce spontaneous opening of the pore, we established all-atomic molecular dynamics (MD) simulations of the PelB β-barrel (residues 877–1193) in triplicates under a set of relevant conditions. The protein was virtually embedded in a membrane of a tailored composition, and environmental factors could be systematically screened while monitoring the dynamics of the extracellular loops (Supplementary Fig. 12 and Table 1). The experiments were initially performed at 25 °C, a relevant condition for the EPS secretion in surface-based biofilms. First, we examined whether Ca^{2+} cations abundant in the extracellular environment, but omitted in the cryo-EM analysis, could alter the protein dynamics due to interactions with the anionic loops. Equilibration of the nanodisc-like phospholipid-based system in presence of different ions revealed remarkable features at the extracellular side of PelB: The highly charged region consistently attracted cations, and Plug-S formed

https://doi.org/10.1038/s41467-025-60605-8

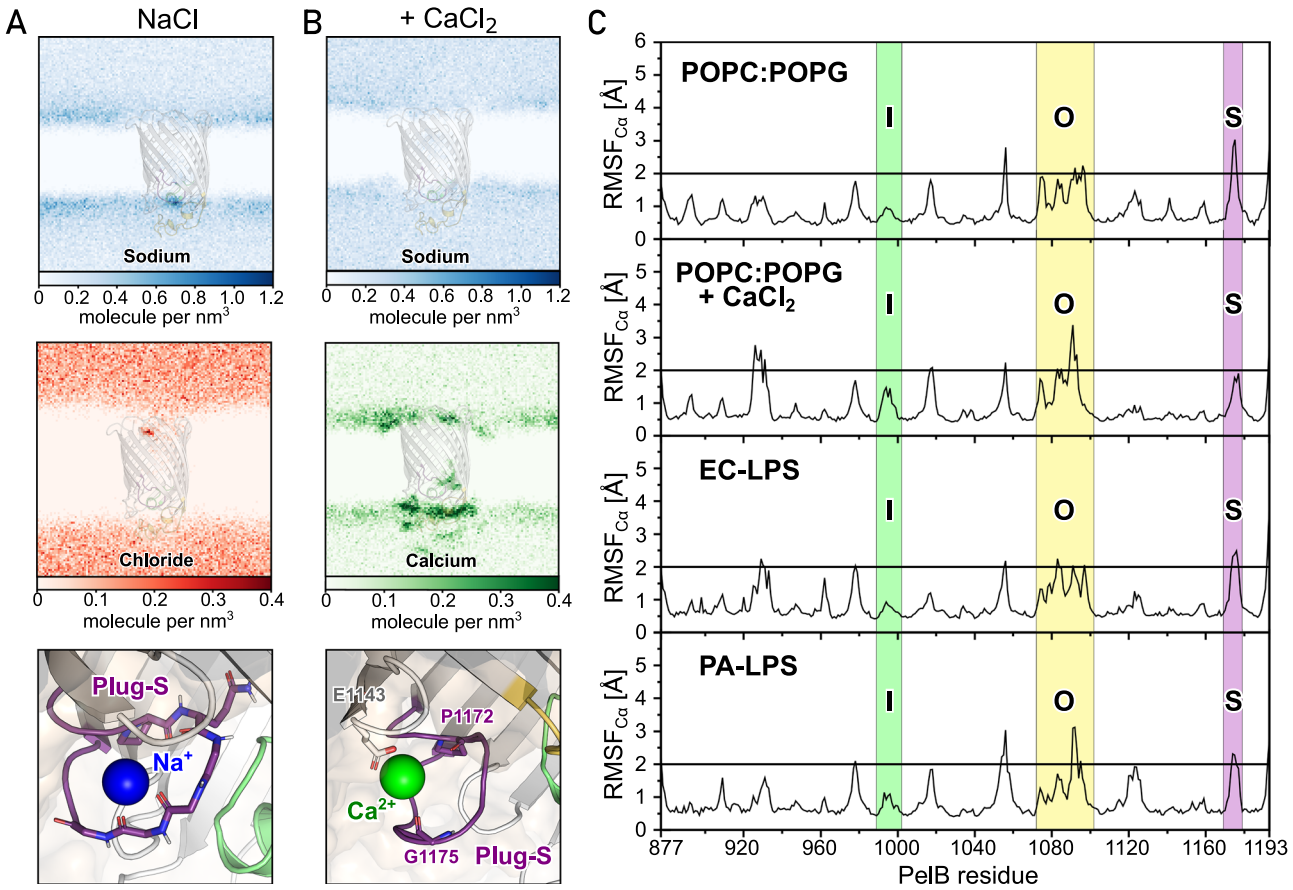

Fig. 6 | The ion distribution and the PelB β-barrel dynamics in silico. A The distribution density maps of sodium (top, blue) and chloride (middle, red) ions across the PelB β-barrel embedded into the symmetric POPC:POPG lipid bilayer in 150 mM NaCl. The Plug-S loop stably binds a sodium ion coordinated via the carbonyl groups (bottom panel). **B** The density maps of sodium (top, blue) and calcium (middle, green) ions in the same settings as (**A**), supplemented with 100 mM $CaCl_2$. A calcium ion binds stably at the side of the Plug-S via the Pro-1172, Gly-1175, and Glu-1143 (bottom panel) and replaces the sodium ion. The density of chloride anions does not change in the presence of calcium. **C** The conformational dynamics of PelB in symmetric POPC:POPG lipid bilayers with and without calcium ions, as well as native-like membranes with an LPS leaflet based on *E. coli* and *P. aeruginosa* models in CHARMM-GUI. The dynamics is depicted via the RMSF of the Cα atoms over the time of 500 ns, and the threshold displacement level of 2 Å is indicated (black line). The regions corresponding to the Plug-I, Plug-O, and Plug-S loops are highlighted in green, yellow, and violet, respectively. Representative simulations of each system are shown. All plots of the triplicates are provided in Supplementary Figs. 13 and 14. Source data are provided as a Source Data file.

stable interactions with a de-solvated sodium ion coordinated by the carbonyl groups of the tetra-glycine loop (Fig. 6A). Once $CaCl_2$ was included in the simulation, a calcium cation displaced Na^+ from Plug-S and was stably docked between Pro-1172, Gly-1175, and Glu-1143 from a proximate extracellular loop (Fig. 6B). Despite the significant difference in the ion distribution, the dynamics of PelB were similar between the tested conditions, where Plug-O and Plug-S repeatedly crossed the threshold displacement of 2 Å and so appeared flexible, while Plug-I remained rather static (Fig. 6C and Supplementary Fig. 13).

The model lipid bilayer of the nanodisc does not reflect the natural asymmetry of the bacterial outer membrane, where the extracellular leaflet is composed of lipopolysaccharide (LPS) molecules. Hence, we questioned whether this specific environment enriched with LPS-bound phosphate groups and divalent cations affects the dynamics of PelB extracellular loops. PelB was incorporated into the mimetics of *P. aeruginosa* and *E. coli* outer membranes provided by CHARMM-GUI. The membranes differ substantially by the length of the O-antigen polysaccharides of LPS, which extend into the solvent by 2.5 and 10 nm, respectively (Supplementary Fig. 12). As PelB Plug-O is exposed to the LPS environment, its interactions were analyzed on the example of *E. coli*-type membrane, where we measured the average distance between the Plug-O residues and the specific regions of the LPS (Fig. 7A). The interactions were clustered around three arginines, i.e., Arg-1071 and Arg-1102 reaching the phosphate groups of the lipid A, and the conserved Arg-1075 interacting with the LPS inner core. As a result of the electrostatic attraction, the former conserved cationic site attracted two LPS molecules (Fig. 7B), and two other LPS molecules were docked by Lys-888, Lys-897, and Arg-921, as predicted from the cryo-EM structure (Fig. 7C). However, no consistent deviations in PelB RMSF values were observed between the simulations in either *E. coli* or *P. aeruginosa* outer membrane models, suggesting that the dynamics of the extracellular loops was not affected by LPS (Fig. 6C and Supplementary Fig. 14).

To test whether the protein dynamics, such as a movement of Plug-O observed in a single trial, are enhanced by the temperature, we repeated the simulations at 37 °C in triplicates. The elevated temperature favored further dislocation of Plug-S, especially for PelB in *P. aeruginosa* membrane (Supplementary Fig. 14). The individual conformations of PelB manifested transient pores, which were sufficiently wide for passage of multiple water molecules, but also for a linear polysaccharide, as exemplified by docking GalNAc-GalN-GalNAc-GalN within the open pore (Supplementary Fig. 15). Thus, the position of Plug-S within the PelB structure together with its high dynamics and the prominent interactions with cations suggest that the loop is the potential gating element for translocation of the cationic polysaccharide.

https://doi.org/10.1038/s41467-025-60605-8

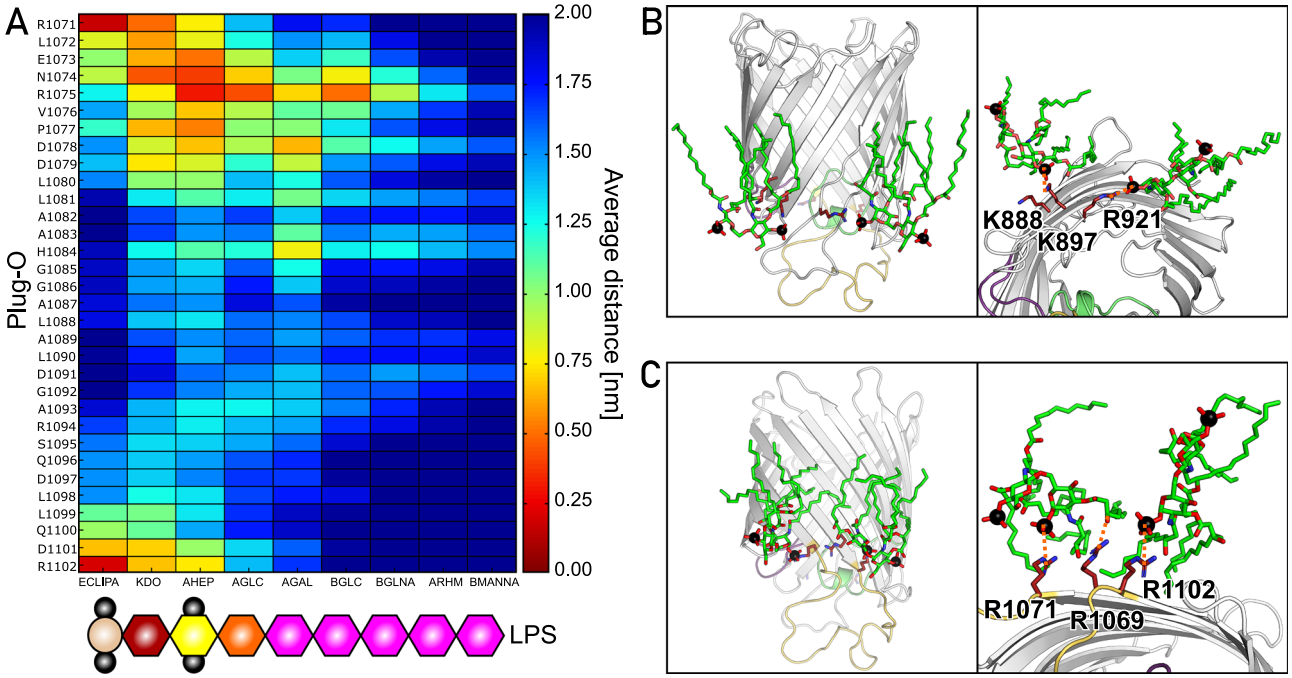

Fig. 7 | Interactions between the PelB β-barrel and LPS molecules in silico. A The average distance map between the exposed Plug-O loop and the EC-LPS elements. The schematic structure of the EC-LPS molecule provided by CHARMM-GUI is shown below; details to the abbreviations are provided in the Supplementary Fig. 10E. Here, red to yellow colors imply an interaction between the groups (distances below 1.0 nm), whereas the green to blue colors indicate no direct interactions (distances above 1.0 nm). **B**, **C** Side and extracellular views of two interaction sides of the PelB β-barrel with LPS molecules. The positively charged key residues Lys-888, Lys-897, Arg-921 (**B**) as well as Arg-1071, Arg-1069, and Arg-1102 (**C**) involved in the interactions with the phosphate groups of the lipid A or carbonyl groups of the fatty acids are indicated. Source data are provided as a Source Data file.

Single-channel conductivity reveals conformational dynamics of PelB

To validate the conformational dynamics of the PelB loops seen in the MD simulations and to document the associated opening of the central pore, we set out to measure the ion conductivity across PelB by means of single-channel electrophysiology. In the electrophysiology set-up, the proteins of interest are embedded into a free-standing lipid bilayer and the ion passage across the membrane is recorded upon applying an electrostatic potential. The conformational dynamics of channel-forming membrane proteins, such as ion channels, toxins, but also outer membrane porins result in the ion flow fluctuations[17], which can be then used to describe the protein dynamics. We assumed that opening of the PelB pore can be monitored in a real-time manner, and contribution of its individual loops can be assessed by testing specific mutants, so the gating element will be identified. As the conductivity experiments require the electrostatic potential applied across the membrane, it could promote dynamics of the charged PelB loops, bringing the protein out of equilibrium. Potentially, the cationic polysaccharide entering the β-barrel of PelB has a similar effect, as it would partially neutralize the charge of the loops and could serve as a trigger for switching the protein conformation.

Similar to the PelBC complex, the PelB protein (residues 762–1193) was expressed in *E. coli* C41(DE3) Δ*acrAB* Δ*ompF* strain, so potential contamination with the major porin OmpF was excluded[11]. To perform the electrophysiology experiment, the detergent-solubilized PelB had to be incorporated into the planar bilayer of 1,2-diphytanoyl-sn-glycero-3-phosphatidylcholine (DPhPC) formed between two chambers of the electrophysiology set-up. The spontaneous incorporation could only be achieved at high ionic strength and pH 3.4, which likely compensated the anionic nature of the extramembrane loops. Upon applying a potential of −150 mV across the membrane, ion currents of various intensities were observed, indicating that the inserted proteins reversibly switched between the conformations of different conductance (Fig. 8A). Due to stochastic bilayer incorporation and switching between the conformations, ion flow through multiple PelB proteins could be measured, resulting in multiplex opening and closing patterns (Supplementary Fig. 16). Based on the largest common denominating current of ~150 pA, we used only single-channel traces for analysis of conductance and open/closing probabilities (Fig. 8B, C and Supplementary Fig. 17). The recordings were characterized by relatively high noise levels, which originated from thermal fluctuations within the protein structure. As deletion of the periplasmic TPR domain did not affect the recordings (Supplementary Fig. 18), the ion current fluctuations were related to dynamics of the extracellular loops. Notably, the recorded traces showed high consistency for each individual molecule, i.e., the signal fluctuated between certain ion current levels, while the signal levels differed substantially between the measured PelB molecules (Fig. 8B and Supplementary Fig. 17). Thus, the single-molecule detection visualized the otherwise hidden heterogeneity within the PelB ensemble, which could be caused by variations in folding or protein:lipid interactions, e.g., due to co-purified and co-reconstituted *E. coli* lipids and the acquired configuration within the membrane.

To handle the data heterogeneity, we grouped the measured currents into three ranges, i.e., those below 25 pA ("low" conductivity range, L), 25 to 100 pA ("median", M), and above 100 pA ("high", H). Each range must have corresponded to an ensemble of PelB conformations/states, characterized by certain pore dimensions. The individual PelB traces allowed to trace how the ion currents, and so the pore dimensions changed over time, so the occupancy of each conductivity range and the associated currents were calculated for individual molecules and then statistically analyzed based on multiple PelB recordings (Fig. 8C and Supplementary Fig. 19). For the wild-type PelB, the conducting M- and H-states were the most abundant, each constituting of approx. 40%. The ion current levels and the conductance of 0.8 nS observed in the H-range matched the values measured for

https://doi.org/10.1038/s41467-025-60605-8

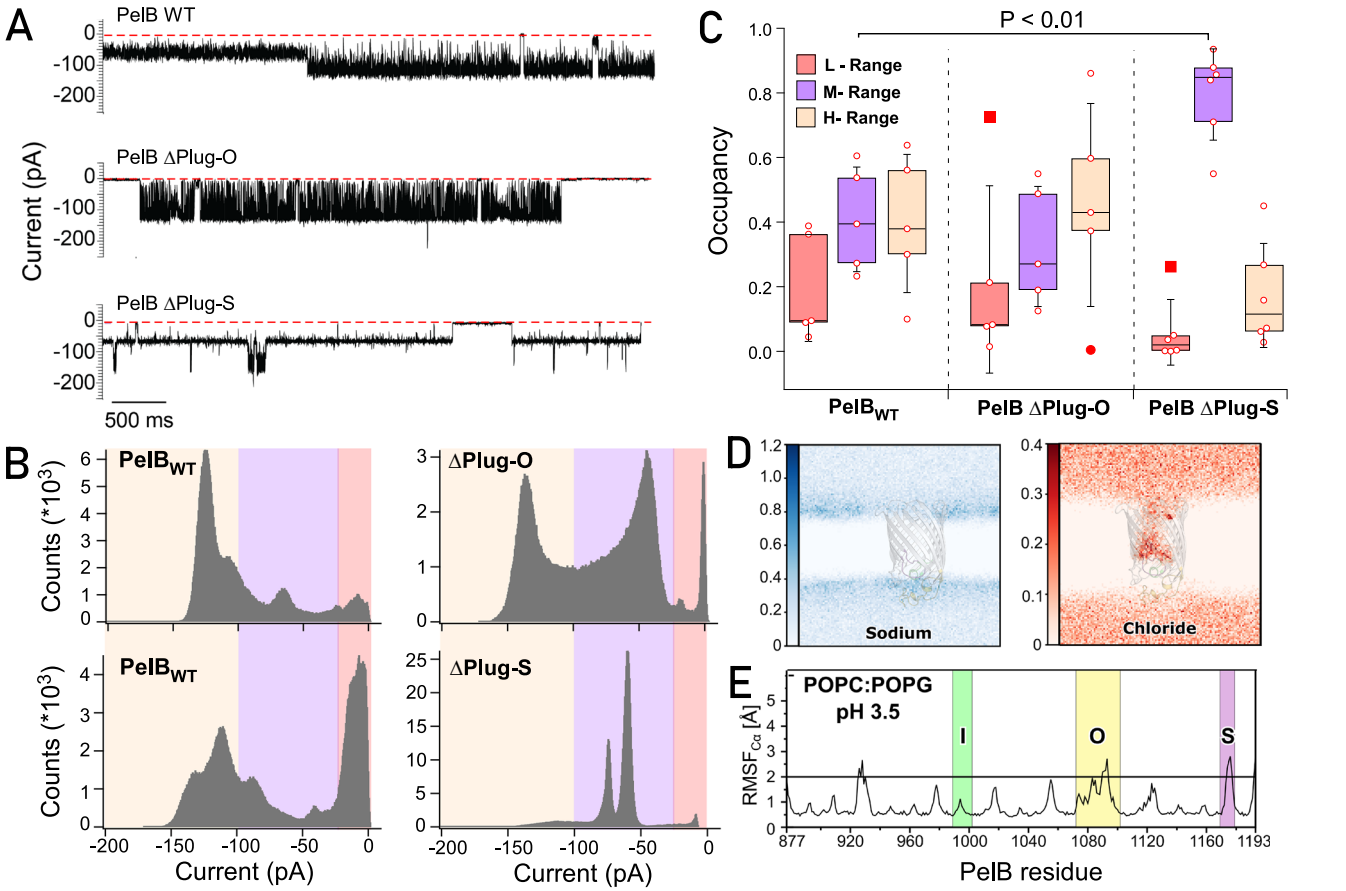

Fig. 8 | PelB dynamics in single-channel conductivity measurements. **A** Recordings of the ion current across individual PelB molecules, either wild-type (WT) or the truncated mutants ΔPlug-O and ΔPlug-S. **B** Representative histograms of the ion current distribution measured for the indicated PelB variants. Colored areas highlight low (up to 25 pA; red), median (25–100 pA; violet) and high (above 100 pA; wheat) conductivity ranges, as described in the text. **C** Occurrence of low (L, red), median (M, violet), and high (H, wheat) conductivity states determined for the PelB variants at the single-molecule level. Each marker indicates a measurement of an individual PelB molecule ($n = 5$ for PelB$_{WT}$ and PelB ΔPlug-O, $n = 6$ for PelB ΔPlug-S). The plots show the median values, the 25th and 75th percentile (boxes) and the standard deviations (whiskers). The outliers are shown as filled markers (defined by Tukey, beyond 1.5 of interquartile range). The statistically significant difference found for the M-range occupancy is indicated ($p = 0.002$; one-way ANOVA test). **D** The distribution density maps of sodium (blue) and chloride (red) ions across the PelB β-barrel embedded into the POPC:POPG lipid bilayer at pH 3.5. Chloride anions may enter the interior of the protonated β-barrel. **E** The conformational dynamics of PelB in the POPC:POPG lipid bilayer at pH 3.5. The representation is identical to that in Fig. 6. The regions corresponding to the Plug-I, Plug-O, and Plug-S loops are highlighted in green, yellow, and violet, respectively. Source data are provided as a Source Data file.

OmpG of *E. coli*, where the pore diameter exceeded 1.5 nm[18]. Based on the resolved structure of PelB, we concluded that a major rearrangement of the sealing loops at the extracellular side would be required to achieve such pore opening, while such conformation was not observed in MD simulations. For the M-state, the conductance of ~0.4 nS matched that of OmpC of *E. coli*, a β-barrel with the pore of ~1 nm[19]. A pore of such dimensions within PelB would be sufficient for translocation of the substrate[16], and the opening could be achieved upon Plug-S dislocation, as suggested by transient conformations seen in MD simulations (Supplementary Fig. 13).

As the conductivity experiment was performed at low pH, we questioned whether PelB retained its conformation and dynamics at these conditions, and so we carried out MD simulations of the lipid-embedded β-barrel while mimicking the solvent acidic environment. The solvent-exposed histidines, glutamate, and aspartates within the β-barrel and at the extracellular surface were protonated at pH 3.5. Differently to the simulations at pH 7.5, we found that Cl^- were abundant inside PelB, in agreement with the altered electrostatics, as the repulsion from the anionic residues was abolished (Fig. 8D and Supplementary Fig. 20). Nevertheless, PelB retained its structure along the simulation, and the dynamics of the extracellular loops was barely affected (Fig. 8E). This high stability of the outer membrane protein may be remarkable, but not surprising: Being exposed to the dynamic environment, the protein must manifest robust stabilization mechanisms, while mild acidification is a common condition met within *P. aeruginosa* biofilms[20].

Single-channel conductivity recordings of the wild-type PelB confirmed the intramolecular dynamics of the protein. As the conductivity fluctuations were likely linked to the movements of the plug domains, we set out to identify their contribution to the gating. Deletion of either Plug-O or Plug-S may affect the channel properties, as suggested by MD simulations and the tunnel calculations (Supplementary Fig. 21). To test the protein dynamics in the conductivity experiments, PelB mutants with the individually deleted/shortened plugs were expressed and isolated (Supplementary Fig. 22A). Among the mutants, deletion of the Plug-I helical region (residues LMRAL) greatly reduced expression and purification yield of the protein, indicating defective folding. The detrimental effect of the Plug-I deletion was further proven when analyzing PelB stability via differential scanning fluorimetry. When measuring the intrinsic fluorescence of the aromatic residues abundant within PelB (15 Trp within the β-barrel), we observed that the wild-type protein, as well as PelB ΔPlug-O and PelB ΔPlug-S underwent cooperative thermal denaturation in the range of 73–75 °C (Supplementary Fig. 22B). In contrast, the construct lacking

https://doi.org/10.1038/s41467-025-60605-8

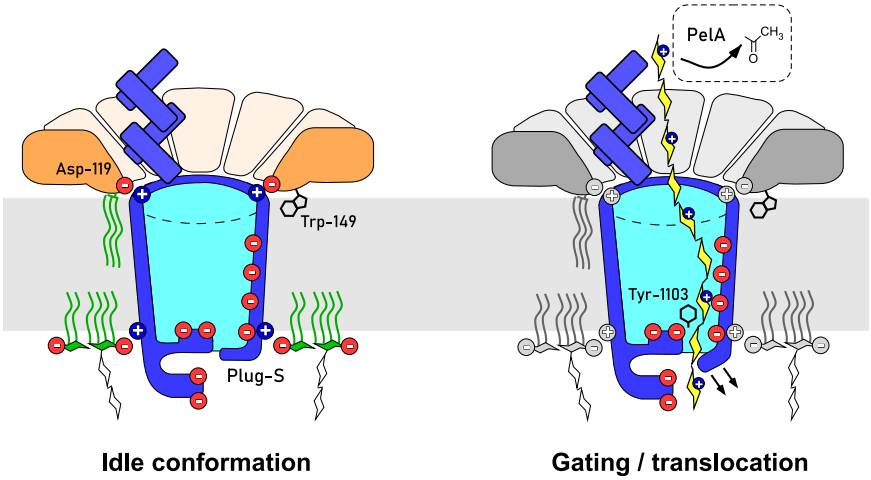

Fig. 9 | Assembly and the gating mechanism of the exopolysaccharide export complex PelBC. Left: Schematical overview of the PelBC structure, the charge distribution and the key protein:protein and protein:lipid interactions resolved in the study. Right: The putative route of the substrate, Pel exopolysaccharide (yellow), across the tunneled conformation of the PelBC export complex. The polysaccharide composed of GalNAc is partially de-acetylated by PelA while bound to the helical scaffold of PelB, and the transport is facilitated by electrostatic interactions with the anionic interior of the PelB β-barrel. The polysaccharide uses the exit tunnel formed upon Plug-S displacement, while being screened by the conserved Tyr-1103 residue.

Plug-I unfolded already at 55 °C, in agreement with the stabilizing role of the domain within the β-barrel structure, so the mutant was excluded from the further analysis. Notably, no thermal denaturation was observed for the liposome-embedded wild-type PelB within the experimentally amenable temperature range up to 95 °C, suggesting that the lipid environment offered further stabilization for the protein (Supplementary Fig. 22C). Once the pH level was reduced to 3.5 to mimic the conditions of the single-channel electrophysiology experiments, a transition was observed above 85 °C, suggesting that the protein remained folded within the physiological temperature range, also in the acidic environment.

While retaining the equal stability, PelB ΔPlug-S and PelB ΔPlug-O variants manifested clearly different behaviors in the single-channel conductivity experiments. Deletion of 14 residues within the non-conserved Plug-O loop did not have a significant effect on the observed ion currents and their distribution, as compared to the wild-type protein, so the M- and H-states were predominantly found among the heterogeneous PelB ensemble (Fig. 8 and Supplementary Figs. 19 and 23). In contrast, removal of the Plug-S loop led to radical changes in the conducting properties: Firstly, the recordings manifested substantially lower noise levels, suggesting that those initially arose from high-frequency structural fluctuations of Plug-S. Secondly, PelB ΔPlug-S predominantly showed the conductance within the M-range (occurrence approx. 80%; $P = 0.002$), occasionally switching to H-states (Fig. 8 and Supplementary Fig. 24). The low-conductance L-state was nearly abolished, so deletion of Plug-S rendered a constitutively open pore in PelB. Remarkably, distinct conductivity sub-states were reproducibly observed within the *M*-range, with the conductance values ranging from 0.42 to 0.57 nS (Supplementary Figs. 24 and 25). Those sub-states must have reflected the dynamics of PelB beyond Plug-S, e.g., movements of the proximate Plug-O loop.

To summarize, the MD simulations and the conductivity measurements jointly suggest that the Plug-S dislocation within the wild-type PelB renders the open state with a pore of approx. 1 nm diameter, which is sufficiently wide for the polysaccharide transport. The dynamics of the gating loop is barely affected by the protein environment, though it is enhanced at elevated temperatures. The high-conductance state observed in the single-channel electrophysiology experiment may be a result of more extensive rearrangements, e.g., displacement/unfolding of the rigid Plug-I or deformation of the barrel under the applied potential. Biophysical and structural analysis in presence of the Pel exopolysaccharide mimetics should provide further insights into the PelBC dynamics and, more generally, the export mechanisms.

Discussion

Despite the abundance of biofilms in nature and the major roles they play in the microbial pathogenicity, the mechanisms of their assembly at the molecular level remain poorly understood. Resolving the structure and function of the cellular machineries involved in the biofilm formation, first of all exopolysaccharide synthesis and secretion, may assist in developing new strategies to suppress the spreading of many pathogens. Here, we focus on the mechanism of a unique secretion machinery for *P. aeruginosa* Pel exopolysaccharide and present the intact structure of the PelBC complex in the lipid environment, describe the determinants for its assembly, and provide the first experimental insights into the conformational dynamics that may facilitate translocation of the substrate exopolysaccharide (summarized in Fig. 9).

Up to date, crystal structures of several exopolysaccharides transporters have been resolved, which mediate secretion of alginate (AlgE), PNAG (PgaA), and bacterial pEtN-cellulose (BcsC) across the outer membrane[14,15,21]. Consistently, they show β-barrels of either 18 or 16 strands occluded with loops at the extracellular side, and routes for the substrate translocation have been suggested based solely on the structural insights. PelB shares a high structural similarity to BcsC and PgaA, but as a unique feature in Pel secretion, the outer membrane barrel is essentially coupled to the ring of the lipoproteins PelC, which is fully resolved in our structure. The assembly is enabled by the conjugated acyl chains and the membrane-embedded Trp-149 of each PelC subunit, and the necessary electrostatic interactions of multiple lipoproteins with PelB, both with the helical TPR domains and the periplasm-exposed loops (Fig. 9). The structure resolved in the lipid environment and the complementary MD simulations in the native-like membranes described the distribution of lipids and LPS molecules around PelB. While the apolar grooves formed at the outer barrel surface serve for docking the acyl chains, Arg/Lys clusters within the otherwise anionic extracellular interface facilitate local interactions with the phosphate groups of LPS. A number of approaches can be employed for characterizing PelBC:lipid interactions, also in its native membranes of *Pseudomonas* species. Recently, multiple studies highlighted the potential of amphipathic polymers for extraction of

membrane proteins, followed by the structural and lipidomics analysis[22], though also effects of specific membrane mimetics on a protein structure have been demonstrated[23]. As a complementary tool, computational simulations of the protein:lipid interactions, also in combination with cryo-EM data, allows identifying the interaction hotspots and even the identity of the involved lipids[24]. Beyond the specific protein:lipid interaction, it remains to be shown whether the observed tilt of the PelC ring relatively to the PelB axis has an effect on the membrane morphology, e.g., increased curvature at the periplasmic side, which could be potentially examined when studying PelBC embedded into nanodiscs of larger dimensions[13].

Although resolved in a uniform conformation and in the absence of the substrate, the structure of the PelBC complex provides valuable hints on the polysaccharide transport mechanism. It has been previously suggested that the negative charge at the central pore of PelC is required for electrostatic funneling of the cationic polysaccharide into the membrane channel. However, our data reveal that Asp-119, the key anionic residue within the flexible loop, is required for PelB:PelC docking, as it builds multiple subunit-specific interactions at the interface within the asymmetric complex (Fig. 9). Thus, the polysaccharide transport is rather dependent on the negative potential within the PelB barrel interior, i.e., the charged β-strands 11–14 and extracellular loops. The structural analysis suggests that PelB is a sealed β-barrel, not permeable in its idle state resolved by cryo-EM. Indeed, the outer membrane of *P. aeruginosa* is known to lack porins, which would possibly allow passage of toxic agents across the membrane. Both the MD simulations of PelB in various environments and in vitro analysis of PelB mutants suggest that the opening of a tunnel for the exopolysaccharide secretion is provided by a movement of Plug-S, the extracellular loop aligned with the periplasmic TPR domains and the anionic wall inside the β-barrel. Remarkably, Plug-S is located in a direct proximity to Tyr-1103 from β-strand 12 (Fig. 3C and Supplementary Figs. 7 and 15), a residue which is highly conserved among PelB homologs from different species, including thermophiles, such as *Sulphurihydrogenibium azorense* (gene SULAZ_0918) and *Persephonella marina* (gene PERMA_1356), and also found in the pEtN-cellulose transporter BcsC as Tyr-1030[14]. The residue likely contributes to the channel, where it may coordinate the polysaccharide chain via CH-pi interactions with pyranose rings. Here, further structural and biophysical analysis will be required to reconstruct the path of the Pel chain across the PelB barrel.

The necessity of the PelC ring and the importance of the involved PelC:lipid and PelC:PelB interactions remain puzzling. PelC subunits extensively interact with the TPR domains of PelB, which potentially serve as molecular rails for the Pel exopolysaccharide through the periplasm, resembling the routes followed by polypeptide chains and/or phospholipids in TamB and lipid A in LptA transport proteins[25,26]. In the resolved structure, the groove of the TPR domain is aligned with the pore at the opposite side of PelB, with a broad electronegative surface in between, thus forming a continuous path for the cationic polysaccharide chain. The PelC assembly may assist in stable positioning of the TPR domains above PelB, though other transporters, BcsC and PgaA, equipped with similar TPR scaffolds do not require additional lipoproteins. Alternatively, PelC may facilitate the functionality of PelA, a bi-modal deacetylase/hydrolase enzyme of 105 kDa[7]. PelA interacts with PelB residues 332–436 within the TRP region, where it can access the exopolysaccharide Pel and de-acetylate GalNAc moieties. The dimensions of the full-size PelA make it possible then to reach the PelC ring at the outer membrane, as it is predicted by the modelled structure (Supplementary Fig. 26). As the high processivity of PelA may be required for efficient translocation of Pel, this additional interaction with PelC subunit K would stabilize the PelB-bound enzyme in the functional position. Testing this interaction in vivo and in vitro, also with help of structural analysis, should explain the necessity of this peculiar architecture and result in a comprehensive model of the exopolysaccharide export at the cellular boundary membrane.

Methods

Molecular cloning and protein expression

Gene sequence encoding *P. aeruginosa* PAO1 PelB (PA3063) residues 762–1193 with the conventional N-terminal pectate lyase signal peptide and an octa-histidine tag was synthesized by GenScript (Leiden, Netherlands). The *pelC* gene (PA3062) with the signal peptide of *E. coli* Lpp was synthesized by BioCat GmbH (Heidelberg, Germany). These synthesized genes were subsequently cloned into pETDuet-1 vector, *pelC* in MCS1 (restriction sites NcoI/HindIII) and *pelB* in MCS2 (NdeI/KpnI) (restriction enzymes from New England Biolabs GmbH). For expression of PelB variants, pETDuet-1-based plasmids contained only the respective *pelB* genes. To introduce deletions in loops of the PelB β-barrel, the plasmid was amplified by PCR excluding the target DNA fragment and the template DNA was eliminated upon treatment with DpnI (all used primer sequences are listed in supplementary Table 2). Subsequently, the purified DNA underwent phosphorylation using T4 polynucleotide kinase and ligation employing T4 ligase. Molecular cloning was performed using chemically competent *E. coli* DH5α cells. All enzymes were from New England Biolabs. DNA isolation was performed with PCR & Gel Clean-Up and NucleoSpin Plasmid isolation kits (Macherey-Nagel). The sequences of the recombinant plasmids were confirmed through sequencing (Eurofins Genomics).

E. coli C41(DE3) Δ*ompF* Δ*acrAB* cells[11] harbouring the recombinant plasmids were cultured in Luria Bertoni (LB) medium containing 100 μg/mL ampicillin at 37 °C with shaking at 180 rpm. Upon reaching optical density at 600 nm (OD_{600}) of 0.6 to 0.8, protein expression was induced by addition of 0.5 mM isopropyl-β-thiogalactopyranoside (IPTG), followed by incubation for 3 h at 30 °C. Cells were harvested by centrifugation at 5000 × *g* for 15 min at 4 °C. The cell pellets were resuspended in 20 mL resuspension buffer (40 mM HEPES pH 7.4, 150 mM NaCl, 5% glycerol). 0.2 mM AEBSF as well as DNase were added prior to the cell lysis step. Cells were lysed using a shear force (LM20 microfluidizer, Microfluidics), followed by centrifugation at 20,000 × *g* for 15 min at 4 °C to remove the debris. To isolate the total membrane fraction, the clarified lysate underwent a further centrifugation step at 205,000 × *g* for 1 h at 4 °C (60Ti rotor, Beckman Coulter). The membrane pellet was then resuspended in the resuspension buffer, shock-frozen and stored at −80 °C until further use.

The localization of the PelBC complex in the outer membrane was verified through ultracentrifugation in sucrose gradient. The total membrane extracts were loaded onto a continuous 20–70% sucrose gradient (w/v) in the resuspension buffer prepared using an automated Gradient Station (BioComp Instruments Ltd.). Subsequently, the gradient was centrifuged at 107,000 × *g* for 16 h at 4 °C (SW 40 rotor, Beckman Coulter). After centrifugation, the gradient was fractionated from top to bottom using the Gradient Station combined with the UV spectrometer and the fractions were analyzed by SDS-PAGE.

PelBC isolation and reconstitution into nanodiscs

For isolation of the PelBC complexes and the variants of PelB, the total membranes were solubilized with 2% DDM (Glycon Biochemicals GmbH) in IMAC buffer (50 mM HEPES pH 7.4, 300 mM KCl, 5% glycerol) in 10x volume relative to the membranes. After 90 min incubation, the non-solubilized material was removed by centrifugation at 21,000 × *g* for 15 min at 4 °C. The soluble fraction was supplemented with 2 mM histidine and loaded onto a gravity-flow column packed with 400 μL pre-equilibrated Ni^{2+}-NTA agarose beads (Protino, Macherey-Nagel). Binding was carried out for 90 min at 4 °C with rotation, the flow-through fraction was collected, and the resin was washed four times with 2 mL of the IMAC buffer supplemented with 20 mM histidine and 0.05% DDM. The target protein complex was eluted with the IMAC buffer supplemented 200 mM histidine and

0.05% DDM. Three elution fractions of 800 μL each were pooled, concentrated to 500 μL and injected onto Superdex 200 Increase 10/300 GL size-exclusion chromatography (SEC) column in SEC buffer (50 mM HEPES pH 7.4, 150 mM NaCl, 0.03% DDM) connected to ÄKTA go system (Cytiva). Elution fractions were analysed via SDS-PAGE, and the protein concentration was determined spectrophotometrically based on calculated extinction coefficients of 95,910 $M^{-1} \times cm^{-1}$ for PelB and 497,430 $M^{-1} \times cm^{-1}$ for PelBC assuming 1:12 stoichiometry. Stability of the isolated PelB variants was analysed by differential scanning fluorimetry (nanoDSF) using Prometheus NT.48 instrument (NanoTemper Technologies GmbH). The thermal denaturation was assessed by monitoring the intrinsic fluorescence at 330 and 350 nm between 20 and 95 °C through a temperature ramp of 1.5 °C/min.

Nanodisc-forming protein MSP1D1 was expressed and isolated as described[13]. A lipid mixture composed of POPC:POPG lipids (molar ratio 70:30, Avanti Polar Lipids) was prepared in chloroform, the solvent was evaporated, and the lipids were suspended to the final concentration of 5 mM in 50 mM HEPES pH 7.4 and 150 mM NaCl. The formed liposomes were extruded stepwise through 1 μm and 200 nm track-etch membranes (Whatman) and solubilized using 0.5% DDM for 15 min at 40 °C. Subsequently, the purified PelBC complex was mixed with MSP1D1 and lipids at the molar ratio of 1:4:500 followed by 20 min incubation on ice. After the incubation, pre-washed Bio-Beads SM-2 sorbent (Bio-Rad Laboratories) was added and incubated overnight at 4 °C with rotation. The reconstitution reaction was loaded onto Superdex 200 Increase 10/300 GL column connected to ÄKTA pure (Cytiva), fractionated in 50 mM HEPES pH 7.4 with 150 mM NaCl and analysed via SDS-PAGE. The fractions containing the assembled PelBC complexes in nanodiscs were pooled together, concentrated using Amicon Ultra filters with cut-off of 30 kDa (Millipore) and flash-frozen prior further usage in cryo-EM experiments.

Cryo-EM sample preparation and data collection

Before plunge-freezing, PelBC nanodiscs at concentration of 0.57 μM (equals to 0.17 mg/mL) were supplemented with (1H, 1H, 2H, 2H-perfluorooctyl)-β-D-maltopyranoside (Anatrace) to a final concentration of 0.03 % to promote random orientation of the particles, and 3.5 μL of the sample were applied to glow-discharged Quantifoil Au 300 mesh R2/2 grids with an additional 3 nm layer of carbon. After incubation for 45 s, the grids were blotted for 3 s and plunge-frozen in liquid ethane using Vitrobot Mark IV (Thermo Fisher Scientific). Data collection was performed at 300 keV using Titan Krios microscope equipped with a Falcon 4i direct electron detector and a SelectrisX Energy Filter (all Thermo Fisher Scientific) at a physical pixel size of 0.727 Å. Dose-fractioned movies were collected in a defocus range from −0.5 to −3.0 μm with a total dose of 60 e- per $Å^2$ and fractionated in 60 frames to obtain a total dose of 1 e- per $Å^2$ per frame.

Cryo-EM data processing and model building

Gain correction, movie alignment, and summation of movie frames was performed using MotionCor2[27]. Further processing was carried out in cryoSPARC v4.4[28]. A total of 31,712 micrographs were selected and CTF parameters were estimated using PatchCTF. Particle picking was carried out by running a Blob Picker job on a subset of 4040 micrographs. An initial set of 2,345,182 particles were extracted with a box size of 360 pixels (corresponds to 261 Å), binned four times. After 2D classification, selected 2D classes containing 584,172 particles were used in one round of ab-initio reconstruction, followed by multiple rounds of heterogeneous refinement, which resulted in one good class with 386,144 particles. The particles of this class were re-extracted, binned two times, and further refined by non-uniform refinement. Selected templates were used to pick particles on the remaining micrographs of the data set. After multiple rounds of 2D classification a set of 4,773,524 particles was selected for downstream processing. The particles were sorted by heterogeneous refinement, using the refined volume and the three additional volumes from the ab-initio job. After multiple rounds of heterogeneous refinement, 3,174,321 particles converged to one good class, which was subsequently refined by non-uniform refinement. To further improve the resolution of the PelB β-barrel, masked 3D classification was performed and particles belonging to the classes with best resolved features were combined in a non-uniform refinement job (613,225 particles). Further 3D classification was carried out to improve the N-terminal TPR domain of PelB. A final set of 124,181 particles that converged to the best-resolved class was extracted without binning and refined by a non-uniform refinement job to a final resolution of 2.52 Å.

The complex model began with an AlphaFold2 prediction, which was fitted into the final cryo-EM volume. Subsequent manual adjustments were performed using the COOT program (WinCoot version 0.9.8.92)[29], with ongoing refinement achieved through the option real-space refinement in the PHENIX program (version 1.20.1-4487)[30]. To model the PelC anchor chains, the fatty acid tails (and the glycerol backbone) of the phosphatidylethanolamine structure (PDB: PTY) were extracted and fitted into the density. The subunits of PelC were labelled from A to L, starting with the subunit closest to the first and last β-strand of the PelB barrel.

Single-channel conductivity recordings

An electrophysiology chamber composed of two 500 μL compartments (*cis* and *trans*) separated by a 20 μm PTFE film with a central aperture of ~100 μm was used for all experiments. To make a lipid bilayer, a drop of hexadecane (4% v/v in pentane) was loaded on the *trans*-side of the PTFE film, and allowed to evaporate for ~2 min. Each compartment was then filled with 400 μL buffer (1 M NaCl, 20 mM citric acid pH 3.4) and ~20 μL DPhPC lipid solution were added (5 g/L in pentane, w/v). Ag/AgCl electrodes were inserted to each compartment: *Trans* was the connecting electrode, *cis* was the ground electrode. By lowering and raising the buffer level in one compartment above the aperture, a lipid bilayer could be formed. The bilayer was equilibrated for 5–10 min before PelB was added. PelB samples were diluted 100–5000× with 15 mM Tris-HCl pH 7.5, 150 mM NaCl, 0.02% DDM and then added to the *cis* chamber in a small volume (below 0.1–0.3 μL). Generally, the protein would insert upon applying the transmembrane potential of −150 mV, while breaking/reforming the bilayer promoted insertion into the membrane. The conductivity data were recorded under a negative applied potential (−150 mV), using an Axopatch 200B patch clamp amplifier connected to a DigiData 1440 A/D converter (Axon Instruments), and using Clampex 10.7 software (Molecular Devices, LLC). Data recordings were made in gap-free setting. Measurements were conducted at 20 °C, 1 M NaCl, 20 mM citric acid pH 3.4 with a 50 kHz sampling frequency and a 10 kHz Bessel filter. Data was digitally filtered with a Gaussian low-pass filter with 2 kHz cut-off prior to analysis. Recordings were analyzed with Clampfit 10.7 software (Molecular Devices, LLC).

In most traces, PelB entered the bilayer in multitude, and the single-channel conductivity was determined from the largest common denominating current. Trace parts with two or more PelB proteins were excluded from the analysis, so only single channels were further examined. Per PelB variant, electrophysiology traces of 8 to 13 s recorded for at least 5 individual molecules were used for analysis. The measured instant currents of individual PelB molecules were plotted as all-points histogram with bin width of 0.5 pA. The regions of low (currents below 25 pA), median (25–100 pA) and high conductivity (above 100 pA) were analyzed individually. The occurrence/occupancy of each conductivity range for individual PelB molecules was calculated by dividing the corresponding count of events over the total counts within the trace and presented as box plots. The outliers were identified according to Tukey's definition, i.e., beyond 1.5 of interquartile range (IQR), while no far outliers were detected (beyond 3 × IQR).

The values were presented as box plots. The average conductance for PelB variants within each range was calculated as:

$$C[\mathrm{nS}] = \frac{I[\mathrm{pA}]}{V[\mathrm{mV}]} \quad (1)$$

The ion currents and the corresponding conductance values of the sub-states resolved for PelB ΔPlug-S were determined based on Gaussian fits of the individual histograms. Graphs were generated with Prism 9.5.0 (GraphPad Software) and Igor Pro 9 (Wavemetrics).

Molecular dynamics simulations

All MD simulations reported were performed on HILBERT from the Heinrich Heine University Düsseldorf and SuperMUC-NG at Leibniz Supercomputing Centre in Munich. All systems are summarized in Table 1 and in Supplementary Fig. 12. Two different LPS molecules with its components which are defined as the default for *E. coli* and *P. aeruginosa* were acquired from in CHARMM-GUI (Supplementary Fig. 12D)[31–33]. All atomistic systems were created by CHARMM-GUI and the Ca^{2+} were added in the LPS layer. Furthermore, we used the *mdp* scripts for energy minimization, equilibration in five steps and production run from CHARMM-GUI web server since they are optimized for protein-membrane simulations. The energy was minimized to 1000 kJ mol^{-1} nm^{-1} using the steepest descent algorithm, followed by five-step equilibration to the desired temperature of 298 K (25 °C) or 310 K (37 °C) and pressure of 1 atm to mimic the physiological environment. First, two *NVT* equilibration steps were applied to keep constant the number of atoms (*N*), the box volume (*V*), and temperature (*T*), followed by three-step *NpT* equilibration to adjust the pressure (*p*). The protein's and lipid's heavy atoms were restrained to allow the water molecules and ions to relax around the solute but they were decreased by every equilibration step. The Berendsen thermostat was employed to regulate the temperature in the *NVT* simulations, while the Berendsen thermostat and the semi–isotropic Berendsen barostat were employed for the *NpT* simulations. The PME method was applied to calculate long-range electrostatic interactions with periodic boundary conditions. The van der Waals and Coulombic interaction cutoffs were set to 1.2 nm using the LINCS algorithm to constrain all bond-lengths to hydrogens. Production MD runs were performed for 0.5 μs with a time step of 2 fs by recording the coordinates and velocities every 20 ps as well as the Nosé-Hoover thermostat and the semi–isotropic Parrinello-Rahman barostat.

For all-atomistic MD simulations, the CHARMM36m force field[34,35], modified TIP3P water and GROMACS 2018/2021[36–38] were accomplished while using a pressure of 1 bar. All systems were created by CHARMM-GUI and Ca^{2+} were added in the LPS layer. As protein structure, we used the cryo-EM structure of the PelB β-barrel (residues 877–1193) and the models of the truncated variants, PelB ΔPlug-O and PelB ΔPlug-S[9,39]. When performing the simulations at pH 3.5, the following solvent-exposed histidine, aspartate and glutamate residues were protonated: Asp-895, His-906, Asp-909, Glu-916, His-923, Glu-963, Glu-983, Glu-991, Glu-994, Glu-1047, Asp-1066, Glu-1073, Asp-1079, His-1084, Glu-1141, Glu-1143, and Asp-1149.

To check whether lipids and ions clustered within and around the PelB β-barrel in the in the *xz*-plane, we created density maps of ions and water via *gmx densmap*. Here, the direction to average was over *y*-axis, the grid size was set to 0.08 and the unit was molecule per nm^3. We used the DuIvyTools (https://github.com/CharlesHahn/DuIvyTools) to change the format from *xpm* to a matrix *dat* file (*dit xpm2dat*), which could use for plotting the density maps via an own python script.

For describing the stability and flexibility of PelB barrel during the MD simulations, the root-mean-square fluctuations (RMSF) of the Cα atoms around their average positions was calculated for each residue. Similarly to the b-factor, the RMSF value represents the positional change of the selected atoms as time–average, where the residue with a value over 2 Å was defined as flexible. To analyze PelB interactions, we generated average distance maps per residue between **(1)** the extracellular loops, as well as **(2)** to the ions and water, and **(3)** to LPS. We calculated the minimal distance (*gmx mindist*) between the groups by following computing the average distance over time.

To determine the geometry and the dimensions of the tunnel within the PelB β-barrel and its variants, HOLE algorithm (Smart et al., 1996) was employed in combination with the algorithm by MDanalysis (https://docs.mdanalysis.org/1.1.1/documentation_pages/analysis/hole2.html). The tunnels were visualized via VMD. To characterize the overall stability of the PelB barrel in the membrane, we further conducted clustering analyses using the relevant algorithm[40] as implemented in GROMACS. Here, the root-mean-square deviation (RMSD) is a measurement of the Cartesian deviation to a reference structure (mostly the start structure of the MD or a crystal structure). The clustering was employed for all Cα atoms with a RMSD cutoff value of 0.15 nm by using the fitting function before calculating the RMSD on the structure to identify cluster membership. Plotting was performed using Python (v3.10.12) or Gnuplot (v5.4 patchlevel 2).

Software

Protein structures were visualized, analyzed, and rendered for figures using PyMOL (v2.5.0, Schrödinger, LLC) and ChimeraX (v1.7.1, UCSF). Figures were assembled using Inkscape (v1.3.1) and Canvas X (ACD Systems Inc.). Software used for data analysis or plotting is listed in the respective section above.

Reporting summary

Further information on research design is available in the Nature Portfolio Reporting Summary linked to this article.

Data availability

Coordinates and EM map have been deposited at the Protein Data Bank (PDB) under accession code 9H80 and the Electron Microscopy Data Bank (EMDB) under accession code EMD-51916. The MD data have been deposited to the Figshare database (https://figshare.com/s/43b1c784579cb156bdc7). Source data are provided with this paper.

References

1. Nelson, R. E. et al. National estimates of healthcare costs associated with multidrug-resistant bacterial infections among hospitalized patients in the United States. *Clin. Infect. Dis.* **72**, S17–S26 (2021).
2. Gheorghita, A. A., Wozniak, D. J., Parsek, M. R. & Howell, P. L. Pseudomonas aeruginosa biofilm exopolysaccharides: assembly, function, and degradation. *FEMS Microbiol Rev.* **47**, fuad060 (2023).
3. Whitfield, G. B. et al. Discovery and characterization of a Gram-positive Pel polysaccharide biosynthetic gene cluster. *PLoS Pathog.* **16**, e1008281 (2020).
4. Le Mauff, F. et al. The Pel polysaccharide is predominantly composed of a dimeric repeat of alpha-1,4 linked galactosamine and N-acetylgalactosamine. *Commun. Biol.* **5**, 502 (2022).
5. Jennings, L. K. et al. Pel is a cationic exopolysaccharide that cross-links extracellular DNA in the Pseudomonas aeruginosa biofilm matrix. *Proc. Natl. Acad. Sci. USA* **112**, 11353–11358 (2015).
6. Whitfield, G. B. et al. Pel polysaccharide biosynthesis requires an inner membrane complex comprised of PelD, PelE, PelF, and PelG. *J. Bacteriol.* **202** https://doi.org/10.1128/JB.00684-19 (2020).
7. Marmont, L. S. et al. PelA and PelB proteins form a modification and secretion complex essential for Pel polysaccharide-dependent biofilm formation in Pseudomonas aeruginosa. *J. Biol. Chem.* **292**, 19411–19422 (2017).
8. Marmont, L. S. et al. Oligomeric lipoprotein PelC guides Pel polysaccharide export across the outer membrane of Pseudomonas aeruginosa. *Proc. Natl. Acad. Sci. USA* **114**, 2892–2897 (2017).

9. Abramson, J. et al. Accurate structure prediction of biomolecular interactions with AlphaFold 3. *Nature* **630**, 493–500 (2024).
10. Goyal, P. et al. Structural and mechanistic insights into the bacterial amyloid secretion channel CsgG. *Nature* **516**, 250–253 (2014).
11. Kanonenberg, K. et al. Shaping the lipid composition of bacterial membranes for membrane protein production. *Micro. Cell Fact.* **18**, 131 (2019).
12. Hagn, F., Etzkorn, M., Raschle, T. & Wagner, G. Optimized phospholipid bilayer nanodiscs facilitate high-resolution structure determination of membrane proteins. *J. Am. Chem. Soc.* **135**, 1919–1925 (2013).
13. Ritchie, T. K. et al. Chapter 11 - Reconstitution of membrane proteins in phospholipid bilayer nanodiscs. *Methods Enzymol.* **464**, 211–231 (2009).
14. Acheson, J. F., Derewenda, Z. S. & Zimmer, J. Architecture of the cellulose synthase outer membrane channel and its association with the periplasmic TPR domain. *Structure* **27**, 1855–1861 e1853 (2019).
15. Wang, Y. et al. Structural basis for translocation of a biofilm-supporting exopolysaccharide across the bacterial outer membrane. *J. Biol. Chem.* **291**, 10046–10057 (2016).
16. Morgan, J. L., Strumillo, J. & Zimmer, J. Crystallographic snapshot of cellulose synthesis and membrane translocation. *Nature* **493**, 181–186 (2013).
17. Willems, K., Van Meervelt, V., Wloka, C. & Maglia, G. Single-molecule nanopore enzymology. *Philos. Trans. R. Soc. Lond. B Biol. Sci.* **372**, 20160230 (2017).
18. Liang, B. & Tamm, L. K. Structure of outer membrane protein G by solution NMR spectroscopy. *Proc. Natl. Acad. Sci. USA* **104**, 16140–16145 (2007).
19. Nikaido, H. & Rosenberg, E. Y. Porin channels in Escherichia coli: studies with liposomes reconstituted from purified proteins. *J. Bacteriol.* **153**, 241–252 (1983).
20. Wilton, M., Charron-Mazenod, L., Moore, R. & Lewenza, S. Extracellular DNA acidifies biofilms and induces aminoglycoside resistance in Pseudomonas aeruginosa. *Antimicrobial Agents Chemother.* **60**, 544–553 (2016).
21. Whitney, J. C. et al. Structural basis for alginate secretion across the bacterial outer membrane. *Proc. Natl. Acad. Sci. USA* **108**, 13083–13088 (2011).
22. Krishnarjuna, B. & Ramamoorthy, A. Detergent-free isolation of membrane proteins and strategies to study them in a near-native membrane environment. *Biomolecules* **12**, 1076 (2022).
23. Hoffmann, L. et al. The ABC transporter MsbA in a dozen environments. *Structure* **33**, 916-923e4 (2025).
24. Ansell, T. B. et al. LipIDens: simulation assisted interpretation of lipid densities in cryo-EM structures of membrane proteins. *Nat. Commun.* **14**, 7774 (2023).
25. Josts, I. et al. The structure of a conserved domain of TamB reveals a hydrophobic beta taco fold. *Structure* **25**, 1898–1906.e1895 (2017).
26. Suits, M. D., Sperandeo, P., Deho, G., Polissi, A. & Jia, Z. Novel structure of the conserved gram-negative lipopolysaccharide transport protein A and mutagenesis analysis. *J. Mol. Biol.* **380**, 476–488 (2008).
27. Zheng, S. Q. et al. MotionCor2: anisotropic correction of beam-induced motion for improved cryo-electron microscopy. *Nat. Methods* **14**, 331–332 (2017).
28. Punjani, A., Rubinstein, J. L., Fleet, D. J. & Brubaker, M. A. cryoSPARC: algorithms for rapid unsupervised cryo-EM structure determination. *Nat. Methods* **14**, 290–296 (2017).
29. Emsley, P., Lohkamp, B., Scott, W. G. & Cowtan, K. Features and development of Coot. *Acta Crystallogr. Sect. D.* **66**, 486–501 (2010).
30. Liebschner, D. et al. Macromolecular structure determination using X-rays, neutrons and electrons: recent developments in Phenix. *Acta Crystallogr. D. Struct. Biol.* **75**, 861–877 (2019).
31. Jo, S., Kim, T., Iyer, V. G. & Im, W. CHARMM-GUI: a web-based graphical user interface for CHARMM. *J. Comput. Chem.* **29**, 1859–1865 (2008).
32. Wu, E. L. et al. CHARMM-GUI Membrane Builder toward realistic biological membrane simulations. *J. Comput. Chem.* **35**, 1997–2004 (2014).
33. Lee, J. et al. CHARMM-GUI membrane builder for complex biological membrane simulations with glycolipids and lipoglycans. *J. Chem. Theory Comput.* **15**, 775–786 (2019).
34. Huang, J. & MacKerell, A. D. Jr. CHARMM36 all-atom additive protein force field: validation based on comparison to NMR data. *J. Comput. Chem.* **34**, 2135–2145 (2013).
35. Huang, J. et al. CHARMM36m: an improved force field for folded and intrinsically disordered proteins. *Nat. Methods* **14**, 71–73 (2017).
36. Abraham, M. J. et al. GROMACS: high performance molecular simulations through multi-level parallelism from laptops to supercomputers. *SoftwareX* **1-2**, 19–25 (2015).
37. GROMACS 2021.6 Source code (2021.5) https://doi.org/10.5281/zenodo.6801839 (Zenodo, 2022).
38. GROMACS 2021.6 Manual (2021.5) https://doi.org/10.5281/zenodo.6801839 (Zenodo, 2022).
39. Mirdita, M. et al. ColabFold: making protein folding accessible to all. *Nat. Methods* **19**, 679–682 (2022).
40. Daura, X. et al. Peptide folding: when simulation meets experiment. *Angew. Chem. Int. Ed.* **38**, 236–240 (1999).
41. Li, A., Schertzer, J. W. & Yong, X. Molecular dynamics modeling of Pseudomonas aeruginosa outer membranes. *Phys. Chem. Chem. Phys.* **20**, 23635–23648 (2018).

Acknowledgements

We would like to thank Susanne Rieder and Charlotte Ungewickell for the support with cryo-EM sample preparation, and Albert Guskov (University of Groningen) for the initial cryo-EM trials. We thank Birgit Strodel, Florian Altegoer, and Sakshi Khosa (HHU Düsseldorf) and Jens Reiners (Center for Structural Studies, HHU Düsseldorf) for fruitful discussions and commenting on the manuscript. We gratefully acknowledge the computing time granted through the Leibniz Supercomputing Centre (LRZ) of the Bavarian Academy of Sciences on the supercomputer SuperMUC-NG (project pn39gu). Computational infrastructure and support at Heinrich Heine University Düsseldorf were provided by the Centre for Information and Media Technology. The hybrid computer cluster purchased from funding by DFG, project number INST 208/704-1 FUGG, and the Centre for Information and Media Technology (HHU Düsseldorf). The study was supported by the German Research Foundation (Deutsche Forschungsgemeinschaft, DFG; grants Nr. Ke1879/6 to A.K. and Nr. 510674444 to R.B.), the Ministry of Culture and Science of the State of Northern Rhine-Westfalen (project "ACCeSS" to A.K.), the European Research Council (ERC, Advanced Grant Nr. ADG 885711 to R.B.) and the Dutch Research Council (Nederlandse Organisatie voor Wetenschappelijk Onderzoek, NWO; grant Nr. VI.C.192.068 to G.M.).

Author contributions

M.B. carried out sample preparations and biochemical analysis, and built the structural model based on the cryo-EM data. C.R.H. curated the cryo-EM data collection and carried out the data processing and analysis. S.A.P.S. carried out and analyzed single-channel conductivity experiments. J.L. performed molecular dynamics simulations. O.B. collected and curated the cryo-EM data. R.B. and G.M. curated the data analysis and secured funding. A.K. designed and coordinated the project, curated the data analysis, and secured funding. All the authors wrote and edited the manuscript.

Funding

Open Access funding enabled and organized by Projekt DEAL.

Competing interests
The authors declare no competing interests.

Additional information
Supplementary information The online version contains supplementary material available at https://doi.org/10.1038/s41467-025-60605-8.

Correspondence and requests for materials should be addressed to Roland Beckmann or Alexej Kedrov.

Peer review information *Nature Communications* thanks Tim Rasmussen and the other, anonymous, reviewer for their contribution to the peer review of this work. A peer review file is available.

Chapter 3

Discussion and Outlook

3.1 SecYEG-YidC-mediated insertion of a multi-pass membrane protein in bacteria

A long-standing model of multi-pass membrane insertion is the sequential model, which posits that after the first or the second TMD has been inserted in the (N_{exo}) topology, downstream TMDs are inserted via the Sec61/SecY lateral gate in successive (N_{cyt}) and (N_{exo}) orientations (**Figure 3.1**). Even though the requirement of Sec61/SecY, central to this sequential insertion, has been experimentally confirmed for signal peptides, single-pass type II and single-pass type III proteins, there are exceptions where, for example, YidC can insert a sequence of two TMDs connected through a short loop, probably as a single unit (i.e. pairwise insertion), in a Sec61/SecY independent fashion [Facey et al., 2007, Celebi et al., 2006, van Bloois et al., 2006, Smalinskaitė and Hegde, 2023]. In addition, the downstream TMDs of some multi-pass proteins are not able to open Sec61/SecY's lateral gate, while others are insensitive to lateral gate inhibitors, suggesting that alternative mechanisms of insertion exist. Notably, Oxa1 and YidC can insert all the TMDs of some multi-pass membrane proteins when the connecting loops are shorter than about 50 amino acids [Hegde and Keenan, 2022, Hennon et al., 2015], further suggesting that an expanded model, where SecY and Oxa1 members associate and alternate during the insertion of successive TMDs, depending on the length of the interconnecting loops or the hydrophobicity of their sequence, would reconcile experimental observations that are not

expected from the sequential insertion model. The cryo-EM structures and biochemical evidence of Sec61-associated multiprotein complexes, designated as the multi-pass translocon (MPT) [Smalinskaitė et al., 2022, Sundaram et al., 2022], which include members of the Oxa1 family and membrane protein chaperones located at the opposite side of Sec61/SecY's lateral gate, have provided experimental evidence for such an expanded model by visualising an alternative insertion route at the back of Sec61/SecY (**Figure 1.6C**). However, the fact that many of the constituent proteins do not have homologs in prokaryotes has limited its generalisation, as it could, in principle, represent an evolutionary feature of higher eukaryotes.

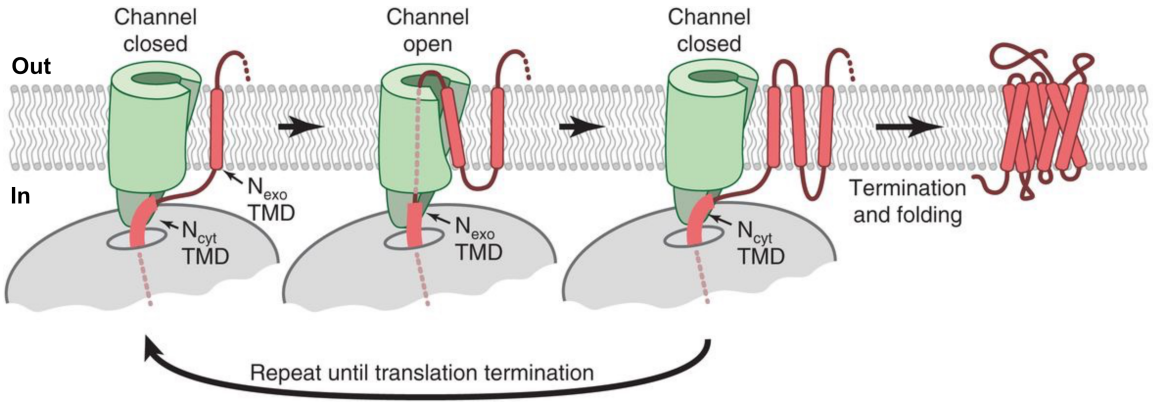

Figure 3.1: The sequential insertion model. After the first TMD of a multi-pass membrane protein has been inserted in the N_{exo} topology, subsequent TMDs are inserted through SecY/Sec61α's lateral gate in a sequential N_{cyt}-N_{exo} topology. This cycle can repeat until all the TMDs have been inserted. Figure adapted from [Smalinskaitė and Hegde, 2023].

In Publication 1, the structure of a bacterial multi-pass translocon constituted by the heterotrimeric complex SecYEG and the Oxa1 family member YidC is reported for the first time, revealing a route of insertion for the multi-pass membrane protein NuoK (**Figure 3.2**). In line with the organisation of the eukaryotic MPT, YidC is found at the back of SecYEG, enclosing a lipid-filled cavity where density for one NuoK's TMDs (TMD2) is present. NuoK consists of three TMDs, the first of which is inserted in a type III (N_{exo}) topology, followed by a short (three amino acids), positively charged cytoplasmic loop that connects it to TMD2 (N_{cyt}). TMD3 (N_{exo}) is connected to TMD2 by a loop of seven amino

acids, and has a cytoplasmic, C-terminal extension of 13 amino acids (**Figure 3.3A**). The insertion of these TMDs depends on both SecYEG and YidC [Price and Driessen, 2010], yet the role and order of recruitment of each component is unclear. Cell-free synthesis of a modified NuoK substrate (NuoK^{86}), containing all three TMDs but replacing the C-terminal extension by a SecM derived stalling sequence (**Figure 3.3B**), led to the isolation of an insertion intermediate displaying continuous substrate density from the PTC to the lipid bilayer in the nanodisc. This allowed building an atomic model for the nascent chain *de novo*, enabling the assignment of TMD2 and TMD3 to the α-helical densities observed exiting the ribosome tunnel (TMD3) and inserted between SecYEG and YidC (TMD2).

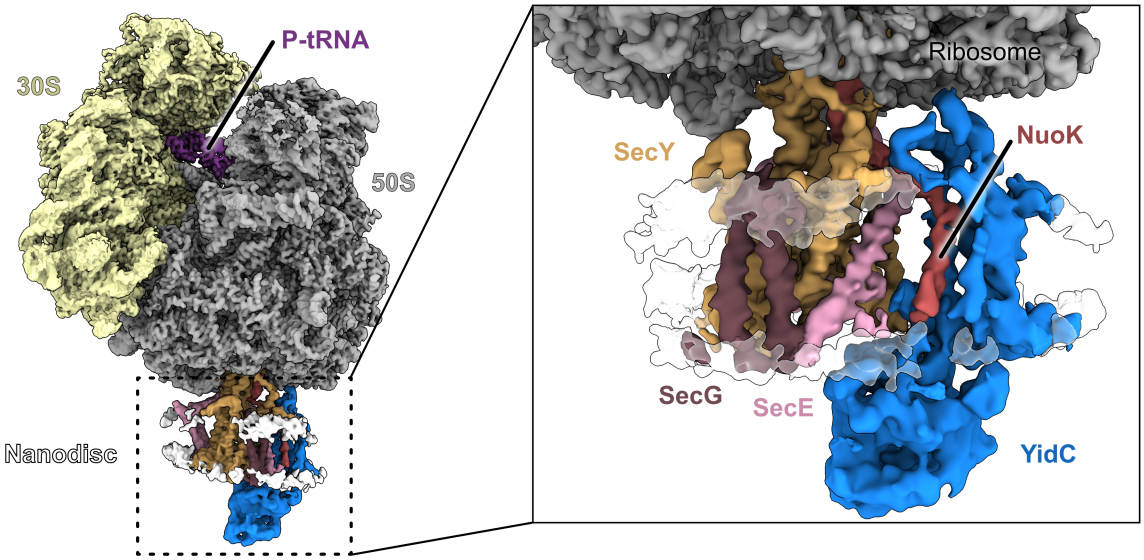

Figure 3.2: Structure of the SecYEG-YidC-NuoK complex. Main panel: cryo-EM reconstruction of the NuoK-RNC, displaying the 70S ribosome docked on the nanodisc-reconstituted SecYEG-YidC complex and the NuoK substrate inserted at the back of SecYEG, between SecE and YidC. The 30S subunit is shown in light yellow, the 50S in grey, the P-tRNA in purple, SecY in yellow, SecE in pink, SecG in brown, YidC in blue, NuoK in red and the nanodisc density in white. Inset: close-up view of the nanodisc region of the map shown in the same colouring scheme as in the main panel, but displaying the nanodisc density in transparency for clarity. Figure adapted from [Busch et al., 2025].

One determining factor of YidC recruitment during NuoK insertion seems to be the length of the substrate protruding from the ribosome exit tunnel, as revealed by studying a shorter version where the TMD3 is deleted (NuoK^{48}, **Figure 3.3B**). The cryo-EM data

collected from a sample obtained by cell-free synthesis of NuoK^{48} reveals only classes where the ribosome is already docked at the membrane via interactions with the loops 6/7 and 8/9 of SecYEG, in a similar conformation to one previously observed for another membrane protein substrate [Kater et al., 2019], without detectable YidC density in the nanodisc or substrate density beyond the exit tunnel [Busch et al., 2025]. This would suggest that, in the *in vitro* setting used in Publication 1, only after a certain length of NuoK has exited the ribosome tunnel, YidC is recruited to assemble the MPT. Different conformational changes are concomitant with this recruitment, such as the bending of the C-terminal helix of SecYEG, potentially occluding the access to the protein channel, and a tilting of the ribosome relative to the membrane plane, with a hinge point at loop 6/7 [Busch et al., 2025], all absent when NuoK^{48} is synthesised instead of NuoK^{86}. Altogether, this suggests that the order of events in the *in vitro* system starts with the docking of the ribosome at SecYEG, followed by YidC recruitment and TMD1-TMD2 insertion. It is likely that the recruitment *in vivo* also depends on the length of substrate, however, it is not clear whether SecYEG would insert TMD1, triggering YidC recruitment, or if TMD1 is inserted after handing over from SRP to YidC, as observed for some type III substrates [Chitwood et al., 2018], followed by ribosome docking at SecYEG.

If TMD1 was inserted by SecYEG, the NuoK insertion could easily follow a sequential insertion, independently of YidC activity (**Figure 3.1**). This is, however, not the case *in vivo*, where reduced YidC expression leads to a defect in the assembly of the bacterial complex I (NADH dehydrogenase I) due to low levels of NuoK insertion [Price and Driessen, 2008]. Previously, to study the role of YidC, the negatively charged residues E36 and E72 in TMD2 and TMD3 (**Figure 3.3A**), respectively, were mutated to lysines, the main hypothesis being that YidC is required for the insertion of said negative residues into the membrane. This was verified by the observation that insertion levels for the E36K, E72K mutant in absence of YidC were in the same range as when both YidC and SecYEG were present in the membrane, as measured in an *in vitro* insertion experiment [Price and Driessen, 2010]. Although it can be concluded that SecYEG is able to take over the task of insertion of TMD2 and TMD3 when the negative charges are

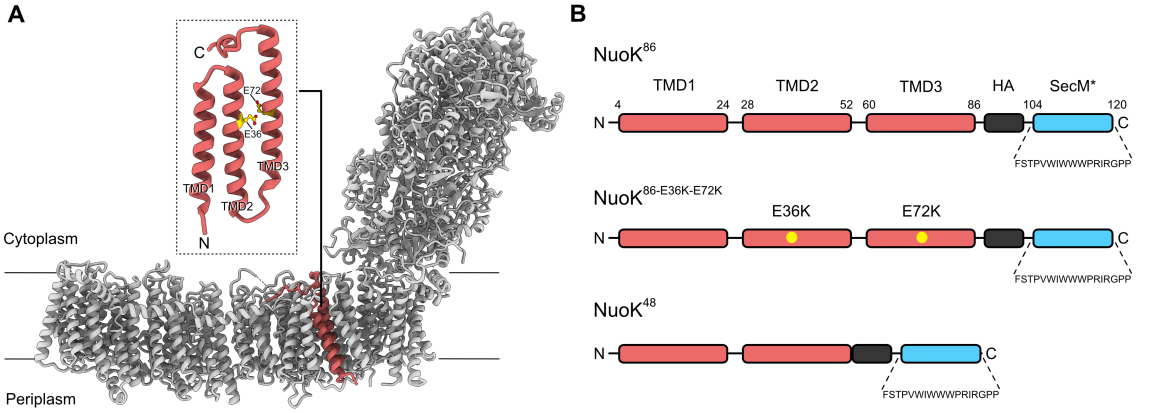

Figure 3.3: The NuoK substrate. (**A**) Localisation and topology of NuoK in the *E. coli* respiratory complex I (NADH dehydrogenase I, PDB: 7NYR). The position of residues E36 and E73 in TMD2 and TMD3, respectively, is highlighted. (**B**) Scheme of the constructs employed to obtain NuoK insertion intermediates. SecM*: stalling sequence based on SecM, HA: HA tag. Yellow circles represent the approximate position of mutations E36K and E72K in $NuoK^{86}$.

inverted, this does not necessarily imply that YidC becomes unable to handle the task. Furthermore, in the same study, single mutations were still more efficiently inserted by the combined action of SecYEG and YidC than by only SecYEG, indicating that the effect of the charge substitution on the overall insertion route is not solely due to a reduced capacity of YidC at handling positive charges in the TMDs. Consistent with this idea, cell-free expression of a mutant version of the NuoK construct containing the same mutations ($NuoK^{86-E36K-E72K}$) also leads to the assembly of the SecYEG-YidC MPT, as visualised by cryo-EM [Busch et al., 2025]. Despite the fact that the resolution in the nanodisc region is not high enough to allow a clear identification of NuoK density, it can be concluded that the charge inversion does not prevent YidC recruitment and subsequent assembly of the MPT.

A puzzling feature of the structure reported in Publication 1 is that TMD2 is inserted in the nanodisc in an N_{exo} orientation, in contrast with the topology observed *in vivo* (**Figure 3.3A**). One possibility is that this is the case *in vivo*, and the initial inverted topology is resolved when the (last) TMD3 is inserted, as observed for some multi-pass membrane proteins [Seppälä et al., 2010, Woodall et al., 2017, Seurig et al., 2019]. An-

other explanation is that a pairwise insertion of TMD1-TMD2 takes place because the *in vitro* system lacks a PMF, which would otherwise disfavour the translocation of the positively charged loop such that connects TMD1 and TMD2.

Taken together, these results provide, for the first time, a structural basis for the assembly of a bacterial MPT consisting of SecYEG and YidC. The "back-of sec" route followed by the nascent peptide is analogous to the one observed in eukaryotes, suggesting a conserved insertion mechanism for multi-pass membrane proteins. However, several questions regarding the mechanism of insertion of the SecYEG-YidC MPT remain open. One of them is whether the TMD1 is inserted via SecYEG or YidC. Even though it is likely that the insertion of TMD1 follows a similar route as other type III substrates and is thus inserted by YidC, an insertion by SecYEG cannot be ruled out. Studies of insertion in presence of lateral gate inhibitors might provide insights into the preferred route. Another unclear aspect is how the insertion of TMD2 and TMD3 proceeds after TMD1 has been inserted. As discussed before, they are not readily inserted by SecYEG, unless the negative charged residues E36 and E72 have both been replaced by positive charges, indicating that YidC preferentially inserts them either individually or in a pairwise manner. This leaves SecYEG with a more structural/chaperone role in the MPT for NuoK insertion. Indeed, it has recently been shown that apart from its translocase/insertase activity, SecYEG can act as a chaperone, facilitating folding of the TMDs [Ou et al., 2025]. Based on the results of Publication 1, a hydrophobic pocket formed at the exit of the tunnel, appears to facilitate the folding of the substrate as it leaves the ribosome, further supporting this role. Future investigation of different types of membrane protein substrates would shed light into the labour division of YidC and SecYEG in the assembled bacterial MPT. In that regard, the experimental strategy outlined in Publication 1 provides a robust approach to the systematic study of membrane protein insertion.

3.2 Bcs1-mediated Rip1 translocation across the inner mitochondrial membrane

Rip1, one of the three catalytic subunits of the mitochondrial respiratory complex bc1, undergoes a characteristic biogenesis process where, after synthesis in a precursor form, it is targeted to the mitochondrial matrix to be folded and acquire the Fe_2S_2 cluster, essential for its activity. The folded substrate, chaperoned by Mzm1, is handed over to Bcs1, the AAA-ATPase responsible for its translocation across the IM and posterior lateral release. Structural and biophysical studies [Kater et al., 2020, Tang et al., 2020, Pan et al., 2023] have provided insights into how Bcs1 might be able to accommodate a folded substrate of the size of Rip1 (around 30 Å) and move it across the IM without disrupting the proton electrochemical gradient. A concerted, airlock-like mechanism has been proposed based on the different conformational changes Bcs1 goes through during the ATP hydrolysis cycle (**Figure 1.10**) [Kater et al., 2020].

Publication 2 reports two substrate-bound states of Bcs1 from *S. cerevisiae*, a Bcs1-Rip1 loading complex and a Bcs1-Rip1 translocation complex . The loading complex was resolved to a resolution of 3.4 Å, allowing for a confident assignment of the Bcs1 nucleotide state and the relative orientation of Rip1's globular domain inside the matrix vestibule (**Figure 3.4**). Moreover, it permitted the identification of specific contacts between the Rip1 substrate and individual Bcs1 protomers, shedding light into the nature of the interaction between the two proteins. The Bcs1-Rip1 loading complex exhibits an overall conformation resembling that of Bcs1-Apo1 [Kater et al., 2020] and no nucleotide density is found in any of the seven ATP binding pockets [Rosales-Hernandez et al., 2025].

Bcs1 binds Rip1 through highly conserved motifs (BSB and PL1) which, adopting different binding modes on each protomer, interact with a negatively charged patch on Rip1's surface. The residues on these motifs, EWR and DDR, respectively, are essential for Bcs1's function, as mutations where the charge is neutralised or inverted result in a lethal or severely impaired growth phenotype in a non-fermentable carbon source. Correspondingly, charge-inversion mutations of the residues on Rip1's negatively charged patch

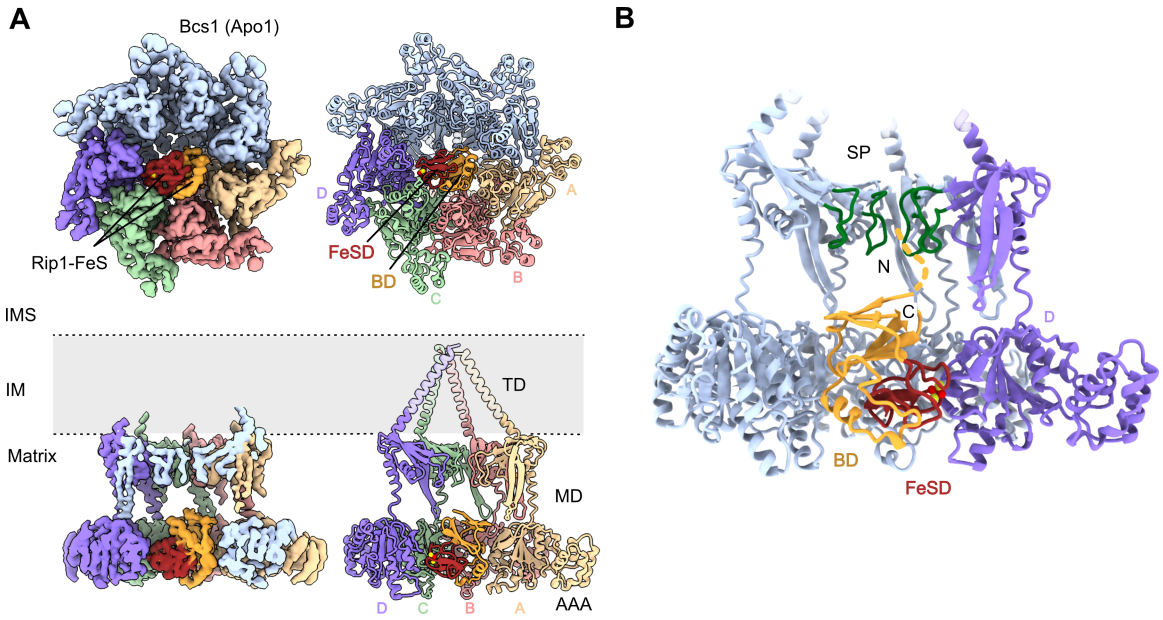

Figure 3.4: The Bcs1-Rip1 loading complex. (**A**) Cryo-EM reconstruction (left panel) and atomic model (right panel) of the loading complex, shown in bottom (upper row) and cut side views (lower row). The four protomers of Bcs1 forming direct contacts to Rip1 are labeled A to D. The FeSD and BD domains of Rip1 are highlighted, and the Fe_2S_2 cluster is shown as red (iron) and yellow (sulphur) spheres. TD: transmembrane domain, MD: middle domain, AAA: AAA-ATPase domain. (**B**) Cut side view displaying the relative orientation of Rip1's N- and C-terminus inside the matrix vestibule of Bcs1. Protomers A to C have been omitted for clarity. SP: seal pore. Figure adapted from [Rosales-Hernandez et al., 2025].

lead to a negative growth phenotype. Interestingly, this effect is virtually absent when the residues are mutated individually, ruling out an effect on Rip1 folding or catalytic function and pointing instead to a disruption of the interaction between Bcs1 and Rip1. A close inspection of the localisation of this surface in a fully assembled active bc1, reveals that it is neither in direct contact with other subunits of the complex nor involved in super complex formation [Hunte et al., 2000, Hartley et al., 2019]. Being highly conserved, this could imply that mutations on these residues are negatively selected in species where the only possible route of translocation is the Bcs1 pathway.

Notably, during the development of this thesis, a low-resolution reconstruction of mBcs1 bound to the C-terminal domain of *B. taurus* Rip1 was published, revealing a

substrate density on the matrix vestibule similar to the one in the yBcs1 loading complex, indicating a conserved architecture of the Rip1-Bcs1 loading complex [Zhan et al., 2024]. This structure, however, neither allowed for unambiguous determination of the nucleotide state nor for analysis of the Bcs1 substate interaction. Interestingly, in contrast to yBcs1, mBcs1 apo and ADP-bound states have a very similar conformation. In yBcs1, a clear difference between the two states was observed, with Apo1 having a slightly smaller opening of the matrix vestibule than the ADP-bound state [Kater et al., 2020]. Thus, the question remains whether the apo- or the ADP-bound state of Bcs1 is required for initial binding of the substate and whether there are differences between species. In yBcs1, the structure suggests that Rip1 might directly bind to Bcs1 in the apo state. This, however, doesn't exclude the possibility that Rip1 triggers the transition from ADP-bound Bcs1 to Apo1 state Bcs1, leading to ADP release and stable substrate accommodation. In light of the new data in Publication 2, the inwards rotation of the AAA domains, which reduces the size of the matrix vestibule, could happen concomitantly with substrate binding. This contrasts with mBcs1, where no major conformational difference is observed between the Apo and ADP states [Tang et al., 2020]. The limited resolution of the substrate bound mBcs1 reconstruction prevents a confident assignment of the nucleotide state, leaving open the possibility of a similar ADP to Apo transition upon substrate binding [Zhan et al., 2024].

An additional aspect of the loading complex is the orientation of Rip1's N-terminus inside the matrix vestibule of Bcs1, found to be pointing towards the IMS, in an apparent inverted topology compared to when it is assembled in bc1 (N_{MATRIX}-C_{IMS}). This implies that Rip1 must flip during translocation to acquire the correct topology, a process potentially chaperoned by Bcs1. However, the lack of a proper density for the N-terminus indicates that this region of Rip1 is rather unstructured or that it does not bind Bcs1 in a specific mode. It is possible that Mzm1, the chaperone that stabilizes transport competent Rip1 in the mitochondrial matrix [Cui et al., 2012, Atkinson et al., 2011], plays a role in handling the Rip1 N-terminus before and during handover to Bcs1. In *M. musculus*, Rip1's N-terminus is fused to another subunit of the bc1 complex, increasing the complexity of substrate handling and delivery. Future studies focused on folding and posterior handling

of Rip1 by Mzm1 will contribute to a better understanding of this process.

Bcs1 undergoes a major conformational change where the matrix vestibule is constricted and the seal pore is opened upon ATPγS binding [Rosales-Hernandez et al., 2025], as was also described for mBcs1 [Tang et al., 2020]. This constriction is incompatible with substrate binding and permanence in the matrix vestibule, indicating that binding of ATP to a Bcs1-Rip1 loading complex would trigger the conformational change, causing the AAA domains to rotate further inwards forcing out Rip1, while opening the seal pore to allow its movement towards the IMS vestibule. The identification of two ATPγS-bound states that differ only by a rotation of the middle domain and flexibility of the TMDs suggests that the conformational change caused by ATP binding also destabilises the TM basket. The gating intermediate state described in Publication 2, obtained by incubation of a preformed Bcs1-Rip1 loading complex with ATPγS, confirms this prediction and reveals further details of their interaction (**Figure 3.5**). The substrate density is observed in close vicinity of a positively charged patch on the TM helices of Bcs1 containing two highly conserved arginine residues, R69 and R81. While neutralisation or charge inversion of R69 led to a lethal phenotype in a non-fermentable carbon source, the growth defect on R81 mutants was only mild. This, however, is consistent with the fact that R81C in *H. sapiens* (R45C) is one of the mutations associated with the GRACILE syndrome. Together, these observations indicate that electrostatic interactions between Bcs1 and Rip1 are, apart from ATP, a major driver of Rip1 movement across the IM.

An updated version of the airlock-like mechanism summarises the findings of the Publication 2 (**Figure 3.6**), but several questions, especially related to the release of Rip1 into the IM, remain open. It is not clear, for example, how ATP hydrolysis is coupled to the opening of the TM basket and the insertion of the N-terminus of Rip1 into the lipid bilayer. Energy calculations [Pan et al., 2023, Zhan et al., 2024] have shown that the concerted hydrolysis of seven ATP molecules per cycle would be able to drive the opening of the helices embedded in the lipid bilayer, allowing the Rip1 N-terminus to laterally diffuse during release. Unfortunately, this open state is expected to be short-lived in order to maintain the proton gradient, and thus not readily captured during plunge-freezing.

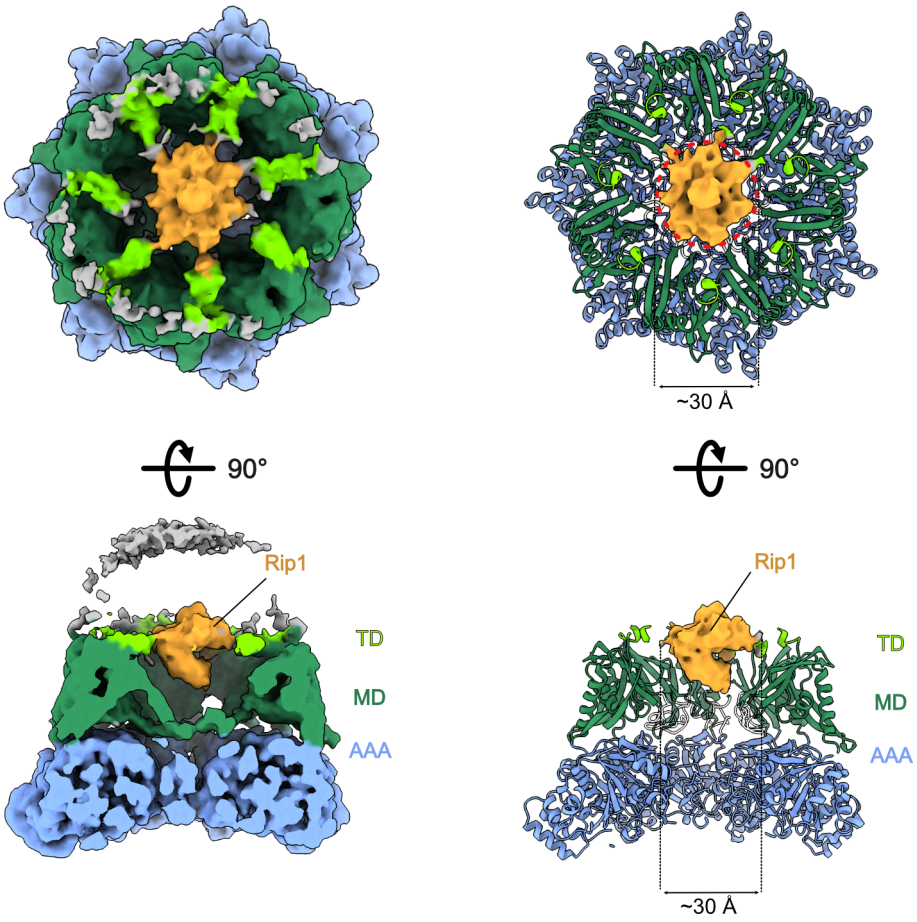

Figure 3.5: A Bcs1-Rip1 gating intermediate. Cryo-EM reconstruction (left panel) and atomic model (right panel) of the gating intermediate, shown in bottom (upper row) and cut side views (lower row). Bcs1 is observed in the ATPγS-bound state, and the substrate density is located in the IM vestibule. The seal loops forming the SP of Bcs1 are shown in transparency. TD: transmembrane domain, MD: middle domain, AAA: AAA-ATPase domain. Figure adapted from [Rosales-Hernandez et al., 2025].

Another unresolved aspect of the mechanism is how Bcs1 resets and returns to the ADP or Apo states. *In vitro*, Bcs1 hydrolyses ATP in absence of Rip1, but this is less likely to be the case *in vivo*. Assuming that the ATP hydrolysis of Bcs1 is indeed regulated, the question remains how this is accomplished in mitochondria. One possibility is that the pre-bc1 complex or another factor locks Bcs1 in the ADP state until Rip1 binds it, causing the transition to the Apo state. Next, Bcs1 binds and hydrolyses ATP, translocates Rip1 and, after insertion, returns to the ADP state. Alternatively, the hydrolysis of ATP might not directly lead to insertion of Rip1, but to a loosely bound Rip1 which, upon interaction with a factor, would trigger the N-terminus insertion and reset of Bcs1 to the ADP state. Future studies of Bcs1 in the context of the lipid bilayer and the nascent bc1 complex could help complete the picture of Bcs1's ATP hydrolysis cycle.

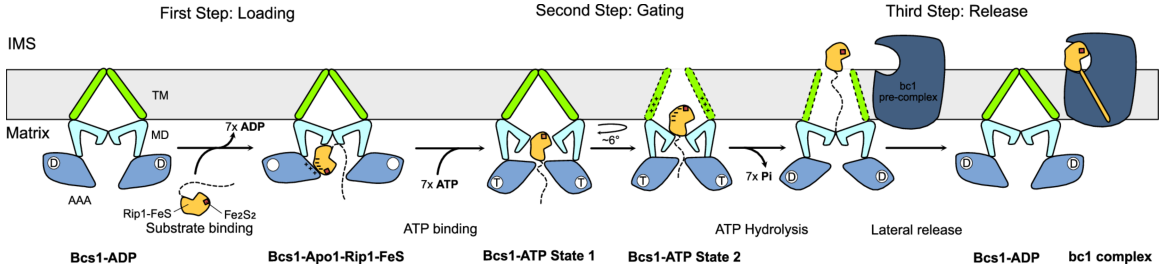

Figure 3.6: Bcs1-mediated Rip1 translocation. During the first step, or loading step, Rip1 binds to the matrix of Bcs1, probably resetting its nucleotide state to the Apo1 state. In the gating step, ATP binding promotes a conformational change, where the matrix vestibule is constricted and the middle domain opens, allowing the access of Rip1 to the IM vestibule. A positively charged patch in the TM domain might drive the movement of the substrate. In the release state, the TM domain is flexible, allowing the lateral release of the substrate into the IM. Figure adapted from [Rosales-Hernandez et al., 2025].

3.3 Pel export across the outer membrane of *Pseudomonas aeruginosa*

Outer membrane porins that handle OM exopolysaccharide transport, such as AlgE (alginate), PgaA (PNAG) or BcsC (pEtN-cellulose), display a similar architecture, where 16 to

18 β strands form a membrane embedded barrel through which the polymer is exported to the extracellular space [Acheson et al., 2019, Wang et al., 2016]. In the case of Pel export, PelB has been proposed as the channel forming multi-pass β-barrel porin in the OM [Marmont et al., 2017a]. Accordingly, AlphaFold models of PelB predict with high confidence a C-terminal β-barrel arrangement of 16 strands and an N-terminal TPR domain extending towards the IM. In addition, a special feature of the Pel export machinery is the presence of the lipoprotein PelC in the inner leaflet of the OM, potentially assembled in a dodecameric ring, as indicated by the crystal structure of an ortholog from *Paraburkholderia phytofirmans* [Marmont et al., 2017a]. However, models of PelBC with 1:11 and 1:13 stoichiometries are predicted with similar high confidence as a 1:12 complex, preventing the designation of a unique stoichiometry. The cryo-EM structure of PelBC in Publication 3 reveals for the first time how the PelB β-barrel is stabilised by interactions with a dodecameric assembly of PelC subunits (**Figure 3.7**). The data strongly favours a 1:12 stoichiometry, as particles with a different number of PelC subunits in the ring were not observed.

In the 3D reconstruction, the different elements that mediate the interaction between PelB and PelC are visualised at high resolution. This clarifies the role of conserved residues W149 and D119 in PelC, whose mutation impairs biofilm formation. W149 was proposed as a site of contact with the membrane [Marmont et al., 2017a]. However, the structure shows that W149 is rather involved in positioning the acyl chains of the lipoprotein, which themselves act as lipid anchors, in their defined configuration around PelB. The role of D119, presumed to be related to substrate handling across the ring, can now be assigned to the stabilisation of the β-barrel, achieved through interactions with positively charged residues in the periplasmic exposed loops of PelB. This also explains why a charge inversion to R119 severely impairs biofilm formation [Marmont et al., 2017a]. Moreover, the contacts between some of the subunits of the PelC ring to the stalk helix and two helices of the TPR domain in PelB explain the importance of these elements in the overall stability of the complex, as their deletion disrupts PelBC assembly [Benedens et al., 2025].

The transport of positively charged Pel towards the extracellular space is facilitated

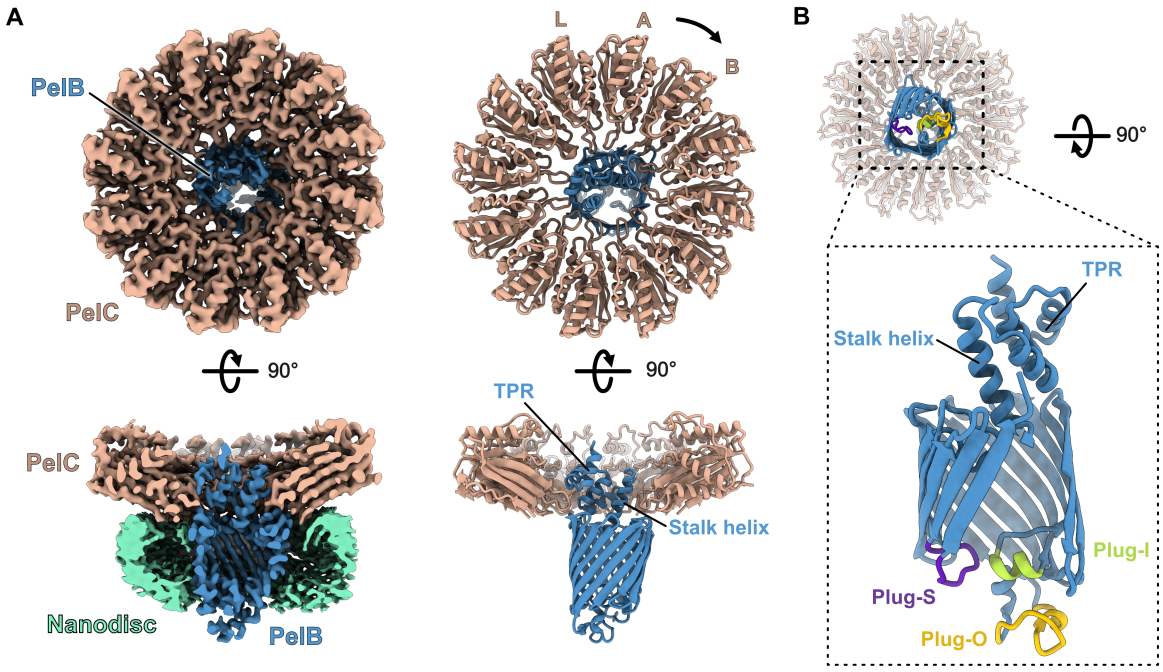

Figure 3.7: Structure of the PelBC complex. (**A**) Cryo-EM reconstruction (left panel) and atomic model (right panel) of the PelBC complex, shown in bottom (upper row) and cut side views (lower row). The PelC subunits are labeled A to L in a clockwise sense. (**B**) Main panel: top view of the PelBC complex, highlighting the PelB β-barrel and the periplasmic exposed loops, Plug-I, Plug-O and Plug-S. Inset: close-up view of the region enclosed in the main panel, displaying the relative position of the loops in PelB. Some strands of the β-barrel have been omitted for clarity. Figure adapted from [Benedens et al., 2025].

and regulated by different features of PelB. A negatively charged surface located predominantly along strands 11 to 14 could provide a driving force for the movement of the polysaccharide inside the water filled channel formed by the β-barrel. At the extracellular end, three main loops occlude the channel forming a gap of 4 Å, small enough to control the passage of water molecules and to impede the free movement of Pel, which would require an opening of at least 8 Å[Benedens et al., 2025], implying that a gating mechanism must be in place to allow the export of polysaccharide outside PelB. While the loop between strand 7 and 8, Plug-I, forms different contacts to strands 2 and 3, probably serving a structural role, the loop between strands 11 and 12, Plug-O, sits facing the extracellular space acting as a dome or lid for the β-barrel. This reduces the list of elements that could act as a gate to the glycine-rich loop between strands 15 and 16, Plug-S. At the outer

surface of PelB, additional negatively charged residues might further drive the movement of the positively charged Pel towards the extracellular space, as proposed for PgaA and BcsC [Wang et al., 2016], or clear the exit path from negatively charged phosphate groups or LPS [Benedens et al., 2025].

A combined approach of molecular dynamics simulations and single-channel conductivity experiments was employed to study the conformational flexibility of the loops mentioned above [Benedens et al., 2025]. Simulations of PelB under different ion/membrane lipid conditions not only displayed a relative rigidity in the case of Plug-I but also corroborated the predicted flexibility of Plug-O and Plug-S and their ability to form transient pores, wide enough to allow for the passage of a linear GalNAc-GalN-GalNAc-GalN polysaccharide. Nonetheless, Plug-O is the least conserved of all three loops, making it less likely to be a key element for the gating of the channel. This was verified during single-channel conductivity measurements, where a deletion in the Plug-O did not impact measured ion currents, as opposed to a deletion of the Plug-S, which led to ion currents typical of a constitutively open pore. These findings, further supported by differential scanning fluorimetry measurements of deletion mutants for all loops, confirm the structural role of Plug-I and the assignment of Plug-S as the gating element of PelB.

Considering all the evidence reported in Publication 3, a Pel export pathway and gating mechanism based on the structural features of PelB is proposed (**Figure 3.8**). Electrostatic charge complementarity appears to be a major driver for the transport of the de-acetylated polymer, as the negatively charged surface inside PelB, near the extracellular space, attracts the positive charges in the GalNAc-GalN chain, guiding it towards the exterior of the β-barrel. In the state visualised by cryo-EM, defined as idle (resting) state, three loops occlude the exit of the PelB channel, restricting the free movement of water molecules and the polymer itself. This fact is in line with a general absence of non-specific porins in *P. aeruginosa*, denoting a tightly controlled transport of solutes across the OM. In the case of PelB, this control is exerted through the Plug-S, which potentially dislocates during export of Pel, allowing its passage and release to the extracellular space. The localisation of Plug-S near the conserved Y1103 [Acheson et al., 2019], potentially

involved in substrate handling via CH-pi interactions, suggests that the dislocation could be triggered by the arrival of the substrate. Further investigation on the PelBC complex in presence of its substrate, aiming to capture the gating (translocating) state, could provide a clearer picture of how this conformational change is coordinated with the threading of substrate across the open channel.

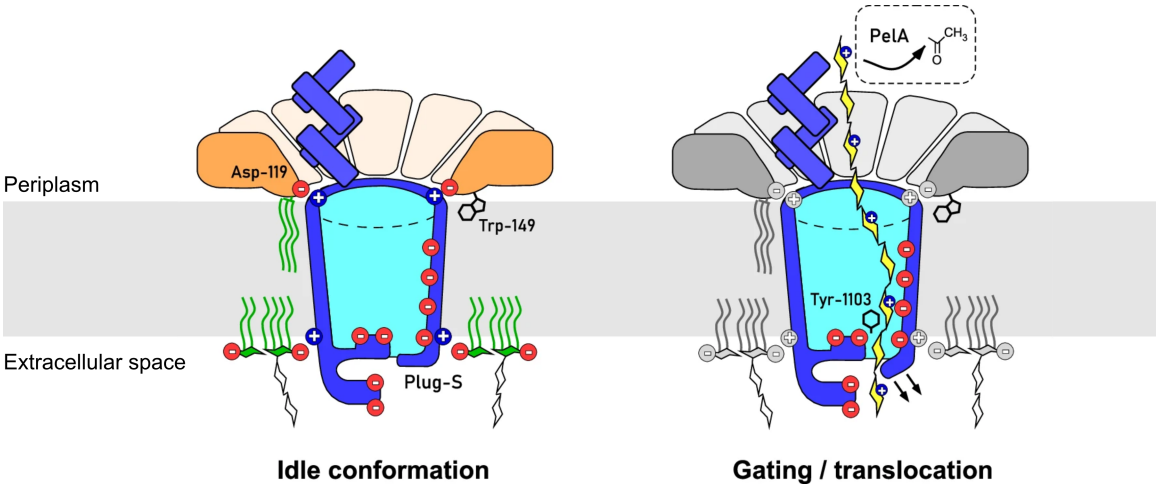

Figure 3.8: Mechanism of Pel threading through PelBC. A negatively charged patch in the extracellular end of PelB directs the positively charged polysaccharide towards the gating element, Plug-S, which opens to allow the export of Pel. Figure adapted from [Benedens et al., 2025].

Several open questions remain regarding the export mechanism of Pel. A future line of investigation will be the elucidation of the role of PelC in substrate handling. The contacts between PelC subunits and the TPR domain of PelB might serve the purpose of aligning the TPR with the exit pore, as observed in the cryo-EM structure. This particular orientation might constitute the path across which the substrate is threaded into the water filled cavity of the β-barrel. Furthermore, PelC is predicted to interact with TPR (PelB) bound PelA [Van Loon et al., 2025], implying that the ring might also help positioning PelA during substrate modification. Another open question is related to the nature and function of the structural lipids that occupy the hydrophobic grooves around PelB's outer surface. A detergent or nanodisc free approach, involving the direct extraction of the complex by means of amphipathic polymers and further characterisation of the extracted lipids, as well

as structural studies by cryo-EM, would provide insights into the organisation of PelB's lipid environment *in vivo*. In the long term, functional and structural characterisation of the IM biosynthesis machinery, PelDEFG, which might interact with the IM embedded TMD at the N-terminus of PelB, will unveil additional mechanistical aspects of Pel export, particularly regarding the handover of Pel to the TPR domains and PelA.

References

[Acheson et al., 2019] Acheson, J. F., Derewenda, Z. S., and Zimmer, J. (2019). Architecture of the cellulose synthase outer membrane channel and its association with the periplasmic tpr domain. *Structure*, 27(12):1855–1861.e3.

[Alcock et al., 2013] Alcock, F., Baker, M. A., Greene, N. P., Palmer, T., Wallace, M. I., and Berks, B. C. (2013). Live cell imaging shows reversible assembly of the tata component of the twin-arginine protein transport system. *Proc Natl Acad Sci U S A*, 110(38):E3650–9.

[Alcock et al., 2016] Alcock, F., Stansfeld, P. J., Basit, H., Habersetzer, J., Baker, M. A., Palmer, T., Wallace, M. I., and Berks, B. C. (2016). Assembling the tat protein translocase. *Elife*, 5.

[Anghel et al., 2017] Anghel, S. A., McGilvray, P. T., Hegde, R. S., and Keenan, R. J. (2017). Identification of oxa1 homologs operating in the eukaryotic endoplasmic reticulum. *Cell Rep*, 21(13):3708–3716.

[Atkinson et al., 2011] Atkinson, A., Smith, P., Fox, J. L., Cui, T. Z., Khalimonchuk, O., and Winge, D. R. (2011). The lyr protein mzm1 functions in the insertion of the rieske fe/s protein in yeast mitochondria. *Mol Cell Biol*, 31(19):3988–96.

[Aviram et al., 2016] Aviram, N., Ast, T., Costa, E. A., Arakel, E. C., Chuartzman, S. G., Jan, C. H., Haßdenteufel, S., Dudek, J., Jung, M., Schorr, S., Zimmermann, R., Schwappach, B., Weissman, J. S., and Schuldiner, M. (2016). The snd proteins constitute an alternative targeting route to the endoplasmic reticulum. *Nature*, 540(7631):134–138.

[Aviram and Schuldiner, 2017] Aviram, N. and Schuldiner, M. (2017). Targeting and translocation of proteins to the endoplasmic reticulum at a glance. *J Cell Sci*, 130(24):4079–4085.

[Baum and Baum, 2014] Baum, D. A. and Baum, B. (2014). An inside-out origin for the eukaryotic cell. *BMC Biol*, 12:76.

[Benedens et al., 2025] Benedens, M., Rosales-Hernandez, C., Straathof, S. A. P., Loschwitz, J., Berninghausen, O., Maglia, G., Beckmann, R., and Kedrov, A. (2025). Assembly and the gating mechanism of the pel exopolysaccharide export complex pelbc of pseudomonas aeruginosa. *Nat Commun*, 16(1):5249.

[Benz et al., 2009] Benz, M., Bals, T., Gügel, I. L., Piotrowski, M., Kuhn, A., Schünemann, D., Soll, J., and Ankele, E. (2009). Alb4 of arabidopsis promotes assembly and stabilization of a non chlorophyll-binding photosynthetic complex, the cf1cf0-atp synthase. *Mol Plant*, 2(6):1410–24.

[Berks, 1996] Berks, B. C. (1996). A common export pathway for proteins binding complex redox cofactors? *Mol Microbiol*, 22(3):393–404.

[Berks, 2015] Berks, B. C. (2015). The twin-arginine protein translocation pathway. *Annu Rev Biochem*, 84:843–64.

[Berks et al., 2014] Berks, B. C., Lea, S. M., and Stansfeld, P. J. (2014). Structural biology of tat protein transport. *Curr Opin Struct Biol*, 27:32–7.

[Blobel and Dobberstein, 1975] Blobel, G. and Dobberstein, B. (1975). Transfer of proteins across membranes. i. presence of proteolytically processed and unprocessed nascent immunoglobulin light chains on membrane-bound ribosomes of murine myeloma. *J Cell Biol*, 67(3):835–51.

[Bogsch et al., 1997] Bogsch, E., Brink, S., and Robinson, C. (1997). Pathway specificity for a delta ph-dependent precursor thylakoid lumen protein is governed by a 'sec-avoidance' motif in the transfer peptide and a 'sec-incompatible' mature protein. *EMBO J*, 16(13):3851–9.

[Brandt et al., 1993] Brandt, U., Yu, L., Yu, C. A., and Trumpower, B. L. (1993). The mitochondrial targeting presequence of the rieske iron-sulfur protein is processed in a single step after insertion into the cytochrome bc1 complex in mammals and retained as a subunit in the complex. *J Biol Chem*, 268(12):8387–90.

[Brocard and Hartig, 2006] Brocard, C. and Hartig, A. (2006). Peroxisome targeting signal 1: is it really a simple tripeptide? *Biochim Biophys Acta*, 1763(12):1565–73.

[Burger et al., 2003] Burger, G., Forget, L., Zhu, Y., Gray, M. W., and Lang, B. F. (2003). Unique mitochondrial genome architecture in unicellular relatives of animals. *Proc Natl Acad Sci U S A*, 100(3):892–7.

[Busch et al., 2023] Busch, J. D., Fielden, L. F., Pfanner, N., and Wiedemann, N. (2023). Mitochondrial protein transport: Versatility of translocases and mechanisms. *Mol Cell*, 83(6):890–910.

[Busch et al., 2025] Busch, M., Rosales-Hernandez, C., Kamel, M., Schaumkessel, Y., van der Sluis, E., Berninghausen, O., Becker, T., Beckmann, R., and Kedrov, A. (2025). Substrate-induced assembly and functional mechanism of the bacterial membrane protein insertase secyeg-yidc. *bioRxiv*.

[Bölter and Soll, 2001] Bölter, B. and Soll, J. (2001). Ion channels in the outer membranes of chloroplasts and mitochondria: open doors or regulated gates? *EMBO J*, 20(5):935–40.

[Carrie et al., 2016] Carrie, C., Weißenberger, S., and Soll, J. (2016). Plant mitochondria contain the protein translocase subunits tatb and tatc. *J Cell Sci*, 129(20):3935–3947.

[Catacuzzeno et al., 2025] Catacuzzeno, L., Michelucci, A., and Franciolini, F. (2025). The crucial decade that ion channels were proven to exist : The vision of bertil hille and clay armstrong and how it came through. *Pflugers Arch*, 477(7):903–917.

[Celebi et al., 2006] Celebi, N., Yi, L., Facey, S. J., Kuhn, A., and Dalbey, R. E. (2006). Membrane biogenesis of subunit ii of cytochrome bo oxidase: contrasting requirements for insertion of n-terminal and c-terminal domains. *J Mol Biol*, 357(5):1428–36.

[Chen et al., 2022] Chen, F., Kang, R., Liu, J., and Tang, D. (2022). The v-atpases in cancer and cell death. *Cancer Gene Ther*, 29(11):1529–1541.

[Chen and Phelix, 2019] Chen, L. Y. and Phelix, C. F. (2019). Extracellular gating of glucose transport through glut 1. *Biochem Biophys Res Commun*, 511(3):573–578.

[Chitwood and Hegde, 2019] Chitwood, P. J. and Hegde, R. S. (2019). The role of emc during membrane protein biogenesis. *Trends Cell Biol*, 29(5):371–384.

[Chitwood and Hegde, 2020] Chitwood, P. J. and Hegde, R. S. (2020). An intramembrane chaperone complex facilitates membrane protein biogenesis. *Nature*, 584(7822):630–634.

[Chitwood et al., 2018] Chitwood, P. J., Juszkiewicz, S., Guna, A., Shao, S., and Hegde, R. S. (2018). Emc is required to initiate accurate membrane protein topogenesis. *Cell*, 175(6):1507–1519.e16.

[Colvin et al., 2013] Colvin, K. M., Alnabelseya, N., Baker, P., Whitney, J. C., Howell, P. L., and Parsek, M. R. (2013). Pela deacetylase activity is required for pel polysaccharide synthesis in pseudomonas aeruginosa. *J Bacteriol*, 195(10):2329–39.

[Conte et al., 2015] Conte, A., Papa, B., Ferramosca, A., and Zara, V. (2015). The dimerization of the yeast cytochrome bc1 complex is an early event and is independent of rip1. *Biochim Biophys Acta*, 1853(5):987–95.

[Cowan et al., 1992] Cowan, S. W., Schirmer, T., Rummel, G., Steiert, M., Ghosh, R., Pauptit, R. A., Jansonius, J. N., and Rosenbusch, J. P. (1992). Crystal structures explain functional properties of two e. coli porins. *Nature*, 358(6389):727–33.

[Cristóbal et al., 1999] Cristóbal, S., de Gier, J. W., Nielsen, H., and von Heijne, G. (1999). Competition between sec- and tat-dependent protein translocation in escherichia coli. *EMBO J*, 18(11):2982–90.

[Cruciat et al., 1999] Cruciat, C., Hell, K., Fölsch, H., Neupert, W., and Stuart, R. A. (1999). Bcs1p, an aaa‐family member, is a chaperone for the assembly of the cytochrome bc₁ complex. *The EMBO Journal*, 18(19):5226–5233.

[Cruciat et al., 2000] Cruciat, C. M., Brunner, S., Baumann, F., Neupert, W., and Stuart, R. A. (2000). The cytochrome bc1 and cytochrome c oxidase complexes associate to form a single supracomplex in yeast mitochondria. *J Biol Chem*, 275(24):18093–8.

[Cui et al., 2012] Cui, T. Z., Smith, P. M., Fox, J. L., Khalimonchuk, O., and Winge, D. R. (2012). Late-stage maturation of the rieske fe/s protein: Mzm1 stabilizes rip1 but does not facilitate its translocation by the aaa atpase bcs1. *Mol Cell Biol*, 32(21):4400–9.

[Cymer et al., 2015] Cymer, F., von Heijne, G., and White, S. H. (2015). Mechanisms of integral membrane protein insertion and folding. *J Mol Biol*, 427(5):999–1022.

[De Meirleir et al., 2003] De Meirleir, L., Seneca, S., Damis, E., Sepulchre, B., Hoorens, A., Gerlo, E., García Silva, M. T., Hernandez, E. M., Lissens, W., and Van Coster, R. (2003). Clinical and diagnostic characteristics of complex iii deficiency due to mutations in the bcs1l gene. *Am J Med Genet A*, 121A(2):126–31.

[De Pinto, 2021] De Pinto, V. (2021). Renaissance of vdac: New insights on a protein family at the interface between mitochondria and cytosol. *Biomolecules*, 11(1).

[Deng et al., 2015] Deng, D., Sun, P., Yan, C., Ke, M., Jiang, X., Xiong, L., Ren, W., Hirata, K., Yamamoto, M., Fan, S., and Yan, N. (2015). Molecular basis of ligand recognition and transport by glucose transporters. *Nature*, 526(7573):391–6.

[Dimou and Nickel, 2018] Dimou, E. and Nickel, W. (2018). Unconventional mechanisms of eukaryotic protein secretion. *Curr Biol*, 28(8):R406–R410.

[Do et al., 1996] Do, H., Falcone, D., Lin, J., Andrews, D. W., and Johnson, A. E. (1996). The cotranslational integration of membrane proteins into the phospholipid bilayer is a multistep process. *Cell*, 85(3):369–78.

[Ebner and Götz, 2019] Ebner, P. and Götz, F. (2019). Bacterial excretion of cytoplasmic proteins (ecp): Occurrence, mechanism, and function. *Trends Microbiol*, 27(2):176–187.

[Erdmann et al., 1991] Erdmann, R., Wiebel, F. F., Flessau, A., Rytka, J., Beyer, A., Fröhlich, K. U., and Kunau, W. H. (1991). Pas1, a yeast gene required for peroxisome biogenesis, encodes a member of a novel family of putative atpases. *Cell*, 64(3):499–510.

[Facey et al., 2007] Facey, S. J., Neugebauer, S. A., Krauss, S., and Kuhn, A. (2007). The mechanosensitive channel protein mscl is targeted by the srp to the novel yidc membrane insertion pathway of escherichia coli. *J Mol Biol*, 365(4):995–1004.

[Falk et al., 2010] Falk, S., Ravaud, S., Koch, J., and Sinning, I. (2010). The c terminus of the alb3 membrane insertase recruits cpsrp43 to the thylakoid membrane. *J Biol Chem*, 285(8):5954–62.

[Fleischer et al., 2006] Fleischer, T. C., Weaver, C. M., McAfee, K. J., Jennings, J. L., and Link, A. J. (2006). Systematic identification and functional screens of uncharacterized proteins associated with eukaryotic ribosomal complexes. *Genes Dev*, 20(10):1294–307.

[Folsch et al., 1996] Folsch, H., Guiard, B., Neupert, W., and Stuart, R. A. (1996). Internal targeting signal of the bcs1 protein: a novel mechanism of import into mitochondria. *EMBO J*, 15(3):479–87.

[Franklin et al., 2011] Franklin, M. J., Nivens, D. E., Weadge, J. T., and Howell, P. L. (2011). Biosynthesis of the pseudomonas aeruginosa extracellular polysaccharides, alginate, pel, and psl. *Front Microbiol*, 2:167.

[Frickey and Lupas, 2004] Frickey, T. and Lupas, A. N. (2004). Phylogenetic analysis of aaa proteins. *J Struct Biol*, 146(1-2):2–10.

[Friedman and Kolter, 2004] Friedman, L. and Kolter, R. (2004). Genes involved in matrix formation in pseudomonas aeruginosa pa14 biofilms. *Mol Microbiol*, 51(3):675–90.

[Funes et al., 2004] Funes, S., Nargang, F. E., Neupert, W., and Herrmann, J. M. (2004). The oxa2 protein of neurospora crassa plays a critical role in the biogenesis of cytochrome oxidase and defines a ubiquitous subbranch of the oxa1/yidc/alb3 protein family. *Mol Biol Cell*, 15(4):1853–61.

[Garrahan and Glynn, 1966] Garrahan, P. J. and Glynn, I. M. (1966). Driving the sodium pump backwards to form adenosine triphosphate. *Nature*, 211(5056):1414–5.

[Gerdes et al., 2006] Gerdes, L., Bals, T., Klostermann, E., Karl, M., Philippar, K., Hünken, M., Soll, J., and Schünemann, D. (2006). A second thylakoid membrane-localized alb3/oxai/yidc homologue is involved in proper chloroplast biogenesis in arabidopsis thaliana. *J Biol Chem*, 281(24):16632–42.

[Ghafoor et al., 2013] Ghafoor, A., Jordens, Z., and Rehm, B. H. (2013). Role of pelf in pel polysaccharide biosynthesis in pseudomonas aeruginosa. *Appl Environ Microbiol*, 79(9):2968–78.

[Gogala et al., 2014] Gogala, M., Becker, T., Beatrix, B., Armache, J. P., Barrio-Garcia, C., Berninghausen, O., and Beckmann, R. (2014). Structures of the sec61 complex engaged in nascent peptide translocation or membrane insertion. *Nature*, 506(7486):107–10.

[Guna et al., 2018] Guna, A., Volkmar, N., Christianson, J. C., and Hegde, R. S. (2018). The er membrane protein complex is a transmembrane domain insertase. *Science*, 359(6374):470–473.

[Günsel et al., 2023] Günsel, U., Klöpfer, K., Häusler, E., Hitzenberger, M., Bölter, B., Sperl, L. E., Zacharias, M., Soll, J., and Hagn, F. (2023). Structural basis of metabolite transport by the chloroplast outer envelope channel oep21. *Nat Struct Mol Biol*, 30(6):761–769.

[Habersetzer et al., 2017] Habersetzer, J., Moore, K., Cherry, J., Buchanan, G., Stansfeld, P. J., and Palmer, T. (2017). Substrate-triggered position switching of tata and tatb during tat transport in. *Open Biol*, 7(8).

[Halic and Beckmann, 2005] Halic, M. and Beckmann, R. (2005). The signal recognition particle and its interactions during protein targeting. *Curr Opin Struct Biol*, 15(1):116–25.

[Hartl et al., 1990] Hartl, F. U., Lecker, S., Schiebel, E., Hendrick, J. P., and Wickner, W. (1990). The binding cascade of secb to seca to secy/e mediates preprotein targeting to the e. coli plasma membrane. *Cell*, 63(2):269–79.

[Hartl et al., 1986] Hartl, F. U., Schmidt, B., Wachter, E., Weiss, H., and Neupert, W. (1986). Transport into mitochondria and intramitochondrial sorting of the fe/s protein of ubiquinol-cytochrome c reductase. *Cell*, 47(6):939–51.

[Hartley et al., 2019] Hartley, A. M., Lukoyanova, N., Zhang, Y., Cabrera-Orefice, A., Arnold, S., Meunier, B., Pinotsis, N., and Marechal, A. (2019). Structure of yeast cytochrome c oxidase in a supercomplex with cytochrome bc(1). *Nat Struct Mol Biol*, 26(1):78–83.

[Haupts et al., 1999] Haupts, U., Tittor, J., and Oesterhelt, D. (1999). Closing in on bacteriorhodopsin: progress in understanding the molecule. *Annu Rev Biophys Biomol Struct*, 28:367–99.

[Hegde and Keenan, 2022] Hegde, R. S. and Keenan, R. J. (2022). The mechanisms of integral membrane protein biogenesis. *Nat Rev Mol Cell Biol*, 23(2):107–124.

[Hell et al., 2001] Hell, K., Neupert, W., and Stuart, R. A. (2001). Oxa1p acts as a general membrane insertion machinery for proteins encoded by mitochondrial dna. *EMBO J*, 20(6):1281–8.

[Hennon et al., 2015] Hennon, S. W., Soman, R., Zhu, L., and Dalbey, R. E. (2015). Yidc/alb3/oxa1 family of insertases. *J Biol Chem*, 290(24):14866–74.

[Hessa et al., 2007] Hessa, T., Meindl-Beinker, N. M., Bernsel, A., Kim, H., Sato, Y., Lerch-Bader, M., Nilsson, I., White, S. H., and von Heijne, G. (2007). Molecular code for transmembrane-helix recognition by the sec61 translocon. *Nature*, 450(7172):1026–30.

[Hildenbeutel et al., 2012] Hildenbeutel, M., Theis, M., Geier, M., Haferkamp, I., Neuhaus, H. E., Herrmann, J. M., and Ott, M. (2012). The membrane insertase oxa1 is required for efficient import of carrier proteins into mitochondria. *J Mol Biol*, 423(4):590–9.

[Hinson et al., 2007] Hinson, J. T., Fantin, V. R., Schönberger, J., Breivik, N., Siem, G., McDonough, B., Sharma, P., Keogh, I., Godinho, R., Santos, F., Esparza, A., Nicolau, Y., Selvaag, E., Cohen, B. H., Hoppel, C. L., Tranebjaerg, L., Eavey, R. D., Seidman, J. G., and Seidman, C. E. (2007). Missense mutations in the bcs1l gene as a cause of the björnstad syndrome. *N Engl J Med*, 356(8):809–19.

[Hunte et al., 2000] Hunte, C., Koepke, J., Lange, C., Rossmanith, T., and Michel, H. (2000). Structure at 2.3 a resolution of the cytochrome bc(1) complex from the yeast saccharomyces cerevisiae co-crystallized with an antibody fv fragment. *Structure*, 8(6):669–84.

[Iyer et al., 2004] Iyer, L. M., Leipe, D. D., Koonin, E. V., and Aravind, L. (2004). Evolutionary history and higher order classification of aaa+ atpases. *J Struct Biol*, 146(1-2):11–31.

[Jennings et al., 2015] Jennings, L. K., Storek, K. M., Ledvina, H. E., Coulon, C., Marmont, L. S., Sadovskaya, I., Secor, P. R., Tseng, B. S., Scian, M., Filloux, A., Wozniak, D. J., Howell, P. L., and Parsek, M. R. (2015). Pel is a cationic exopolysaccharide that cross-links extracellular dna in the pseudomonas aeruginosa biofilm matrix. *Proc Natl Acad Sci U S A*, 112(36):11353–8.

[Jiang et al., 2002] Jiang, F., Yi, L., Moore, M., Chen, M., Rohl, T., Van Wijk, K. J., De Gier, J. W., Henry, R., and Dalbey, R. E. (2002). Chloroplast yidc homolog albino3 can functionally complement the bacterial yidc depletion strain and promote membrane insertion of both bacterial and chloroplast thylakoid proteins. *J Biol Chem*, 277(22):19281–8.

[Kater et al., 2019] Kater, L., Frieg, B., Berninghausen, O., Gohlke, H., Beckmann, R., and Kedrov, A. (2019). Partially inserted nascent chain unzips the lateral gate of the sec translocon. *EMBO Rep*, 20(10):e48191.

[Kater et al., 2020] Kater, L., Wagener, N., Berninghausen, O., Becker, T., Neupert, W., and Beckmann, R. (2020). Structure of the bcs1 aaa-atpase suggests an airlock-like translocation mechanism for folded proteins. *Nat Struct Mol Biol*, 27(2):142–149.

[Kato et al., 2022] Kato, T., Kusakizako, T., Jin, C., Zhou, X., Ohgaki, R., Quan, L., Xu, M., Okuda, S., Kobayashi, K., Yamashita, K., Nishizawa, T., Kanai, Y., and Nureki, O. (2022). Structural insights into inhibitory mechanism of human excitatory amino acid transporter eaat2. *Nat Commun*, 13(1):4714.

[Keenan et al., 1998] Keenan, R. J., Freymann, D. M., Walter, P., and Stroud, R. M. (1998). Crystal structure of the signal sequence binding subunit of the signal recognition particle. *Cell*, 94(2):181–91.

[Keiski et al., 2010] Keiski, C. L., Harwich, M., Jain, S., Neculai, A. M., Yip, P., Robinson, H., Whitney, J. C., Riley, L., Burrows, L. L., Ohman, D. E., and Howell, P. L. (2010). Algk is a tpr-containing protein and the periplasmic component of a novel exopolysaccharide secretin. *Structure*, 18(2):265–73.

[Kispal et al., 1999] Kispal, G., Csere, P., Prohl, C., and Lill, R. (1999). The mitochondrial proteins atm1p and nfs1p are essential for biogenesis of cytosolic fe/s proteins. *EMBO J*, 18(14):3981–9.

[Kumazaki et al., 2014a] Kumazaki, K., Chiba, S., Takemoto, M., Furukawa, A., Nishiyama, K., Sugano, Y., Mori, T., Dohmae, N., Hirata, K., Nakada-Nakura, Y., Maturana, A. D., Tanaka, Y., Mori, H., Sugita, Y., Arisaka, F., Ito, K., Ishitani, R., Tsukazaki, T., and Nureki, O. (2014a). Structural basis of sec-independent membrane protein insertion by yidc. *Nature*, 509(7501):516–20.

[Kumazaki et al., 2014b] Kumazaki, K., Kishimoto, T., Furukawa, A., Mori, H., Tanaka, Y., Dohmae, N., Ishitani, R., Tsukazaki, T., and Nureki, O. (2014b). Crystal structure of escherichia coli yidc, a membrane protein chaperone and insertase. *Sci Rep*, 4:7299.

[Kühlbrandt, 2019] Kühlbrandt, W. (2019). Structure and mechanisms of f-type atp synthases. *Annu Rev Biochem*, 88:515–549.

[Laskowski et al., 2021] Laskowski, P. R., Pluhackova, K., Haase, M., Lang, B. M., Nagler, G., Kuhn, A., and Müller, D. J. (2021). Monitoring the binding and insertion of a single transmembrane protein by an insertase. *Nat Commun*, 12(1):7082.

[Le Mauff et al., 2022] Le Mauff, F., Razvi, E., Reichhardt, C., Sivarajah, P., Parsek, M. R., Howell, P. L., and Sheppard, D. C. (2022). The pel polysaccharide is predominantly composed of a dimeric repeat of α-1,4 linked galactosamine and n-acetylgalactosamine. *Commun Biol*, 5(1):502.

[Lee et al., 2007] Lee, V. T., Matewish, J. M., Kessler, J. L., Hyodo, M., Hayakawa, Y., and Lory, S. (2007). A cyclic-di-gmp receptor required for bacterial exopolysaccharide production. *Mol Microbiol*, 65(6):1474–84.

[Lewis and Hegde, 2021] Lewis, A. J. O. and Hegde, R. S. (2021). A unified evolutionary origin for the ubiquitous protein transporters secy and yidc. *BMC Biol*, 19(1):266.

[Li et al., 2016] Li, L., Park, E., Ling, J., Ingram, J., Ploegh, H., and Rapoport, T. A. (2016). Crystal structure of a substrate-engaged secy protein-translocation channel. *Nature*, 531(7594):395–399.

[Lill and Freibert, 2020] Lill, R. and Freibert, S. A. (2020). Mechanisms of mitochondrial iron-sulfur protein biogenesis. *Annu Rev Biochem*, 89:471–499.

[Liu et al., 2024] Liu, H. Y., Prentice, E. L., and Webber, M. A. (2024). Mechanisms of antimicrobial resistance in biofilms. *NPJ Antimicrob Resist*, 2(1):27.

[Léon et al., 2006] Léon, S., Goodman, J. M., and Subramani, S. (2006). Uniqueness of the mechanism of protein import into the peroxisome matrix: transport of folded, co-factor-bound and oligomeric proteins by shuttling receptors. *Biochim Biophys Acta*, 1763(12):1552–64.

[Marmont et al., 2017a] Marmont, L. S., Rich, J. D., Whitney, J. C., Whitfield, G. B., Almblad, H., Robinson, H., Parsek, M. R., Harrison, J. J., and Howell, P. L. (2017a). Oligomeric lipoprotein pelc guides pel polysaccharide export across the outer membrane of. *Proc Natl Acad Sci U S A*, 114(11):2892–2897.

[Marmont et al., 2020] Marmont, L. S., Whitfield, G. B., Pfoh, R., Williams, R. J., Randall, T. E., Ostaszewski, A., Razvi, E., Groves, R. A., Robinson, H., Nitz, M., Parsek, M. R., Lewis, I. A., Whitney, J. C., Harrison, J. J., and Howell, P. L. (2020). Pelx is a udp-n-acetylglucosamine c4-epimerase involved in pel polysaccharide-dependent biofilm formation. *J Biol Chem*, 295(34):11949–11962.

[Marmont et al., 2017b] Marmont, L. S., Whitfield, G. B., Rich, J. D., Yip, P., Giesbrecht, L. B., Stremick, C. A., Whitney, J. C., Parsek, M. R., Harrison, J. J., and Howell, P. L. (2017b). Pela and pelb proteins form a modification and secretion complex essential for pel polysaccharide-dependent biofilm formation in. *J Biol Chem*, 292(47):19411–19422.

[Martin et al., 2008] Martin, A., Baker, T. A., and Sauer, R. T. (2008). Pore loops of the aaa+ clpx machine grip substrates to drive translocation and unfolding. *Nat Struct Mol Biol*, 15(11):1147–51.

[Mateja et al., 2015] Mateja, A., Paduch, M., Chang, H. Y., Szydlowska, A., Kossiakoff, A. A., Hegde, R. S., and Keenan, R. J. (2015). Protein targeting. structure of the get3 targeting factor in complex with its membrane protein cargo. *Science*, 347(6226):1152–5.

[McDowell et al., 2023] McDowell, M. A., Heimes, M., Enkavi, G., Farkas, A., Saar, D., Wild, K., Schwappach, B., Vattulainen, I., and Sinning, I. (2023). The get insertase exhibits conformational plasticity and induces membrane thinning. *Nat Commun*, 14(1):7355.

[McDowell et al., 2020] McDowell, M. A., Heimes, M., Fiorentino, F., Mehmood, S., Farkas, A., Coy-Vergara, J., Wu, D., Bolla, J. R., Schmid, V., Heinze, R., Wild, K., Flemming, D., Pfeffer, S., Schwappach, B., Robinson, C. V., and Sinning, I. (2020). Structural basis of tail-anchored membrane protein biogenesis by the get insertase complex. *Mol Cell*, 80(1):72–86.e7.

[McDowell et al., 2021] McDowell, M. A., Heimes, M., and Sinning, I. (2021). Structural and molecular mechanisms for membrane protein biogenesis by the oxa1 superfamily. *Nat Struct Mol Biol*, 28(3):234–239.

[McGilvray et al., 2020] McGilvray, P. T., Anghel, S. A., Sundaram, A., Zhong, F., Trnka, M. J., Fuller, J. R., Hu, H., Burlingame, A. L., and Keenan, R. J. (2020). An er translocon for multi-pass membrane protein biogenesis. *Elife*, 9.

[Milstein et al., 1972] Milstein, C., Brownlee, G. G., Harrison, T. M., and Mathews, M. B. (1972). A possible precursor of immunoglobulin light chains. *Nat New Biol*, 239(91):117–20.

[Mintz et al., 1990] Mintz, E., Lacapère, J. J., and Guillain, F. (1990). Reversal of the sarcoplasmic reticulum atpase cycle by substituting various cations for magnesium. phosphorylation and atp synthesis when ca2+ replaces mg2+. *J Biol Chem*, 265(31):18762–8.

[Ndi et al., 2018] Ndi, M., Marin-Buera, L., Salvatori, R., Singh, A. P., and Ott, M. (2018). Biogenesis of the bc(1) complex of the mitochondrial respiratory chain. *J Mol Biol*, 430(21):3892–3905.

[Nellaepalli et al., 2023] Nellaepalli, S., Lau, A. S., and Jarvis, R. P. (2023). Chloroplast protein translocation pathways and ubiquitin-dependent regulation at a glance. *J Cell Sci*, 136(18).

[Nett and Trumpower, 1999] Nett, J. H. and Trumpower, B. L. (1999). Intermediate length rieske iron-sulfur protein is present and functionally active in the cytochrome bc1 complex of saccharomyces cerevisiae. *J Biol Chem*, 274(14):9253–7.

[Ngosuwan et al., 2003] Ngosuwan, J., Wang, N. M., Fung, K. L., and Chirico, W. J. (2003). Roles of cytosolic hsp70 and hsp40 molecular chaperones in post-translational translocation of presecretory proteins into the endoplasmic reticulum. *J Biol Chem*, 278(9):7034–42.

[Nobrega et al., 1992] Nobrega, F. G., Nobrega, M. P., and Tzagoloff, A. (1992). Bcs1, a novel gene required for the expression of functional rieske iron-sulfur protein in saccharomyces cerevisiae. *EMBO J*, 11(11):3821–9.

[O'Donnell et al., 2020] O'Donnell, J. P., Phillips, B. P., Yagita, Y., Juszkiewicz, S., Wagner, A., Malinverni, D., Keenan, R. J., Miller, E. A., and Hegde, R. S. (2020). The architecture of emc reveals a path for membrane protein insertion. *Elife*, 9.

[Ou et al., 2025] Ou, X., Ma, C., Sun, D., Xu, J., Wang, Y., Wu, X., Wang, D., Yang, S., Gao, N., Song, C., and Li, L. (2025). Secy translocon chaperones protein folding during membrane protein insertion. *Cell*, 188(7):1912–1924.e13.

[Palmer and Berks, 2012] Palmer, T. and Berks, B. C. (2012). The twin-arginine translocation (tat) protein export pathway. *Nat Rev Microbiol*, 10(7):483–96.

[Palmer and Stansfeld, 2020] Palmer, T. and Stansfeld, P. J. (2020). Targeting of proteins to the twin-arginine translocation pathway. *Mol Microbiol*, 113(5):861–871.

[Palmgren, 2023] Palmgren, M. (2023). P-type atpases: Many more enigmas left to solve. *J Biol Chem*, 299(11):105352.

[Pan et al., 2023] Pan, Y., Zhan, J., Jiang, Y., Xia, D., and Scheuring, S. (2023). A concerted atpase cycle of the protein transporter aaa-atpase bcs1. *Nat Commun*, 14(1):6369.

[Park and Rapoport, 2012] Park, E. and Rapoport, T. A. (2012). Mechanisms of sec61/secy-mediated protein translocation across membranes. *Annu Rev Biophys*, 41:21–40.

[Patel et al., 2014] Patel, R., Smith, S. M., and Robinson, C. (2014). Protein transport by the bacterial tat pathway. *Biochim Biophys Acta*, 1843(8):1620–8.

[Pei and Dalbey, 2022] Pei, D. and Dalbey, R. E. (2022). Membrane translocation of folded proteins. *J Biol Chem*, 298(7):102107.

[Petriv et al., 2004] Petriv, O. I., Tang, L., Titorenko, V. I., and Rachubinski, R. A. (2004). A new definition for the consensus sequence of the peroxisome targeting signal type 2. *J Mol Biol*, 341(1):119–34.

[Petrů et al., 2018] Petrů, M., Wideman, J., Moore, K., Alcock, F., Palmer, T., and Doležal, P. (2018). Evolution of mitochondrial tat translocases illustrates the loss of bacterial protein transport machines in mitochondria. *BMC Biol*, 16(1):141.

[Phillips et al., 1993] Phillips, J. D., Graham, L. A., and Trumpower, B. L. (1993). Subunit 9 of the saccharomyces cerevisiae cytochrome bc1 complex is required for insertion of epr-detectable iron-sulfur cluster into the rieske iron-sulfur protein. *J Biol Chem*, 268(16):11727–36.

[Pleiner et al., 2020] Pleiner, T., Tomaleri, G. P., Januszyk, K., Inglis, A. J., Hazu, M., and Voorhees, R. M. (2020). Structural basis for membrane insertion by the human er membrane protein complex. *Science*, 369(6502):433–436.

[Poulin and Kuperman, 2021] Poulin, M. B. and Kuperman, L. L. (2021). Regulation of biofilm exopolysaccharide production by cyclic di-guanosine monophosphate. *Front Microbiol*, 12:730980.

[Preuss et al., 2005] Preuss, M., Ott, M., Funes, S., Luirink, J., and Herrmann, J. M. (2005). Evolution of mitochondrial oxa proteins from bacterial yidc. inherited and acquired functions of a conserved protein insertion machinery. *J Biol Chem*, 280(13):13004–11.

[Price and Driessen, 2008] Price, C. E. and Driessen, A. J. (2008). Yidc is involved in the biogenesis of anaerobic respiratory complexes in the inner membrane of escherichia coli. *J Biol Chem*, 283(40):26921–7.

[Price and Driessen, 2010] Price, C. E. and Driessen, A. J. M. (2010). Conserved negative charges in the transmembrane segments of subunit k of the nadh:ubiquinone oxidoreductase determine its dependence on yidc for membrane insertion. *J Biol Chem*, 285(6):3575–3581.

[Puchades et al., 2020] Puchades, C., Sandate, C. R., and Lander, G. C. (2020). The molecular principles governing the activity and functional diversity of aaa+ proteins. *Nat Rev Mol Cell Biol*, 21(1):43–58.

[Ramos-Arroyo et al., 2009] Ramos-Arroyo, M. A., Hualde, J., Ayechu, A., De Meirleir, L., Seneca, S., Nadal, N., and Briones, P. (2009). Clinical and biochemical spectrum of mitochondrial complex iii deficiency caused by mutations in the bcs1l gene. *Clin Genet*, 75(6):585–7.

[Rao et al., 2016] Rao, M., Okreglak, V., Chio, U. S., Cho, H., Walter, P., and Shan, S. O. (2016). Multiple selection filters ensure accurate tail-anchored membrane protein targeting. *Elife*, 5.

[Rapoport et al., 2017] Rapoport, T. A., Li, L., and Park, E. (2017). Structural and mechanistic insights into protein translocation. *Annu Rev Cell Dev Biol*, 33:369–390.

[Razvi et al., 2023] Razvi, E., Whitfield, G. B., Reichhardt, C., Dreifus, J. E., Willis, A. R., Gluscencova, O. B., Gloag, E. S., Awad, T. S., Rich, J. D., da Silva, D. P., Bond, W., Le Mauff, F., Sheppard, D. C., Hatton, B. D., Stoodley, P., Reinke, A. W., Boulianne, G. L., Wozniak, D. J., Harrison, J. J., Parsek, M. R., and Howell, P. L. (2023). Glycoside hydrolase processing of the pel polysaccharide alters biofilm biomechanics and pseudomonas aeruginosa virulence. *NPJ Biofilms Microbiomes*, 9(1):7.

[Reimers et al., 2025] Reimers, M., Jakob, M., and Klösgen, R. B. (2025). The thylakoidal tat receptor complex appears as a homo-trimeric tatc core with three associated tatb subunits. *Biochim Biophys Acta Mol Cell Res*, 1872(7):120024.

[Rieske et al., 1964] Rieske, J. S., Zaugg, W. S., and Hansen, R. E. (1964). Studies on the electron transfer sytem. lix. distribution of iron aad of the component giving an electron paramagnetic resonance signal at g = 1.90 in subfractions of complex 3. *J Biol Chem*, 239:3023–30.

[Rodrigue et al., 1999] Rodrigue, A., Chanal, A., Beck, K., Müller, M., and Wu, L. F. (1999). Co-translocation of a periplasmic enzyme complex by a hitchhiker mechanism through the bacterial tat pathway. *J Biol Chem*, 274(19):13223–8.

[Rollauer et al., 2012] Rollauer, S. E., Tarry, M. J., Graham, J. E., Jääskeläinen, M., Jäger, F., Johnson, S., Krehenbrink, M., Liu, S. M., Lukey, M. J., Marcoux, J., McDowell, M. A., Rodriguez, F., Roversi, P., Stansfeld, P. J., Robinson, C. V., Sansom, M. S., Palmer, T., Högbom, M., Berks, B. C., and Lea, S. M. (2012). Structure of the tatc core of the twin-arginine protein transport system. *Nature*, 492(7428):210–4.

[Rosales-Hernandez et al., 2025] Rosales-Hernandez, C., Thoms, M., Berninghausen, O., Becker, T., and Beckmann, R. (2025). Mechanistic insights into bcs1-mediated mitochondrial membrane translocation of the folded rieske protein. *EMBO J*, 44(13):3720–3741.

[Russell and Hall, 1997] Russell, M. J. and Hall, A. J. (1997). The emergence of life from iron monosulphide bubbles at a submarine hydrothermal redox and ph front. *J Geol Soc London*, 154(3):377–402.

[Schuldiner et al., 2008] Schuldiner, M., Metz, J., Schmid, V., Denic, V., Rakwalska, M., Schmitt, H. D., Schwappach, B., and Weissman, J. S. (2008). The get complex mediates insertion of tail-anchored proteins into the er membrane. *Cell*, 134(4):634–45.

[Seppälä et al., 2010] Seppälä, S., Slusky, J. S., Lloris-Garcerá, P., Rapp, M., and von Heijne, G. (2010). Control of membrane protein topology by a single c-terminal residue. *Science*, 328(5986):1698–700.

[Seurig et al., 2019] Seurig, M., Ek, M., von Heijne, G., and Fluman, N. (2019). Dynamic membrane topology in an unassembled membrane protein. *Nat Chem Biol*, 15(10):945–948.

[Shao and Hegde, 2011] Shao, S. and Hegde, R. S. (2011). A calmodulin-dependent translocation pathway for small secretory proteins. *Cell*, 147(7):1576–88.

[Shaw et al., 1988] Shaw, A. S., Rottier, P. J., and Rose, J. K. (1988). Evidence for the loop model of signal-sequence insertion into the endoplasmic reticulum. *Proc Natl Acad Sci U S A*, 85(20):7592–6.

[Skowyra et al., 2024] Skowyra, M. L., Feng, P., and Rapoport, T. A. (2024). Towards solving the mystery of peroxisomal matrix protein import. *Trends Cell Biol*, 34(5):388–405.

[Smalinskaitė and Hegde, 2023] Smalinskaitė, L. and Hegde, R. S. (2023). The biogenesis of multipass membrane proteins. *Cold Spring Harb Perspect Biol*, 15(4).

[Smalinskaitė et al., 2022] Smalinskaitė, L., Kim, M. K., Lewis, A. J. O., Keenan, R. J., and Hegde, R. S. (2022). Mechanism of an intramembrane chaperone for multipass membrane proteins. *Nature*, 611(7934):161–166.

[Stanley et al., 2000] Stanley, N. R., Palmer, T., and Berks, B. C. (2000). The twin arginine consensus motif of tat signal peptides is involved in sec-independent protein targeting in escherichia coli. *J Biol Chem*, 275(16):11591–6.

[Stephan and Ott, 2020] Stephan, K. and Ott, M. (2020). Timing of dimerization of the bc(1) complex during mitochondrial respiratory chain assembly. *Biochim Biophys Acta Bioenerg*, 1861(5-6):148177.

[Sundaram et al., 2022] Sundaram, A., Yamsek, M., Zhong, F., Hooda, Y., Hegde, R. S., and Keenan, R. J. (2022). Substrate-driven assembly of a translocon for multipass membrane proteins. *Nature*, 611(7934):167–172.

[Sundberg et al., 1997] Sundberg, E., Slagter, J. G., Fridborg, I., Cleary, S. P., Robinson, C., and Coupland, G. (1997). Albino3, an arabidopsis nuclear gene essential for chloroplast differentiation, encodes a chloroplast protein that shows homology to proteins present in bacterial membranes and yeast mitochondria. *Plant Cell*, 9(5):717–30.

[Sánchez et al., 2013] Sánchez, E., Lobo, T., Fox, J. L., Zeviani, M., Winge, D. R., and Fernández-Vizarra, E. (2013). Lyrm7/mzm1l is a uqcrfs1 chaperone involved in the last steps of mitochondrial complex iii assembly in human cells. *Biochim Biophys Acta*, 1827(3):285–93.

[Tang et al., 2020] Tang, W. K., Borgnia, M. J., Hsu, A. L., Esser, L., Fox, T., de Val, N., and Xia, D. (2020). Structures of aaa protein translocase bcs1 suggest translocation mechanism of a folded protein. *Nat Struct Mol Biol*, 27(2):202–209.

[Thomas and Tampé, 2020] Thomas, C. and Tampé, R. (2020). Structural and mechanistic principles of abc transporters. *Annu Rev Biochem*, 89:605–636.

[Tomasek and Kahne, 2021] Tomasek, D. and Kahne, D. (2021). The assembly of beta-barrel outer membrane proteins. *Curr Opin Microbiol*, 60:16–23.

[Tomoyasu et al., 1993] Tomoyasu, T., Yuki, T., Morimura, S., Mori, H., Yamanaka, K., Niki, H., Hiraga, S., and Ogura, T. (1993). The escherichia coli ftsh protein is a prokaryotic member of a protein family of putative atpases involved in membrane functions, cell cycle control, and gene expression. *J Bacteriol*, 175(5):1344–51.

[Tripathi et al., 2017] Tripathi, A., Mandon, E. C., Gilmore, R., and Rapoport, T. A. (2017). Two alternative binding mechanisms connect the protein translocation sec71-sec72 complex with heat shock proteins. *J Biol Chem*, 292(19):8007–8018.

[Tsukazaki et al., 2008] Tsukazaki, T., Mori, H., Fukai, S., Ishitani, R., Mori, T., Dohmae, N., Perederina, A., Sugita, Y., Vassylyev, D. G., Ito, K., and Nureki, O. (2008). Conformational transition of sec machinery inferred from bacterial secye structures. *Nature*, 455(7215):988–91.

[Vale, 2000] Vale, R. D. (2000). Aaa proteins. lords of the ring. *J Cell Biol*, 150(1):F13–9.

[van Bloois et al., 2006] van Bloois, E., Haan, G. J., de Gier, J. W., Oudega, B., and Luirink, J. (2006). Distinct requirements for translocation of the n-tail and c-tail of the escherichia coli inner membrane protein cyoa. *J Biol Chem*, 281(15):10002–9.

[van Bloois et al., 2005] van Bloois, E., Nagamori, S., Koningstein, G., Ullers, R. S., Preuss, M., Oudega, B., Harms, N., Kaback, H. R., Herrmann, J. M., and Luirink, J. (2005). The sec-independent function of escherichia coli yidc is evolutionary-conserved and essential. *J Biol Chem*, 280(13):12996–3003.

[Van den Berg et al., 2004] Van den Berg, B., Clemons, W. M., Collinson, I., Modis, Y., Hartmann, E., Harrison, S. C., and Rapoport, T. A. (2004). X-ray structure of a protein-conducting channel. *Nature*, 427(6969):36–44.

[van Loon et al., 1987] van Loon, A. P., Brändli, A. W., Pesold-Hurt, B., Blank, D., and Schatz, G. (1987). Transport of proteins to the mitochondrial intermembrane space: the 'matrix-targeting' and the 'sorting' domains in the cytochrome c1 presequence. *EMBO J*, 6(8):2433–9.

[Van Loon et al., 2025] Van Loon, J. C., Le Mauff, F., Vargas, M. A., Gilbert, S., Pfoh, R., Morrison, Z. A., Razvi, E., Nitz, M., Sheppard, D. C., and Howell, P. L. (2025). Structural and functional analysis of pseudomonas aeruginosa pela provides insight into the modification of the pel exopolysaccharide. *J Biol Chem*, 301(5):108432.

[Vasseur et al., 2007] Vasseur, P., Soscia, C., Voulhoux, R., and Filloux, A. (2007). Pelc is a pseudomonas aeruginosa outer membrane lipoprotein of the oma family of proteins involved in exopolysaccharide transport. *Biochimie*, 89(8):903–15.

[Vasseur et al., 2005] Vasseur, P., Vallet-Gely, I., Soscia, C., Genin, S., and Filloux, A. (2005). The pel genes of the pseudomonas aeruginosa pak strain are involved at early and late stages of biofilm formation. *Microbiology (Reading)*, 151(Pt 3):985–997.

[Vergalli et al., 2020] Vergalli, J., Bodrenko, I. V., Masi, M., Moynié, L., Acosta-Gutiérrez, S., Naismith, J. H., Davin-Regli, A., Ceccarelli, M., van den Berg, B., Winterhalter, M., and Pagès, J. M. (2020). Porins and small-molecule translocation across the outer membrane of gram-negative bacteria. *Nat Rev Microbiol*, 18(3):164–176.

[von Heijne, 2007] von Heijne, G. (2007). The membrane protein universe: what's out there and why bother? *J Intern Med*, 261(6):543–557.

[Voorhees et al., 2014] Voorhees, R. M., Fernández, I. S., Scheres, S. H., and Hegde, R. S. (2014). Structure of the mammalian ribosome-sec61 complex to 3.4 Å resolution. *Cell*, 157(7):1632–43.

[Voorhees and Hegde, 2016] Voorhees, R. M. and Hegde, R. S. (2016). Structure of the sec61 channel opened by a signal sequence. *Science*, 351(6268):88–91.

[Wagener et al., 2011] Wagener, N., Ackermann, M., Funes, S., and Neupert, W. (2011). A pathway of protein translocation in mitochondria mediated by the aaa-atpase bcs1. *Mol Cell*, 44(2):191–202.

[Wagener and Neupert, 2012] Wagener, N. and Neupert, W. (2012). Bcs1, a aaa protein of the mitochondria with a role in the biogenesis of the respiratory chain. *J Struct Biol*, 179(2):121–5.

[Walter and Blobel, 1981a] Walter, P. and Blobel, G. (1981a). Translocation of proteins across the endoplasmic reticulum. ii. signal recognition protein (srp) mediates the selective binding to microsomal membranes of in-vitro-assembled polysomes synthesizing secretory protein. *J Cell Biol*, 91(2 Pt 1):551–6.

[Walter and Blobel, 1981b] Walter, P. and Blobel, G. (1981b). Translocation of proteins across the endoplasmic reticulum iii. signal recognition protein (srp) causes signal sequence-dependent and site-specific arrest of chain elongation that is released by microsomal membranes. *J Cell Biol*, 91(2 Pt 1):557–61.

[Wang and Hegde, 2024] Wang, H. and Hegde, R. S. (2024). Identification of a factor that accelerates substrate release from the signal recognition particle. *Science*, 386(6725):996–1003.

[Wang and Lavrov, 2007] Wang, X. and Lavrov, D. V. (2007). Mitochondrial genome of the homoscleromorph oscarella carmela (porifera, demospongiae) reveals unexpected complexity in the common ancestor of sponges and other animals. *Mol Biol Evol*, 24(2):363–73.

[Wang et al., 2016] Wang, Y., Andole Pannuri, A., Ni, D., Zhou, H., Cao, X., Lu, X., Romeo, T., and Huang, Y. (2016). Structural basis for translocation of a biofilm-supporting exopolysaccharide across the bacterial outer membrane. *J Biol Chem*, 291(19):10046–57.

[White and Wimley, 1999] White, S. H. and Wimley, W. C. (1999). Membrane protein folding and stability: physical principles. *Annu Rev Biophys Biomol Struct*, 28:319–65.

[Whitfield and Howell, 2021] Whitfield, G. B. and Howell, P. L. (2021). The matrix revisited: Opening night for the pel polysaccharide across eubacterial kingdoms. *Microbiol Insights*, 14:1178636120988588.

[Whitfield et al., 2020] Whitfield, G. B., Marmont, L. S., Ostaszewski, A., Rich, J. D., Whitney, J. C., Parsek, M. R., Harrison, J. J., and Howell, P. L. (2020). Pel polysaccharide biosynthesis requires an inner membrane complex comprised of peld, pele, pelf, and pelg. *J Bacteriol*, 202(8).

[Whitney et al., 2012] Whitney, J. C., Colvin, K. M., Marmont, L. S., Robinson, H., Parsek, M. R., and Howell, P. L. (2012). Structure of the cytoplasmic region of peld, a

degenerate diguanylate cyclase receptor that regulates exopolysaccharide production in pseudomonas aeruginosa. *J Biol Chem*, 287(28):23582–93.

[Whitney and Howell, 2013] Whitney, J. C. and Howell, P. L. (2013). Synthase-dependent exopolysaccharide secretion in gram-negative bacteria. *Trends Microbiol*, 21(2):63–72.

[Wikström and Sharma, 2018] Wikström, M. and Sharma, V. (2018). Proton pumping by cytochrome c oxidase - a 40 year anniversary. *Biochim Biophys Acta Bioenerg*, 1859(9):692–698.

[Woodall et al., 2017] Woodall, N. B., Hadley, S., Yin, Y., and Bowie, J. U. (2017). Complete topology inversion can be part of normal membrane protein biogenesis. *Protein Sci*, 26(4):824–833.

[Wu and Zhuang, 2025] Wu, J. and Zhuang, M. (2025). Pieces of the peroxisomal import puzzle. *Nat Cell Biol*, 27(8):1204–1205.

[Yang et al., 2025] Yang, T.-J., Mukherjee, S., Langer, J. D., Hummer, G., and McDowell, M. A. (2025). Snd3 is the membrane insertase within a fungal multipass translocon. *bioRxiv*, page 2025.07.08.663624.

[Yost et al., 1983] Yost, C. S., Hedgpeth, J., and Lingappa, V. R. (1983). A stop transfer sequence confers predictable transmembrane orientation to a previously secreted protein in cell-free systems. *Cell*, 34(3):759–66.

[Zhan et al., 2024] Zhan, J., Zeher, A., Huang, R., Tang, W. K., Jenkins, L. M., and Xia, D. (2024). Conformations of bcs1l undergoing atp hydrolysis suggest a concerted translocation mechanism for folded iron-sulfur protein substrate. *Nat Commun*, 15(1):4655.

[Zhang et al., 2021] Zhang, G., Li, S., Cheng, K. W., and Chou, T. F. (2021). Aaa atpases as therapeutic targets: Structure, functions, and small-molecule inhibitors. *Eur J Med Chem*, 219:113446.

[Zimmer et al., 2008] Zimmer, J., Nam, Y., and Rapoport, T. A. (2008). Structure of a complex of the atpase seca and the protein-translocation channel. *Nature*, 455(7215):936–43.

Acknowledgements

I would like to express my sincere gratitude to Prof. Dr. Roland Beckmann for giving me the chance to join his lab. This experience definitely changed my life in many ways and gave me a broader perspective on what doing science actually means. Thanks to his constant support and positivity, I was able to move all my projects forward, and I learned from him not only about the technical aspects of science but also about its human side.

Secondly, I want to thank Prof. Dr. Alexej Kedrov for the great collaborative projects we worked on. His energetic style and persistence were key factors in reaching our goals and motivated me to accomplish everything we set out to achieve. I also want to thank his colleagues and team members Max, Marius, and Michael for their work, their support, and the fruitful scientific discussions we had.

In addition, I want to thank Dr. Dejana Mokranjac for inviting me to join the Mito-Club. It was a very enriching experience, and the Bcs1 project benefited immensely from all her expertise and scientific input, as well as from discussions with the members of the club.

Next, I would like to thank the members of my Examination Board: Prof. Dr. Roland Beckmann (acting as the first examiner), Prof. Dr. Karl-Peter Hopfner (acting as the second examiner), Prof. Dr. Alexej Kedrov, Prof. Dr. Julian Stingele, PD Dr. Dejana Mokranjac, and PD Dr. Gregor Witte. I am very thankful for your time and willingness to evaluate the results of my PhD work.

I want to thank the Graduate School of Quantitative and Molecular Biosciences Munich (QMB) for their support through lectures, workshops, team-building activities, social events, and funding for German courses, visa fees, and tools. Thanks to the scientific co-

ordinator Prof. Dr. Erwin Frey and the former coordinator Dr. Markus Hohle, as well as the new coordinators Dr. Beate Hafner and Dr. Christophe Jung, and all past and current students for their efforts in keeping QMB alive.

Furthermore, I would like to thank the scientific staff of the Beckmann lab. Thanks to Dr. Thomas Becker for his mentorship and guidance in scientific writing, cryo-EM data processing, visualisation, validation, and for reading the original draft of this thesis. Thanks to Dr. Matthias Thoms for his mentorship and guidance in experimental design and data analysis. Thanks to Dr. Otto Berninghausen for his efficient management of the Cryo-EM facility, his support in data collection and curation, and his scientific input. Thanks to Dr. Birgitta Beatrix for overseeing, among many other tasks, lab documentation and safety, and for her scientific input.

On the same note, I am deeply grateful to our team of technical assistants: Alicia, Andrea, Charlotte, Joanna, and Susi; our former administrative assistant Aleksandra and our new administrative assistant Gudrun; and our labware maintenance team Natasa and Nevena.

Thanks to Alicia, Andrea, and Joanna for all your efforts in keeping the lab organised, clean, and running — it definitely makes work easier and the environment more pleasant. Thank you, Joanna, for all the nice conversations, for letting me practise my German with you, and for your joyful spirit. Thank you, Andrea, for always being ready to help, and thank you, Alicia, for your good vibes. Thanks to Susi and Charlotte for their great work at the microscope facility, for handling samples and taking care of data collection. Thank you, Susi, for your nice attitude and for all the German/Titan Krios training sessions we had. Thank you, Aleksandra, for all your help in getting me started in Germany. Thank you, Gudrun, for your efficiency and reliability. Thank you, Natasa and Nevena, for all the hard work behind the scenes.

Thanks to all my colleagues in the Beckmann lab, past and present, for their team spirit, the nice social events, and the good memories. Thank you, Dandan, Hanna Esser, Hanna Kratzat, Hendrik, Ivan, Jakub, Kathy, Ken, Kohei, Leona, Martin, Petr, Robert, Shuangshuang, Timo and Timur. Thank you, Ivan and Leona, for all the work as the ad

hoc IT Task Force — the core of our work relies on running servers, and you do a great job keeping them in shape. Thank you, Martin and Kohei, for the nice conversations over single-origin, micro-lot, shade-grown, hand-picked, fair-trade, ethically roasted speciality coffee. Thank you, Timur and Leona, for organising our unforgettable social events. Thank you, Matthias and Timo, for sharing your critical views and the nice talks over beer.

I want to thank the students I supervised during my PhD: Annika, Hendrik, Nikolai, and Oktay. Thank you for all your work, positive attitude, and friendliness. It was a pleasure working with you, and I wish you the best of luck for your future.

During my PhD, I had the luck to meet people with whom I have shared nice moments, and I am very grateful to them. I want to thank Thomas and Nives for their friendship. Thank you, Nives, for bringing me up to speed at the beginning of my PhD, for showing me around, and for your scientific input. Thank you, Thomas, for organising hikes, dinners at restaurants, and game nights at home. Thank you, Jing, for the nice conversations during lunch or over coffee.

Moving to Germany has been one of the most challenging endeavours of my life. It has brought many changes and hard moments, but also great opportunities to grow and become a better version of myself. It is certainly a decision I will never regret. I will always be grateful to the people who were there and are there for me, because they have given me the strength to keep going. Thank you, Lina, for your patience, support, and care. Thank you, Cindy, for being my friend for more than 15 years, for sharing the experience of doing a PhD in Germany, and for all the partying and happy memories. Thank you, Andrés, for being my friend despite years of not seeing each other. Thank you, Mum, Dad, Danilo, and Saida, for your unconditional love.

Finally, thank you, Mariia. When I decided to work on Bcs1, I never imagined that this journey would lead me to one of the most extraordinary people in my life. Thank you not only for helping me with the ATPase assays, but also for all the incredible memories that followed and for all the love we share. You are an amazing scientist and an even more amazing human being, and you inspire me every day to be better.